Title	Study of a kaon bound nuclear state in the 3He(K-, Λp)n reaction at pK-=1 GeV/c
Author(s)	山我, 拓巳
Citation	大阪大学, 2018, 博士論文
Version Type	VoR
URL	https://doi.org/10.18910/69337
rights	
Note	

Study of a kaon bound nuclear state in the $^3\mathrm{He}\left(K^-,\Lambda p\right)n$ reaction at $p_{K^-}=1\ GeV/c$
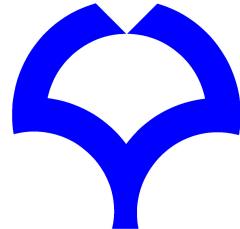
Takumi Yamaga

Department of Physics

Osaka University

This dissertation is submitted for the degree of

Doctor of Philosophy

February 2018

Abstract

The existence of the kaon bound nuclear system has been expected due to the strong attractive force of the $K\bar{N}$ interaction in isospin (I) equal to zero channel ($I = 0$). The kaonic nuclear bound state has been studying for long time both experimental and theoretical side, especially in the simplest system of the K^-pp bound state. Theoretical calculations predicted the existance of the $\bar{K}NN$ bound state with small binding energy, i.e. $\sim$ 40 - 60 MeV respect to the $\bar{K}NN$ threshold. However, no experimental signal has been reported around the region of interest to data. on the other hand, a few experimental groups were claimed the observation of so call K^-pp-like structure, however the reported binding energy were much deeper than any theoretical predictions, namely $\sim$ 100 MeV. Therefore, more experimental study of the K^-pp bound state is strongly desired.

The Λp invariant-mass spectrum in the ${}^3\text{He}\,(K^-, \Lambda p)\,n$ reaction was analyzed to study for a kaon bound nuclear system at J-PARC K1.8BR beam-line. In the analysis, peak structure around the K^-pp mass-threshold in the Λp invariant-mass spectrum have been observed. The peak structure was concentrated with the neutron emission angle $\cos\theta_n^{CM}$ of more than 0.7. To investigate the nature of the peak structure seen around K^-pp threshold, background contribution was subtracted which evaluated by selection neutron emitted toward backward direction, namely $\cos\theta_n^{CM}$ from 0.0 to 0.7.

The peak structure was evaluated with Gaussian and/or Breit-Wigner distribution. In the case of fitting with single distribution either Gaussian or Breit-Wigner distribution, the χ^2/ndf were found to be large, i.e. $\sim$ 3.22, and significant residual events were seen around invariant-mass of around 2.35 and 2.45 GeV/c^2. Therefore, the structure can not be explained as a single distribution. Thus, the structure was evaluated with three cases of two distributions, two Gaussian, two Breit-Wigner and combination of Gaussian and Breit-Wigner. The best value of the χ^2/ndf was found with combination of Gaussian and Breit-Wigner, where the lower and higher peak structure seems Breit-Wigner and Gaussian distribution, respectively. The observed peak structures were located below and above the K^-pp mass-threshold. By studying the fine $\cos\theta_n^{CM}$ sliced invariant-mass spectra, it was observed that the mass position of the higher peak was moved with varying the $\cos\theta_n^{CM}$. In contrast, the mass position and width were not changed in each $\cos\theta_n^{CM}$ region. With this analysis, the peak structure located

above $K-pp$ threshold was concluded as the events created by quasi-elastic K^- scattering following by K^- absorption via two nucleons. On the other hand, the structure below the threshold could not be explained by such processes. Therefore, the peak structure could be the K^-pp bound state. The peak position and width of the observed peak structure were found to be $2.326 \pm 0.004(stat.)^{+0.007}_{-0.002}(sys.)$ GeV/c^2 and $0.064 \pm 0.008(stat.)^{+0.014}_{-0.007}(sys.)$ GeV/c^2, respectively.

Acknowledgements

Table of contents

List of figures

List of tables

Chapter 1

Introduction

1.1 Kaonic nuclear bound system

Strong interaction between meson and baryon is important to understand the hadron. Mesonic atoms, in which a meson is bound in nucleus by the Coulomb interaction, have been studied by measuring the X-ray from mesonic atoms to studying for the interaction between meson and baryon. However, these experiment only have informations of the interaction above the threshold. One of the way to obtain more information about meson-nucleus interaction is direct measuring of the meson-baryon bound systems. In 2004, there was a observation of the low-lying pion-atomic states in the $(d, {}^3\mathrm{He})$ reaction at GSI[1–4]. The deduced reduction of the isovector parameter of the s-wave pion-nucleon potential at the normal nuclear density was considered to be an evidence for the partial restoration of chiral symmetry. On the other hand, there are theoretical calculations which predict the reduction of the effective K^- mass in a nuclear medium[5, 6]. Consequence of a strong attractive interaction between anti-kaon and nucleon in isospin I equal to zero channel, the existence of kaonic nuclear bound state has been predicted theoretically. However, kaonic nuclear bound states have not established yet in both theory and experiment.

1.1.1 $\bar{K}N$ interaction

The $\bar{K}N$ interaction has been investigated by low energy scattering experiments[7] and X-ray measurements of anti-kaonic hydrogen. The data from the two methods were not consistently understood until revising the X-ray data by a new measurement at KEK [8]. After these experimental results, the $\bar{K}N$ interaction in $I = 0$ channel is established as strong attractive interaction. Recently, the X-ray data at KEK was confirmed by the DEAR experiment[9] and the SIDDHARTA experiment[10] at DAΦNE in Italy.

However the $\bar{K}N$ interaction, especially below the threshold, is still not understood well. $\Lambda(1405)$, the mass of which is located just below the $\bar{K}N$ threshold, is a hyperon resonance, whose spin-parity J^P and isospin are equal to $(1/2)^-$, and $I = 0$, respectively. The mass of $\Lambda(1405)$ is too light to be described as a 3-quark state in a constituent quark model. Therefore, it can be interpreted as a quasi-bound state of $\bar{K}N$ with a binding energy of 27 MeV[11]. On the other hand, a theoretical calculation based on a chiral unitary model claims that $\Lambda(1405)$ is dynamically generated by the meson-baryon interactions and consists of two poles coupled to the $\pi\Sigma$ and $\bar{K}N$ states[12]. According to the model calculation, the pole position in the S-wave $\bar{K}N$ scattering amplitude is located at 1426-16i MeV. Thus, the $\bar{K}N$ interaction is expected to be weaker than that predicted by other phenomenological model calculations. Experimental study of the structure of $\Lambda(1405)$ is now being performed. New data of $\pi\Sigma$ mass spectra below the $\bar{K}N$ mass threshold are reported in different charge states produced by γ-induced reaction at CLAS[13, 14] and LEPS[15] spectrometers, and *pp* collisions at COSY[16] and with HADES spectrometer at GSI[17]. These data support the structure of the $\Lambda(1405)$ resonance as two poles state. Further experiment with a kaon beam at J-PARC[18] will come, and be helpful for further understanding of the nature of $\Lambda(1405)$ and the $\bar{K}N$ interaction.

1.1.2 $\bar{K}$-nucleus interaction

$\bar{K}$-nucleus interaction has been studied by the systematic measurement of *X*-rays from excited kaonic atoms. Intensive measurements of *X*-rays from *X*-ray were performed in 1970's and 1980's. A global fit of those data with a density-dependent potential resulted in a deep potential in the real part -160∼-200 MeV[19]. On the other hand, chirally motivated calculations reproducing the *X*-ray data suggest a relatively shallow potential -40∼-60 MeV[20]. Moreover, experimental observation of kaonic nuclear states is expected to provide more important information on the $\bar{K}$-nucleus interaction.

1.1.3 Prediction of kaonic nuclear bound state

The idea of kaon nuclear bound state was proposed by Nogami in 1963 for the first time[21] soon after the discovery of $\Lambda(1405)$[22]. A hypothesis of the possible existence of deeply-bound $\bar{K}$ states was advocated by Wycech in 1986 based on the kaonic atom data[23]. However, we had to wait for the establishment of the attractive $\bar{K}N$ interaction by the new kaonic hydrogen X-ray data[8] to motivate further study on this topic. Recent extensive studies on the kaonic nuclei were triggered by Akaishi and Yamazaki, who carried out a pioneering work on the light kaonic nuclear systems[11][24]. Their calculation was based

on a phenomenological $\bar{K}N$ interaction, where $\Lambda(1405)$ was assumed to be a K^-p bound state with $I=0$. They predicted a narrow ($\sim$20 MeV) state below the $\Sigma\pi$ emission threshold in the case of K^- in ^{3}He nuclei. They also pointed out a unique feature of the kaonic nuclear system that the central density of such system becomes 5-10 times higher than the normal nuclear density[25].

1.2 Experimental researches of kaonic nuclear bound state

Many experiments to search for the kaonic nuclear bound states were performed. A some of experimental researches are reviewed below.

1.2.1 Stopped K^- experiment at KEK

A series of experiments with the $^4(K^-_{stopped}, N)$ reaction were performed in KEK (KEK PS E471[26],E549[27][28]). These experiments reported that a branching fraction to form a deeply bound $\bar{K}NNN$ state with a narrow width of 20 or 40 MeV/c^2 (claimed once as a tribaryon state) was less than 1% of stopped kaon events. The inclusive proton spectrum is shown in Fig. 1.1. Although the statistics and the experimental resolution were high, they suffered from rather large background contributions in the region of interest which come from the hyperon decays and multi-nucleon absorptions. An exclusive analysis in the ^{4}He($K^-_{stop}, n\pi^{\pm}$) reaction based on these data shows that even ^{4}He is too complicated to obtain the conclusive evidence of the formation of kaonic nuclear states[29]

1.2.2 In-flight K^- experiment

Experiments via the $K^-_{in-flight}, N$ reaction on ^{12}C was proposed[30] and performed at BNL[31] and at KEK[32]. The semi-inclusive spectra of the (K^-, n) and (K^-, p) reactions measured at KEK are shown in Fig.1.2. The measured spectra were compared to calculated spectra by a Green's function method. They reported that the (K^-, n) and (K^-, p) spectra were reproduced for kaon nucleus optical potentials of $(-190-i40)$ MeV and $(-160-i50)$ MeV, respectively. However, there is a claim from theoretical calculation that the spectrum shape can be reproduced by a moderate potential depth of -60 MeV[33].

In the in-flight reaction, non-mesonic two nucleon absorption processes are suppressed.
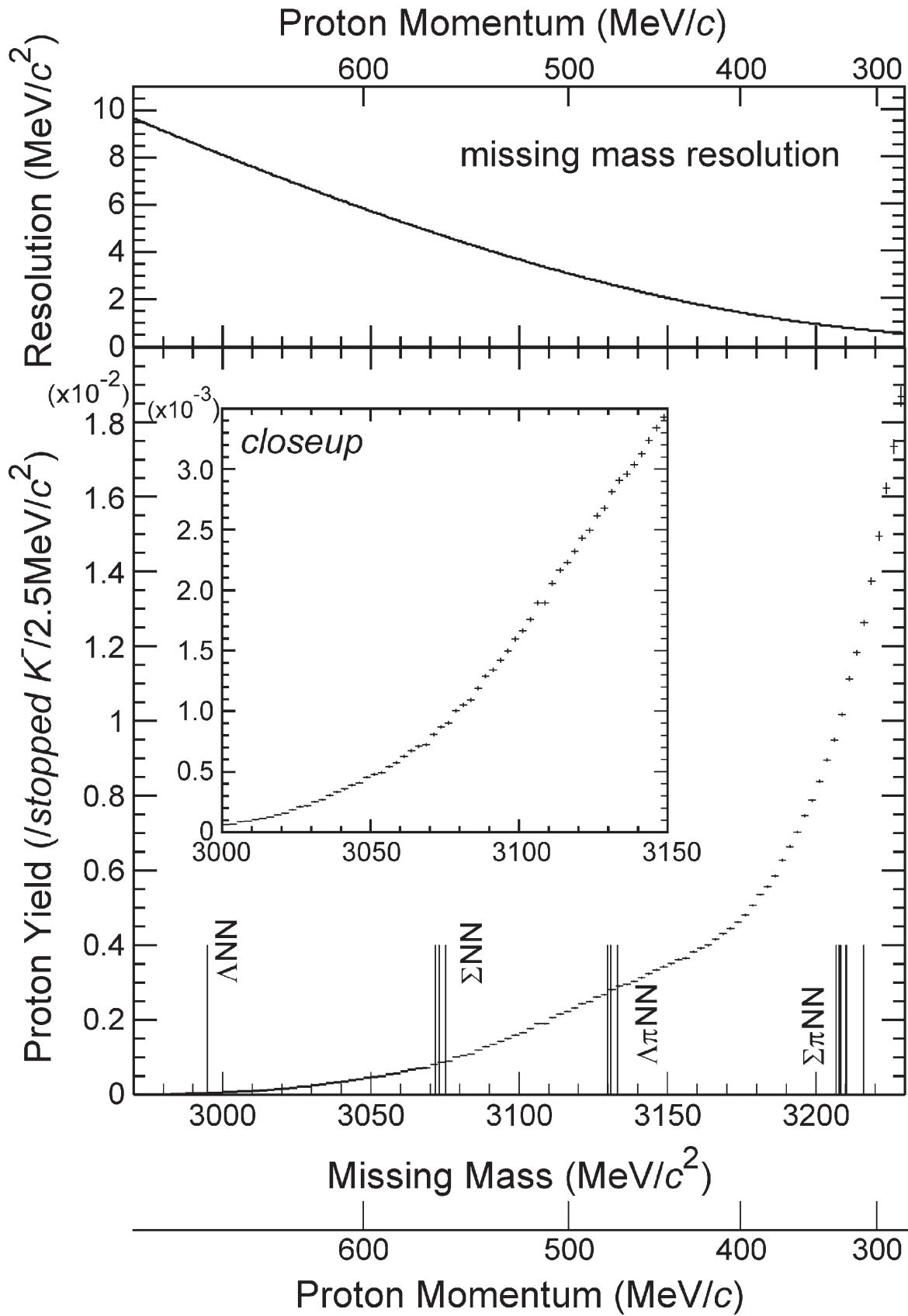
Fig. 1.1 The proton inclusive missing mass spectrum obtained in the KEK E549/570 experiment[27].
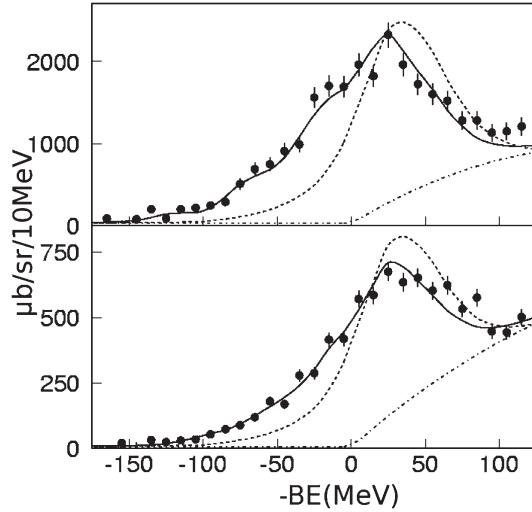
Fig. 1.2 Missing mass spectra of the $^{12}\text{C}(K^-,n)$ reaction (upper) and $^{12}\text{C}(K^-,p)$ reaction (lower) in the KEK E548 experiment. The solid curves represent the calculated best fit spectra for potentials with Re(V)=-190 MeV and Im(V)=-40 MeV (upper) and Re(V)=-160 MeV Im(V)=-50 MeV (lower). The dotted curves represent the calculated spectra for Re(V)=-60 MeV and Im(V)=-60 MeV. The dot-dashed curves represent a background process. Taken from Ref. [32].

1.2.3 Results of the $K^- pp$ bound system searching

The lightest kaonic nucleus is expected to be $\bar{K}NN$ bound state. It is more generally expressed as $[\bar{K} \otimes \{NN\}_{I=1}]_{I=1/2}$, where the maximum combinations of the strongly attractive I=0 channel is realized among the three-body systems. The configurations of the lightest $\bar{K}NN$ bound state are $K^- pp$ and $\bar{K}^0 pn$ system, so-called $K^- pp$ bound state.

FINUDA experiment

The FINUDA collaboration at DAΦNE reported a possible evidence of a deeply-bound $K^- pp$ state in the invariant mass spectrum of back-to-back Λp pairs from the stopped K^- absorption on ^{6}Li, ^{7}Li and ^{12}C[34]. The observed spectrum is shown in Fig. 1.3. They reported that a binding energy and width of the observed peak were 115^{+6}_{-6}(stat.)$^{+3}_{-4}$(sys.) MeV and 67^{+14}_{-11}(stat.)$^{+2}_{-3}$(sys.) MeV, respectively. However, quasi-free two-nucleon reaction followed by secondary processes would contribute to the region around the observed bump structure[35, 36]. They are now finalizing an analysis of the data obtained in the second data taking during 2006 and 2007, where such processes are considered in the global fit of the Λp distributions[37]. Another criticism sometimes quoted to the result is that the acceptance of
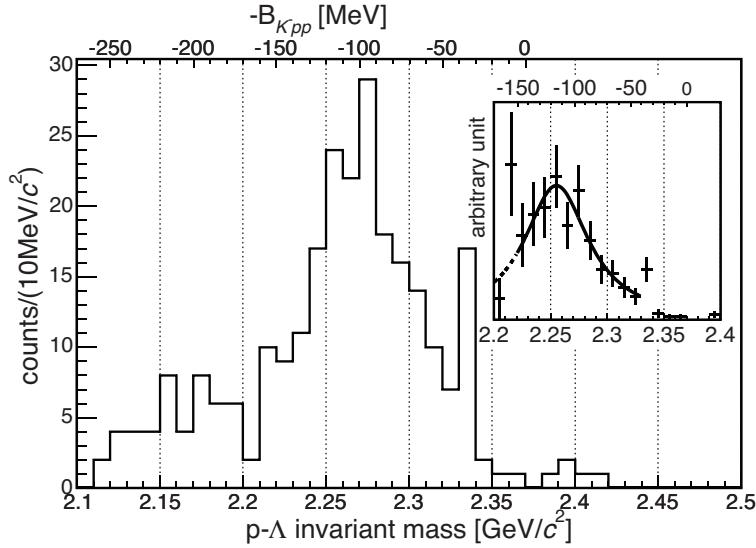
Fig. 1.3 Invariant mass of a Λ and a proton in back-to-back correlation ($\cos\theta^{Lab} < -0.8$) from light targets before the acceptance correction in the FINUDA experiment. The inset shows the result after the acceptance correction. Taken from Ref.[34]

the given spectrum is too narrow for the clear determination of the background below the suggested peak structure.

DISTO experiment

A large formation probability of the K^-pp bound state in pp collision was predicted by Yamazaki, *et al.*[38]. They calculated the process Λ^* and p form to K^-pp following the elementary process, $p + p \rightarrow p + \Lambda^* + K^+$. They insisted the Λ^*p sticking become dominant due to the matching of the small impact parameter (large momentum transfer) with the compact bound state.

The DISTO collaboration at SATURNE re-analyzed their data on the exclusive $p + p \rightarrow p + \Lambda + K^+$ events at T_p= 2.85 GeV[39], assuming K^-pp decaying into Λp. The K^+ missing mass spectrum obtained as the deviation to the uniform phase space distribution of the ΛpK^+ final state is shown in Fig. 1.4(left). A broad peak structure was observed at a mass of 2265.2 MeV/c^2 and a width of 118.8 MeV/c^2, and they associated it to the dibaryon state with strangeness -1 as X(2265). They also analyzed the data at T_p= 2.5 GeV and found no corresponding peak observed at T_p= 2.85 GeV[40].

If $X(2265)$ follows the excitation function in a semi-empirical universal form of Sibirtsev[41], the peak should be observed also at T_p=2.5 GeV as shown in Fig. 1.4(right). Furthermore, they ignored N^* resonances, whose contributions in the pp collision were pointed out by the
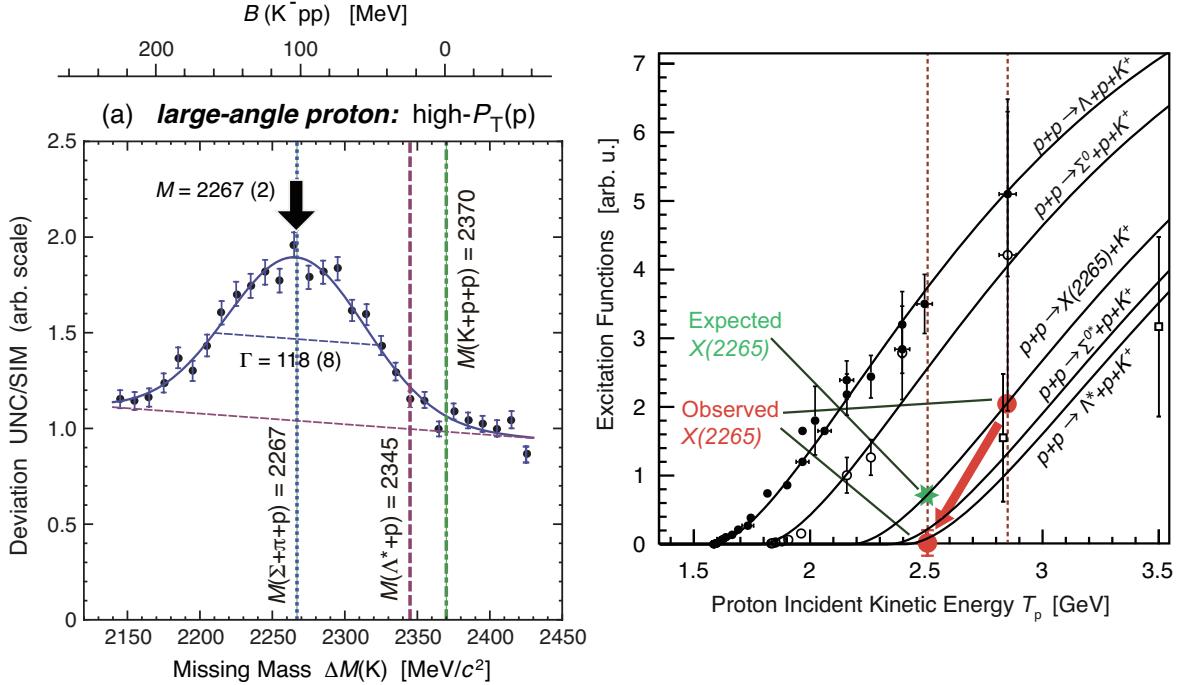
Fig. 1.4 (left)K^+ missing mass spectrum of $p + p \rightarrow \Lambda + K^+ + p$ channel observed in DISTO[39] with selecting large momentum transfer protons and kaons. (right) Relative excitation functions of the reactions $p + p \rightarrow p + \Lambda + K^+, \rightarrow p + \Sigma^0 + K^+, \rightarrow X(2265) + K^+, \rightarrow p + \Sigma^{0*} + K^+$ and $\rightarrow p + \Lambda^* + K^+$. The observed relative cross-sections for X(2265) at 2.50 and 2.85 GeV are shown by large red circles, and the expected one at 2.50 GeV relative to that at 2.85 GeV is shown by a green star. Taken from Ref. [40].

COSY-TOF experiment[42]. In the $N*$ production, the final state products are $\Lambda p K^+$, via $pp \rightarrow pN^*, N^* \rightarrow K^+\Lambda$ as is the case of K^-pp production. These N^* resonances could be sources of non-uniform background distribution and make the observed broad spectrum.

γ-induced production at LEPS

The $\gamma d \rightarrow K^+\pi^- X$ reaction at $E_\gamma = 1.5 - 2.4$ GeV was carried out at LEPS/SPring-8[43]. They found that there is no structure in the mass region of 2.22 to 2.36 GeV/c^2 in the missing mass spectrum of $d(\gamma, K^+\pi^-)X$. The upper limits of the cross sections for the K^-pp bound state with were obtained to be from 0.1 to 0.7 μb at the 95% C.L.

HADES experiment

The HADES experiment at GSI searched for K^-pp by the same reaction used in the DISTO experiment, pp-collision. However, with a higher kinetic energy of T_p=3.5 GeV, they reported no peak observation as DISTO observed[44].
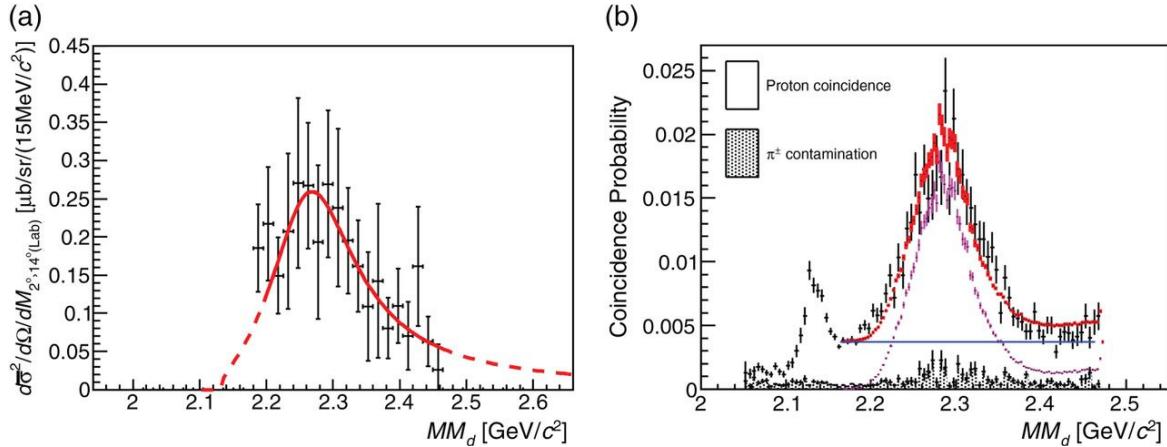
Fig. 1.5 Missing-mass of the $d(\pi^+, K^+)"X"$ reaction for two-proton coinsidence, measured in the J-PARC E27 experiment. The $\Sigma^0 p$-decay mode is selected in the analysis. Taken from Ref.[46]

J-PARC E27 experiment

The J-PARC E27 collaboration searched for $K^- pp$ in the $d(\pi^+, K^+)$ reaction[45]. In this reaction, $\Lambda(1405)$ is produced on a neutron in a deuteron and the Λ^* is considered to merges with a proton in the deuteron to form $K^- pp$[38]. They constructed a range array counter to tag fast protons from $K^- pp$ decay, while the scattered K^+ were analyzed with the SKS spectrometer system. The reported $d(\pi^+, K^+)"X"$ missing-mass spectrum is shown in Fig.1.5. In the analysis, $\Sigma^0 p$-decay mode is selected. They reported that the binding energy of $K^- pp$-like structure is $95^{+18}_{-17}(stat.)^{+30}_{-21}(syst.)$ MeV and its width is $162^{+87}_{-45}(stat.)^{+66}_{-78}$ MeV. These values are consistent with that in DISTO experiment.

$^3\mathrm{He}(K^-, n)$ reaction at J-PARC E15

A searching for the $K^- pp$ bound state is being performed by the J-PARC E15 collaboration, by using the $^3\mathrm{He}(K^-, n)$ reaction. A semi-inclusive spectrum of the $^3\mathrm{He}(K^-, n)$ reaction was measured at a forward angle of a neutron scattering angle, as shown in Fig.1.6. One finds no peak structure in a mass region around 100 MeV below the $K^- pp$ threshold, where some experiments claimed a peak structure.

The E15 collaboration reported the Λp invariant-mass spectrum in the $^3\mathrm{He}(K^-, \Lambda p)n$ reaction, obtained in the first physics run carried out in 2013, as shown in Fig.1.7. A peak structure near the $K^- pp$ threshold was observed. A peak position and width, assuming a Breit-Wigner peak with an S-wave Gaussian form factor, were obtained to be $2355^{+6}_{-8}(stat.) \pm$

Table 1.1 Calculated K^-pp binding energies B & widths Γ (in MeV). Taken from Ref. [49]

	chiral, energy dependent			non-chiral, static calculations			
	var. [50]	var. [51]	Fad. [52]	var. [24]	Fad. [53, 54]	Fad. [55, 56]	var. [57]
B	16	17-23	9-16	48	50-70	60-95	40-80
Γ	41	40-70	34-46	61	90-110	45-80	40-85

$12(sys.)\ MeV/c^2$ and $100^{+19}_{-17}(stat.) \pm 27\ MeV/c^2$, respectively. The observed peak was different from those reported in the previous experiments.

1.3 Theoretical situation on K^-pp

Many theoretical calculations of the K^-pp system have been reported. Their results for binding energies and widths of the K^-pp state are summarized in Table 1.1. All calculations agree on the existence of the K^-pp bound state. However the binding energy and the width are widely disributed.

The large difference of the binding energy between these theoretical calculations comes from the treatment of the $\bar{K}N$ interaction in the energy below the threshold. The $\bar{K}N$ interaction predicted by chiral SU(3) based calculations is smaller than that by phenomenological potential based calculations. This difference of interaction is directly related to the binding energy of the predicted K^-pp bound state.

None of the few-body calculations predicted the binding energy over 100 MeV despite the experimental observations of DISTO and FINUDA. Furthermore, the main decay channel of $\bar{K}NN \to \pi\Sigma N$ is not opened at the binding energy around 100 MeV. Thus a deeply binding state is naturally expected to have narrow width as the originally-predicted K^-ppn bound state by Akaishi and Yamazaki.

1.4 J-PARC E15 experiment

Although there is many studies on the K^-pp bound state from both theoretical and experimental side, the K^-pp bound state has not been understood even its existence. Event though there are experimental studies about the K^-pp candidates, the situation is still not clear since the observed peak position is much larger than that predicted by theoretical calculations. Furthermore, different interpretations other than the K^-pp assumption are discussed for the FINUDA and DISTO observation.
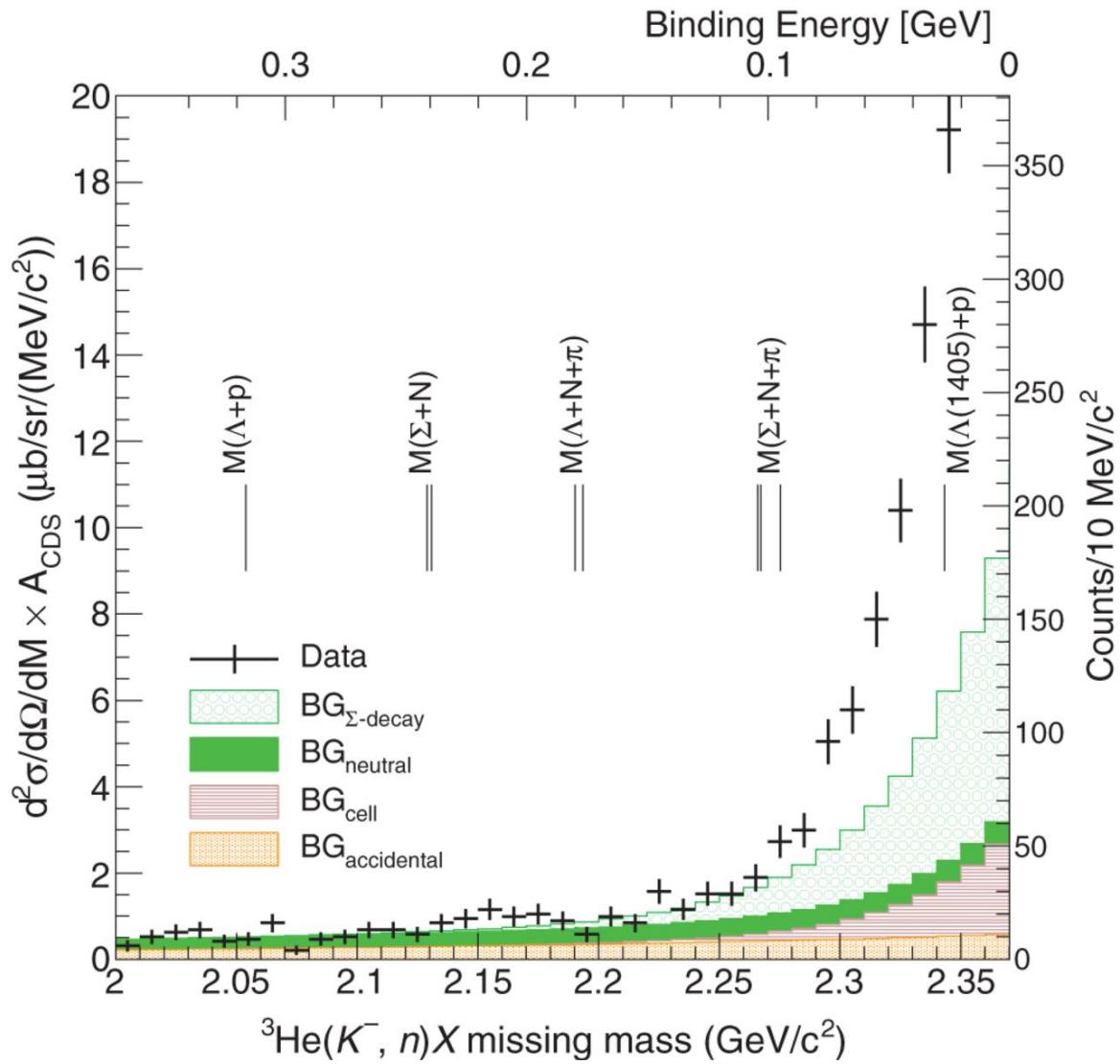
Fig. 1.6 Missing-mass of the $^3\text{He}\,(K^-, n)\,"X"$ reaction measured in the J-PARC E15 experiment. Taken from Ref.[47]
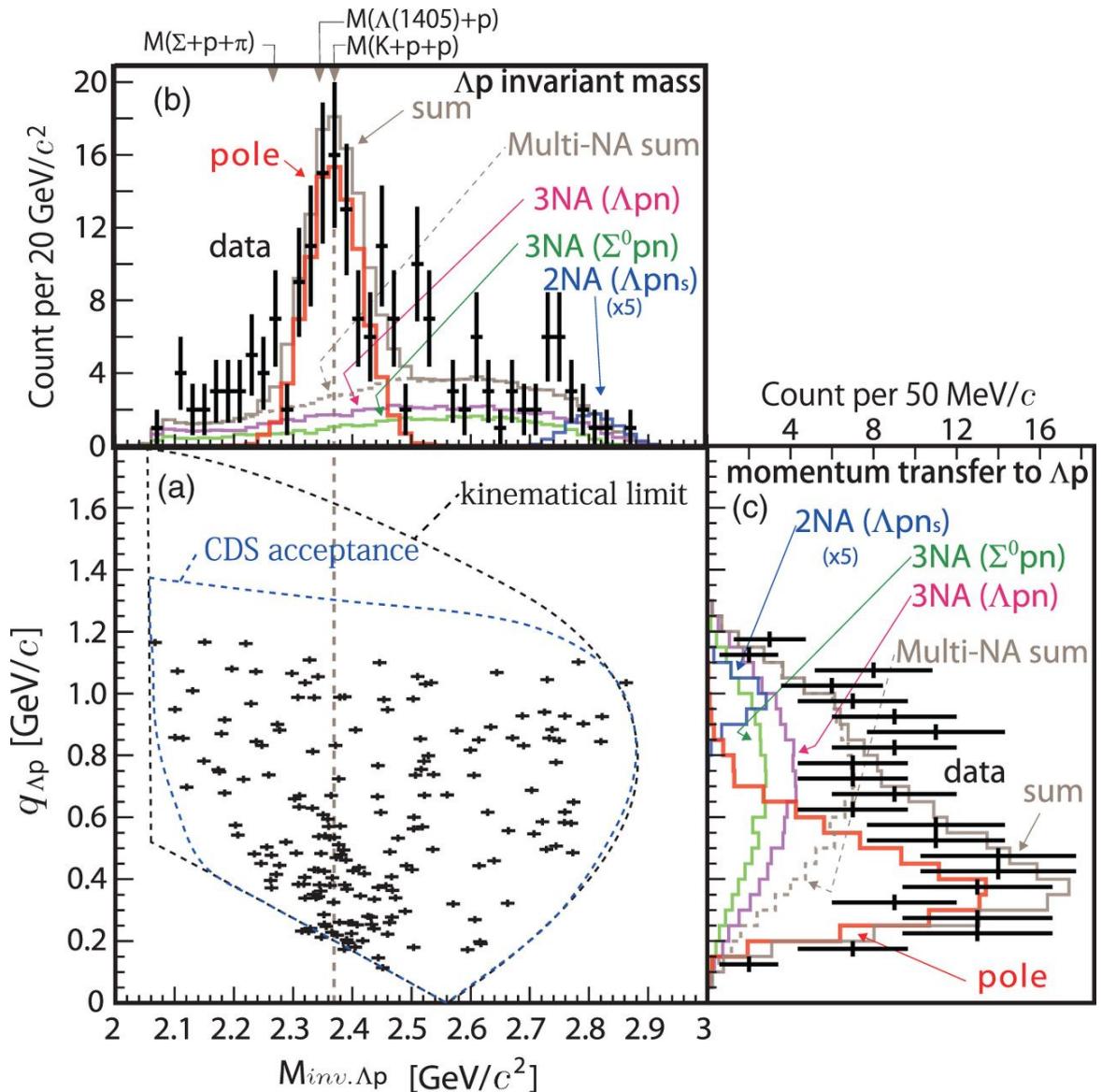
Fig. 1.7 Invariant-mass of the Λp pair with selecting the $^3\mathrm{He}\,(K^-,n)\,n$ reaction measured in the J-PARC E15 experiment. Taken from Ref.[48]
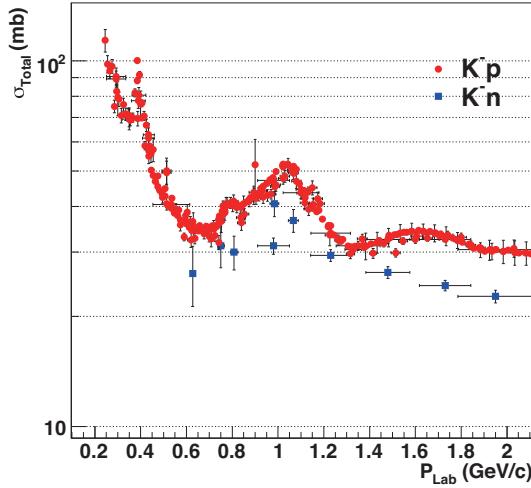
Fig. 1.8 Total cross section of the elementally $K^- N$ reactions. Taken from Particle Data Group.

The previous experiments also told us that an exclusive measurement is essential for the clear identification of the observed structure. Moreover, an in-flight reaction suppresses or kinematically separates the background processes such as multi-nucleon absorptions and hyperon decays in the $K^- pp$ measurement.

These ideas are supported in our experiment, J-PARC E15[58]. We performed an experiment with an in-flight (K^-, n) reaction at incident kaon momentum of 1 GeV/c. The beam-kaon momentum was chosen so that the cross-section of the elementary $K^- N$ reaction is a maximum as shown in Fig. 1.8. In E15 experiment, the $K^- pp$ bound state is investigated by measuring the Λp invariant-mass spectrum which is one of the expected decay mode of the $K^- pp$ bound state. An high intensity kaon beam at J-PARC makes such a measurement possible. The details of the experimental method are described in the next chapter.

1.5   Thesis overview

This thesis is dedicated to an analysis of Λp invariant-mass in the $^3\text{He}(K^-, \Lambda p)n$ reaction with data in the second physics run of the J-PARC E15 experiment. The details of the experiment and detector setup are described in chapter 2. In chapter 3, the basic analysis procedure and evaluated detector performances are shown. The stream of analysis for the exclusive $^3\text{He}(K^-, \Lambda p)n$ reaction is described in chapter 4. The results are shown in chapter 5, with discussing the structure of the Λp invariant-mass spectrum in the $^3\text{He}(K^-, \Lambda p)n$ reaction. Finally, a conclusion is given in chapter 6.

Chapter 2

Experimental apparatus

2.1 Experimental facility at J-PARC

Japan Proton Accelerator Research Complex (J-PARC), built in Tokai village, Ibaraki, Japan, is the facility that provides a intensive kaon beam. J-PARC consists of three proton accelerators, an H^- linac (LINAC), 3 GeV Rapid Cycling Synchrotron (RCS), and 30 GeV Main Ring (MR). MR provides a fast extracted (FX) beam to produce neutrino beam to Kamioka (T2K experiment) and a slow extracted (SX) beam to the hadron experimental facility, where experiments of particle and nuclear physics are performed by using primary proton and secondary pion, kaon and anti-proton beams. In the SX operation, the beam in the MR is slowly extracted by gradually shaving bunched beam while the remaining beam is kept circulating in the MR. The spill length was about two seconds with a 5.5 sec. repetition cycle. The intensity of the SX beam in the present experiment was about 42 kW during the experiment.

A typical operation condition of the SX beam in December, 2015 is summarized in Table 2.1.

2.2 K1.8BR beam-line in the hadron experimental facility

The primary proton beam is transported to a production target, called T1, in the hadron experimental facility. In the experiment, gold was used as the T1 target, and the secondary particle beam is generated.

The E15 experiment is performed at the K1.8BR beam line located at the north side of the hadron experimental hall. The K1.8BR beam line is branched from the K1.8 beam line and has shorter beam line length of 31.3 m from the T1 target to the final focus point(FF).

Table 2.1 Typical operational condition of the SX beam as of Dec., 2015.

Primary beam momentum	30 GeV/c
Primary beam power	39-42 kW
Protons per spill	4.4-4.8 $\times 10^{13}$
Repetition cycle	5.5 sec
Spill Length	2.0 sec
Spill duty factor	40%
Spill extraction efficiency	99.5%
Frequency of transverse RF	47 MHz

Table 2.2 Parameters of K1.8BR beam line as of December, 2015.

Production target	Au (50% loss)
Extraction Angle	$6°$
Momentum range	1.2 GeV/c max.
Acceptance	2.0 msr $\cdot$ %
Momentum bite	$\pm$ 3 %
Beam Length (T1-FF)	31.3 m

The beam momentum capability of the beam-line is upto 1.2 GeV/c. The configuration of the K1.8BR beam line is shown in Fig.2.1, and its parameters are listed in Table 2.2.

A good mass separation is realized with two vertical slits, an electrostatic separator (ES1), and a pair of correction magnets(CM1 and CM2). We also have two horizontal slits, an IF-H at the internal focus point and a MOM just downstream of the MS1, where the optics is designed to be dispersive.

After the D3 magnet, an SQDQD system is employed to focus the beam on the experimental target at FF of the K1.8BR beam line. The most downstream magnet D5 is required to change the beam direction to keep a flight-length of scattered neutron as long as 15 m. The D5 magnet is also used as a beam momentum analyzer.

The first-order beam envelope calculated by the TRANSPORT code[59] is shown in Fig. 2.2.

2.2.1   Kaon beam tuning

Kaon beam tune was performed to maximize the number of kaons on the experimental target while keeping a pion contamination to the acceptable level.

D: dipole magnet
Q: quadrupole magnet
S: sextupole magnet
O: octupole magnet
T1: production target
IF: intermediate focus
MS: mass slit
ES: electrostatic separator
CM: correction magnet
FF: final focus
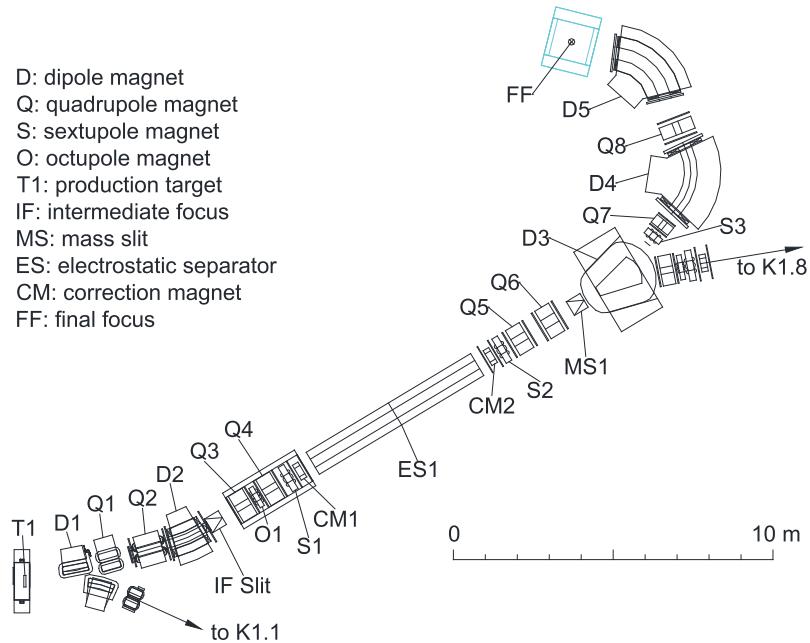
Fig. 2.1 Schematic drawing of K1.8BR beam line in the J-PARC hadron experimental facility. Taken from Ref.[60].

After the establishment of online particle identification triggers, we optimized the combination of ES1, CM1 and CM2 setting to maximize the kaon yield. Then the center of the vertical beam position was measured by changing two vertical slit positions. The horizontal position of beam was optimized by D3,D4 and D5 with a narrowed setting for the momentum slit. Currents of quadruple magnets were also scanned to increase the kaon yield and for better focus at FF. Finally, opening widths of two vertical slits and two horizontal slits were optimized in terms of a K/π ratio and a total beam intensity.

A typical kaon intensity during the experimental period was 1.9×10^5 per spill with the K^-/π^- ratio of ~ 0.50. The optimized magnet settings and slit settings are summarized in Table 2.3 and Table 2.4, respectively.

2.3   K1.8BR spectrometer system

Fig. 2.3 shows the K1.8BR spectrometer system which we have constructed in the K1.8BR experimental area. The spectrometer consists of a beam-line detectors, a cylindrical detector system (CDS) which surrounds the liquid ^{3}He target system to detect the decay particles from the target region, and a neutron and a proton time-of-flight counters located $\sim$15 m
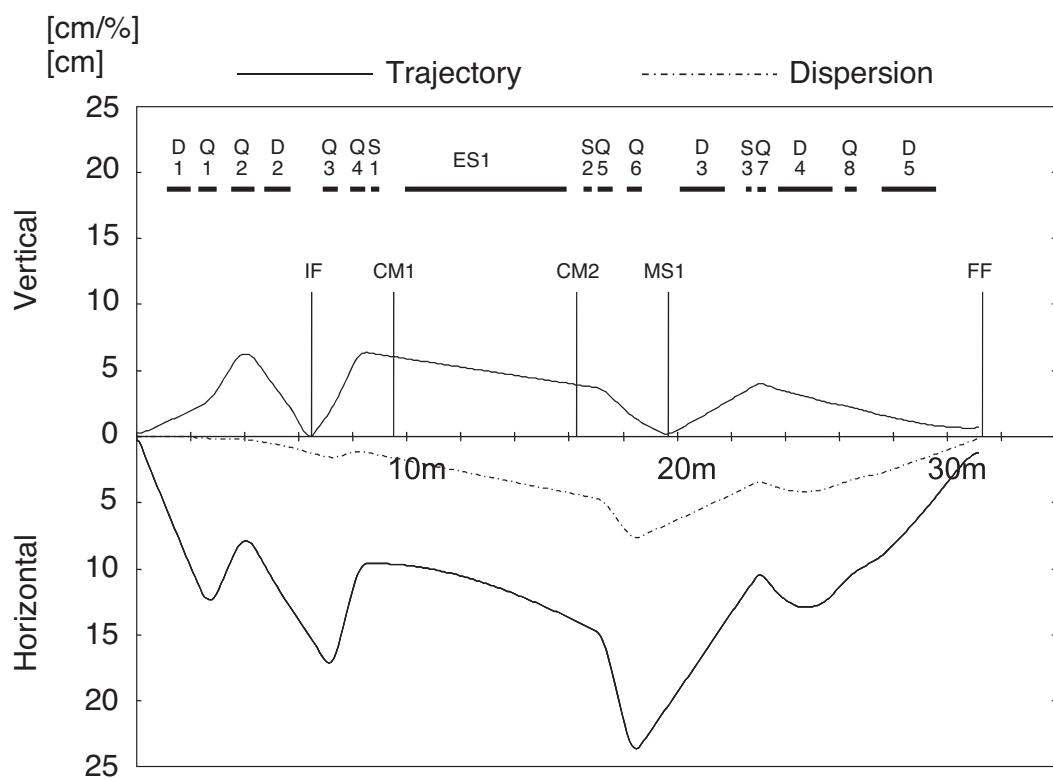
Fig. 2.2 First-order beam envelope. Taken from [61]

Table 2.3 Parameters of the beam-line magnets. D5 field is a typical monitored value. Other field values are interpolations of measured points.

Element	J-PARC designation	Gap or bore/2 (cm)	Effective length (cm)	Bend (deg)	Current (A)	Field at pole (kG)
D1	5C216SMIC	8	90.05	10	-363	-6.5808~-6.7444
Q1	NQ312MIC	8	67.84		-357	-3.075
Q2	Q416MIC	10	87.04		-668	3.872
D2	8D218SMIC	15	99.65	15	-698	-8.7673
IF-H	Movable horizontal slit for acceptance control					
IF-V	Movable vertical slit, $(y\|\phi)=0$					
Q3	Q410	10	54.72		-679	-4.108
O1	O503	12.5	15		-15	-0.29
Q4	Q410	10	54.72		-776	4.692
S1	SX504	12.5	27.6		-42	-0.29
CM1	4D604V	10	20	(0.856)	335	1.943
ES1	Separator	10	600			E=$\pm$200 kV
CM2	4D604V	10	20	(0.856)	360	1.940
S2	SX504	12.5	27.6		-136	1.02
Q5	NQ510	12.5	56		-498	4.218
Q6	NQ610	15	57.2		-535	-4.316
MOM	Movable horizontal slit for momentum acceptance control					
MS1	Movable vertical slit for K-π separation $(y\|\phi)=0$, $(y\|y)=0.844$, $(y\|\theta\phi)=(y\|\phi\delta)=0$					
D3	6D330S	15	165.1	20	210	-7.064
S3	SX404	10	20		-34	-1.062
Q7	Q306	7.5	30.34		-464	4.026
D4	8D440S	20	198.9	60	-1938	-17.8907
Q8	NQ408	10	46.5		-110	0.671
D5	8D240S	20	195.9	55	-1663	-16.413

Table 2.4 Optimized slit settings. All unit in mm.

IF-H	110	-110
IF-V	3.8	-0.2
Mass	3.30	-1.40
Mom	L 160.0	R -100.0
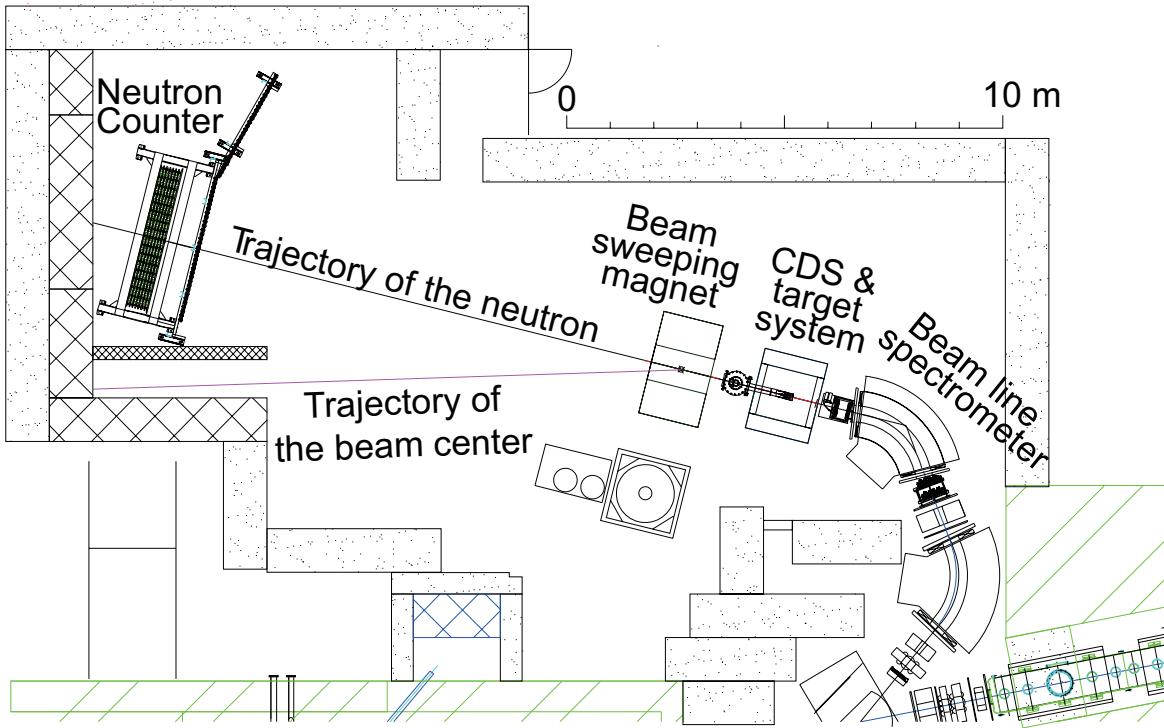
Fig. 2.3 Schematic view of the K1.8BR spectrometer. Taken from Ref.[60].

downstream from the target position with a beam weeping magnet. In the successive 4 sections, details of these components are described.

2.4   Beam-line detectors

It is composed of beam line magnets, trigger counters, beam-line drift chambers, and a kaon identification counter. The beam trigger is generated by a coincidence signal of two trigger counters, a beam hodoscope detector (BHD) and a time zero counter (T0). The flight length between the BHD and T0 is $\sim$7.7 m. We additionally installed a beam definition counter (DEF) just upstream of the target to remove beam outside of the target cell from triggered event. The kaon beam with momentum around 1.0 GeV/c is identified by using an aerogel Cherenkov counter (AC) with a refractive index of 1.05. The kaon beam is tracked with two beam-line drift chambers, a beam line chamber 1 (BLC1) and a beam line chamber 2 (BLC2). The momentum of the kaon is analyzed with this tracking information together with the beam optics of the D5 beam line magnet. Finally, beam trajectory just upstream of the experimental target is detected by a drift chamber (BPC) to determine the reaction vertex.

2.4.1   Trigger counters

BHD

The BHD is segmented plastic scintillation counters located downstream of the D3 magnet.

The BHD has an effective area of 400 mm (horizontal) × 160 mm (vertical) segmented into 20 units horizontally, and T0 is 160 mm (horizontal) × 160 mm (vertical) segmented into 5 units horizontally. The BHD scintillator is made of Saint-Gobain BC412 with a unit size of 160 mm (height) × 20 mm (width) × 5 mm (thickness). The scintillation light is detected by a pair of 3/4 inch Hamamatsu H6612B photomultipliers that are attached to the top and bottom ends.

T0

The T0 is also segmented plastic scintillation counters located downstream of the D5 magnet. To avoid over-concentration of the beam on one segment, T0 is rotated by 45 degrees in the *xy* plane. The unit size of T0 made of the Saint-Gobain BC420 scintillator is 160 mm (height) × 32 mm (width) × 10 mm (thickness). The scintillation light is detected by a pair of 3/4 inch Hamamatsu H6612B photomultipliers that are attached to the top and bottom ends. Since the coincidence rate of the top and bottom photomultipliers is too high, the high voltage boosters of all the photomultipliers are modified to supply adequate current to the last three dynodes.

DEF

The DEF is installed just upstream of the target vacuum vessel to improve data quality and an efficiency of data acquisition. Under the current magnetic spectrometer setup, only half of the kaon beam hits the liquid ^{3}He target due to the large beam spot size. So the DEF is used for selecting the central region of the beam at the trigger level by adding the DEF signal to the beam trigger made by the coincidence signal of the BHD and T0.

For the DEF, thin scintillation counter array is adopted. The scintillation light is detected by a wavelength-shifting (WLS) fiber, Kuraray Y-11(200)M with 1 mm diameter. The light from the fiber is read from both ends with multi-pixel photon counters (MPPCs) made by Hamamatsu (S10362-11-100C). The WLS fiber is embedded in a 3 mm thick scintillator (ELJEN EJ-202) with 1.1mm depth, and fixed by optical cement ELJEN EJ-510 as illustrated in Fig. 2.4. MPPCs are coupled to the fiber by using GOMI connectors developed by the T2K experiment[62].
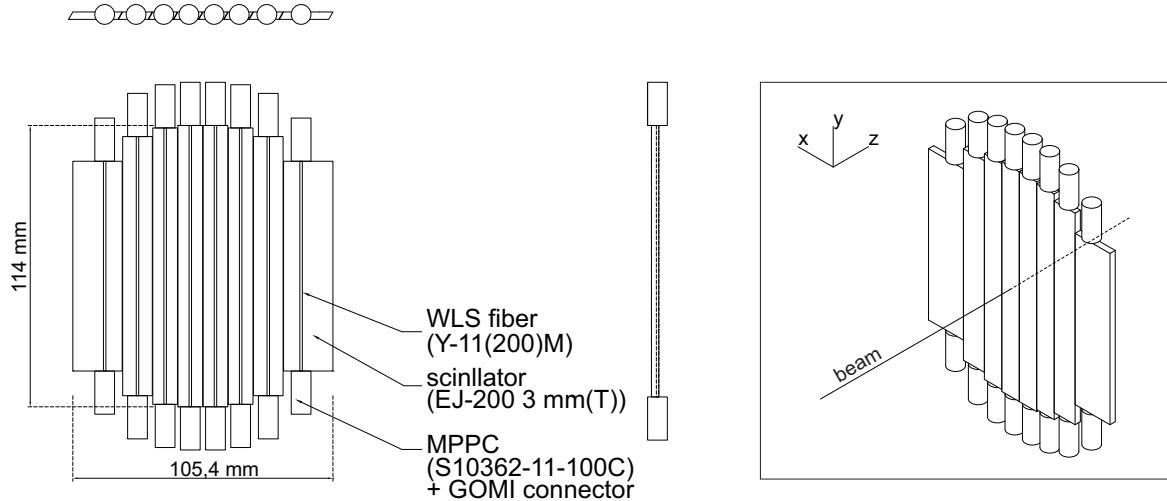
Fig. 2.4 Schematic drawing of the DEF counter.

2.4.2   Kaon identification counter; AC

The AC, shown in Fig.2.5, located downstream of T0 is used to identify the kaon at the
trigger level. In the experiment, an aerogel radiator with a refraction index of 1.05 is used as
a threshold-type Cherenkov counter to reject pions with momenta around 1.0 GeV/c. The
AC has an effective area of 180 mm (width) $\times$ 100 mm (height) $\times$ 100 mm (thickness)
which covers the whole distribution of the kaon beam. Cherenkov photons radiated in the
beam direction are diffused in the aerogel and reflected by the thin mirror foils sorrounding
it, and reached at four photomultipliers on the top and bottom. Three-inch fine-mesh type
photomultipliers (Hamamatsu R5543) are used to keep working with fringing fields of the
D5 magnet and the CDS magnet. A typical pion detection efficiency is more than 99%. The
miss identification ratio of a kaon as a pion is about 1%.

2.4.3   Beam momentum measurement

Two drift chambers, BLC1 and BLC2, are installed in the entrance and the exit of the beam
spectrometer magnet, called D5 magnet. Their tracks are combined by a second-order
transport matrix to reconstruct the kaon beam momentum. A typical resolution of 200 μm of
BLC1 and BLC2 achieves the momentum resolution of about 0.1%. The magnetic field of
D5 is monitored during the experiment with a high-precision Hall probe, Lakeshore 475 (
$\sim 10^{-5}$ T resolution). The fluctuation of the magnetic field was $\sim 2 \times 10^{-4}$ corresponding
to 0.2 MeV/c for the 1 GeV/c beam. We also install a helium bag into the D5 magnet to
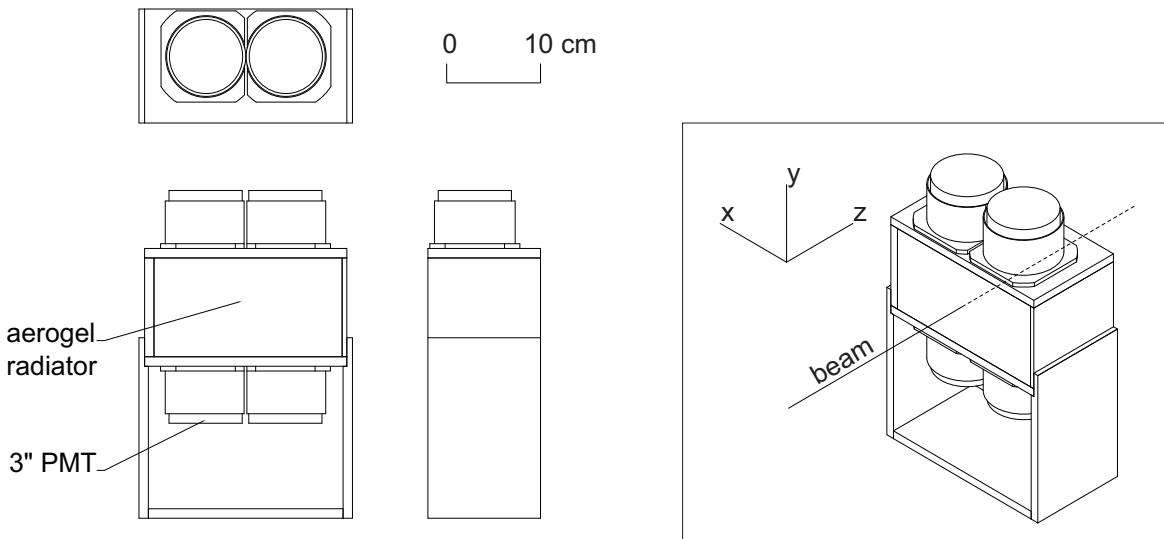
Fig. 2.5 Schematic drawing of the aerogel Cherenkov counter.

suppress the scattering effects in the air. The helium bag was refilled every day during the experiment.

BLC1

BLC1 consists of two sets of drift chamber with the same design, BLC1a and BLC1b, which have 8 layers ($UU'VV'UU'VV'$ configuration). In the U and V layers the wires are tilted by ± 45 degrees. Each layer contains 32 sense wires with a drift length of 4 mm corresponding to an effective area of 256 mm × 256 mm. The number of readout channels is 256 for both BLC1a and BLC1b, which are installed 300 mm apart upstream of the D5 magnet.

BLC2

BLC2 is similar to BLC1; BLC2 consists of two sets of the same drift chamber, BLC2a and BLC2b. Each chamber has a $UU'VV'UU'VV'$ configuration and 32 sense wires per layer, i.e, the number of readout channels is 256 for both BLC2a and BLC2b. In the U and V layers the wires are tilted by ± 45 degrees. The drift length of 2.5 mm corresponds to an effective area of 160 mm × 160 mm. BLC2a and BLC2b are installed 275 mm apart downstream of the D5 magnet.

Both BLC1 and BLC2 use 12.5 μm diameter gold-plated tungsten wires with 3% rhenium and 75 μm diameter copper-beryllium wires for the sense and potential wires, respectively. The cathode planes are made of 12.5 μm aluminized Kapton. The readout electronics of both chambers consist of a preamplifier card with amplifier-shaper-discriminator ICs (ASD,
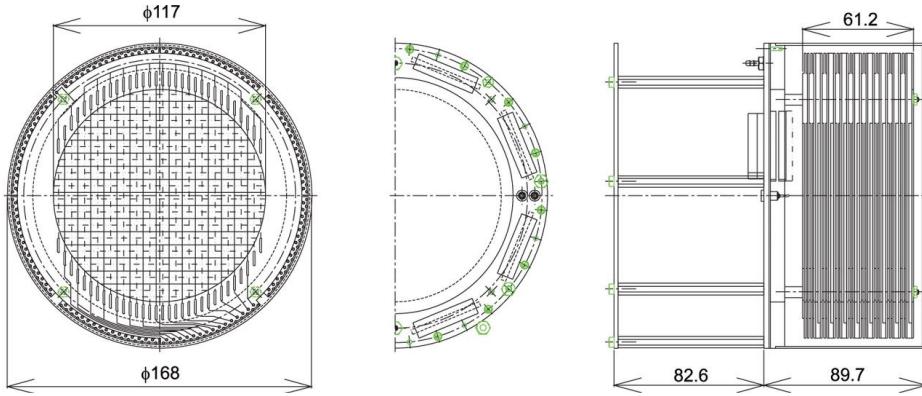
Fig. 2.6 Design of the BPC (all dimensions in mm). Taken from Ref.[60].

SONY-CXA3653Q, τ = 16 ns) mounted on the chambers, an LVDS-ECL converter, and a TDC. The output signal of the ASD board is sent to the LVDS-ECL converter board via 7 m long twisted-pair cables. From the LVDS-ECL converter, the signal is transferred to the counting house with 50 m long twisted-pair cables. The chamber gas is an argon-isobutane mixture passed through a methylal (dimethoxy-methane) bubbler at a refrigerator temperature of 4 °C with a ratio of 76% (Ar), 20% (isobutane) and 4% (methylal). The operating voltages of BLC1 and BLC2 are set at -1.25 kV on both the potential wires and the cathode planes.

2.4.4 BPC

A backward proton chamber (BPC) is installed just upstream the target cell to determine the reaction vertex point precisely.

The BPC is a compact circular planar drift chamber whose size is 168 mm in diameter and 89.7 mm in height. Fig. 2.6 shows the design of the BPC, which consists of 8 layers ($XX'YY'X'XY'Y$), where the wires of the Y layer are tilted by 90 degrees. Each layer contains 15 sense wires with a drift length of 3.6 mm corresponding to an effective area with a 111.6 mm diameter. The number of readout channels is 120. The cathode planes are made of 9 μm carbon aramid foil, and the sense and potential wires, readout electronics, and gas mixture of the BPC are the same as those for the beam line chambers. The operational voltage of the BPC is set at -1.50 kV on both the potential wires and the cathode planes.

Fig. 2.7 shows the cell geometries of the beam-drift chambers. The parameters of the beam line chambers are summarized in Table 2.5.

(a) BLC1/2

Beam

Cathod plane , Al-Kapton, T=12.5 μm

2.5 mm

Anode (U', V')

4.0 (2.5) mm

2.5 mm

Anode (U, V)

- ●   Sense wire, ϕ=12 μm, W w/ 3% Re (Au plated)

- ○   Potential wire, ϕ=75 μm, Cu-Be (Au plated)

(b) BPC

Beam

Cathod plane , Cu-aramid, T=9 μm

3.6 mm

Anode (X', Y')

3.6 mm

3.6 mm

Anode (X, Y)

- ●   Sense wire, ϕ=12 μm, W w/ 3% Re (Au plated)

- ○   Potential wire, ϕ=75 μm, Cu-Be (Au plated)

(c) FDC1

5.67 mm

6 mm

X'

X

● Sense wire   ○ Field wire   ● Shield wire
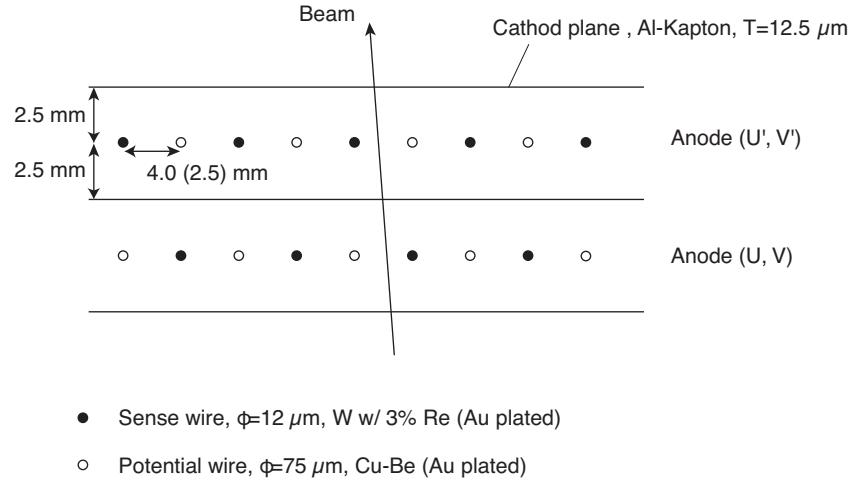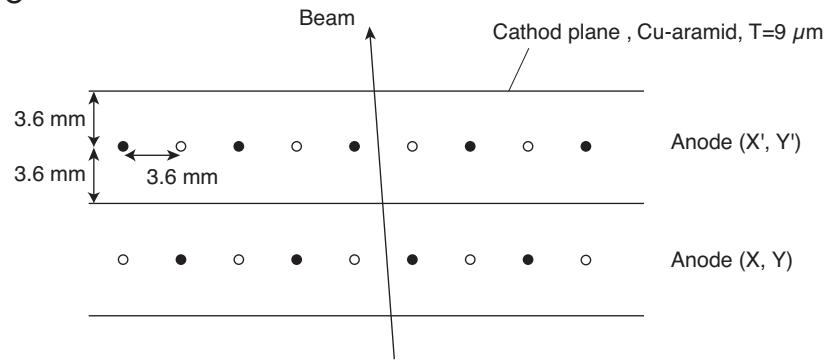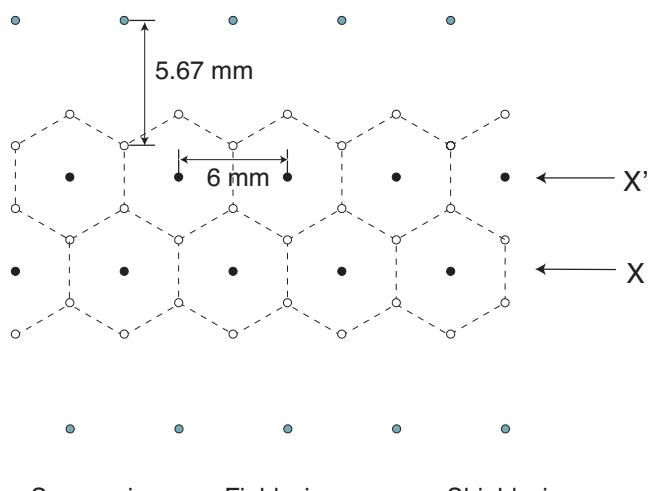
Fig. 2.7 Cell geometries of (a)BLC1/2, (b)BPC, and (c)FDC.

Table 2.5 Summary of the beam-line chamber parameters.

	BLC1a	BLC1b	BLC2a	BLC2b	BPC	FDC
number of planes	8	8	8	8	8	6
plane configuration	UU'VV'UU'VV'	UU'VV'UU'VV'	UU'VV'UU'VV'	VV'UU'VV'UU'	XX'YY'X'XY'Y	UU'XX'VV'
number of sense wires in a plane	32	32	32	32	15	64
wire spacing (mm)	4	4	2.5	2.5	3.6	3
effective area (mm)	256 × 256	256 × 256	160 × 160	160 × 160	111.6 mmϕ	
Sense wire						
material			Au-plated W (3% Re)			Au-W(Re)
diameter (μm)			12			20
Potential wire						(field wire)
material			Au-plated Cu-Be			Au-Al
diameter (μm)			75			80
Cathode plane						(shield wire)
material			alminized-Kapton		Cu aramid	Au-Al
thickness (μm)			12.5		9	80
Gas			Ar : isoC$_4$H$_{10}$: Metylal = 76 : 20 :4			
flow (cc/min)			100			
operation voltage						
potential	-1.25	-1.25	-1.25	-1.25	-1.5	-1.45
cathord	-1.25	-1.25	-1.25	-1.25	-1.5	-1.45

2.5 Liquid ^{3}He target system

To gain larger luminosity, a liquid target was employed and a cryogenic target system was developed for the current experiment based on the liquid ^{4}He target[63]. A schematic drawing of the liquid ^{3}He cryostat is shown in Fig.2.8 and the details can be found in Ref. [64].

   The experimental requirements for the target system are stable heat transport to the target cell located at the center of the cylindrical detector system and thin and low-Z materials around the target to suppress the energy loss effect. The former was achieved by an L-shape cryostat and a siphon method with two pipes connecting between cooling part and the target cell. For the latter requirement, a target cell made by beryllium and a vacuum chamber made by carbon fiber reinforced plastic (CFRP) were employed.

2.5.1 Cooling mechanism

The major cryogenic component is divided into three sections: a ^{4}He separator, a ^{4}He evaporator, and a heat exchanger between ^{3}He and ^{4}He. The target cell is connected to the bottom of the heat exchanger with two 1 m long pipes. To reduce the radiation from room temperature components, all low-temperature parts are covered with a radiation shield anchored to the liquid nitrogen tank (LN$_2$ tank).

   A cooling power is generated by an evacuation of ^{4}He in the evaporator with a rotary pump. The rotary pump has a pumping speed of 120 m^3/h, resulting in a heat-removal capability of 2.5 W at 2 K. The cooling power was used to liquify ^{3}He gas at the heat exchanger. The scarce ^{3}He gas is controlled by a gas-tight handling system (leak rate less than 10^{-10} Pa·m^3/sec). An effective heat transport to the 1 m apart target cell was accomplished by the application of the *siphon method* as described in Ref. [64], which uses convection of the liquid ^{3}He. The liquid ^{3}He warmed by the heat load inside the target cell returns to the heat exchanger through an upper pipe while ^{3}He is cooled again in the heat exchanger and fed to the target cell through the lower pipe.

2.5.2 Target cell

Fig.2.9 shows the target cell. The side wall of the target cell is made of pure beryllium (more than 99.4% purity) of 0.3 mm thick. The caps of both ends are made by AlBeMet, which is an alloy of aluminum and beryllium.The volume of the target cell is 0.48 ℓ in which the volume of 269 ℓ gaseous ^{3}He at room temperature is necessary to fill up with liquid at 1.3 K.
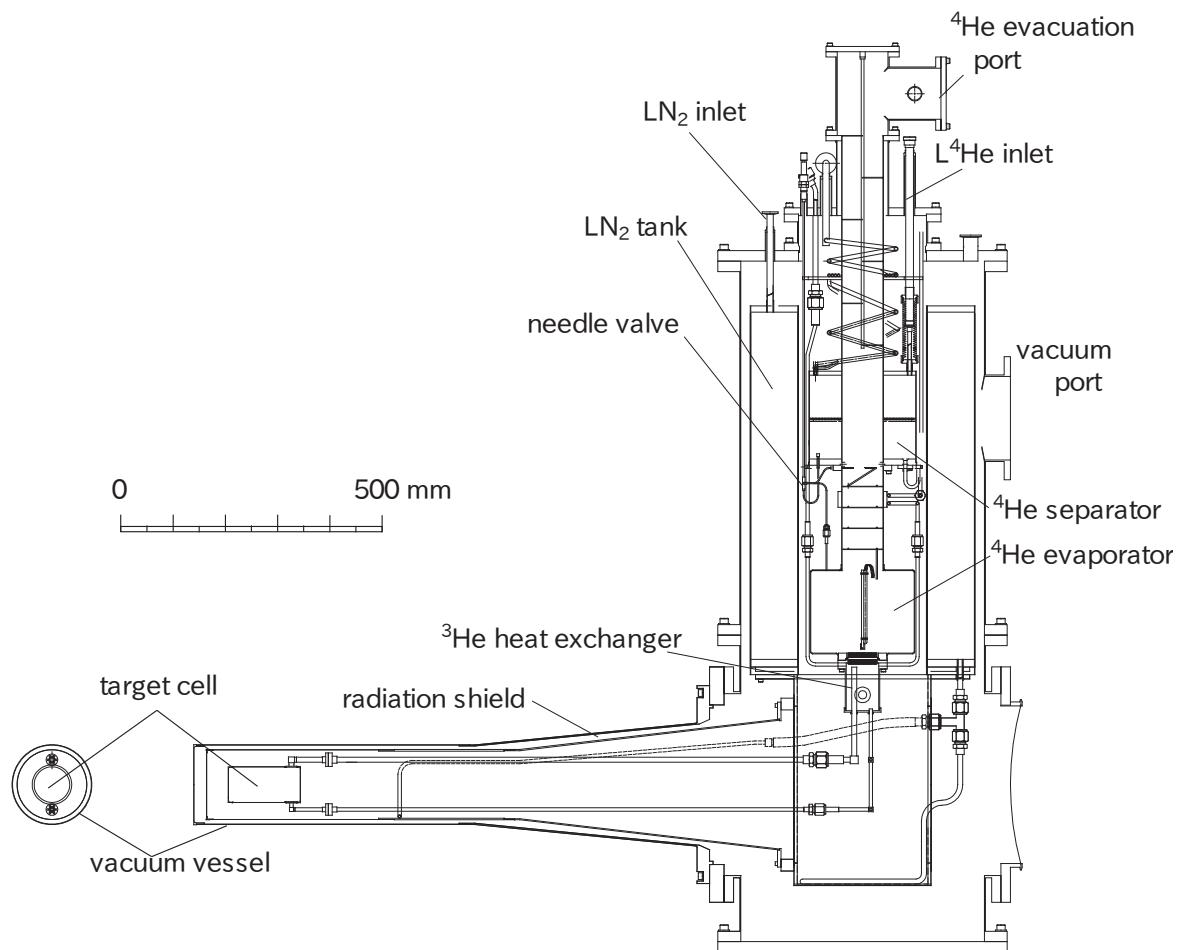
Fig. 2.8 Schematic drawing of the liquid ^{3}He cryostat. Taken form Ref. [64].
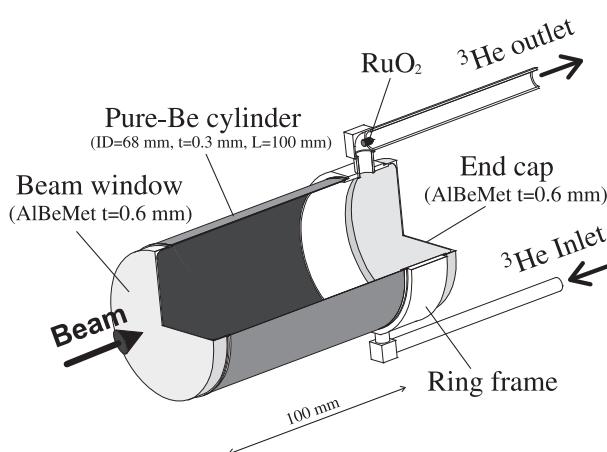
Fig. 2.9 Schematic drawing of the target cell. Taken form Ref. [64].

Table 2.6 Operational results of the liquid ^{3}He target system.

Vacuum level	[mbar]	$< 10^{-6}$
Leak rate of the ^{3}He system	[Pa·m^3/sec]	$< 10^{-10}$
Temperature in the target cell	[K]	1.4
Vapor pressure in the target	[mbar]	33
Heat load to low-temperature part	[W]	0.21
Liquid ^{4}He consumption	(ℓ/day)	50
Liquid N$_2$ consumption	(ℓ/day)	50

2.5.3   Operation and performance

After a pre-cooling of the cryogenic system to the liquid nitrogen temperature, it took about 6 hours to liquify the ^{3}He gas in the heat exchanger and achieve thermal equilibrium at around 1.4 K.

Fig. 2.10 shows the stability of the density of the liquid ^{3}He target during the experiment. The spike-like structures are the periods when we refilled the liquid ^{4}He to the evaporator. We need to refill the ^{4}He once per about 24 hours and it takes about 1 hour including a recovery time to thermal equilibrium. Liquid ^{4}He at 4.2 K is transported to the evaporator through the separator, which is closed off during the normal operation. In the data taking period, the temperature was in the range between 1.37 and 1.44 K, which corresponds to the density fluctuation of $\sim 0.2\%$ as the density equation of ^{3}He[65]. Since the equilibrium temperature of ~ 1.4 K was ~ 0.1 K higher than that of the test operation in Ref. [64]. The temperature differences between the evaporator, the heat exchanger, and the target cell were less than 0.01 K. This means that the heat transfer by the *siphon method* was working well. From the reduction rate of the liquid ^{4}He in the evaporator, the heat load of the low-temperature region was estimated to be 0.21 W. The operational results of the cryostat are tabulated in Table 2.6.

2.6   Cylindrical detector system

A schematic view of the cylindrical detector system (CDS) with the target system is shown in Fig. 2.11. Charged particles generated by the reaction at the target are tracked by a cylindrical drift chamber (CDC), which operates in a magnetic field of ± 0.7 T provided by a solenoid magnet. A cylindrical detector hodoscope (CDH) is used for particle identification via TOF measurement and as a charged particle trigger. An inner hodoscope (IH) is installed to enlarge the acceptance for the tracks out of CDH acceptance.
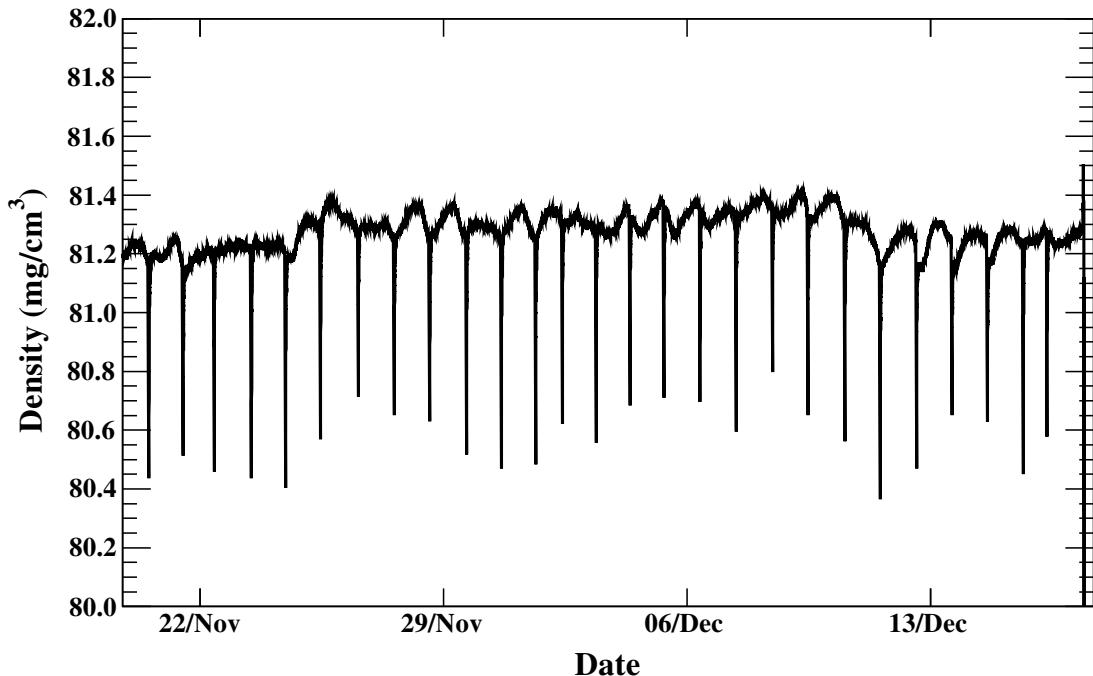
Fig. 2.10 Stability of the density during the experiment.

2.6.1   Solenoid magnet

The spectrometer magnet of the CDS is of a solenoidal type, whose bore diameter is 1.18 m and whose length is 1.17 m with an overall weight of 23 tons. The design of the solenoid magnet is shown in Fig. 2.12. It is located on the final focus point of the K1.8BR beam line. The magnet provides a uniform field strength inside the tracking volume ($|z| < 420$ mm). In the experiment, to evaluate the systematic difference between negative and position magnetic field, it is operated at +0.7 T and -0.7T with a half experimental time.

2.6.2   Cylindrical drift chamber

The CDC is a cylindrical wire drift chamber that contains 15 layers of anode wires whose structure is shown in Fig. 2.13. The outer radius is 530 mm and the inner radius is 150 mm, with a total length of 950 mm. The wire length of axial layers is 833.8 mm, thus the angular coverage is $49° < \theta < 131°$ in the polar angle region corresponding to a solid angle coverage of 66% of 4π. The CDC consists of two aluminum end-plates of 20 mm thickness, a 1 mm thick CFRP cylinder as the inner wall of the CDC, and six aluminum posts that are placed outside the tracking volume. The CDC uses gold-plated tungsten of 30 μm ϕ for the sense
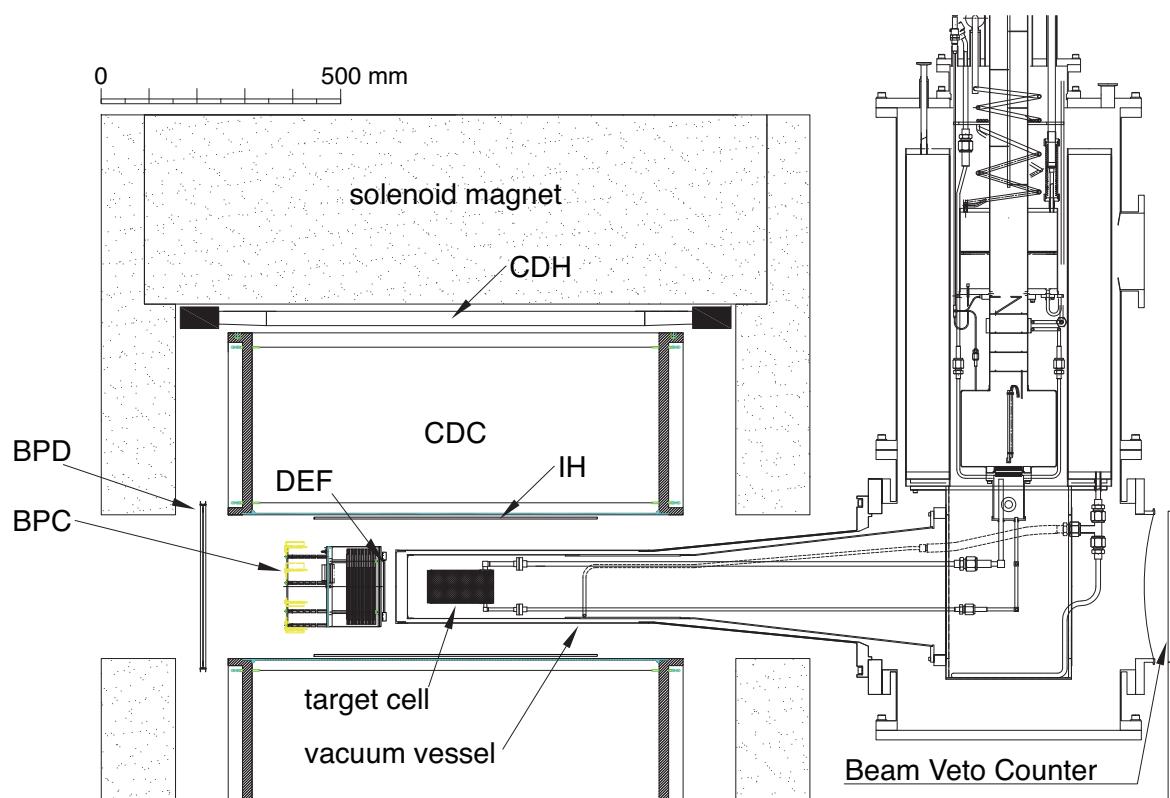
Fig. 2.11 Schematic drawing of the CDS with the target system.
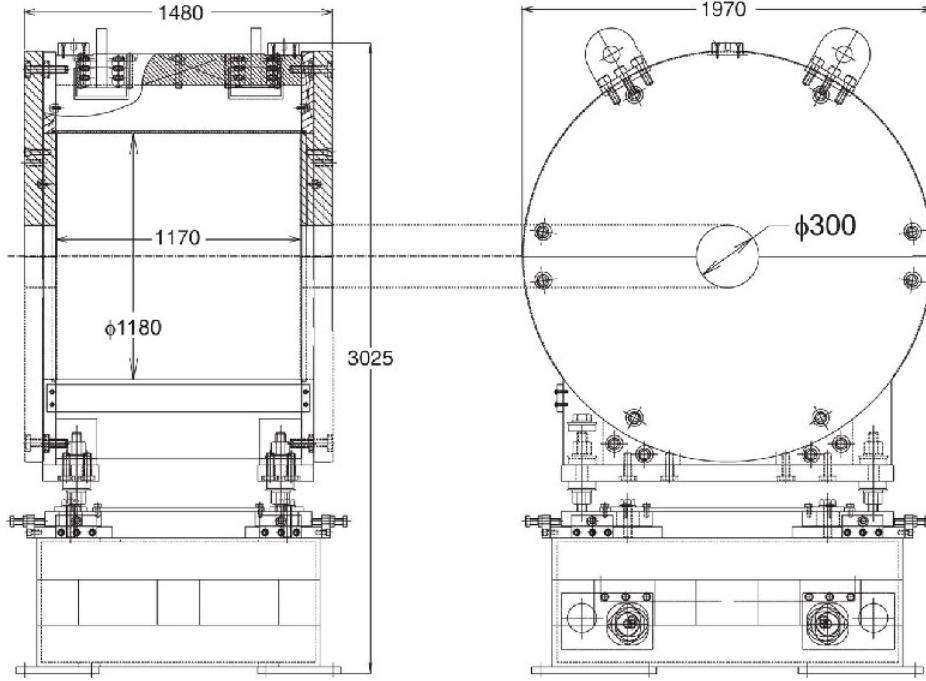
Fig. 2.12 Design of the solenoid magnet (all dimensions in mm). Taken from Ref.[60].

wires, and gold-plated aluminum of 100 μm ϕ for the field and guard wires. These wires are supported by feedthroughs with a bushing inserted at the end. Bushes with an 80 and 200 μm ϕ hole are used for the sense and field/guard wires, respectively.

The CDC has small hexagonal cells with a typical drift length of 9 mm, which are grouped into 7 super-layers as shown in Fig. 2.14. Table 2.7 gives the detailed parameters of the wire configuration. The layers are in the radial region from 190.5 mm (layer #1) to 484.5 mm (layer #15). The 8 stereo layers tilted by about 3.5° are used to obtain longitudinal position information. The number of readout channels is 1816.

The drift gas is 1 atm of mixed argon (50%)-ethane (50%). A high voltage is applied to the field and guard wires, and the sense wires are kept at ground potential. For the first super-layer (A1) and the second one (U1), a high voltage of -2.8 kV is applied to the potential wires, and -2.7 kV to the potential wires of the other super-layers. In addition, -1.5 kV, -1.8 kV, and -0.6 kV are applied to the innermost, the outermost, and the other guard wires, respectively. The readout electronics of the CDC consists of a preamp card with ASDs (SONY-CXA3653Q, τ = 16 ns), an LVDS-ECL converter, and a TDC which is the same as those for the beam line chambers.
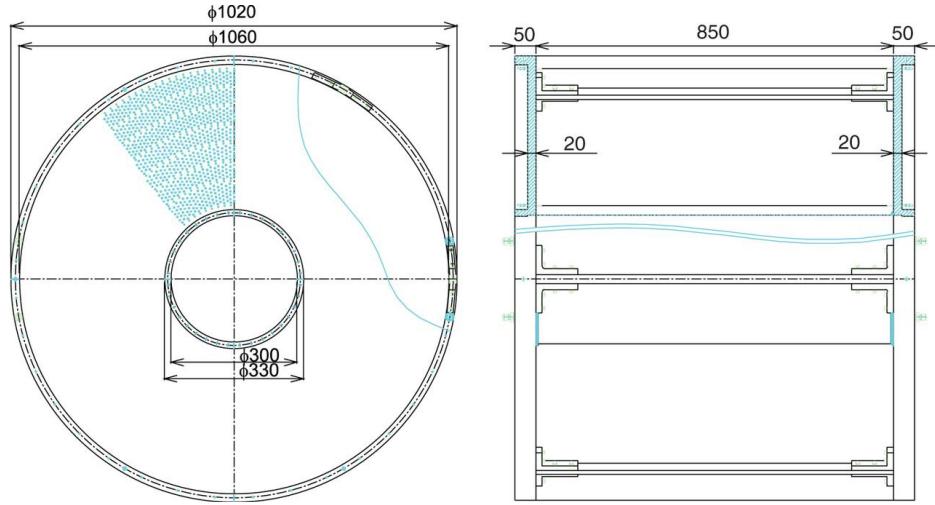
Fig. 2.13 Design of the CDC (all dimensions in mm). The CDC consists of two aluminum end-plates, a 1 mm thick CFRP cylinder as an inner wall, and six aluminum posts that are placed outside the tracking volume. Taken from Ref.[60].
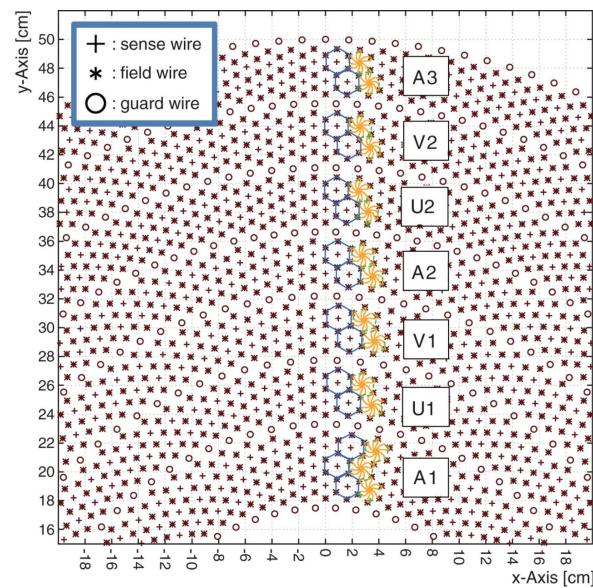
Fig. 2.14 Cell structure of the CDC. Taken from Ref.[60].

Table 2.7 Wire configuration of the CDC.

Super-layer	layer	Wire direction	Radius (mm)	Cell width (degree)	(mm)	Stereo angle (degree)	Signal channels
A1	1	X	190.5		16.7	0	72
	2	X'	204	5.00	17.8	0	72
	3	X	217.5		19	0	72
U1	4	U	248.5	4.00	17.3	-3.55	90
	5	U'	262		18.3	-3.74	90
V1	6	V	293	3.60	18.4	3.77	100
	7	V'	306.5		19.3	3.94	100
A2	8	X	337.5	3.00	17.7	0	120
	9	X'	351		18.4	0	120
U2	10	U	382	2.40	16	-3.28	150
	11	U'	395.5		16.6	-3.39	150
V2	12	V	426.5	2.25	16.7	3.43	160
	13	V'	440		17.3	3.54	160
A3	14	X	471	2.00	16.4	0	180
	15	X'	484.5		16.9	0	180

2.6.3   Cylindrical detector hodoscope

The CDH is a segmented plastic scintillation counter used for the charged particle trigger and particle identification with TOF measurement. The CDH is located at a radius of 544 mm from the beam axis covering a polar angle range from 54 to 126 degrees corresponding to a solid angle coverage of 59% of 4π.

The CDH consists of 36 segments, individually mounted on the inner wall of the solenoid magnet. The scintillators are made of Eljen EJ-200, with dimensions of 790 mm in length, 99 mm in width, and 30 mm in thickness. The scintillation light is detected by a pair of Hamamatsu R7761 fine-mesh 19-dynode photomultipliers 1.5 inches in diameter.

2.6.4   Inner Hodoscope

An inner hodoscope (IH) is a segmented plastic scintillation counter mounted on the inner wall of the CFRP cylinder of the CDC at a radius of 140 mm from the beam axis. The IH covers a polar angle range from 27 to 153 degrees corresponding to a solid angle coverage of 89% of 4π.

The IH consists of 24 ELJEN EJ-200 scintillators with dimensions of 600 mm in length, 37 mm in width, and 3 mm in thickness. Each segment is overlapped by 1 mm. Due to

the strong magnetic field and a limited space, multi-pixel photon counters (MPPCs) with a 3 mm × 3 mm sensitive area were used (Hamamatsu S10362-33-100C). The scintillation light is detected by 4 wavelength-shifting fibers embedded in the scintillator and connected to an MPPC with a specially designed connector. The MPPC signal is read out by using a preamplifier (HOSHIN). In this thesis, IH is not used to analyze the decayed particles.

2.6.5 Backward proton detector

A backward proton detector (BPD) is installed at the most upstream of the CDS to enlarge the acceptance for backward-going charged particles. In particular, it aims to detect a proton from the $\Lambda(1405) \to \Sigma^0 \pi^0, \Sigma^0 \to \Lambda \gamma, \Lambda \to p\pi^-$ decay chain in another experiment with the $d(K^-, n)$ reaction (J-PARC E31).

The BPD is a plastic scintillator hodoscope array with the size of 350 mm (horizontal) × 340 mm (vertical). It is segmented into 70 units of 5 mm × 5 mm × 340 mm scintillation counter made of Eljen EJ-230. Two MPPCs with a 3 mm × 3 mm sensitive area (Hamamatsu S10362-33-050C) were directly put on both sides of each slab. Signals from the MPPCs are read out by fast timing amps (ORTEC FTA820). The BPD is not used in the present analysis except for an energy loss calculation for the kaon beam.

2.7 Forward particle detector system

A forward TOF counters at 0 degrees with respect to the beam direction, which is installed to detect kicked-out neutrons and protons in the ^{3}He(K^-, N) reactions. Flight lengths are kept more than 14 m for both neutrons and protons to achieve enough momentum resolution, while keeping acceptance as much as ∼20 msr with a large volume of scintillator arrays. The forward TOF counter system is composed of a neutron counter array (NC), a proton counter array (PC) and a charged veto counter array (CVC) as illustrated in Fig. 2.15. The CVC located front of the NC vetoes charged particles injected on the NC, not only detects fast protons. Trajectories of protons are reconstructed with a forward drift chamber (FDC) installed just downstream the target system, and bended by a dipole magnet called as Ushiwaka towards the PC. Kaon beams without any reaction are swept out by Ushiwaka to suppress background events in the neutron spectrum. A beam veto counter (BVC) which is placed just downstream of the target system is used to remove the events which has forward charged particle form the neutral trigger.
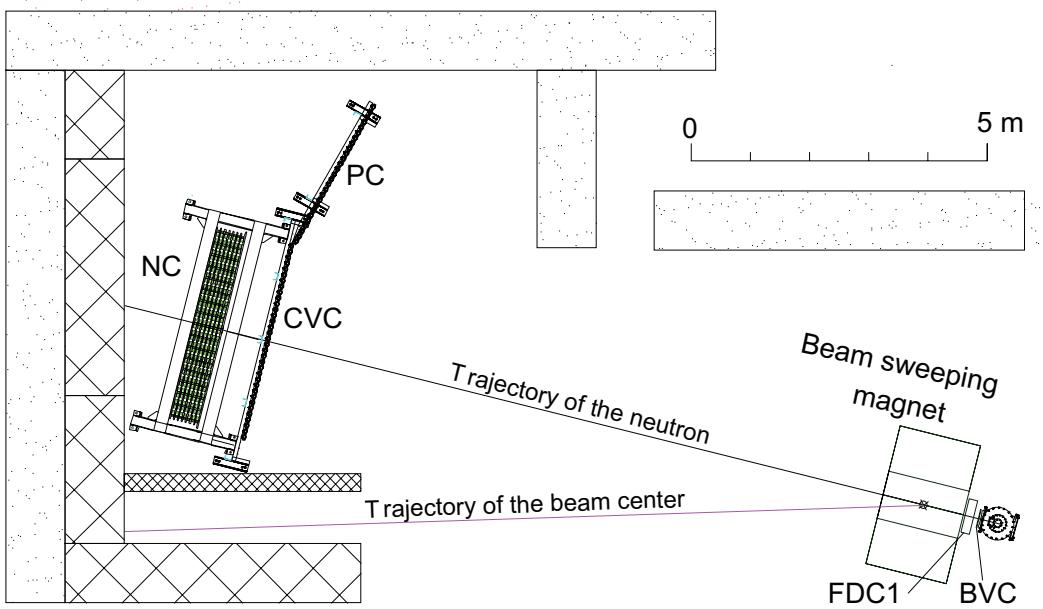
Fig. 2.15 Schematic view of the forward detectors; the beam veto counter(BVC), forward drift chamber 1 (FDC), the beam sweeping magnet, the neutron counter (NC), the charge veto counter (CVC), and the proton counter (PC). The NC is located 14.7 m away from the final focus position. Taken from Ref.[60].

2.7.1   Neutron time-of-flight counter

A neutron TOF counter (NC), located 14.7 m away from the final focus point, consists of an array of scintillation counters and has an effective volume of 3.2 m (horizontal) $\times$ 1.5 m (vertical) $\times$ 0.35 m (depth) segmented into 16-column (horizontal) $\times$ 7-layer (depth) units. The acceptance of the neutron counter is ~ 20 msr ; $\pm 6.2°$ in the horizontal direction and $\pm 2.9°$ in the vertical. Each scintillation counter has dimensions of 20 cm (width) $\times$ 150 cm (height) $\times$ 5 cm (thickness) with two 2 inch Hamamatsu H6410 photomultipliers attached to both long sides of the scintillator through a Lucite light guide. The scintillators for the first three layers are made of Saint-Gobain BC408, and the other four layers are made of Saint-Gobain BC412. The average time resolution of the neutron counter, measured with cosmic rays, is 92 ± 10 ps (σ). The error represents the variation among the segments.

2.7.2   Charge veto counter

The charge veto counter (CVC) is located upstream of the neutron counter, 14.0 m away from the final focus point and has an effective area of 3.4 m (horizontal) $\times$ 1.5 m (vertical) segmented into 34 units. Each scintillation counter has dimensions of 10 cm (width) $\times$

150 cm (height) $\times$ 3 cm (thickness), and is equipped with two 2 inch Hamamatsu H6410 photomultipliers attached to both long sides of the scintillator through a Lucite light guide. The scintillators are of Eljen EJ-200 type. The average time resolution measured with cosmic rays is 78 $\pm$ 7 ps (σ). The error represents the variation among the segments.

2.7.3   Proton time-of-flight counter

The proton TOF counter is installed as the extended wall of the charge veto counter. It has an effective area of 2.7 m (horizontal) $\times$ 1.5 m (vertical) segmented into 27 units. The configuration of each scintillation counter is same with that of the charge veto counter except that a Saint-Gobain BC408 scintillator is used. The average time resolution of the proton counter, obtained from cosmic ray data, is 75 $\pm$ 6 ps (σ). The error represents the variation among the segments.

2.7.4   Beam veto counter

The beam veto counter (BVC) is attached on the downstream flange of the target cryostat as shown in Fig. 2.11. The coverage size of the beam veto counter is 320 mm (height) $\times$ 320 mm (width) $\times$ 10 mm (thickness) made of Eljen EJ-200. The BVC covers the acceptance of the neutron counter. The BVC is horizontally segmented into 8 units with different sizes as shown in Fig. 2.16 to avoid the over-concentration of the beam on the central segments. 1-inch fine-mesh Hamamatsu R5505 photomultipliers are attached on the both ends of each scintillator segment through Lucite light guides. The signals are read out with an amplification with HOSHIN preamplifier.

2.7.5   Forward drift chamber

The forward drift chamber (FDC) is a feedthrough type chamber which has 6 planes (VV'XX'UU'). The tilt angles of U and V layers are ± 15 degrees. Each layer has 64 sense wires with a drift length of 3 mm which corresponds to an effective area of 384 mm (horizontal) $\times$ 264 mm (vertical). The cell geometry is shown in Fig 2.7(c) and the parameters of the chamber are summarized in Table 2.5. The readout method is the same as those for the beam line chambers.

2.7.6   Beam sweeping magnet

A dipole magnet called as Ushiwaka is located downstream of the CDS and the FDC is attached on upstream of the magnet. The magnet has an aperture of 82 cm (horizontal) $\times$
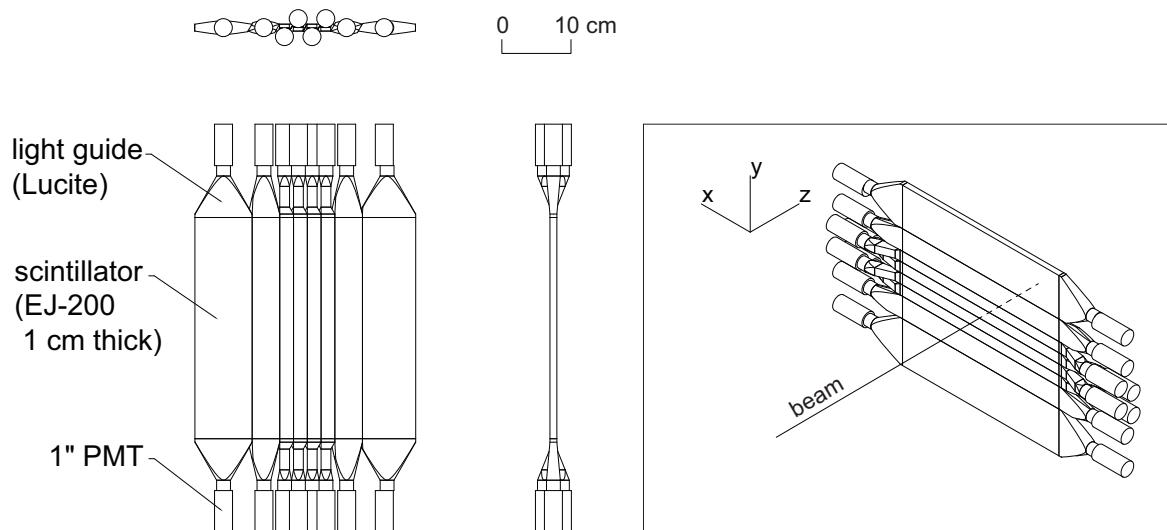
Fig. 2.16 Schematic drawing of the beam veto counter.

40 cm (vertical) and a pole length of 70 cm, which accommodates whole acceptance of the neutron counter. Ushiwaka is capable of providing a maximum field of 1.6 T and operated at ~1.0 T in the production run.

2.8   Materials in the spectrometer system

The materials in the spectrometer system cause the energy losses, the multiple scattering, and the reaction with other than target for the particles. The net effects are expected to result in systematic shifts of the measured momenta, event losses, and additional deteriorations of the spectrometer resolutions. The momenta of the charged particles are corrected particle by particle taking into account the materials on their trajectory. We developed the correction routine for the kaon beam, the charged particles in the CDS and the forward-going charged particles, where the materials summarized in Table 2.8, Table 2.9, and Table 2.10 were considered, respectively. The wires, the cathode planes and the windows of the chambers, the windows and the reflection sheet of the AC, and the wrapping of the scintillator bars were not taken into account, since their contribution is negligible compared to the required precision of a few MeV/c.

Table 2.8 Summary of beam-line materials between the center of BLC2 (z=-130 cm) and the FF. Typical momentum reductions of the kaon and the proton beams at 1 GeV/c are calculated using the Bethe-Bloch formula.

Component	Material	Density g/cm^3	Thickness mm	Thickness g/cm^2	$-\delta p$ (MeV/c) 1 GeV/c kaon	$-\delta p$ (MeV/c) proton
BLC2b	Ar-isoC$_4$H$_{10}$	0.0016	100	0.02	0.03	0.07
T0	Scintillator	1.03	10	1.03	2.4	4.2
AC	Aerogel	0.20	100	2.00	4	6.8
BPD	Scintillator	1.03	5	0.52	1.2	2.1
DEF	Scintillator	1.03	3	0.31	0.72	1.2
BPC	Ar-isoC$_4$H$_{10}$	0.0016	60	0.01	0.02	0.03
Target system						
Chamber cap	aluminum	2.7	0.6	0.16	0.3	0.51
Radiation shield	aluminum	2.7	0.3	0.08	0.15	0.26
Cell cap	AlBeMet	2.07	0.6	0.12	0.23	0.51
Target	helium-3	0.081	60	0.49	1.45	2.45
Air	Air	0.0012	940	0.11	0.24	0.40
Total				5.02	10.7	18.5

Table 2.9 Summary of materials used in the energy loss correction of the CDC track.

Component	Material	Density g/cm^3	Thickness mm	Thickness g/cm^2
Target system				0
Target	helium-3	0.081	34	0.28
Cell wall	beryllium	1.85	0.3	0.06
Radiation shield	aluminum	2.70	0.3	0.08
CFRP	CFRP	1.70	1	0.17
Air	Air	0.0012	70	0.0084
IH	Scintillator	1.03	3	0.31
CDC				
CFRP	CFRP	1.70	1	0.17
Gas	Ar-C$_2$H$_6$	0.0015	380	0.057
Total				1.13

Table 2.10 Summary of materials between the FF and the forward counters. Typical momentum reduction of the proton beam at 1 GeV/c is calculated using the Bethe-Bloch formula.

Component	Material	Density	Thickness		$-\delta p$ (MeV/c)
		g/cm^3	mm	g/cm^2	1 GeV/c proton
Target					
Target	helium-3	0.081	80	0.65	3.3
Cell cap	AlBeMet	2.07	0.6	0.12	0.39
Rad. shield	aluminum	2.7	0.3	0.081	0.26
Frange	SUS304	8.9	0.3	0.27	0.26
BVC	Scintillator	1.03	10	1.03	4.2
FDC	Ar-C_6H_{10}	0.0016	100	0.016	0.053
to PC					
Air	Air	0.0012	1.3E+04	1.57	5.2
Total				3.71	13.6
to NC					
Air	Air	0.0012	1.4E+04	1.69	
CVC	Scintillator	1.03	30	3.09	
Total				6.92	

2.9   Data acquisition

2.9.1   Data acquisition system

The on-line data acquisition system (DAQ) consists of the TKO[66, 67], VME, and PC Linux. The signals from the detectors are fed into ADC and TDC modules slotted into 10 TKO crates. They are read in parallel with 10 VME-SMPs (super memory partner[68]) via a TKO SCH (super controller head). The data stored in a buffer memory of the SMP is transferred to the DAQ-PC through SBS Bit3 VME-to-PCI bridges. Additionally, two DAQ systems consist of VME and PC Linux are used. One is for spill by spill readout of scalers, and the other one is for multi-hit TDC readout for beam-line counters. To secure event matching in the offline analysis, an event and a spill numbers are distributed the three DAQ systems by using a master trigger module and receiver modules and event matching is done offline. The status of the detector system, such as temperature of the cryogenic target system and the magnetic field of the D5 magnet was recorded by using LabVIEW based program.

Since current DAQ system has no buffer memory in TDC and ADC modules, the fast clear scheme is adopted to efficiently accumulate the (K^-, N) events. The 1st level trigger is constructed by the beam line detectors and CDS, and then TDC common start/stop signals and ADC timing gates are distributed to each module, followed by analog-to-digital

conversion. Signals of the forward counters reach the DAQ system 100 ns or more after 1st level decision. Then 2nd level trigger is generated by the forward-counter signals. If 2nd level is not acceptable, the analog-to-digital conversion is suspended and the modules are initialized for the next event (*FastClear*).

The dead time of conversion in ADC/TDC and data-transfer from TKO-SCH to VME-SMP is $\sim 120\ \mu s$ and $\sim 230\ \mu s$, respectively. The dead time caused by a data-transfer from VME-SMP to the PC-Linux is negligible by using two buffers in the VME-SMP. In the case of *FastClear*, it takes only $\sim 3\ \mu s$ to be ready for the next event. During the main data taking period, a typical DAQ rate was about 900 events per spill with the live rate of about $\sim 70\%$.

2.9.2 Trigger scheme

Kaon beam trigger

The beam trigger is constructed by coincidence signals from the beam line counters, the BHD, T0 and the DEF. The kaon beam trigger (K_{beam}) is selected from the beam trigger by using the kaon identification counter, i.e., a veto signal of the AC ($\overline{\mathrm{AC}}$) defines the kaon beam. It should be noted that antiprotons in the beam are removed upstream of the beam line by using the ES1, CM1, and CM2. A logical expression of the kaon beam trigger is given as

$$(K_{\mathrm{beam}}) \equiv (\mathrm{BHD}) \otimes (\mathrm{T0}) \otimes (\mathrm{DEF}) \otimes (\overline{\mathrm{AC}}).$$

A pion beam trigger requires coincidence signal of AC. Then,

$$(\pi_{\mathrm{beam}}) \equiv (\mathrm{BHD}) \otimes (\mathrm{T0}) \otimes (\mathrm{DEF}) \otimes (\mathrm{AC}).$$

Main trigger

A two-level trigger logic for the in-flight $^3\mathrm{He}(K^-, N)$ reaction is applied. To detect the Λ and proton in the CDS, the main trigger for the E15 experiment is set to three or more CDH hits (CDH^{3hit}). The E15 main trigger is given as

$$(\mathrm{Main}) \equiv (K_{\mathrm{beam}}) \otimes (\mathrm{CDH}^{3hit})$$

Triggers for normalization

For the evaluation of reaction cross sections, the total kaon flux on the target is crucial. Therefore, elementary kaon beam data (K_{beam}) is also recorded. Minimum-biased beam data ($\mathrm{BHD} \otimes \mathrm{T0}$) is also mixed to monitor the performance of the AC and the DEF.

$K_{beam}\otimes$**CDH triggers**

Since the main trigger rate is few hundreds per spill, the DAQ has still room to take additional data. Although primary purpose of the present experiment is the study with forward-going nucleons, some physical output without forward counters are also expected. Among them, the Λp events in the CDS are most interested in. Therefore, kaon beam triggers with the coincidence of the CDH hit(s) are mixed as much as possible to keep DAQ live rate better than 70%.

Cosmic trigger

A cosmic data triggered by two or more CDH hits were recorded to evaluate the CDS performance between the spills.

Chapter 3

Data analysis and calibration

3.1 Basic data analysis

3.1.1 Conversion of the raw data

In the experiment, the detector informations are stored as TDC and QDC data, and these are converted to time and deposit energy scale in the analysis.

To measure a hit time, TKO 32 channel Drift Chamber TDC (DR.T) and TKO 16/64 channel High Resolution TDC (HR-TDC) modules are used for drift chambers and scintillation counters, respectively. TDC information is converted to time information by using gain function, which is evaluated by calibration data with time calibrator (ORTEC 462) as shown in Fig. 3.1 for every channel. A TDC channel (T) is converted to time scale (t) by using following equation

$$t = T \cdot G_1 \left(+ T^2 \cdot G_2 \right), \tag{3.1}$$

where G_1 and G_2 are gain parameters for 1 and 2 order component, respectively. A correlation between TDC and time is assumed to be linear for every HR-TDCs. In DR.T type TDC, due to the time range is much wider than HR-TDC, the correlation has higher order component so that the second order polynomial function is used for fitting. The TDC gain fluctuation, which comes from temperature change or other difference of environmental conditions, is checked during the experiment, and it is found to be negligible small.

For the scintillation counters, the charge integration of the analog signal is recorded to evaluate a deposit energy of particles in the counter. The TKO 32 channel charge-integration ADC is used for doing this, and the conversion from QDC (Q) to deposit energy (dE)is performed using following equation

$$dE = (Q - Q_0) \cdot G_{ADC}, \tag{3.2}$$
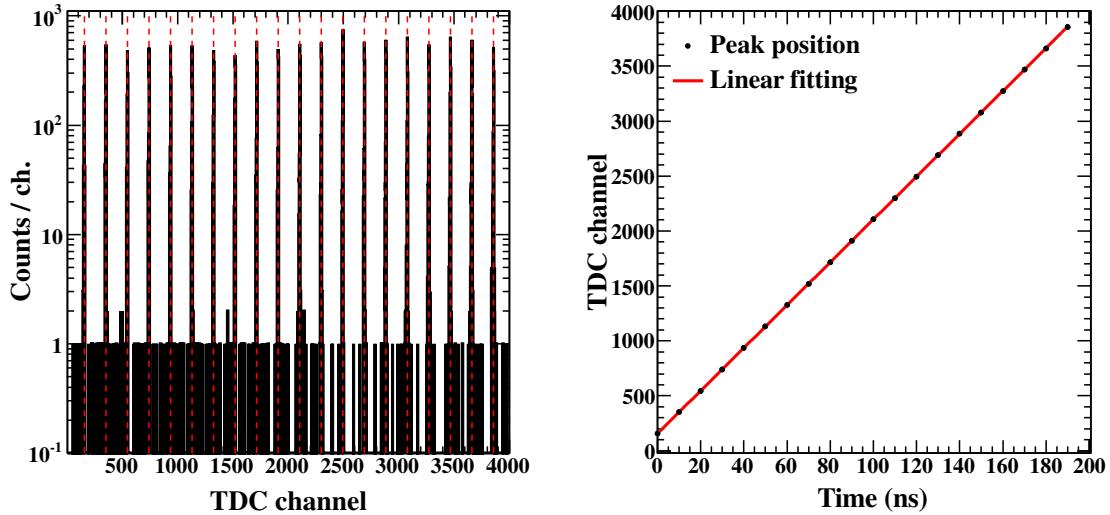
Fig. 3.1 (left) Calibration data to evaluate TDC time gain. (right) TDC channel and time correlation. The black plots correspond to peak positions indicated by red dotted-lines in left figure, and red line shows linear fitting result of the plots.

where Q_0 and G_{ADC} denote QDC value of pedestal peak and ADC gain parameter, respectively. The Q_0 and G_{ADC} are evaluated by fitting the pedestal peak with Gaussian distribution and peak from minimum-ionizing particle with Landau distribution as shown in Fig. 3.2. An energy deposit in one-cm-thick plastic scintillator is about 2 MeV*ee*, so that an ADC gain parameter, G_{ADC} is calculated as $G_{ADC} = 2.0 \cdot z / (Q_{MIP} - Q_0)$, where Q_{MIP} is peak position for MIP. The parameters for QDC conversion would slightly vary during the experiment due to temperature change. Accordingly, the gain parameters are evaluated for every several hours data.

3.1.2 Analysis for hodoscope detectors

A segment of a hodoscope detector has two data sets of time and deposit energy, which come from its two detection devices on both detector edges. In the analysis, these four informations are used to decide the correct hit timing and deposit energy in a segment. The measured time information of each edges has time walk effect, which is caused by pulse height effect for a discriminator: a timing of signal outputting from discriminator slightly depends on the pulse height or the charge of the inputted analog signal. This effect can be found in the time and deposit energy correlation shown in Fig. 3.3. This effect is corrected in the analysis by using
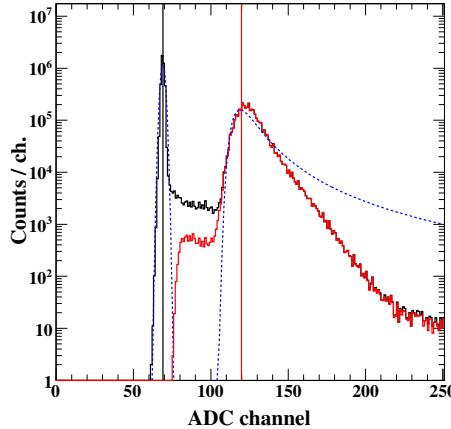
Fig. 3.2 Typical QDC spectrum of scintillation counter. The red histogram shows QDC spectrum required that a coincidence hit in the corresponding TDC. The pedestal peak and the MIP peak positions are evaluated by fitting the strong peak in the black spectrum and broad peak in the red histogram, respectively. Each peak positions and fitting results are indicated by black line, red line and blue dashed-lines.

following correlation function

$$t_c = t + p_0 + \frac{p_1}{\sqrt{dE}} + p_2 \cdot dE, \tag{3.3}$$

where t denotes time information calculated by Eq. 3.1 and p_i are correction parameters. In this correction, p_0 is an time offset parameter, p_1 and p_2 are time-walk effect parameters. These parameters are obtained by iterating correction and adjusted for every runs.

The hit timing and deposit energy of one of the detection devices in a segment depend on distance between hit position and the detection device, l. This dependence can be compensated with arithmetic mean for hit timing and geometrical mean for deposit energy as following equations.

$$t_m = \frac{t_u + t_d}{2} \tag{3.4}$$

$$dE_m = \sqrt{dE_u \cdot dE_d}, \tag{3.5}$$

where $t_{u,d}$ and $dE_{u,d}$ are hit time and deposit energy of one of the edge detectors.

In contrast, this position dependence can be extracted by subtracting two edge hit timings, thus the distance between hit position and one edge side (l) can be calculated as

$$l = \frac{t_u - t_d}{2v}, \tag{3.6}$$

where v denotes effective light velocity in the scintillator.
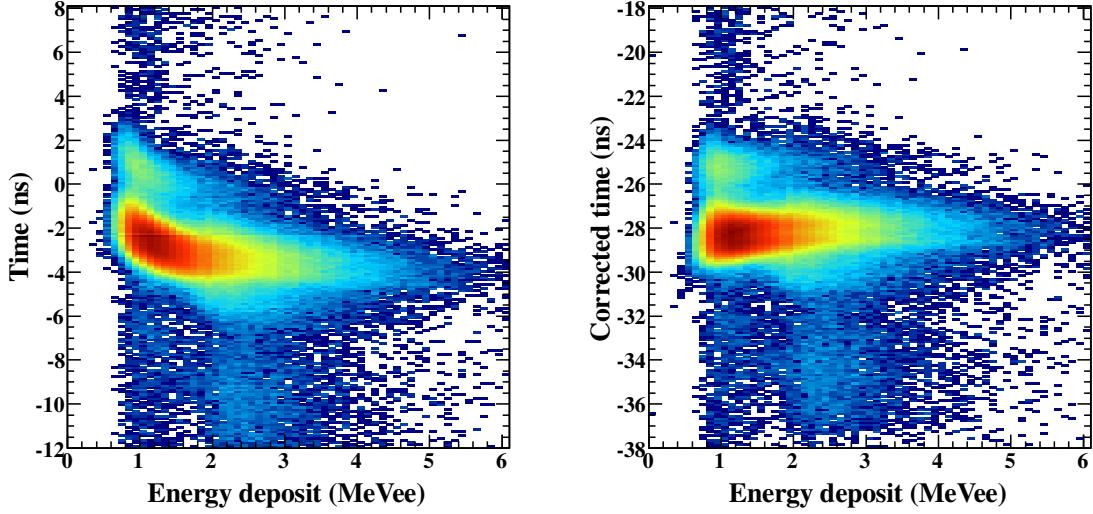
Fig. 3.3 Typical time and energy deposit correlation (left) and that of after correction (right).

3.1.3 Analysis for drift chambers

Beam-line drift chambers

The time of the drift chambers are calculated from the TDC information. Fig.3.4-(top) shows time distribution of a typical beam-line drift chamber. The drift time of each wires are calibrated using differential distribution to the maximum point is set to be 0 ns, as shown in the bottom figure in the Fig.3.4. The correlation function between drift time and drift length is evaluated by using integral distribution, by assuming that the particles pass through a drift chamber at right angle and are uniformly distributed in each cell.

A drift length can be calculated by using correlation function, but still the drift direction is not well known. To track using the all hit informations, all combinations of the drift directions are examined and the combination which gives minimum χ^2/ndf is selected. In the three dimensional linear fitting, the χ^2/ndf is defined as

$$\chi^2/ndf = \frac{1}{N-4}\sum_i^N \left(\frac{x_i' - f(z_i)}{\sigma_i}\right), \tag{3.7}$$

$$f(z) = \cos\theta(a+zb) + \sin\theta(c+zd), \tag{3.8}$$

where N is the number of the given hits, x' is the positions perpendicular to the wire and the particle direction, $f(z)$ is the calculated position in a rotated plane with an angle of θ, and
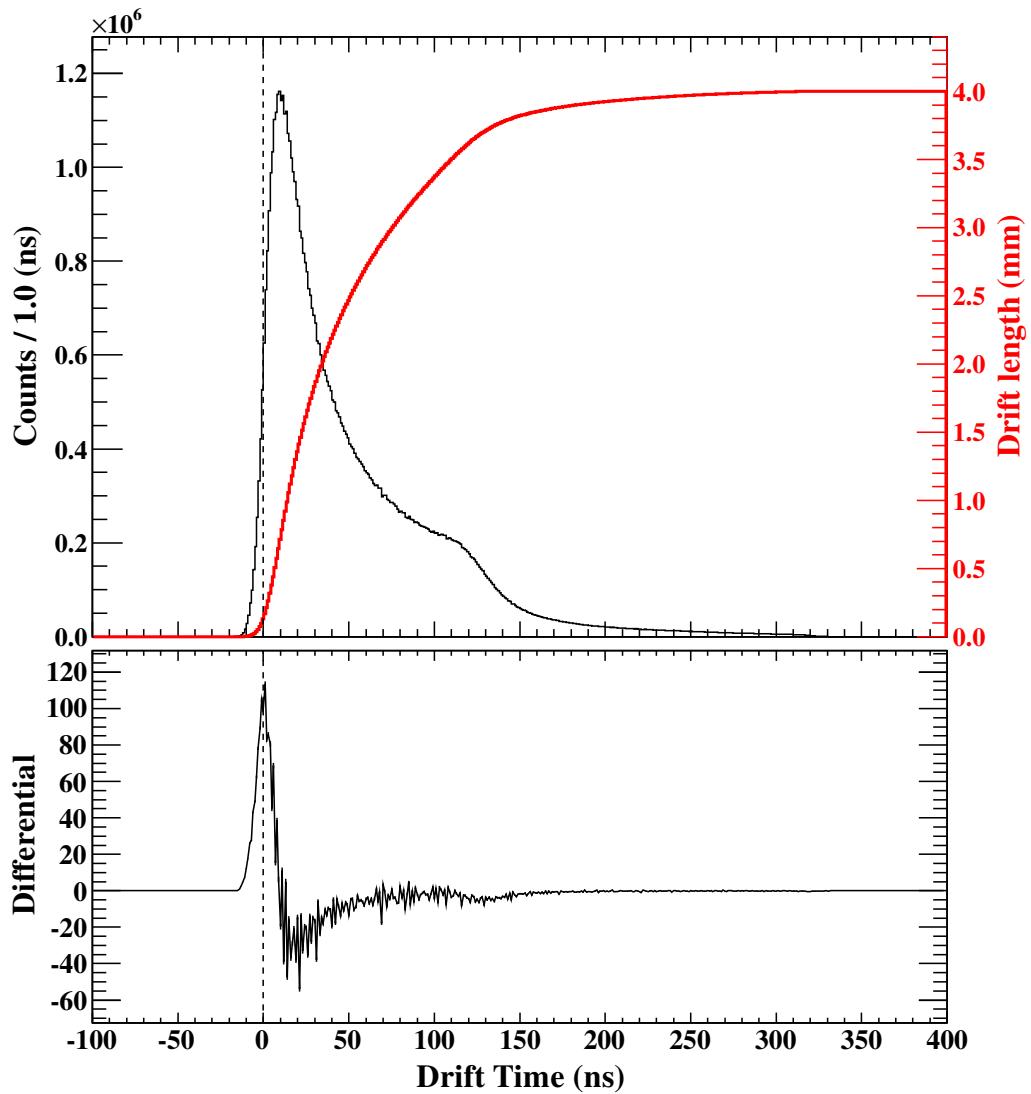
Fig. 3.4 (top) A typical drift time distribution of BLDC and calculated drift length shown by led line. A function of the drift length is the integral of the drift time distribution. (bottom) A differential distribution of drift time. The offset of the drift time is corrected by using a peak position of the differential distribution.

σ is the assumed position resolution. The four parameters a, b, c, and d at the minimum χ^2/ndf can be analytically calculated for the given set of the hits.

All beam-line drift chambers consist of pairs of staggered planes by a half of the cell size. Thus, a sum of the drift lengths of the paired hits should be about the cell width. Fig.3.5 shows the relation between a differential and a mean of drift times in the paired planes. In the Fig.3.5-(left) has correlation between a differential and a mean of drift times, so that this correlation is corrected as shown in Fig.3.5-(right). The correction function is defined by fitting this correlation, and it is evaluated for every paired planes. In this way, the hit timing of the drift chambers can be calculated by using the corrected mean drift time. In this analysis, when the paired-hits searching is failed, then those paired planes are excluded from the timing analysis.
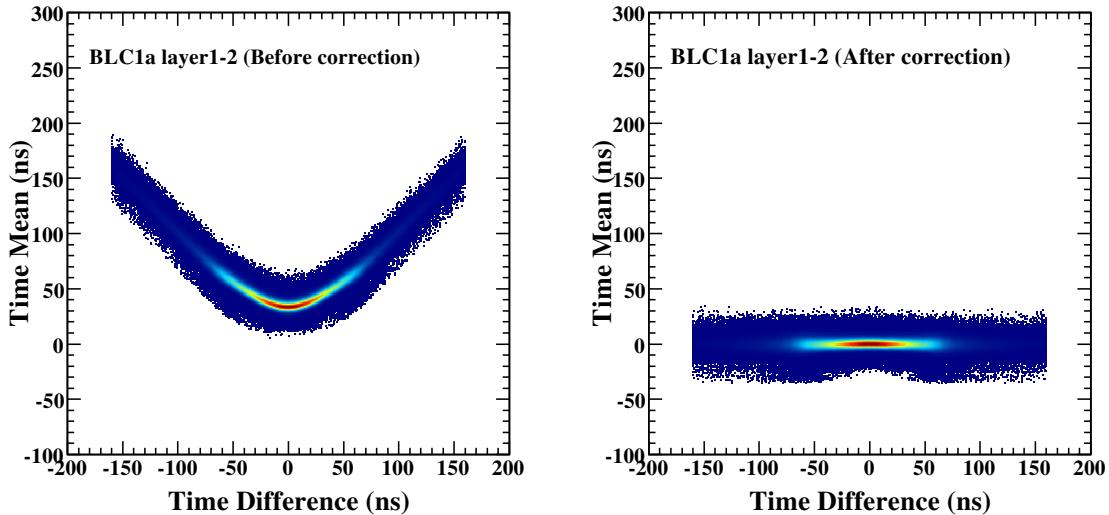
Fig. 3.5 (left) A typical correlation between time difference and time mean of paired hits. (right) Same figure after applying the correction.

In the beam-line drift chambers, there are BLC1, BLC2 and BPC. For tracking at the BLC1 and BLC2, a candidate is required to have hits more than 5 planes out of 8 planes in each U and V planes. In the case of BPC, due to a redundancy of the BPC is less than BLC1 and BLC2, all 8 planes is required to have hits. First of all, the pre-fitting is performed with MWPC mode, which is fitting without drift time consideration. Then a hit combination with a minimum χ^2/ndf is selected as a first track. This procedure is iteratively done with hits not included in reconstructed tracks, until remaining hits can not be used to reconstruct an additional track. After these tracking procedure, the procedure is performed again for BLC1 and BLC2 without a hit which has the largest distance between hit position and track

position to distinguish a hit from accidental hits. Fig.3.6 shows comparison between χ^2 distribution in first and second tracking procedure. Because the χ^2/ndf reduces in second tracking procedure, accidental hits or other dummy hits is successfully removed from each track candidate. This procedure is used for BLC1, BLC2 and cylindrical drift chamber which have large redundancy layer. However, in BPC, this procedure could not be used due to lack of number of layers.
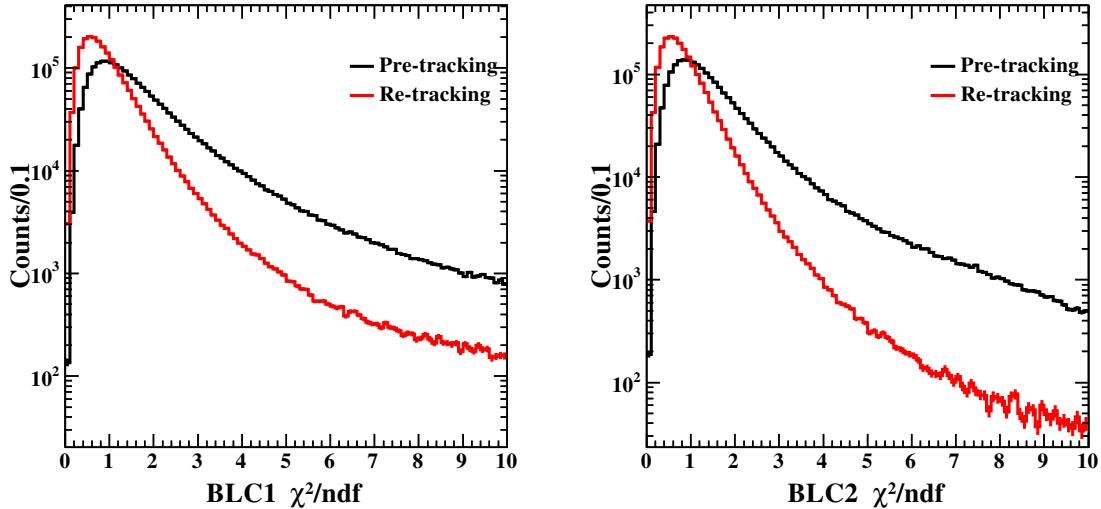
Fig. 3.6 χ^2/ndf distribution of BLC1(left) and BLC2(right) in Pre- and Re-tracking.

Cylindrical drift chamber

The calibration of the drift time in the CDC is the same as that in the beam-line drift chambers. An evaluating the correlation function between drift time and drift length is performed by fitting the residual distribution as a function of drift time. In this fitting, the fifth polynomial function is used. The evaluation is done iteratively. Fig.3.7 shows drift time distribution and relation between drift time and drift length after adjusting the relative time and correlation between drift time and drift length.

The tracking for the CDC is performed by using a helix curve, which can be parametrized as

$$x(\phi) = d_\rho \cos\phi_0 + \frac{1}{\rho}\left(\cos\phi_0 - \cos(\phi_0 + \phi)\right), \tag{3.9}$$

$$y(\phi) = d_\rho \sin\phi_0 + \frac{1}{\rho}\left(\sin\phi_0 - \sin(\phi_0 + \phi)\right), \tag{3.10}$$
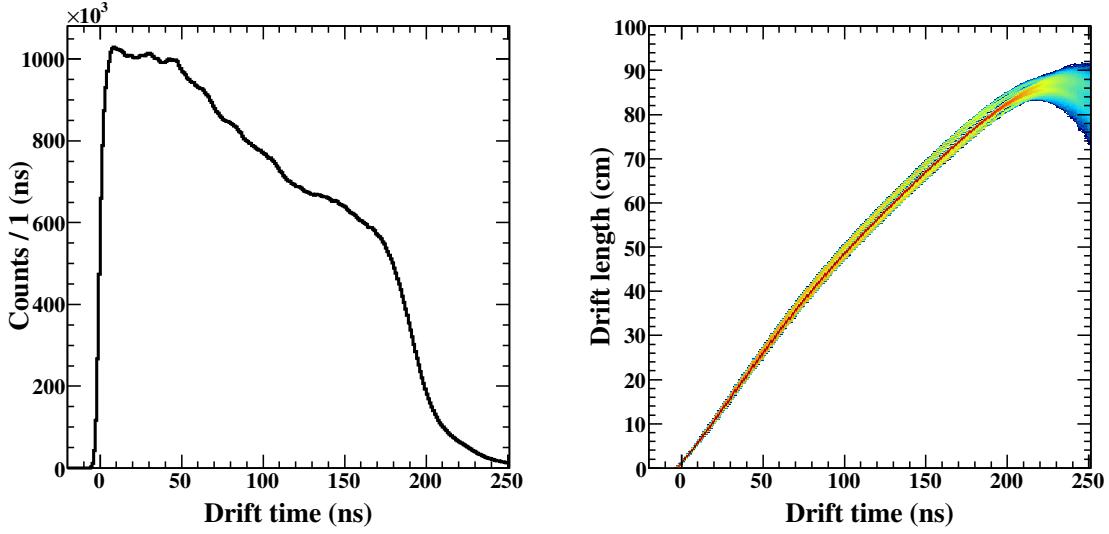
Fig. 3.7 (left) The drift time distribution of a typical CDC layer. (right) The drift length versus drift time correlation. The correlation function is evaluated by using 5th polynomial function.

$$z(\phi) = d_z - \frac{1}{\rho}\tan\lambda \cdot \phi, \tag{3.11}$$

where d_ρ is the distance of the helix from pivotal point in the xy plane, ϕ_0 is the azimuthal angle to specify the pivotal point with respect to the helix center, ρ is the inverse of the signed radius of the helix, d_z is the distance of the helix from the pivotal point in the z direction, and $\tan\lambda$ is the dip angle. The momentum of a charged particles is calculated by using its helix parameters as

$$\mathbf{p} = \frac{cB}{\rho}\left(-\sin(\phi_0 + \phi), \cos(\phi_0 + \phi), \tan\lambda\right), \tag{3.12}$$

where c is the light velocity and B is the strength of the magnetic field in the z direction.

In the tracking of the CDC, track candidates are searched in $x - y$ plane using only axial layers at first. To determine the combination of hits in axial layers and to estimate helix parameters d_ρ, ϕ_0, and ρ, the circle fitting is performed. After that, associated hits in the stereo layers are searched in $z - \phi$ plane to estimate d_z and $\tan\lambda$. Finally, full helix fitting is performed by using *TMinuit* to minimize the χ^2/ndf, which is defined as

$$\chi^2/ndf = \frac{1}{N-5}\sum_i^N \left(\frac{\delta_i - dl_i}{\sigma_i}\right)^2, \tag{3.13}$$

where N is the number of hits, δ_i is the shortest distance between the hit wire and the helix track, dl_i is the drift length, and σ_i is the spatial resolution. A track is required to have at

least one hit in each axial super layer. In addition, at least 5 hits in the stereo layers and at least 10 hits in total are required.

3.2   Beam line analysis

Using basic informations of beam line counters and drift chambers, the beam particle is analyzed to identify the particle and calculated its momentum. This analysis part can be roughly separated into two part, which are identification part and momentum calculation part. At the identification part, time of flight information is used to ensure that the beam particle is kaon, even the beam particles have been already identified at on-line trigger level using aerogel Chrenkov counter. In the second part, beam momentum calculation, a momentum vector is analyzed by using three drift chambers. In these analysis, it is also important to remove beam pile-up event to clearly select an kaon induced reaction. To do this, these analysis are applied in stage with selecting pure single kaon beam event. Overview of the beam line analysis is as follows,

1. T0 single hit event selection

2. Kaon beam selection by using time of flight between BHD and T0

3. BLC1 and BLC2 tracking, and single track request

4. Momentum analysis

5. BPC (vertex chamber) tracking and single track request

6. Track matching between BLC2 and BPC.

In this section, the beam line analysis is shown from the top to end. Used data set is unbiased kaon trigger event which is produced by only beam line counters, namely there is no bias from other downstream counters.

3.2.1   Particle identification of beam particle

To identify the beam particle, time of flight between BHD and T0 counters is used. In the analysis, T0 counter is used as time zero counter, so that number of hits in T0 counter is always required to be 1 to ensure the correct timing of triggered event. On the other hand, hit multiplicity in the BHD is much higher than that in T0 because of the BHD is located at up stream of the beam line. Therefore, this requirement is not applied for the BHD to avoid over killing the event number.
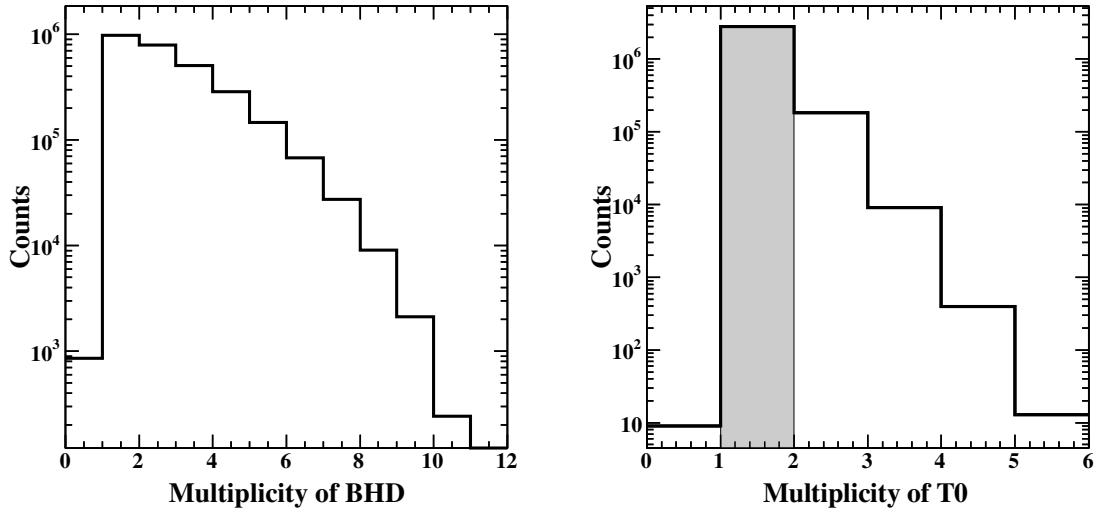
Fig. 3.8 Hit multiplicity of BHD (left) and T0 (right). Because of BHD is located at the most upstream of the beam-line, BHD has much higher number of fired segments than T0. To ensure the correct timing of time-zero and single beam particle event, T0 multiplicity is required to be 1 which is indicated by gray filled region in right figure.

The time of flight between all fired BHD segments and T0 is calculated as shown in Fig. 3.9. In the wide range TOF distribution, the continuum structure is observed whose repetition cycle is 47 MHz. This structure comes from the Transverse-RF in the MR accelerator, and most of particles in this structure are not delivered to the experimental target, basically these particles hit beam duct or other materials in the beam line. The peak structure around the 27 ns corresponds to triggered particle which is certainly transport the beam line system. The TOF resolution is evaluated to be about 250 ps by fitting the peak comes from kaon, which is located at 29 ns. The region corresponding to $\pm 3\sigma$ from the center of the kaon peak is selected in this analysis.

3.2.2 BLDC tracking and momentum analysis

The particle momentum is calculated from the bending angle in the D5 magnet which is measured by two drift chambers, BLC1 and BLC2, located in and out of the magnet. Because the time range of the TDC for the drift chambers is much wider than that for hodoscope detectors, there are many multi track events in each drift chambers. In Fig. 3.10, a strong peak located at zero-ns corresponds to track of triggered particle, and other small structure comes from the transverse-RT which is the same as described in the previous subsection. To avoid multi particle events, it is required that there is only single track in BLC1 and BLC2 in
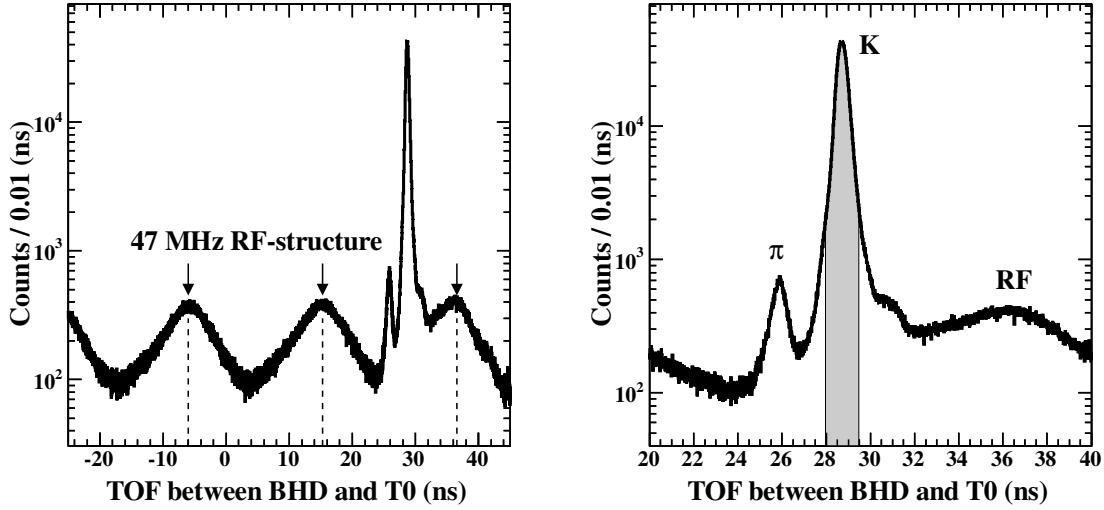
Fig. 3.9 (left) TOF distribution between BHD and T0. Broad structures below arrows come from 47 MHz transverse RF in the MR accelerator. (right) A enlarged TOF distribution in the range from 20 to 40 ns. π and K peaks are clearly observed around 26 and 29 ns, respectively. Beam particles whose TOF is in gray filled region are identified as Kaon where the region is corresponding to $\pm 3.0\sigma$ of the TOF resolution.

the time range from -30 to 100 ns. Additionally, to ensure the each single tracks is attributed to the triggered particle, the track time is required in the triggered time region which is from -10 to 10 ns. The tracks in the BLC1 and BLC2 is checked its χ^2 which is shown in Fig. 3.11. In this analysis, each track is required that χ^2 is less than 10.

To calculate the momentum, each tracks in the BLC1 and BLC2 is connected by using second-order transfer matrix calculated by TRANSPORT code with an additional parameters for the beam momentum. The definition of the χ^2/ndf is almost the same as Eq.3.7, except for the additional degree of freedom of the beam momentum. The minimization of the χ^2/ndf is performed with *TMinuit*. Fig.3.12 shows the reconstructed momentum distribution. The center of the beam momentum was about 1.01 GeV/*c*. In this analysis, events which have χ^2/ndf of less than 20 pass the next step of the analysis as shown in Fig.3.13.

3.2.3   BPC tracking and define of the beam direction

For the tracking in the BPC is essentially the same as other beam-line drift chambers. Fig.3.14 shows the tracking time distribution of the BPC. To reduce the multi particle events, a gate of tracking time from -30 to 100 ns is applied. Also, a track whose tracking time is from -10 to
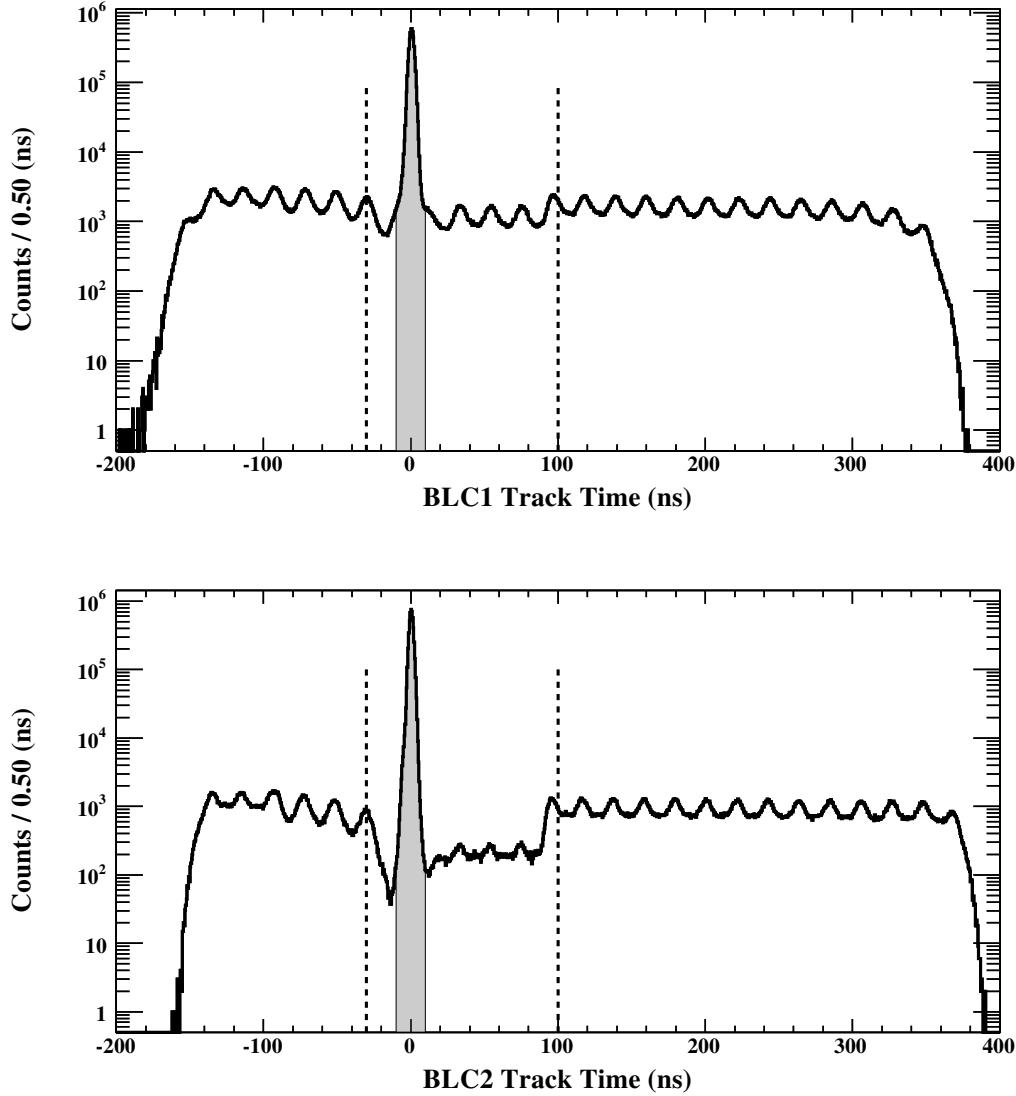
Fig. 3.10 Track time distribution of BLC1 (up) and BLC2 (bottom). There are periodic wave structure over the time range comes from pile-up events and strong peak around 0 ns corresponds to triggered event. To avoid beam pile-up events, it is required that there is only one track in a time window from -30 to 100 ns. Additionally, only a track corresponds to triggered event is accepted by requiring that the track time is in time gate indicated by gray color.
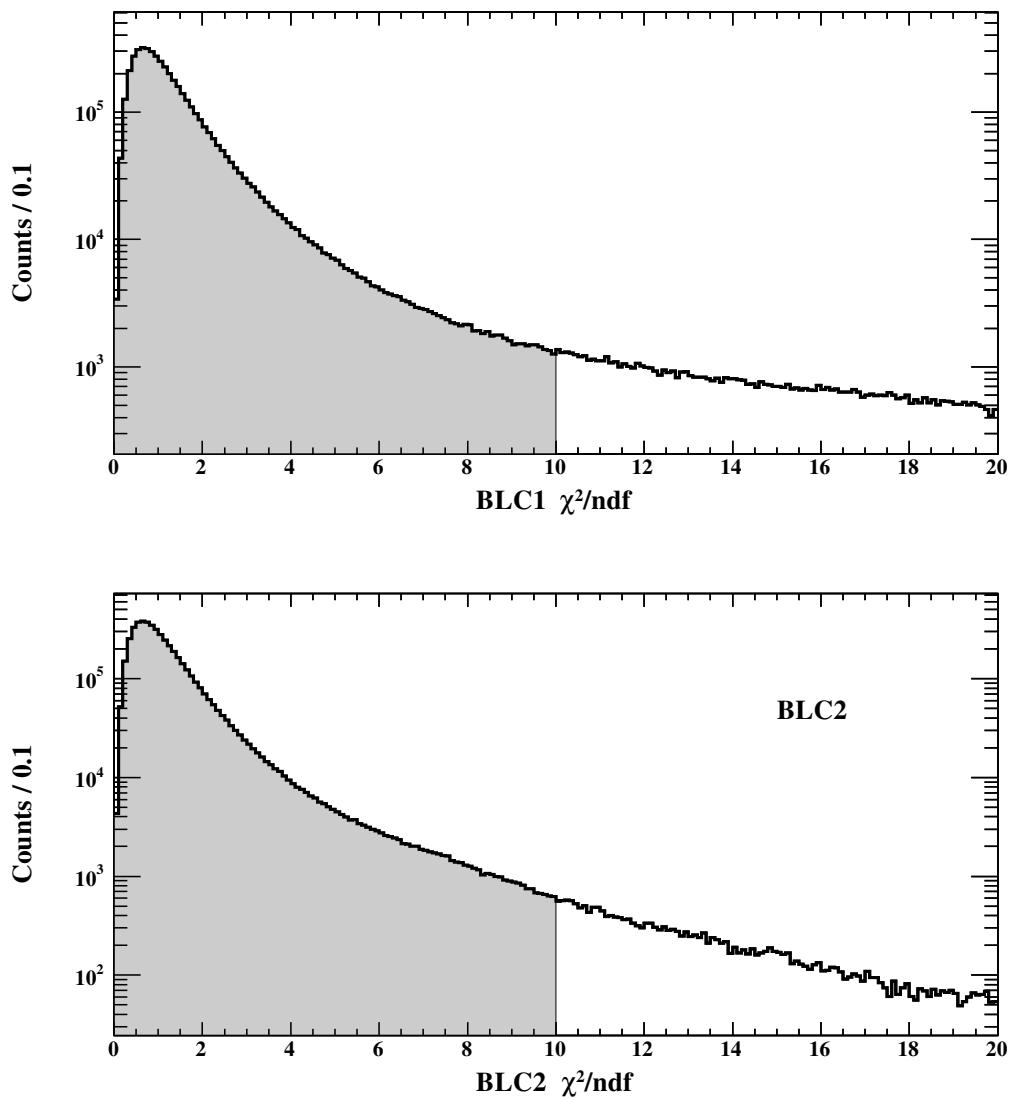
Fig. 3.11 Chi-square distributions of BLC1 (up) and BLC2 (bottom). Chi-square less than 10 is required to decide tracks as a good track candidate.
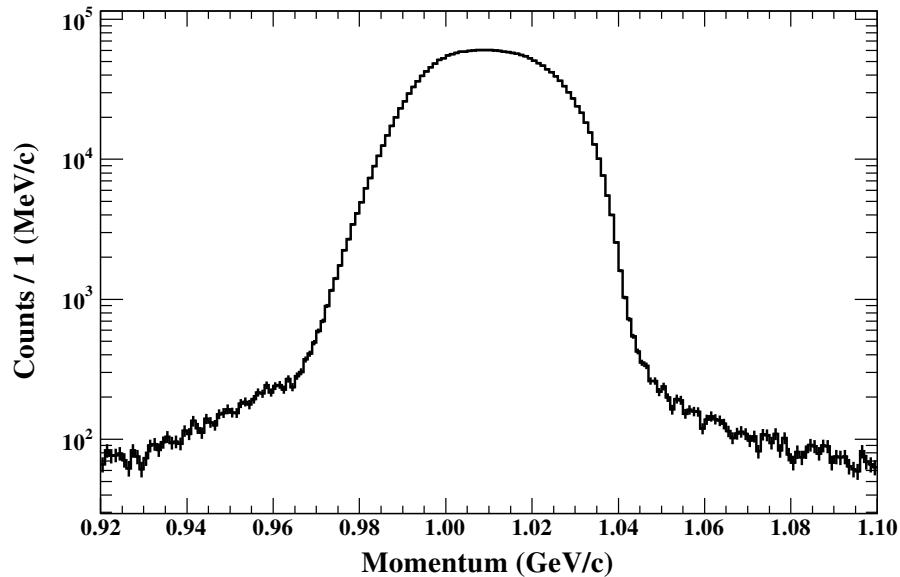
Fig. 3.12 The beam momentum distribution measured by beam spectrometer system.
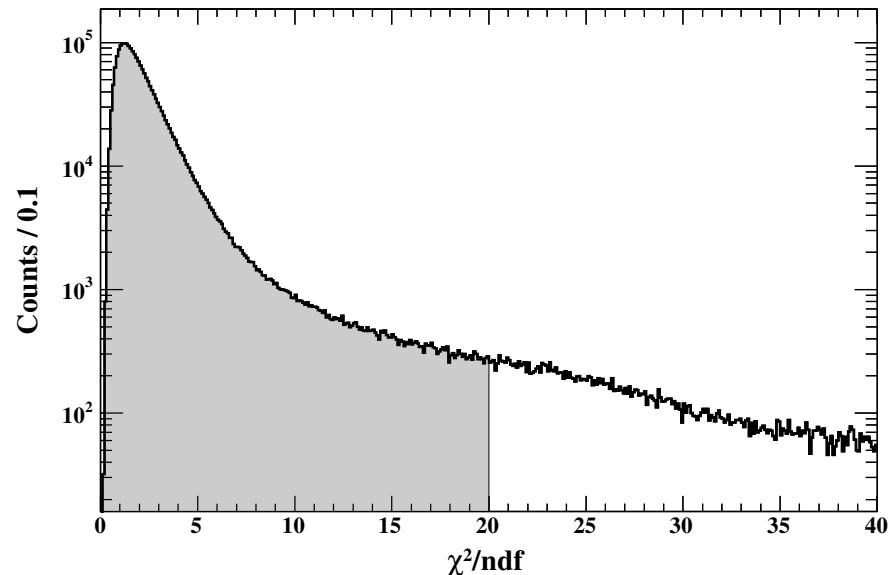
Fig. 3.13 The χ^2 distribution of the matching two drift chambers to reconstruct the beam momentum. The gray region shows accepted events where the χ^2 is less than 20.

10 ns is selected as triggered particle. Then, tracking χ^2 is selected less than 10, as shown in Fig.3.15.
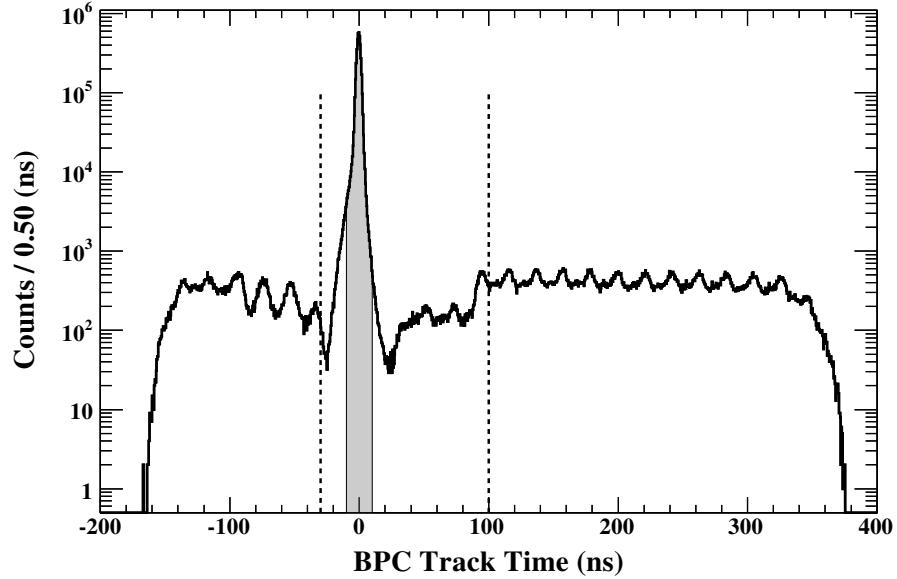
Fig. 3.14 The track time distribution of the BPC. The procedure of the event selection is the same as the BLCs.
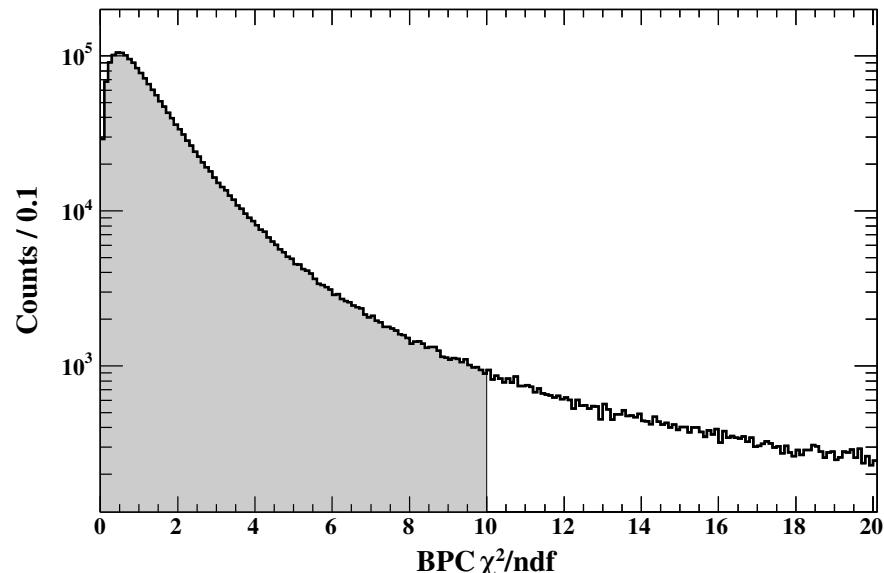
Fig. 3.15 The χ^2 distribution of the BPC. The track whose χ^2 is less than 20 as indicated by gray filled region is accepted.

Track matching of BLC2 and BPC

The track information of the BPC is used for define the beam direction. Before doing that, the tracks of BLC2 and BPC are checked its matching to reduce events comes from multiple scattering and to ensure the track comes from kaon. Track matching is checked for the position difference and angle difference between the tracks of BLC2 and BPC. Fig.3.16 shows position difference between BLC2 and BPC. The difference is evaluated at $z = 75$ cm upstream from the final focus point, where is the center position of the BLC2 and BPC. In this analysis, x and y difference are selected within the region from -0.75 to 0.75 cm. The track angle difference is also checked as shown in Fig.3.17. The events that dx/dz and dy/dz are in the region from -0.02 to 0.02 is pass through to next analysis.

Then, track of the BPC is determined as a beam track.
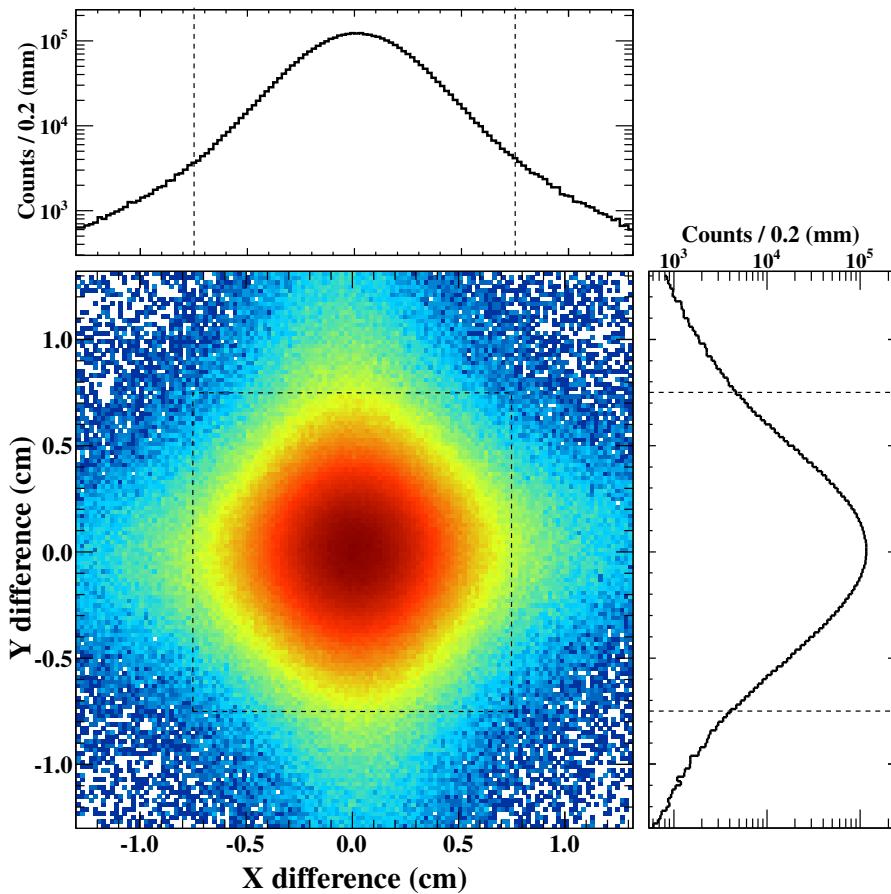
Fig. 3.16 The position difference between tracks of BPC and BLC2 at 75 cm upstream form the final focus point. The black bashed box in the 2D plot shows accepted region which x and y are selected from -0.75 to 0.75 cm.
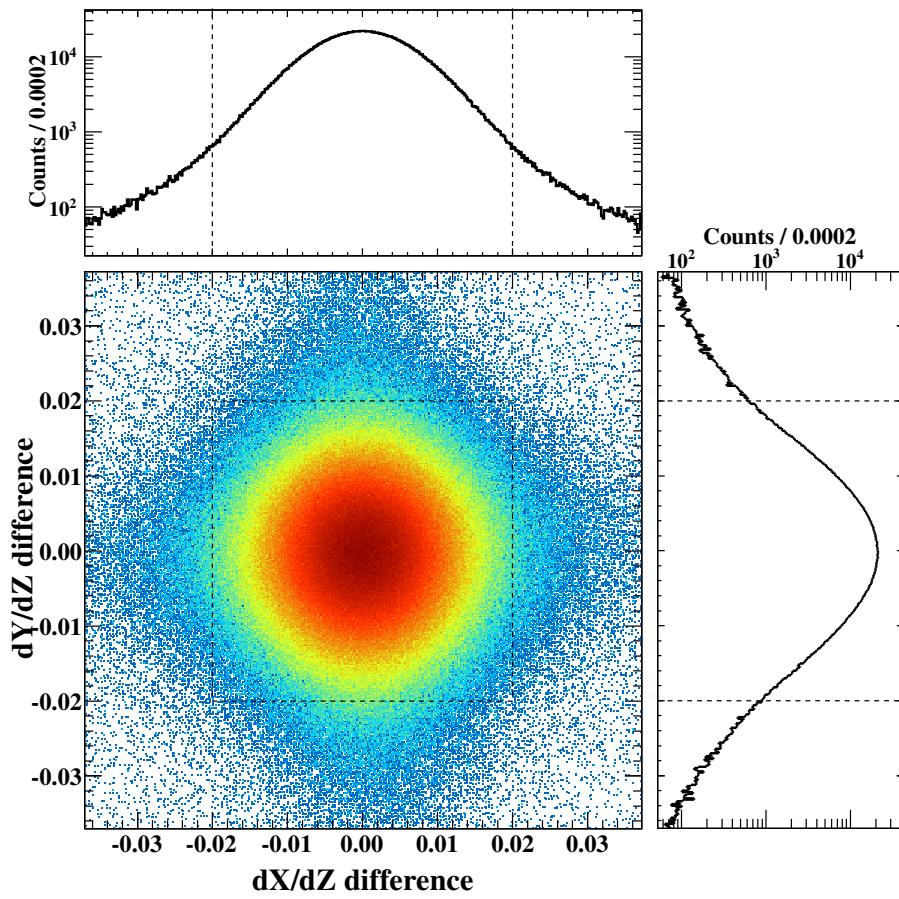
Fig. 3.17 The angle difference between tracks of BPC and BLC2. To select the matching events, each angle differences of dx/dz and dy/dz is required to be in the region between -0.02 and 0.02 which is indicated by black dashed box in the 2D plot.

3.2.4   Fiducial selection

Fig.3.18 shows the beam image on the final focus points, which beam position is determined by using the BPC track. In Fig.3.18-(left) shows the beam image with unbias-kaon trigger. On the other hand, Fig.3.18-(right) shows that with CDH hit trigger, so that the target image is observed in this case. To select the beam which passes through the target fiducial region, black circle region in Fig.3.18 is selected. The analysis for the beam-line counters is the end till this selection.
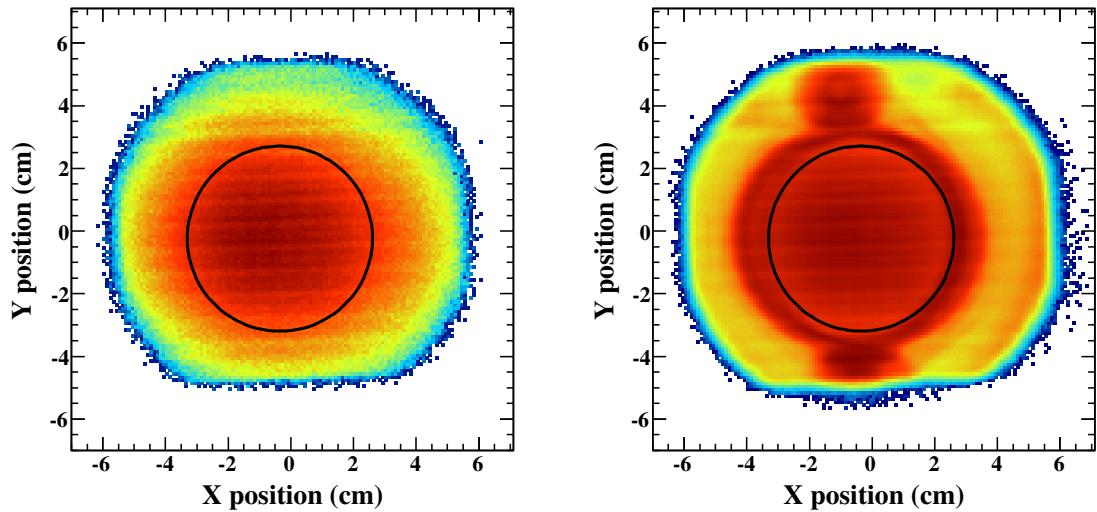
Fig. 3.18 Beam image at the final focus point with requiring the unbias-kaon trigger (left) and CDH 2 hits trigger (right). The target image is observed by selecting the CDH 2 hit trigger. The black circles shows fiducial region of the experimental target.

3.2.5   Number of irradiated kaon on the target

Now, analysis for the beam-line counters has been finished, so that number of irradiated kaon on the target can be evaluated. The number of kaon trigger is counted during the experiment as shown in Fig.3.19. Essentially, the number of kaon during the run is almost same because a run is separated by about 1 hour if there is no accident. However, the beam intensity was once increased during the experiment, so that there is a step in Fig.3.19.

The survival ratio during the beam-line analysis is also checked as shown in Fig.3.20. The ratio is flat during the experiment.

The DAQ efficiency and density of the ^{3}He target is also check for each run, as shown in Fig.3.21 and Fig.3.22. The DAQ efficiency and target density were almost steady around 70 - 80 % for the DAQ efficiency, and 81.2 mg for the target density.

By using these values, integrated luminosity can be evaluated which is described follows.
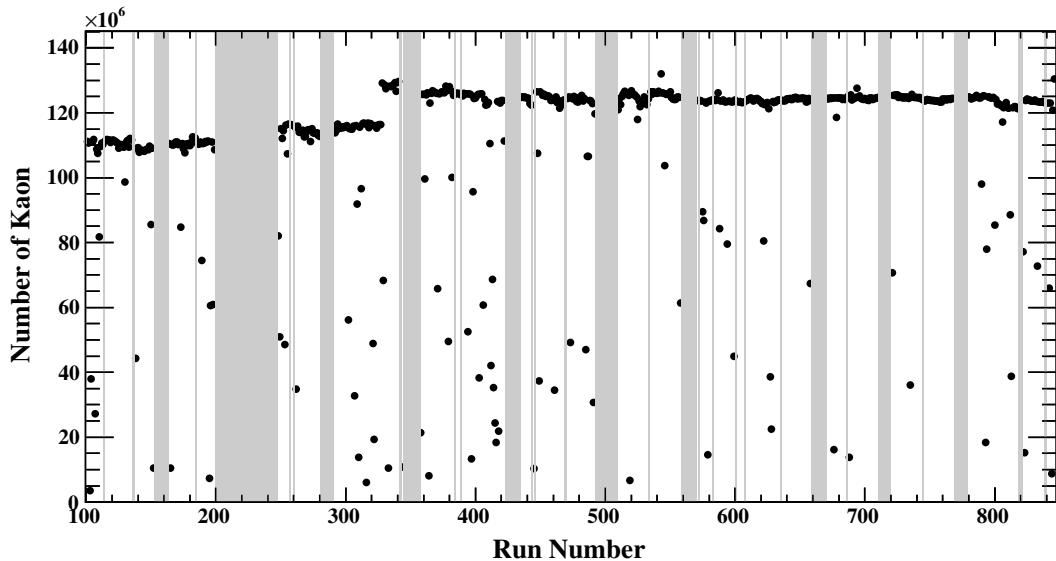
Fig. 3.19 The scaler counts of the kaon trigger for each experimental data. The horizontal axis shows data number where the one data is accumulated for about a hour. Around the run number of 320, there is step coming from increasing of the beam intensity.
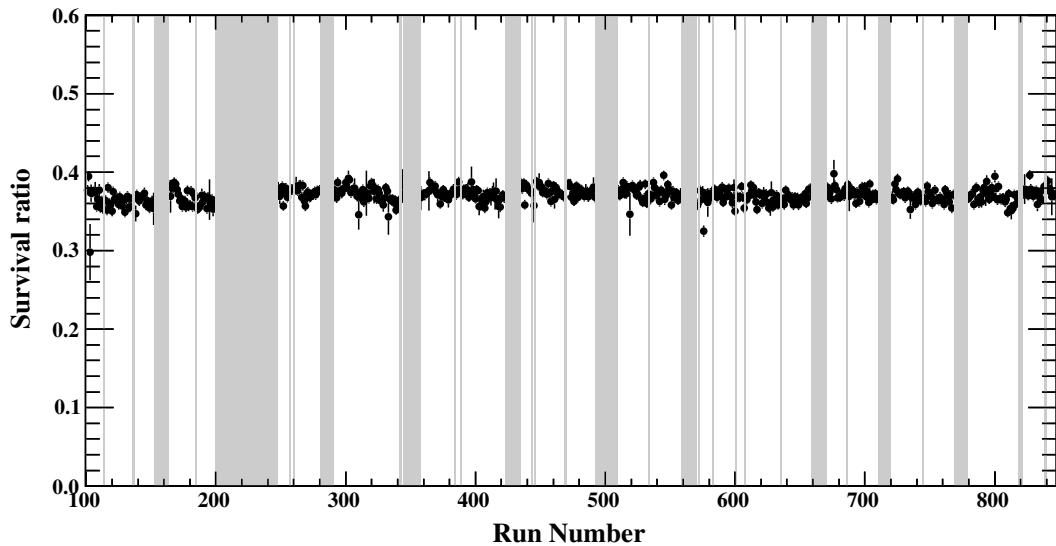
Fig. 3.20 Total survival ratio of the beam-line analysis to the fiducial region selection.
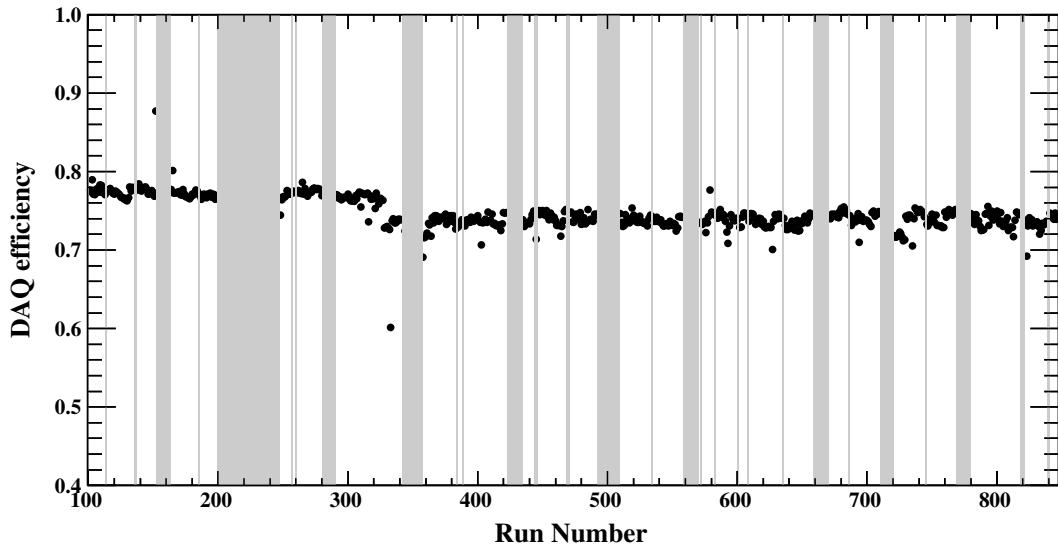
Fig. 3.21 The accept efficiency of the DAQ system evaluated by $N_{accept}/N_{request}$. The step around the run number of 320 corresponds to increasing the beam intensity. The efficiency is stable during the experiment.
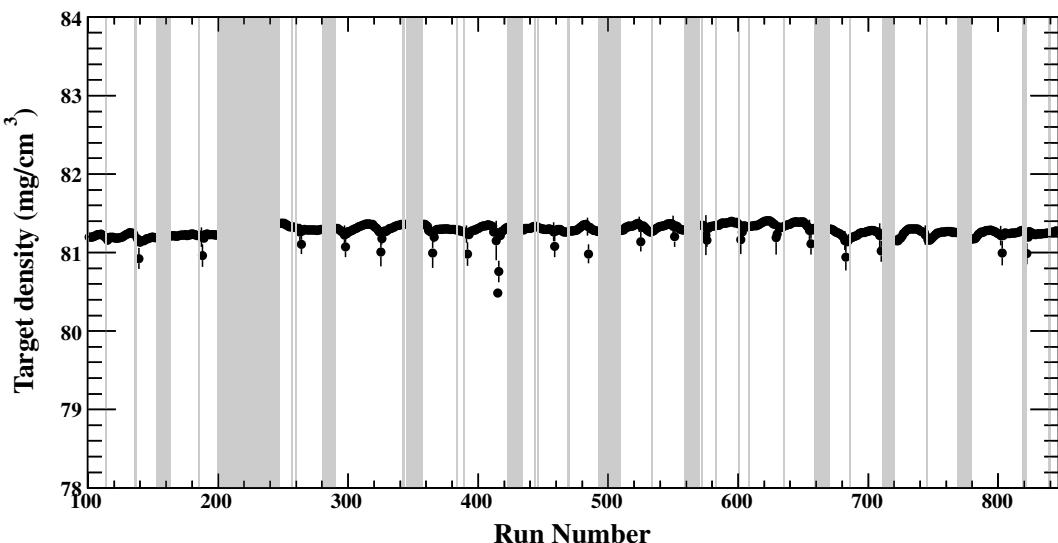
Fig. 3.22 The density of the liquid ^{3}He target during the experiment. The spike structures come from the refiling timing of liquid ^{4}He to the evaporator.

Table 3.1 Trigger efficiency and effective luminosity

Trigger	Trigger Efficiency (%)	Effective luminosity	
		Luminosity	Error (%)
KCDH3	93.3	3.0 nb^{-1}	0.1
KCDH1/100	0.99	$31 \, \mu\text{b}^{-1}$	0.02
KCDH2/20	4.9	$157 \, \mu\text{b}^{-1}$	0.1

Integrated luminosity

The integrated luminosity L is calculated as follows

$$L = N_b \cdot N_t = N_b \cdot \frac{N_A \cdot d \cdot l}{M_{^3\text{He}}}, \tag{3.14}$$

where N_b provides effective beam number which contains DAQ efficiency and survival ratio in the beam-line analysis, N_t is number of beam particle and target, d and l are density and length along beam direction, N_A and $M_{^3\text{He}}$ are Avogadro constant and molar mass of the ^{3}He, respectively. The N_b and d are evaluated for every run to cancel its fluctuation during the experiment. In summary, the integrated luminosity in the experiment was evaluated to be 3.21nb^{-1}. For the integrated luminosity, uncertainty comes from only statistical error in the scaler count of the kaon, which is negligible small (less than 0.01%).

Trigger efficiency and effective luminosity

The integrated luminosity with containing the trigger efficiency is defined as effective luminosity. The effective luminosity is summarized in Tab.3.1. For the main trigger of KCDH3 trigger, the effective luminosity was found to be 3.0 nb^{-1}.

3.3   Analysis for the cylindrical detector system

The next step of the analysis is for the cylindrical detector system (CDS). In the CDS analysis, the momentum is calculated by using track information of the CDC. Then, the particle identification is performed by using reconstructed momentum and TOF information. The CDS analysis procedure is as follows,

1. Tracking the CDC and momentum reconstruction

2. Re-tracking the CDC with fine correction

3. Particle identification

4. Vertex decision

3.3.1 CDC tracking and momentum reconstruction

CDC tracking is performed as described in Sec.3.1.3. In this analysis, the track whose χ^2/ndf is less than 30 is selected and pass the analysis. Then, the particle momentum can be calculated by using Eq.3.12. From the track information, the flight length between starting vertex point and detected point on the CDH can be calculated. Thus, the particle velocity can be calculated as

$$\beta = \frac{L_{CDC_{in}-CDH}}{\left((T_{CDH} - T_{T0}) - \left(T^{Calc}_{T0-vertex} + T^{Calc}_{vertex-CDC_{in}} \right) \right) \cdot c}, \tag{3.15}$$

where $L_{CDC_{in}-CDH}$ is the track length between the entrance of the CDC volume and the detected point on the CDH, T_{CDH} and T_{T0} are the measured time information of the CDH and T0, respectively, and $T^{Calc}_{T0-vertex}$ and $T^{Calc}_{vertex-CDC_{in}}$ are calculated flight times between T0 and the starting vertex point, and between starting vertex point and entrance of the CDC volume, respectively. The starting vertex point is defined as shown in Fig.3.26. Then, the relation between momentum and particle velocity can be observed as shown in Fig.3.24. There are clearly stripe corresponding to each particle, electron, pion, kaon, proton, and other particles.
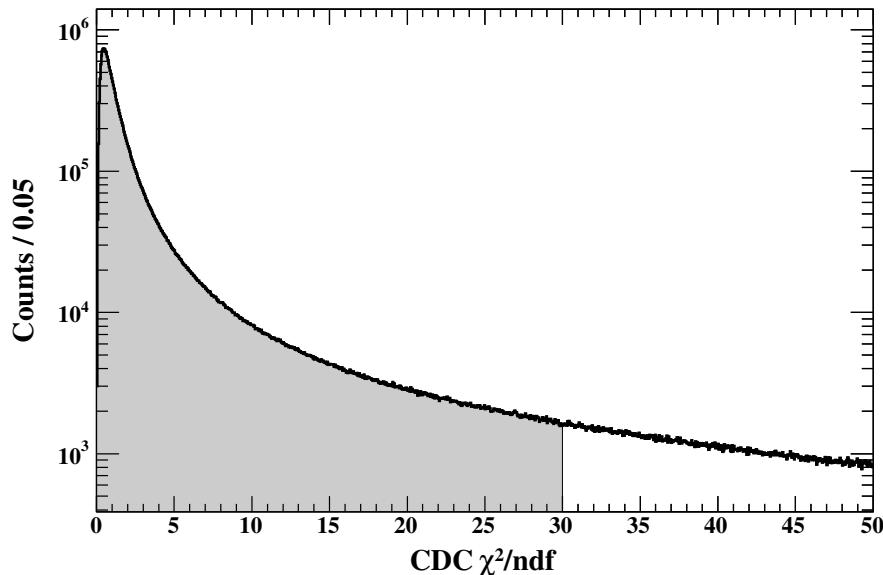
Fig. 3.23 The χ^2 distribution of the CDC tracks. Tracks whose χ^2 is less than 30 is accepted as shown by gray filled region.
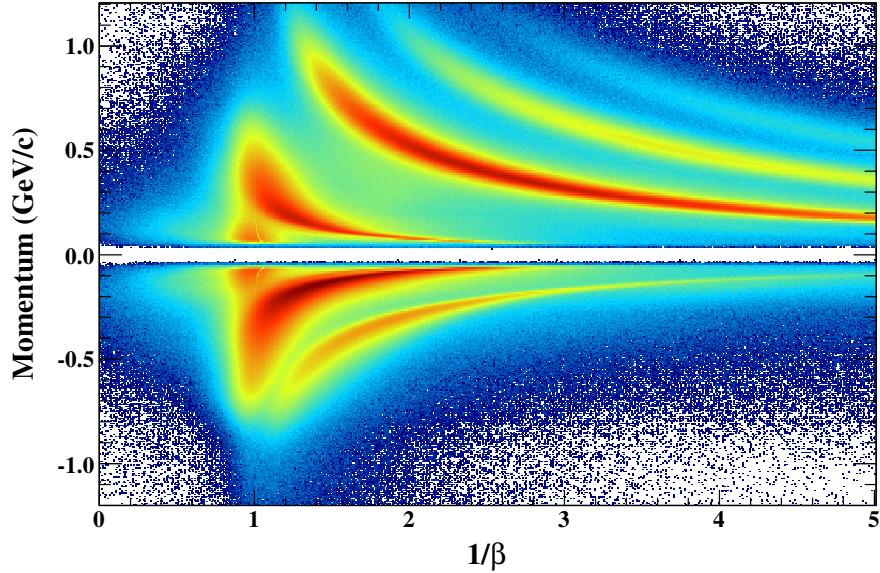
Fig. 3.24 Momentum and $1/\beta^2$ correlation reconstructed by the CDS. Each belt where many events are concentrating is coming from different particles.

CDC fine correction

In the CDC drift time, there are correlation between residual drift time and particle velocity as shown in Fig.3.25-(left). This correlation is the same as a time-walk effect in the photon sensors, which is collected by using the correlation of the integral charge or the pulse height as described in Sec.3.1.2. For the CDC, we did not take a integral charge information in the experiment, so that the particle velocity is used to correct this correlation. The correlation function is evaluated by fitting the Fig.3.25-(left) with the fifth polynomial function for each wires. By using the collection function, the correlation between residual drift time and particle velocity is negated as shown in Fig.3.25. After corrected this correlation, tracking of the CDC, momentum reconstruction, and calculation of the particle velocity are performed again with corrected drift time.

3.3.2   Reaction vertex reconstruction

The starting vertex point of the particle detected by the CDS should be defined to calculate the particle velocity and define the reaction vertex point. There are two method for defining the starting vertex point in the CDS. One of the case is the definition of the vertex point with one CDC track and a beam track. In this case, the vertex point is defined as the closest point of the CDC track and the beam track as described in Fig.3.26-(left). The another case is
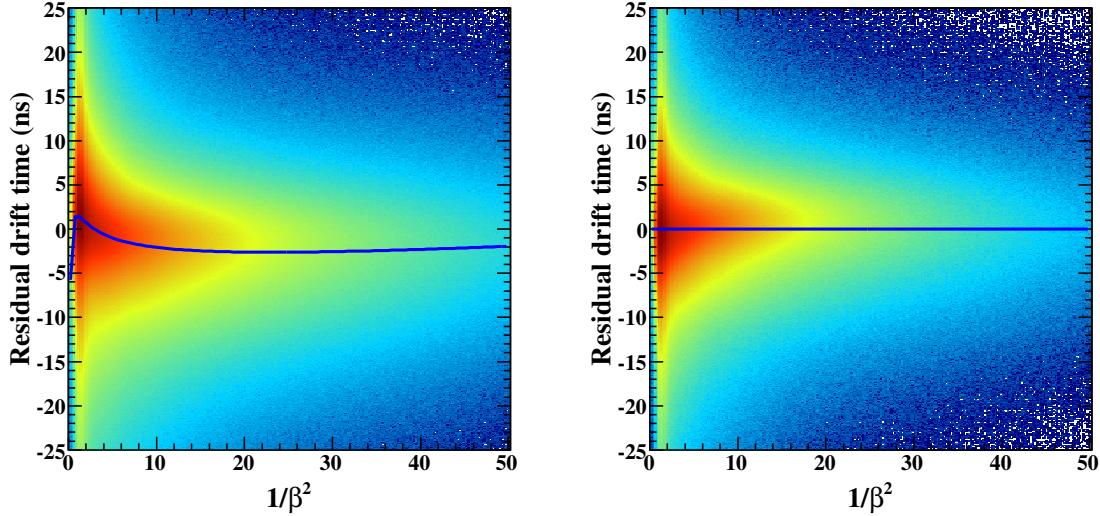
Fig. 3.25 Calculated residual drift time versus $1/\beta^2$ distribution of the CDC. (left) The correlation that is before the correction. The correlation between residual drift time and $1/\beta^2$ is evaluated by using 5th polynomial function. (right) After applying the collection for every wires.

that there are two CDC tracks and a beam track. In this case, firstly the closest point of two CDC tracks is searched and its momentum vector is calculated as sum of the two momentum vector. Then, the vertex point is defined as the closest point between the summed momentum vector and the beam track, as shown in Fig.3.26-(right).

The reconstructed vertex images in the empty target data and the ^{3}He target data are shown in Fig.3.27 and Fig.3.28, respectively. For the vertex image in the empty data, the target cell is clearly observed. And in the ^{3}He data, the number of events is really enhanced in the target fiducial region which is indicated by blue line in Fig.3.28.

3.3.3 Particle identification by the CDS

For the particle identification of the detected particles in the CDS is performed by calculated its mass as

$$M = p \cdot \sqrt{\frac{1-\beta^2}{\beta^2}}, (3.16)$$

where p and β are reconstructed momentum and calculated particle velocity by the CDS information. The momentum versus mass-square plot is shown in Fig.3.29. Clear localizations corresponding to each particles are observed. To identify the particle, the 2 dimensional PID function is applied, which is described as lines in Fig.3.29. The PID function was evaluated
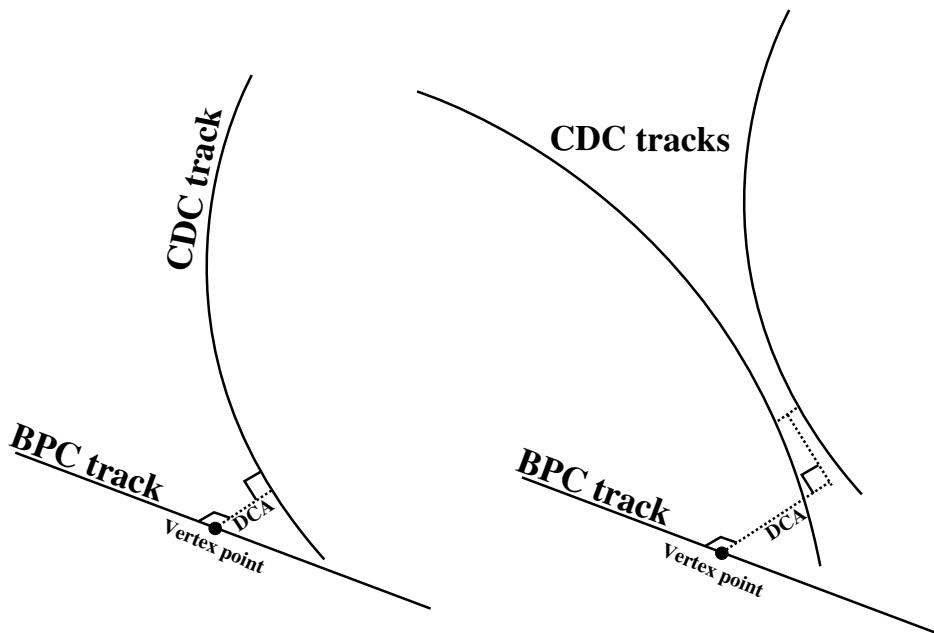
Fig. 3.26 Schematic drawing of the vertex definition. (left) The vertex definition when there is one CDC track. The vertex point is defined on the BPC track where the distance between BPC and CDC track is the closest. (right) The vertex definition when there are two CDC tracks. First of all, the closest point of two CDC tracks is found to determine the stating point of the two CDC tracks, and the two CDC tracks is paired. Then, the vertex point is defined as the closest point between BPC track and line of the paired tracks where the direction of the line is determined as synthetic momentum of two CDC tracks.
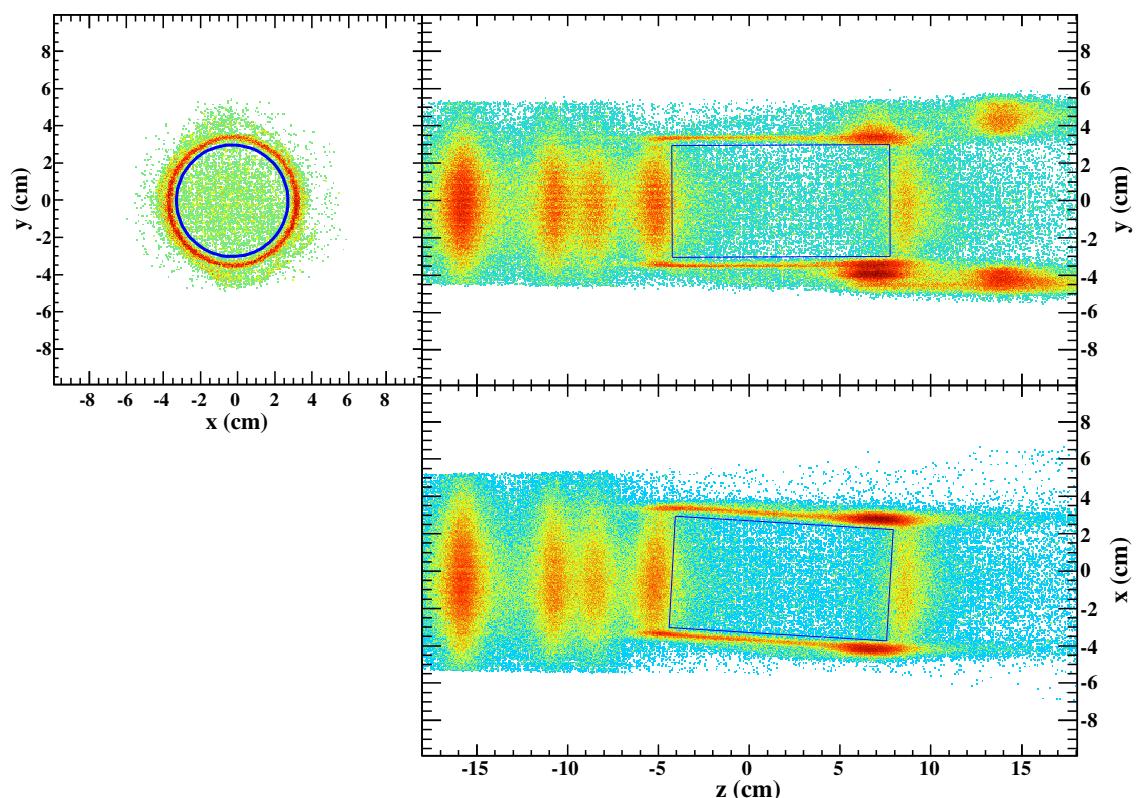
Fig. 3.27 Reconstructed vertex distribution when the target is empty. The target cell image is clearly observed in each X-Y, Z-X and Z-Y plane. Each drawing require that the position on the residual axis is around 0 cm. The blue line shows fiducial region of the target.
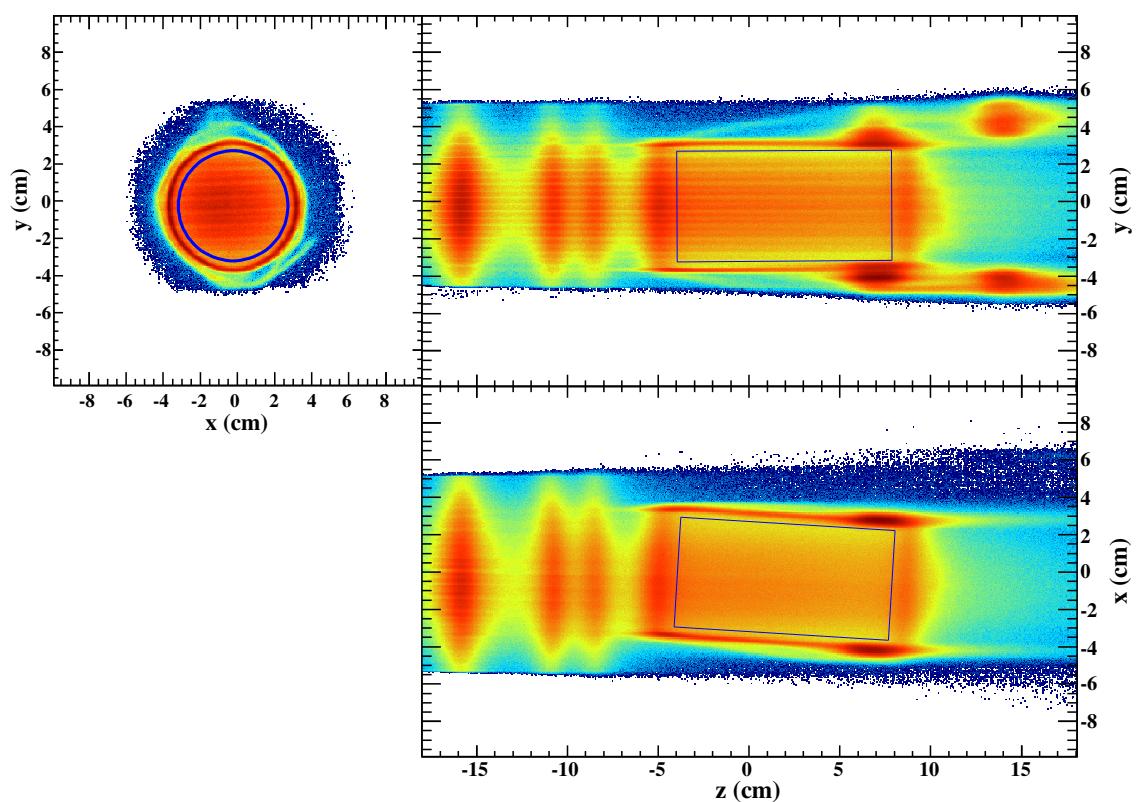
Fig. 3.28 Reconstructed vertex distribution with filling the ^{3}He target. The blue line shows fiducial region of the target.

by fitting mass distributions sliced with each momenta of Fig.3.29 by using Gaussian distribution, and $\pm 2.5\sigma$ region is identified as each particles. In this analysis, overlap regions of two PID functions are removed to reduce the background from wrong identification.
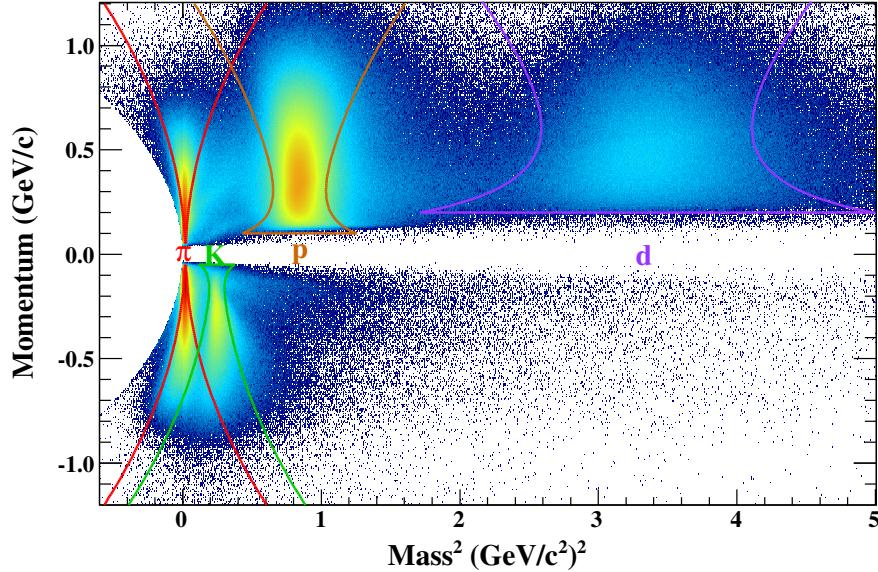
Fig. 3.29 Momentum and mass-square distribution measured by the CDS. The pion, kaon, proton and deuteron are clearly separated in this plot. Each lines show the boundary of the particle identification. The overlap region of two different particle is ignored in this analysis to remove the background comes from wrong-identification.

3.3.4   Absolute value of the solenoid magnetic field

Because of the momentum of the detected particle in the CDS is calculated by using magnetic field strength of the solenoid magnet, the absolute value of the magnetic field strength must be calibrated. For calibration of the magnetic field strength, the mass of the K_s^0 and Λ are checked by changing the magnetic field strength. The mass of the K_s^0 and Λ are reconstructed by the $\pi^- \pi^+$ and $\pi^- p$ -pairs, respectively. Fig.3.30 shows the results of the study for the magnetic field strength. In this figure, difference between PDG value and reconstructed masses of the K_s^0 and the Λ plotted as a function of the magnetic filed strength. In this analysis, the absolute value of the magnetic filed is setted to 0.715 T, where the differences of the K_s^0 and the Λ masses are the same value of about 0.5 MeV/c^2.
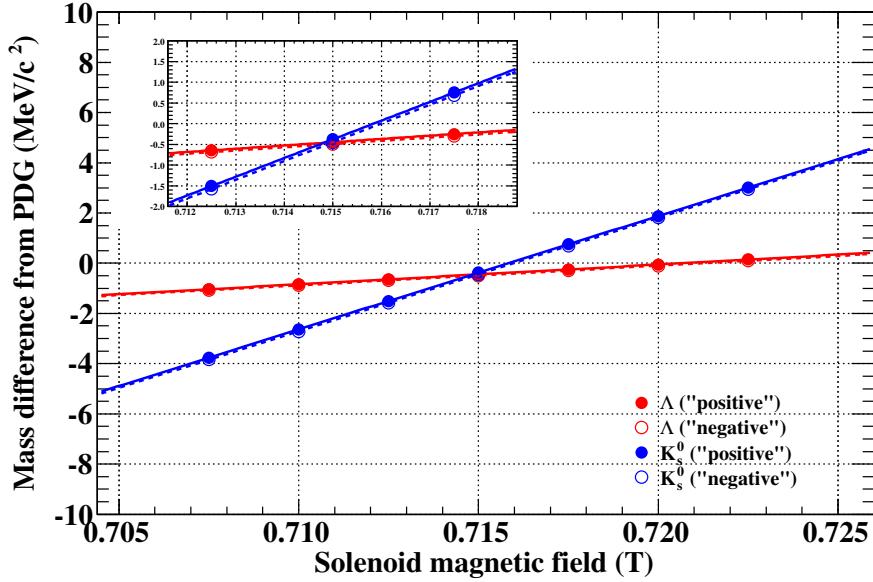
Fig. 3.30 Mass difference from PDG values of reconstructed K^0 and shown by blue and red line, respectively. The inserted figure is close-up view around magnetic field of 0.715 T. The absolute value of the solenoid magnetic filed is set to 0.715 T where the K^0 and Λ mass difference are the almost same value. Each mass difference is within 0.5 MeV/c^2.

3.3.5 Reconstruction of the invariant mass

To check the absolute value and mass resolution of the reconstructed particles, the K_s^0, Λ, and $\Lambda(1520)$ were checked its mass position and width. The K_s^0, Λ, and $\Lambda(1520)$ are reconstructed by $\pi^-\pi^+$, $\pi^- p$, and $K^- p$ -pairs, respectively. In Fig.3.31, 3.32, and 3.33 show the invariant mass distribution of each pairs. To evaluate the mass position and its width, the distribution were fitted by using Gaussian for the Λ and K_s^0 and Breit-Wigner for the $\Lambda(1520)$ signal, and background distributions were fitted by the third polynomial function. The mass positions of K_s^0 and Λ is well consistent with its PDG value within the 0.5 MeV/c^2, and that of $\Lambda(1520)$ is consistent within about 4 MeV/c^2 after adjustment of the magnetic field strength of the solenoid magnet as described previously. The invariant mass resolution of the $\pi^-\pi^+$ and $\pi^- p$ -pairs are found to be about 6 and 2 MeV/c^2, respectively.
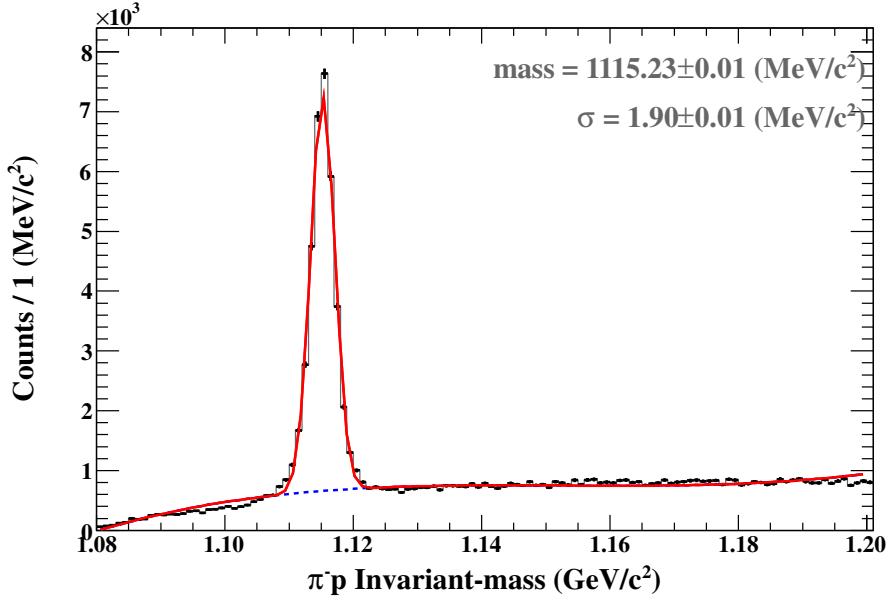
Fig. 3.31 The invariant-mass distribution of the $\pi^- p$ pair detected by the CDS. The red and blue dotted-line show the fitting result by using Gaussian and 3rd polynomial background function. The peak coming form Λ-decay is well reproduced and its, mass and resolution is evaluated to be 1115.23 MeV/c^2 and 1.9 MeV/c^2, respectively.
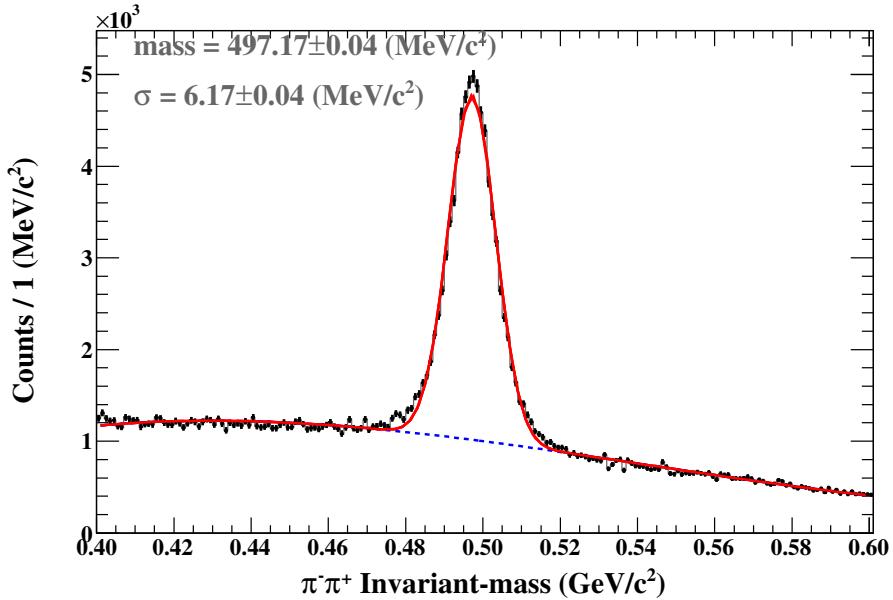
Fig. 3.32 The invariant-mass distribution of the $\pi^- \pi^+$ pair detected by the CDS. The red and blue dotted-line show the fitting result by using Gaussian and 3rd polynomial background function. The peak coming form K^0-decay is well reproduced and its, mass and resolution is evaluated to be 497.17 MeV/c^2 and 6.2 MeV/c^2, respectively.
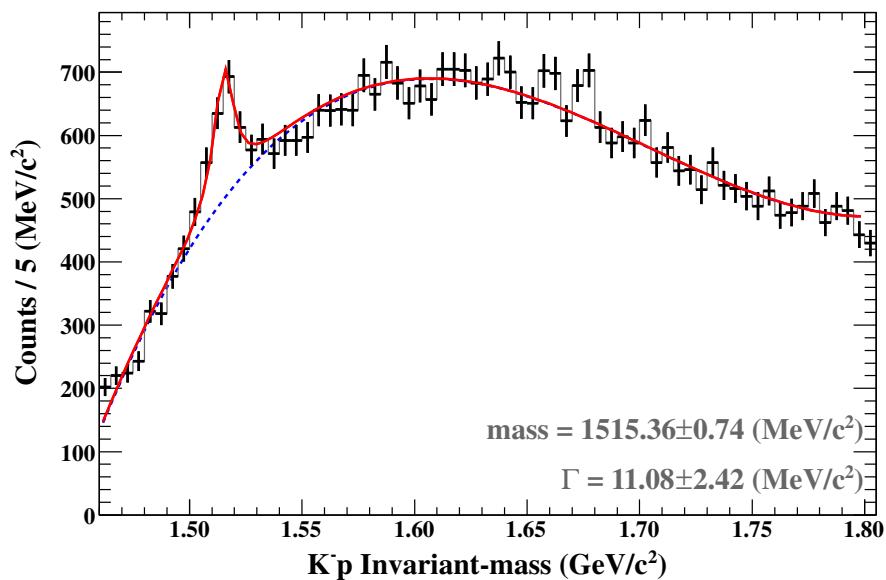
Fig. 3.33 The invariant-mass distribution of the $K^- p$ pair detected by the CDS. The red and blue dotted-line show the fitting result by using Breit-Wigner function and 3rd polynomial background function due to the resolution is much smaller the is width. The peak coming form $\Lambda(1520)$-decay is well reproduced and its, mass and decay width is evaluated to be 1515.4 MeV/c^2 and 11.1 MeV/c^2, respectively.

Chapter 4

Analysis of exclusive ${}^3\mathrm{He}\,(K^-,\Lambda p)\,n$ channel

In this section, analysis procedure of an exclusive ${}^3\mathrm{He}\,(K^-,\Lambda p)$ channel is described. Basically, analysis is performed by following steps.

1. First level event selection with number of hits and tracks in CDS and other counters

2. Λ-reconstruction with the likelihood method

3. Reaction vertex decision

4. Missing neutron selection to select the ${}^3\mathrm{He}\,(K^-,\Lambda p)\,n$ reaction

5. Kinematic fitting with constraints of the reaction

After these analysis, the Λp invariant-mass spectrum of the ${}^3\mathrm{He}\,(K^-,\Lambda p)\,n$ reaction is obtained.

4.1 First level event selection

At first, events which have 3 hits in CDH and 3 tracks in CDC were selected. Fig.4.1 shows the multiplicities of the CDH hits and the CDS tracks. It is required that there are three fired segments in CDH, then number of tracks in CDC is checked. To reduce the background, events with more than four CDH hits and CDS tracks were removed in this analysis.

Furthermore, charged particle detection in the forward counter is also checked. Fig.4.2 shows hit multiplicity of the BVC, CVC and PC. No hit in all these counters were also required so that there are only three charged particle detection in an event.

After these selections, the CDS hits and CDS tracks were combined to reconstruct the charged particles. The three combinations in CDS are required in this analysis whose distribution are shown in Fig.4.3. Then, particle identification was performed for these three detected particles. Number of each particle is also shown in Fig.4.3. The two protons and one π^- were selected to select as a candidate of the events of Λp pair detection.
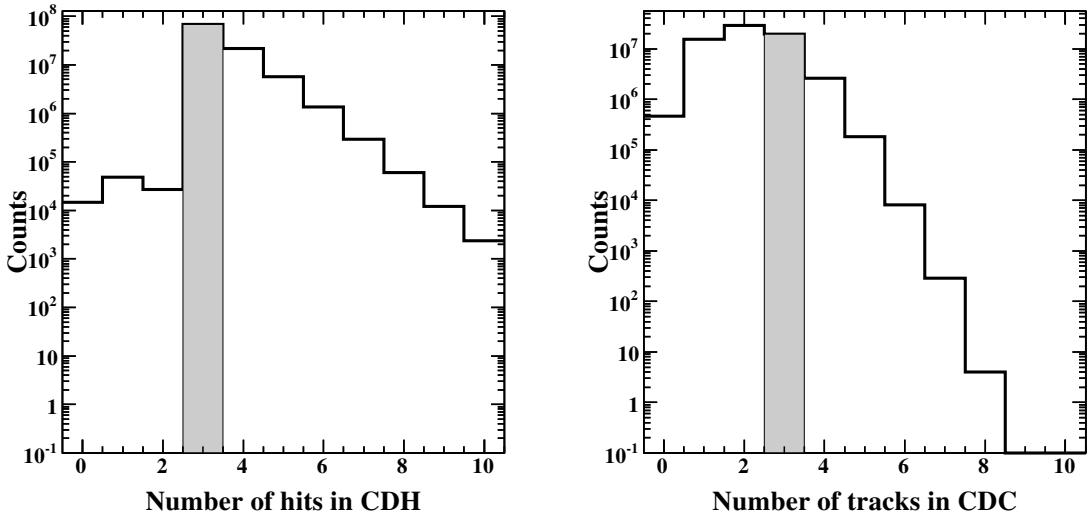
Fig. 4.1 (left) Number of hit segments in CDH in the KCDH3 triggered events. The hits number of 3 is selected in this analysis which shown by grayed region. (right) Number of tracks in CDC after requiring number of hits of CDH to be 3. It is also required that there are three tracks in the CDC.
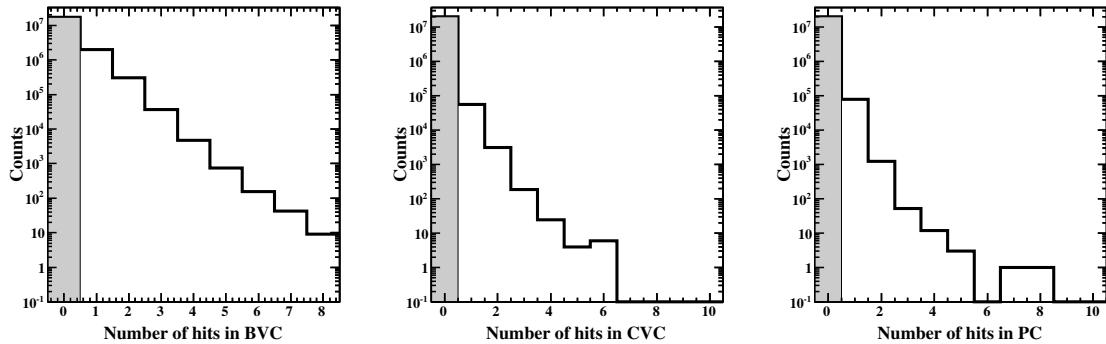
Fig. 4.2 Number of fired segments in BVC, CVC and PC. To remove the events which have charged particles in the forward direction, it is required that there are no fired segment in all forward counters, shown by gray filled region.
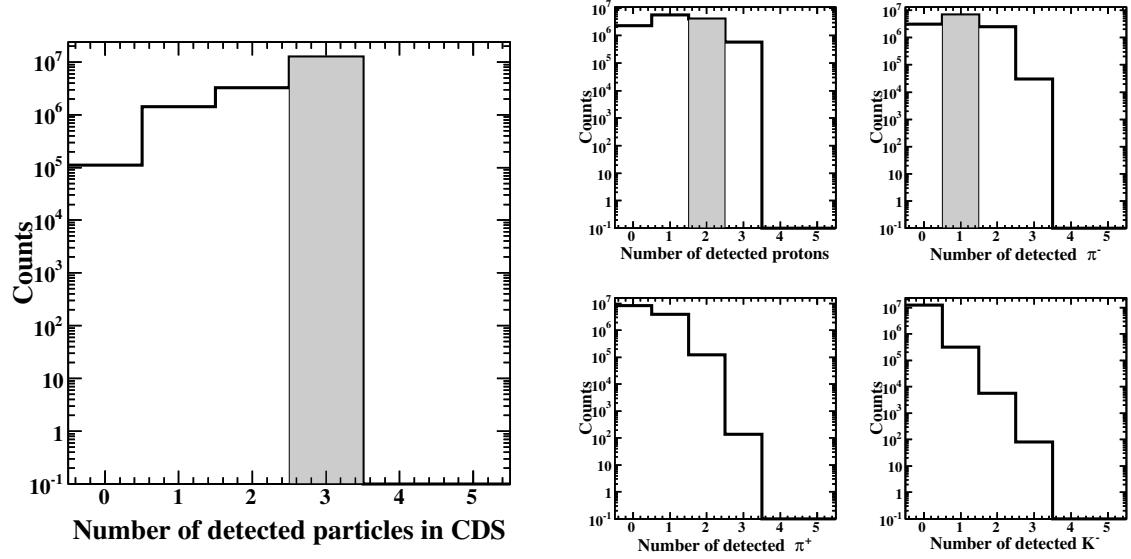
Fig. 4.3 (left) Number of particles which path the analysis in CDS. In the CDS analysis, energy-loss correction and particle identification are performed. The three particle events are selected in this event selection. (right 4 figures) Number of protons, π^-s, π^+s and K^-s detected by CDS after requiring that there are three analyzed particles in CDS. The gray regions, two protons and one π^- are selected.

Now, we have got two protons and one π^- detected in CDS. The next step is to select the pair of each proton and π^-. Fig.4.4 shows the determination scheme of the two protons. The distance between closest approach (DCA) of each proton and beam track is calculated as shown in Fig.4.4, and closest proton to beam track is selected as proton-1 (p_1). The other is called proton-2 (p_1). Two pairs of $\pi^- p_1$ and $\pi^- p_2$ are combined to calculate correct energy loss in the materials. At this energy correction, the energy loss is calculated from closest points of each proton and π^-. The invariant-mass of each $\pi^- p$ pair can be calculated as described in Fig.4.5. We find two loci around Λ-mass in both invariant-mass of $\pi^- p$ pairs. The cross-point of the Λ region of both $\pi^- p$ pairs can not be identified which pair comes from Λ-decay, by using only the invariant-mass information. Naively, $\pi^- p_2$ pair could be considered as Λ-decay because the DCA tends to larger in the proton from Λ-decay due to the flight length of Λ. In this analysis, to ensure the identification of the Λ-decay pair, the log-likelihood method is applied to identify the correct pair from Λ-decay, which is described in the next section.
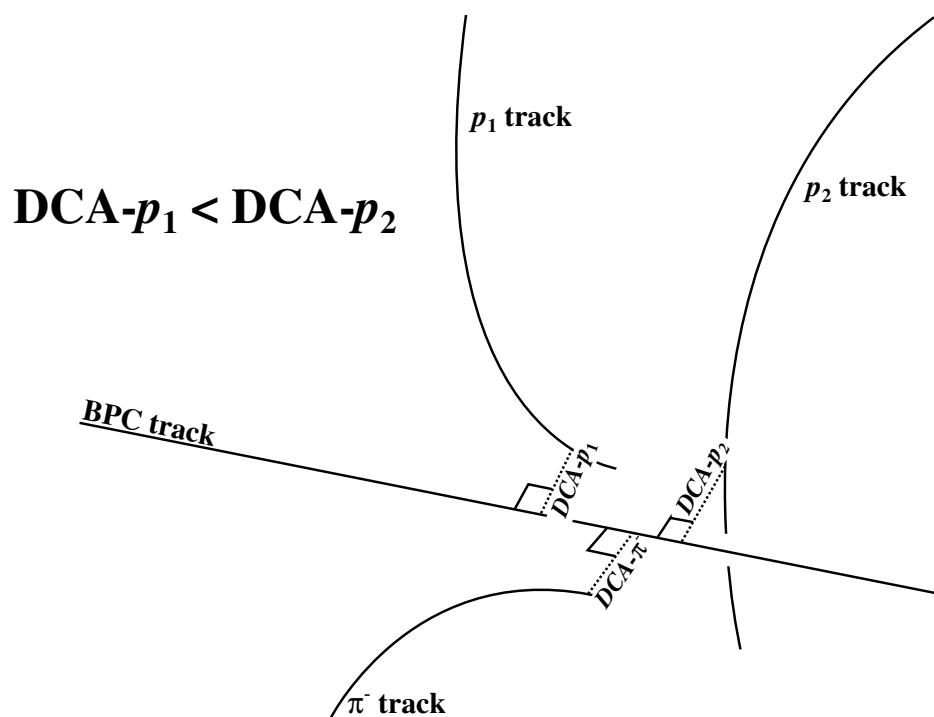
Fig. 4.4 Schematic view of the three helix tracks of protons and π^- and beam. Each DCA is evaluated, and proton whose DCA is smaller than the other proton is tagged as p_1 in this analysis.
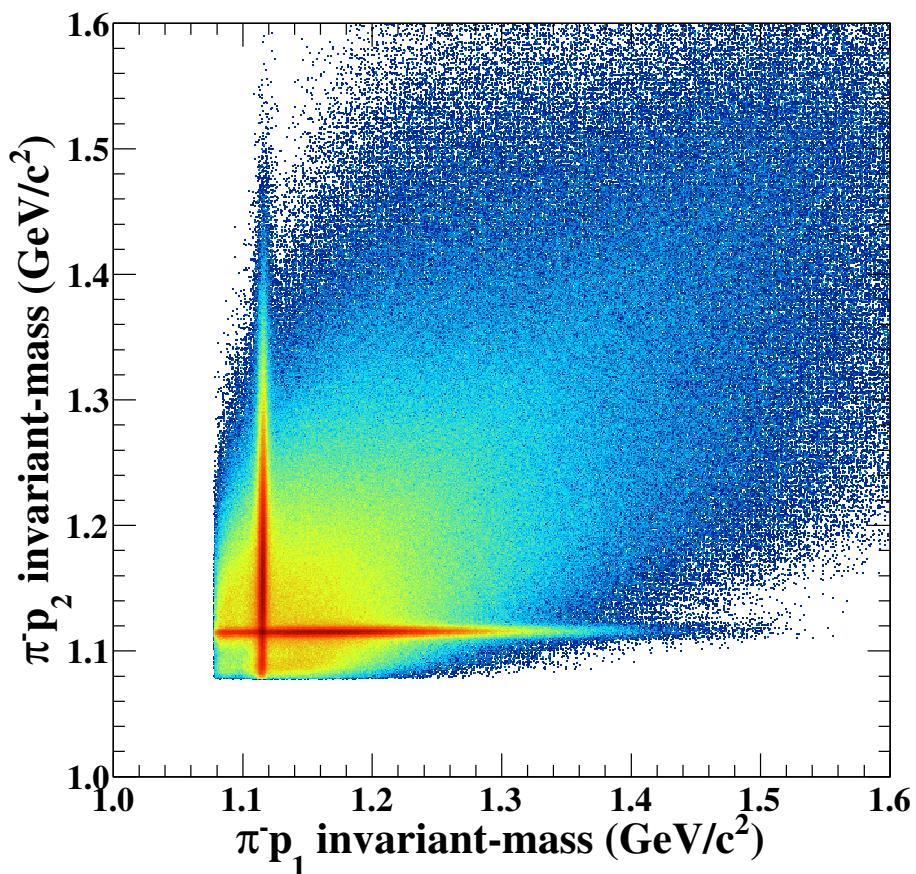
Fig. 4.5 Plot of the invariant-mass of $\pi^- p_1$ versus that of $\pi^- p_2$. The strong focusing cross-image corresponds to Λ-decay event.

4.2 Λ identification by using the log-likelihood method

To decide the correct $\pi^- p$ pair from the Λ decay, the log-likelihood method was applied. In the log-likelihood function, following four variables are used.

1. Invariant-mass of $\pi^- p$ pair

2. DCA between proton and beam tracks

3. DCA between proton and π^- tracks

4. DCA between π^- and beam tracks

5. DCA between Λ and another proton tracks

Distributions of each variable were generated by using the Monte Calro simulation with the $K^- + {}^3\mathrm{He} \to \Lambda pn$ reaction in the three nuclear absorption processes. In the simulation, particles in the final state is produced uniformly. Fig.4.6 shows distribution of four variables generated by simulation. The probability function is made by fitting these distributions, and formulas and parameters for each variables are listed in Tab.4.1.

4.2.1 Λ identification efficiency and wrong pairing ratio

Now, the log-likelihood function (L) is defined as

$$L = -ln\left(f_{mass} \times f_{DCA_{pK^-}} \times f_{DCA_{p\pi^-}} \times f_{DCA_{\Lambda K^-}} \times f_{DCA_{\Lambda p}}\right),\tag{4.1}$$

where f_{mass}, $f_{DCA_{pK^-}}$, $f_{DCA_{p\pi^-}}$, $f_{DCA_{\Lambda K^-}}$, and $f_{DCA_{\Lambda p}}$ denote probability function for invariant-mass, DCA between proton and K^-, DCA between proton and π^-, DCA between Λ and K^-, and DCA between Λ and another proton, respectively. In this analysis, the log-likelihood (L) of two $\pi^- p$ pair were compared, and smaller one was decided to the correct pair from Λ-decay. Fig.4.7 shows L distribution of the Λ-decay pair and the other pair which are plotted by black and blue lines, respectively. The bottom figure in Fig.4.7 shows efficiency and wrong identification ratio as a function of the L value. By selecting smaller $\pi^- p$ pair, Λ-decay pair can be identified with high efficiency. As mention in later, it is necessary to remove the background from other processes, such as Σ^- production, so that the cut condition of L will be modified to reduce the background contaminations. The efficiency and wrong pairing ratio are almost saturated around $L = 10$.
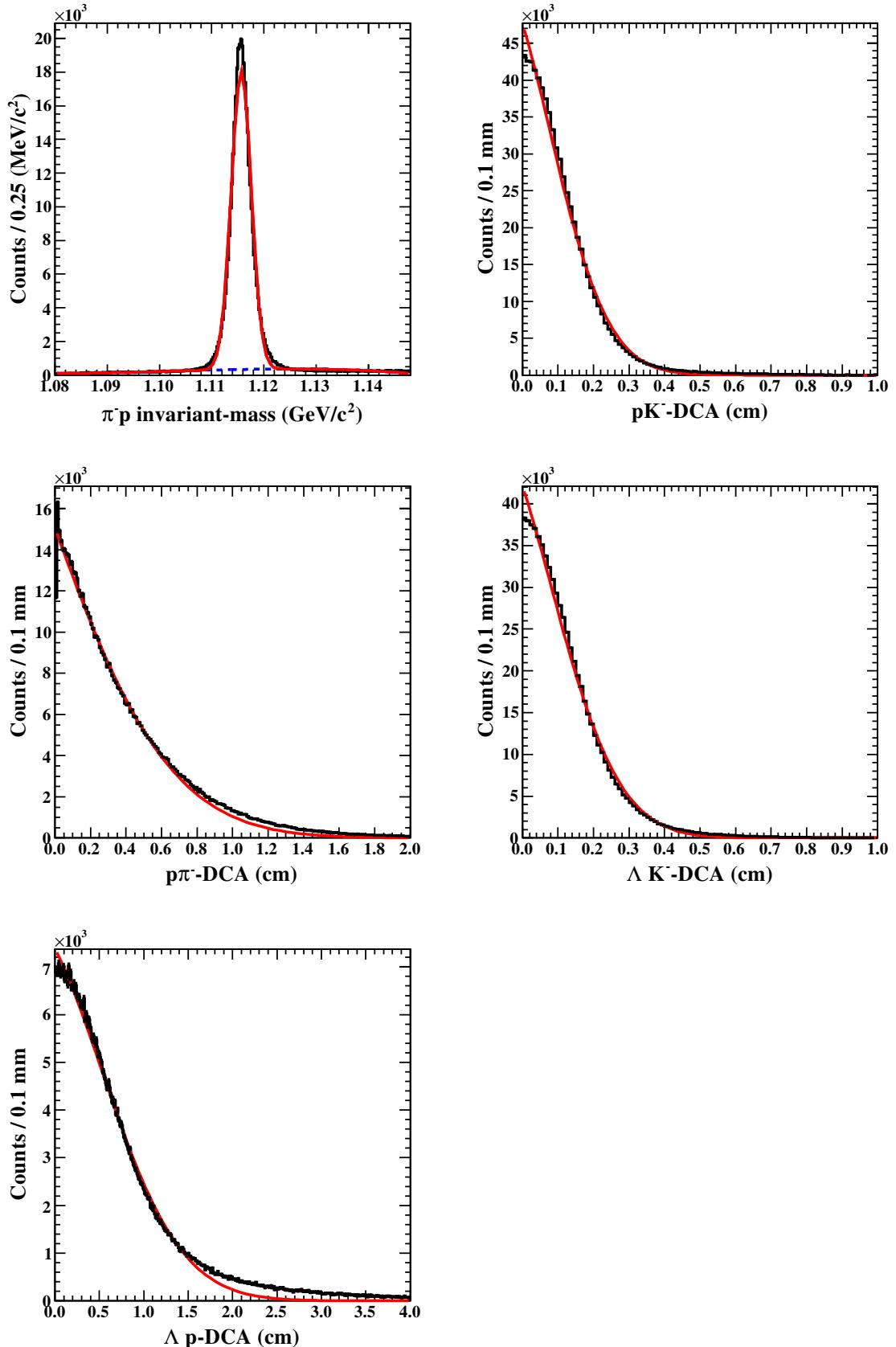
Fig. 4.6 $\pi^- p$ invariant mass, DCA_{pK^-}, $DCA_{\pi^- p}$, $DCA_{\Lambda K^-}$, and $DCA_{\Lambda p}$ distributions generated by the Monte Calro simulation. Red lines show fitting results which are used as probability function for each quantity.
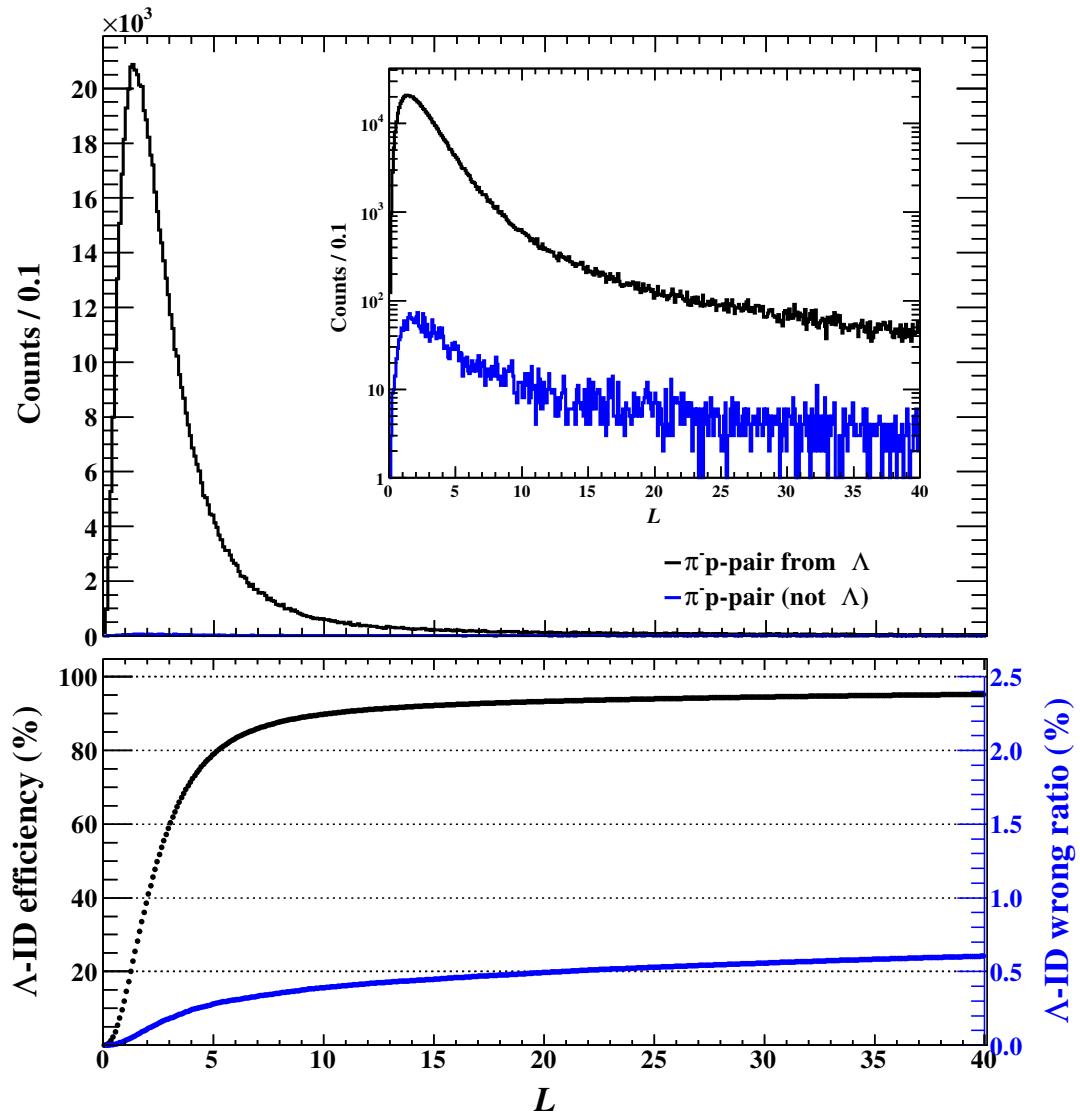
Fig. 4.7 (top) Log-likelihood distribution for $\pi^{-}p$ pair from Λ-decay and the other pair, shown by black and blue line, respectively. The inserted spectrum is drawn by semi-log plot. (bottom) Identification efficiency of Λ-decay pair and wrong pairing ratio.

Table 4.1 Probability function for each values

Value	Function	Parameters		
		p_0	p_1	p_2
$\pi^- p$-mass	$p_0 \cdot exp\left(\frac{-(x-p_1)^2}{2p_2}\right)$	1.0	1.1155	0.002
pK^--DCA		1.0	-3.403185	-18.076275
$p\pi^-$-DCA	$p_0 \cdot exp\left(p_1 \cdot x + p_2 \cdot x^2\right)$	1.0	-1.578198	-1.055050
ΛK^--DCA		1.0	-3.078679	-13.117345
Λp-DCA		1.0	-1.437093	0.039362

4.2.2 Rejection power of other background contaminations by log-likelihood

By using the log-likelihood method, $\pi^- p$ pair from Λ-decay can be identified with high efficiency and low wrong pairing ratio. However, it is important that if Λ is not generated in the reaction, how many wrong events can path Λ identification scheme. Simply, the reaction without Λ generation could be considered as a reaction such as

$$K^- + {}^3\text{He} \to \pi^- ppn.$$
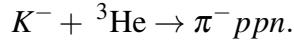
In principle, just simple reaction described above can not occur because the strangeness is not conserved in the reaction. A possible reaction of the contamination is

$$K^- + {}^3\text{He} \to \Sigma^- pp \to \pi^- ppn$$
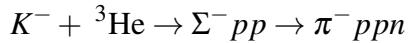
reaction. In this reaction, $\pi^- n$ pair is from Σ^--decay, but the number of protons and π^- is the same as of the true Λpn event. There is also two $\pi^- p$ pairs in the final state. In Fig.4.8, contributions from these background processes are considered as a rejection power of the contamination. The rejection power is defined as

$$R = 1 - p_{missID}, \tag{4.2}$$

where p_{missID} is wrong identification of uncorrelated $\pi^- p$ pair as Λ. The L distribution in Fig.4.8 is different from that in Fig.4.7, for two processes. The bottom figure in Fig.4.8 shows the rejection power for $\pi^- ppn$ and $\Sigma^- pp$ processes as a function of L. The rejection power is decreased by increasing the cut position of L. In contrast, the Λ identification efficiency is increasing with cut position of L. Therefore, it is necessary to optimize the cut position by taking into account the identification efficiency and rejection power.
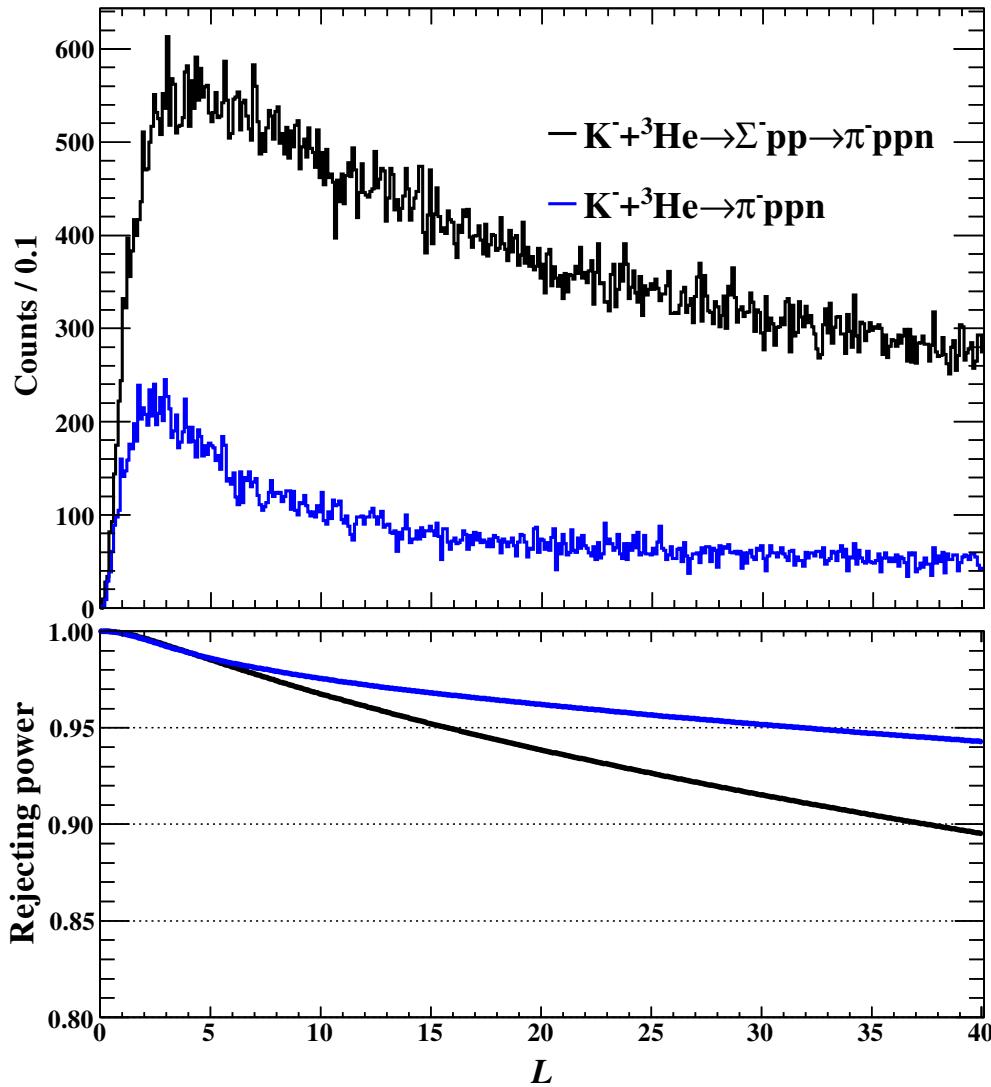
Fig. 4.8 (top) Log-likelihood distribution for the $K^{-} + {}^{3}He \rightarrow \Sigma^{-} pp \rightarrow \pi^{-} ppn$ events and the uncorrelated $\pi^{-} ppn$ production which are shown by black and blue lines, respectively. (bottom) Rejecting power for each events. The rejecting power is calculated as $1 - p_{missID}$, where p_{missID} denotes that the wrong identification ratio of that uncorrelated $\pi^{-} p$ pair is identified as Λ.

4.2.3 Optimization of cut condition of log-likelihood

To optimize the cut condition of log-likelihood for Λ identification, a performance value, k is introduced. The k value is defined as

$$k = \varepsilon_{\Lambda ID} \cdot R, \tag{4.3}$$

where $\varepsilon_{\Lambda ID}$ and R are identification efficiency of Λ and rejection power of background process, respectively. The rejection power is only considered for the $\Sigma^- pp$ process. Fig.4.9 shows k value as a function of L. The distribution has a maximum point so that the cut condition is set to L of k value to be maximum. In this analysis, the cut condition is optimized to be 15.75. In this value, the Λ identification efficiency and the rejection power of the $\Sigma^- pp$ process are 92% and 95%, respectively, while wrong pairing ratio of the $\pi^- p$ pair is 0.4 % at this cut condition.
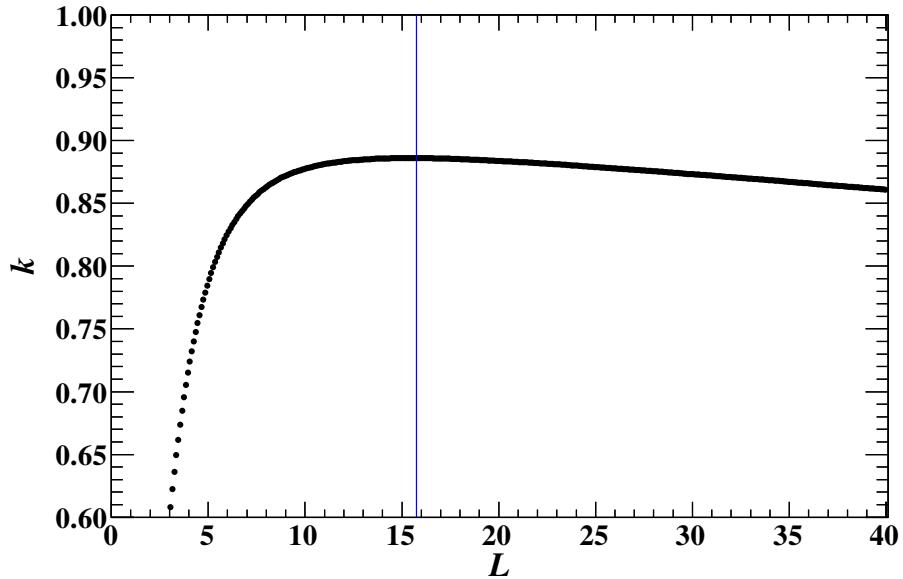
Fig. 4.9 Log-likelihood performance value (k) distribution. The k value is maximized at $L = 15.75$, so that the selection threshold is set to this value which is indicated by blue line in the figure.

4.3 Vertex decision

The reaction vertex which is used for energy loss correction for K^--beam is decided at the closest point of the proton and beam tracks. We did not adopt the closest point of the Λ and

beam tracks, however, the position resolution of single proton track is better than that of Λ which is determined by two CDS tracks.

To ensure the reaction point is in the target region, the closest point of proton and beam tracks, and Λ and beam tracks in the target fiducial region are required. Firstly, the closest point of proton and beam tracks is checked whether it is in the target fiducial region. It is called as "Vertex decision-1", in this analysis. Then, a decision of the closest point of Λ and beam tracks is called as "Vertex decision-2".

4.4   Selecting the $^3\mathrm{He}\,(K^-,\Lambda p)\,n$ reaction

Before selecting the $^3\mathrm{He}\,(K^-,\Lambda p)\,n$ reaction, inclusive spectrum of the invariant-mass of Λp pair and the $^3\mathrm{He}\,(K^-,\Lambda p)\,"X"$ missing-mass are shown.

Fig.4.10 shows the inclusive Λp invariant-mass spectrum. Many events located around mass region of 2.2 GeV/c^2, which come from multi pion production process. And, no other characteristic structure was observed in the invariant-mass spectrum.

The missing-mass of $^3\mathrm{He}\,(K^-,\Lambda p)\,"X"$ is calculated as

$$M_X = \sqrt{\left(M_{^3\mathrm{He}} + \sqrt{M_{K^-}^2 + p_{K^-}^2} - \sqrt{M_\Lambda^2 + p_\Lambda^2} - \sqrt{M_p^2 + p_p^2} \right)^2 - (p_{K^-} - p_\Lambda - p_p)^2},$$

(4.4)

where M_i and p_i denote mass and momentum vector of particle "i". Fig.4.11 shows $^3\mathrm{He}\,(K^-,\Lambda p)\,"X"$ spectrum. The peak of missing-neutron was observed at the neutron mass position. The dominant contribution in the Λp channel is multi pion production process, which is located higher mass region in the missing-mass spectrum.

To obtain the relationship between invariant-mass and missing-mass, a 2-dimensional plot is shown in Fig.4.12. In the 2D plot, events, which mainly come from two pion production process; $K^- + {}^3\mathrm{He} \to Y pn\pi\pi$, are dominant around $M(\Lambda p) \sim 2.2$ GeV/c^2 and $MM(\Lambda p) \sim 1.5$ GeV/c^2.

In this analysis, the neutron mass gate is selected in $0.85 - 1.03$ GeV/c^2, which is indicated by blue line in Fig.4.12. The top figure in Fig.4.12 is the Λp invariant-mass spectrum by selecting the neutron window in the missing-mass spectrum. Fig.4.13 also shows invariant-mass spectrum by 20 MeV/c^2-bin in the $^3\mathrm{He}\,(K^-,\Lambda p)\,n$ reaction with selecting neutron window. It was observed that there are roughly two components in the invariant-mass spectrum, one is the continuum contribution which can be considered as non resonant process followed by Λpn final state, the other one is peak structure located around $K^- pp$ mass-threshold.
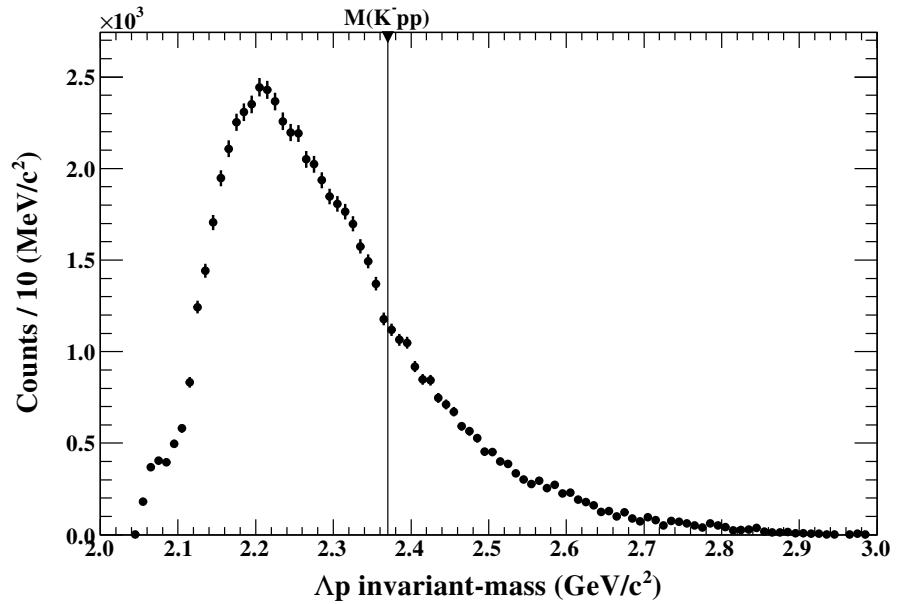
Fig. 4.10 Inclusive Λp invariant-mass distribution. The mass of $K^- + p + p$ is shown by line at the $M(K^-pp) = 2.37\,\mathrm{GeV}/c^2$.
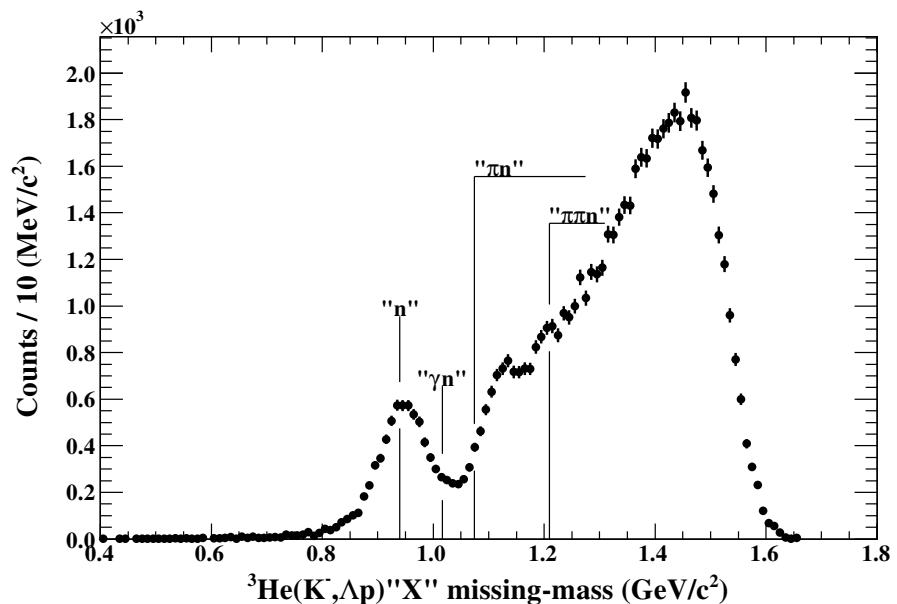
Fig. 4.11 $^3\mathrm{He}(K^-, \Lambda p)"X"$ missing-mass distribution. The neutron peak is observed around M.M. $(\Lambda p) = 0.94\,\mathrm{GeV}/c^2$.
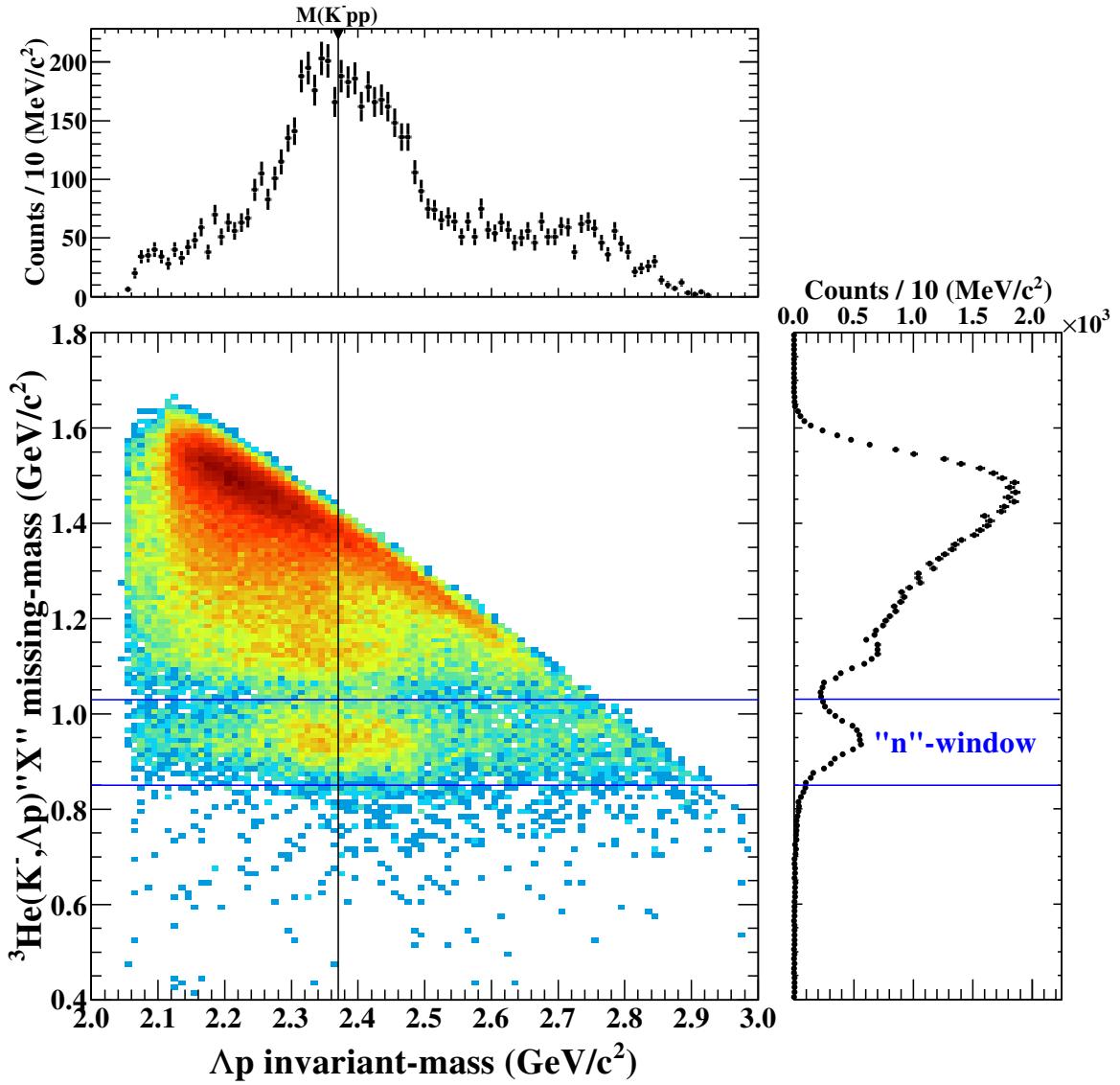
Fig. 4.12 2D plot of Λp invariant-mass versus ^{3}He$(K^-, \Lambda p)$"X" missing-mass. The region indicated by blue lines in the 2D plot and projection distribution of missing-mass side corresponds to neutron selection region which is from 0.85 to 1.03 GeV/c^2. The projection of invariant-mass side is shown with selection neutron region.
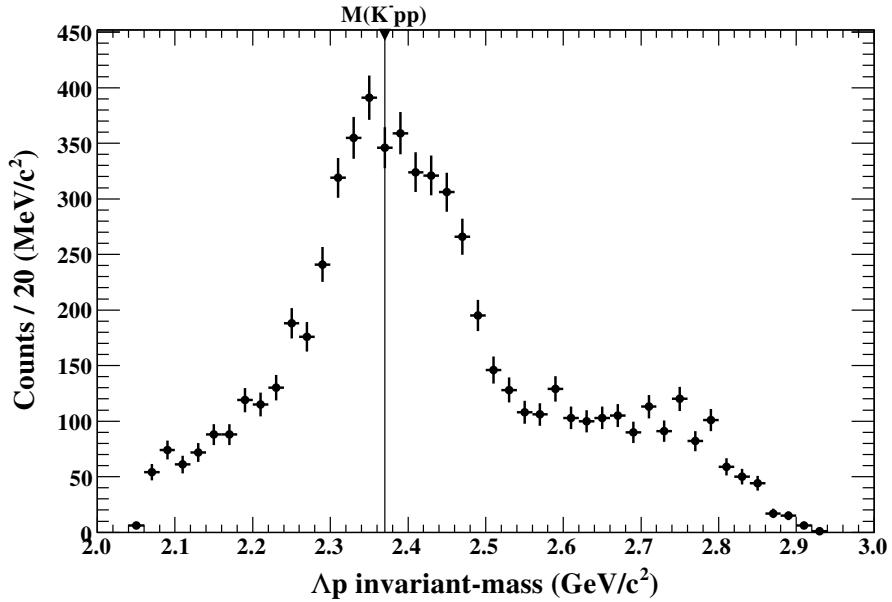
Fig. 4.13 Λp invariant-mass distribution in the $^3\mathrm{He}\,(K^-,\Lambda p)\,"n"$ reaction by selecting neutron window in the M.M. (Λp) spectrum.

To check the survival and contaminated ratio of the Λpn process and other multi pion production processes, these values are evaluated by using a Monte Calro simulation. The survival ratio at Λ reconstruction by using log-likelihood method and the selecting neutron window for each processes are listed in Tab.4.2. In this evaluation, the multi charged pion production processes are ignored because these processes have more than three charged tracks in CDS, and were rejected before reconstructing Λ. Only Σ production process is considered, because of only Σ^0 can decay into $\Lambda\gamma$. $\Sigma^- pp$ process is considered to evaluate the contamination from non Λ production process. Two and three nucleon absorption (2NA/3NA) processes are evaluated in this analysis. In the 2NA processes, because the proton must be detected by the CDS, where only a neutron which acts as a spectator in the reaction is considered.

The Λ reconstruction ratios are more than 94 % in 3NA-Λpn process. This ratio becomes smaller in the multi pion production process, because the probability function for log-likelihood method is generated by using 3NA-Λpn process, namely the log-likelihood is optimized only for 3NA-Λpn process.

In selecting the neutron window, about 90 % and 40 % of events are passed in the 3NA-Λpn and the 3NA-$\Sigma^0 pn$ process, respectively. Other multi pion production processes can not pass this selection because the missing-mass is much higher than neutron window.

Therefore, dominant contributions after Λ reconstruction and selection of the neutron window are only 2NA- and 3NA-Λpn and $\Sigma^0 pn$ processes. Since the cross section of the 2NA-Ypn processes is much smaller than that of the 3NA processes, the 3NA-Ypn process mainly contributes to the continuum component in the Λp invariant-mass spectrum.

Table 4.2 Survival ratio for each process

3NA-Process	Λ reconst. (%)	"n" selection (%)	Total (%)	Relative ratio
Λpn	94.0	91.0	85.5	1.00
$\Lambda pn\pi^0$	93.4	0.941	0.850	1.03×10^{-2}
$\Lambda pp\pi^-$	18.7	1.36	0.254	2.97×10^{-3}
$\Lambda pn\pi^0\pi^0$	92.3	7.80×10^{-3}	7.20×10^{-3}	8.42×10^{-5}
$\Lambda pp\pi^-\pi^0$	23.5	3.40×10^{-2}	7.99×10^{-3}	9.35×10^{-5}
$\Lambda pn\pi^0\pi^0\pi^0$	90.1	0	0	0
$\Sigma^0 pn$	94.0	43.0	40.4	0.473
$\Sigma^0 pn\pi^0$	93.2	0.104	9.72×10^{-2}	1.14×10^{-3}
$\Sigma^0 pp\pi^-$	19.1	0.173	3.30×10^{-2}	3.86×10^{-4}
$\Sigma^0 pn\pi^0\pi^0$	91.7	2.97×10^{-3}	2.72×10^{-3}	3.18×10^{-5}
$\Sigma^0 pp\pi^-\pi^0$	25.0	2.51×10^{-2}	6.28×10^{-3}	7.34×10^{-5}
$\Sigma^0 pn\pi^0\pi^0\pi^0$	89.1	0	0	0
$\Sigma^{*0} pn$	88.9	1.11	0.989	1.16×10^{-2}
$\Sigma^{*0} pn\pi^0$	87.6	1.28×10^{-2}	1.12×10^{-2}	1.31×10^{-4}
$\Sigma^- pp$	4.97	89.0	4.42	5.17×10^{-2}
2NA-Process	**Λ reconst. (%)**	**"n" selection (%)**	**Total (%)**	**Relative ratio**
Λpn_s	93.4	93.2	87.0	1.02
$\Lambda pn_s\pi^0$	92.8	0.897	0.832	9.73×10^{-3}
$\Lambda pn_s\pi^0\pi^0$	90.3	0	0	0
$\Lambda pn_s\pi^0\pi^0\pi^0$	83.3	0	0	0
$\Sigma^0 pn_s$	93.5	65.3	61.1	0.714
$\Sigma^0 pn_s\pi^0$	92.0	7.59×10^{-2}	6.98×10^{-2}	8.16×10^{-4}
$\Sigma^0 pn_s\pi^0\pi^0$	88.5	1.14×10^{-2}	1.00×10^{-2}	1.18×10^{-4}
$\Sigma^0 pn_s\pi^0\pi^0\pi^0$	75.2	0	0	0

4.5 Evaluating the contributions for "n"-window

In order to evaluate the contributions for selecting neutron window, the template fitting for $^3\text{He}(K^-,\Lambda p)"X"$ missing-mass spectrum was performed. In Fig.4.14 shows the fitting result with each three nucleon absorption processes produced by using a Monte Calro simulation. In the simulation, the processes listed in Tab.4.2 are considered. The χ^2/ndf of 169.2/66 was observed in this fitting. Evaluated ratios of each contribution are listed in Tab.4.3. The

results of ratio in the all missing-mass region are totally consistent with that observed in previous E15 experiment, which is described in Ref.[48]. The most dominant contribution in the neutron-window is Λpn final state, the ratio of which is 80% of all contributions. The $\Sigma^0 pn$ and $YNN+\pi$ contaminations in the selecting events are evaluated to be 17.8% and 2.24%, respectively. The $YNN+\pi$ contamination is negligible small in the final selecting events. The small contamination from the $\Sigma^0 pn$ final state should be considered to study the structure observed in the Λp invariant-mass spectrum shown in Fig.4.13.
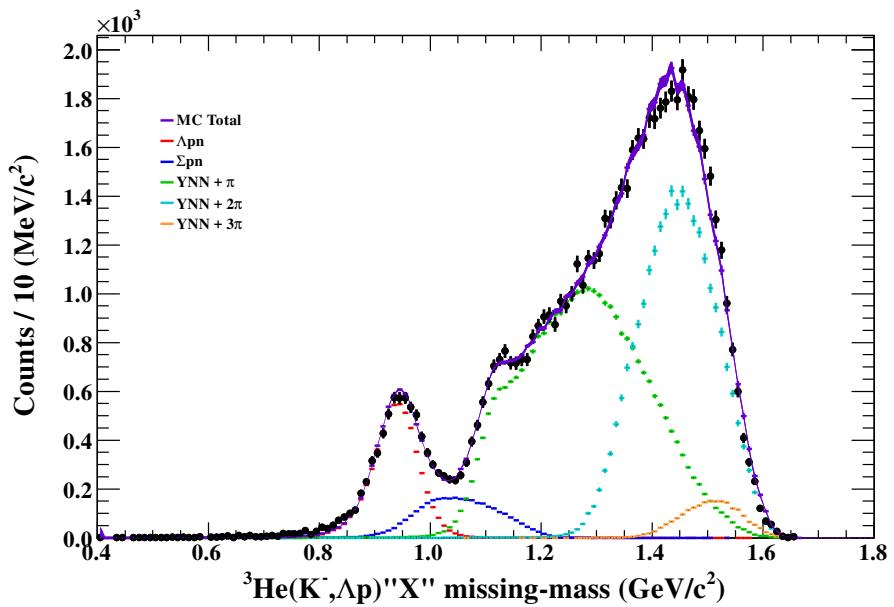
Fig. 4.14 Fitting result of $^3\mathrm{He}(K^-,\Lambda p)$"X" missing-mass spectrum. Black and colored plots show data and simulated spectra, respectively. In the Monte Calro simulation, Ypn, $YNN+\pi$, $YNN+2\pi$, and $YNN+3\pi$ final states are considered.

Table 4.3 Relative yield of each contributions

Final state	Ratio (%)		Relative yield
	All	"*n*"-window	
Λpn	8.28	80.0	1.0
$\Sigma^0 pn$	4.09	17.8	0.223
$YNN+\pi$	42.4	2.24	0.028
$YNN+2\pi$	40.4	0.03	4×10^{-4}
$YNN+3\pi$	4.80	0.0	0.0

4.5.1 Background evaluation from other materials

To evaluate the background from other materials such as target cell, the empty target data is analyzed as same as the ^{3}He data. In this analysis, to focus on the spectrum from other materials, requirement of vertex in the target fiducial region is not applied. Fig.4.15 shows spectra of the $^3\text{He}\,(K^-,\Lambda p)\,"X"$ missing-mass and the Λp invariant mass with selecting neutron window. In the missing-mass spectrum, there was no peak structure from the missing neutron, in contrast the clear peak was observed in the ^{3}He data. Nevertheless, the selection window for the missing neutron is the same as that in the ^{3}He data analysis. In the invariant-mass spectrum with selecting the neutron window, the spectrum shape is much different from that in the ^{3}He data. The number of events become larger in lower mass region in the empty data. And, the peak structure around K^-pp mass-threshold observed in the ^{3}He data did not appear in the empty data. If the requirement of the vertex in the target fiducial region is applied, only two events remains in the missing neutron window. Therefore, the background contribution from other materials is small. The effective luminosities in the ^{3}He and empty data are 3.21nb^{-1} and $69.4\mu\text{b}^{-1}$, respectively, so that the total yield from the other materials with requiring the vertex in the target fiducial region is $2 \times 3.21/69.4 \times 10^3 \sim 92$ events. Fig.4.16 shows comparison between obtained Λp invariant-mass spectrum in the ^{3}He data and background contribution evaluated by using empty data. For the empty data, spectrum without vertex requirement is used and its integral value is normalized to be 92. From this result, the background contribution from other materials are negligibly small in this analysis.

4.5.2 Mixed event analysis

To confirm the observed peak structure, mixed event analysis is performed. In the mixed event analysis, different event samples are mixed and Lorentz vector of Λ and proton from different events are used to calculate the Λp invariant-mass and missing-mass. Fig.4.17 shows the results of mixed event analysis. In the $^3\text{He}\,(K^-,\Lambda p)\,"X"$ missing-mass distribution, the clear neutron peak disappears in the mixed event analysis. By selecting the same missing neutron region in the missing-mass spectrum, the Λp invariant-mass spectrum is much different from the correct data analysis. The events in the mixed event analysis are localized in the lower mass side than correct data analysis. And the peak structure around K^-pp mass-threshold is not observed.

From studies of background contribution from other materials and mixed event analysis, it is concluded that the peak structure around K^-pp mass-threshold is really observed in the $^3\text{He}\,(K^-,\Lambda p)\,n$ reaction.
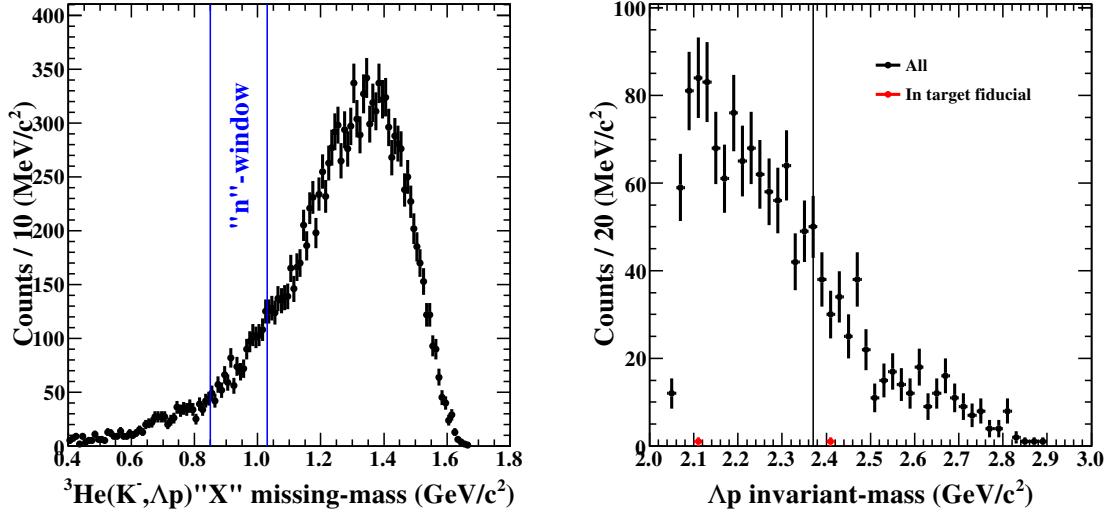
Fig. 4.15 (left) $^3\mathrm{He}\,(K^-,\Lambda p)\,"X"$ missing-mass spectrum in the empty data. Any vertex cut is not applied, so that contribution from target cell materials is seen in here. The blue lines show selected neutron window which is the same as the $^3\mathrm{He}$ data. (right) Λp invariant-mass distribution in the empty data with selecting n-window in the missing-mass spectrum. Black and red plots show without vertex selection and with requiring the vertex is in the target fiducial region. There are only 2 events in the target fiducial region.
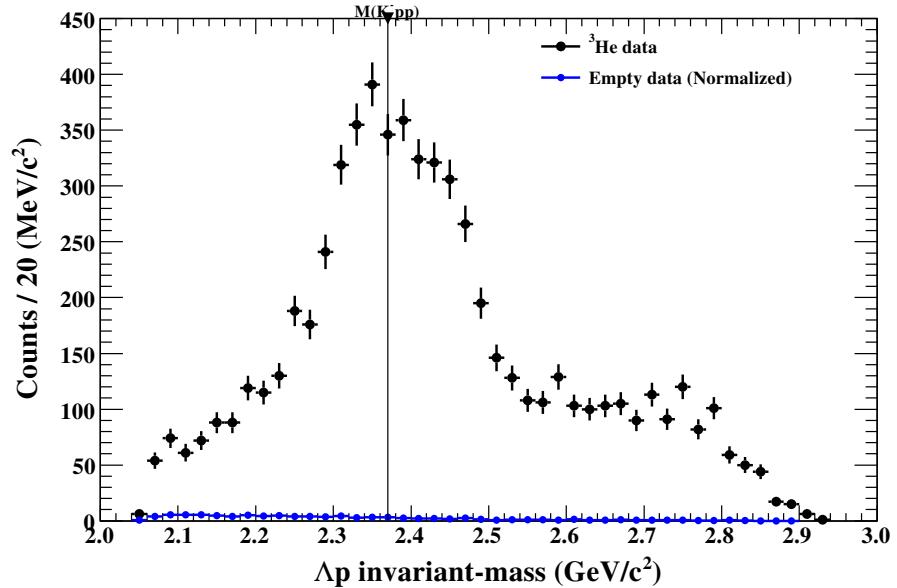
Fig. 4.16 Λp invariant-mass spectrum in the $^3\mathrm{He}$ and the empty data plotted by black and blue point, respectively. For the empty data, the integrated event number is normalized to be $92\,(= 2 \times 46)$ which value is assumed contribution from other materials.
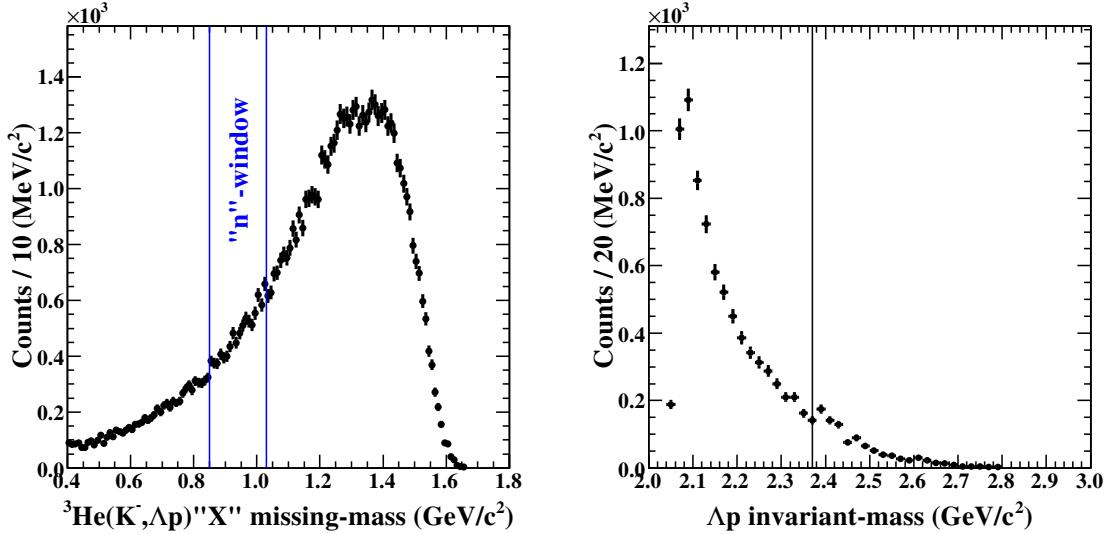
Fig. 4.17 (left) ^{3}He $(K^-, \Lambda p)$"X" missing-mass spectrum with mixed event analysis. (right) Λp invariant-mass distribution in mixed event analysis with selecting n-window in the missing-mass spectrum. There is no structure around $K^- pp$ mass-threshold indicated by black line.

4.6   Kinematic fit

The next step is performing the kinematic fit to improve the invariant-mass resolution.

In this analysis, the package of *KinFitter* in the ROOT is used for performing the kinematic fit. The fitting method is based on least square fit with non-linear constraint, which is well described in Ref.[69]. For the kinematical fit, kinematical constraint is as follows.

1. invariant mass constraint; invariant-mass of $\pi^- p$ equals to Λ-mass.

2. 4 momentum vector conservation; missing-mass of Λp equals to neutron mass.

In the kinematical fit, the 4 momentum vector is varied within its resolution, so that the resolution parameter is desired.

To check the effect of the kinematical fit, the invariant-mass resolution is evaluated by using a Monte Calro simulation. In this simulation, 3NA-Λpn and 3NA-$\Sigma^0 pn$ processes are considered. Fig.4.18 shows the invariant-mass resolution as a function of Λp invariant-mass. The result is well understood that the resolution is much improved by using kinematic fit. At the $K^- pp$ mass-threshold, about 1.5 times better resolution was obtained with the kinematical fit. In contrast, the improvement of invariant-mass resolution in the $\Sigma^0 pn$ process is not so good compared with that in the Λpn process. The cause of this can be considered as the one missing γ is ignored in the kinematical fit. The resolution curve obtained by a Monte Calro

simulation was fitted with the third order polynomial function and the resolution parameters are listed in Tab.4.4.

To check the obtained Λp invariant-mass is correct, difference between measured and truth Λp invariant-mass is studied as Fig.4.19. For the Λpn events, the obtained mass is close to truth value as expected. On the other hand, difference is much bigger for the $\Sigma^0 pn$ events due to missing γ-ray from Σ^0 decay. This mass shift correlation is also fitted with the third order polynomial function and its parameters are listed in Tab.4.5.
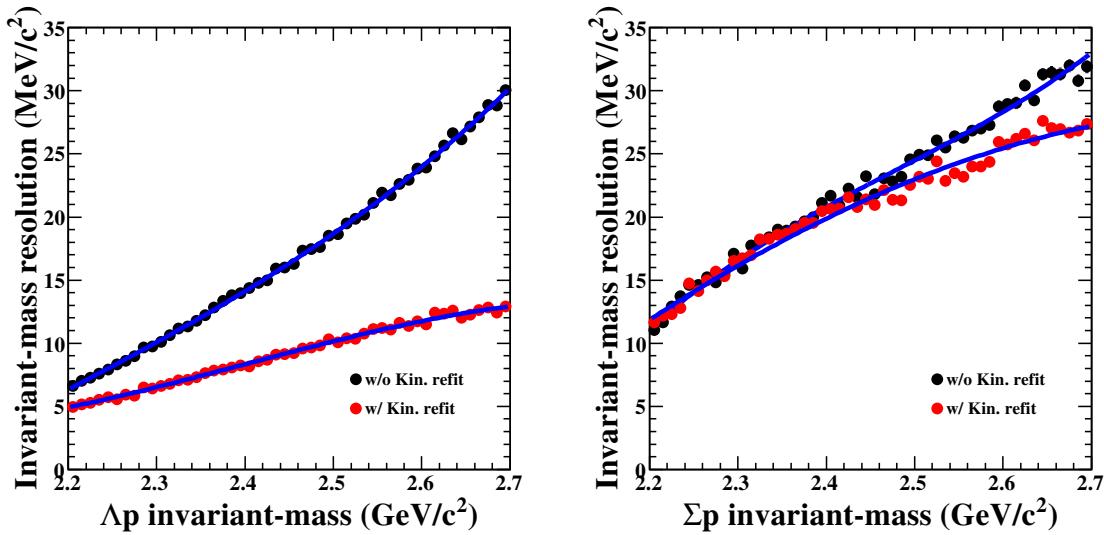
Fig. 4.18 Λp invariant-mass resolution for each Λp invariant-mass obtained by using Monte Calro simulation. (left) Resolution curve for $K^- + {}^3\text{He} \to \Lambda pn$ reaction. (right) Resolution curve for $K^- + {}^3\text{He} \to \Sigma^0 pn$ reaction. Black and red plots show results with and without kinematic fit, respectively. Each resolution curves are fitted by using third polynomial function which results are indicated by blue line.

Table 4.4 Parameters for resolution curve

Channel		Parameters $F(x) = p_0 + p_1 \cdot x + p_1 \cdot x^2 + p_2 \cdot x^3$			
		p_0	p_1	p_2	p_3
$K^- + {}^3\text{He} \to \Lambda pn$	w/o Kin. fit	-434.625	537.619	-232.069	35.8203
	w/ Kin. fit	455.297	-595.899	256.085	-35.5796
$K^- + {}^3\text{He} \to \Sigma^0 pn$	w/o Kin. fit	-1812.6	2150.58	-853.258	114.784
	w/ Kin. fit	-134.685	51.3273	23.4427	-7.49824
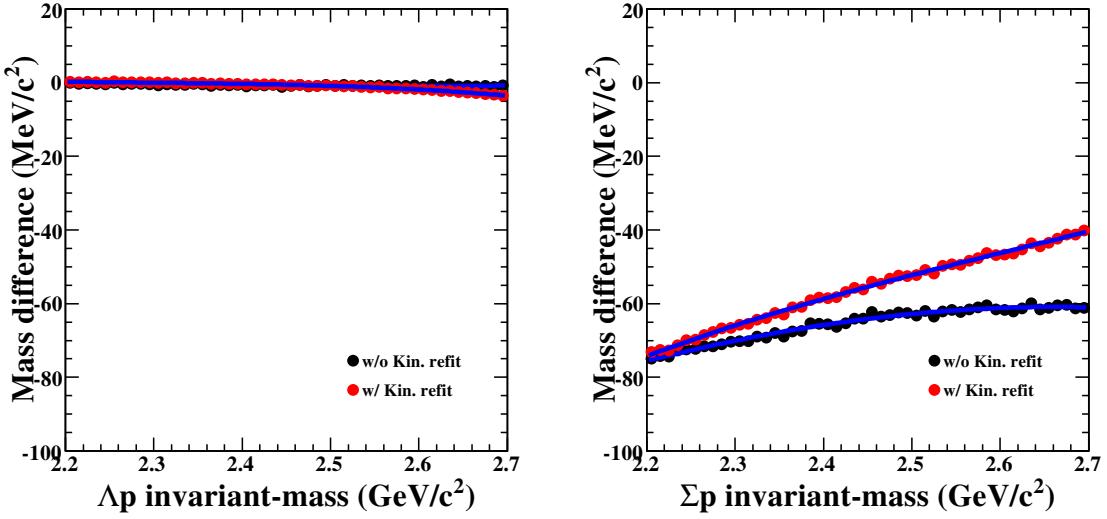
Fig. 4.19 Mass difference between measured and truth Λp invariant-mass obtained by using Monte Calro simulation. (left) Mass shift curve for $K^- + {}^3$He $\rightarrow \Lambda pn$ reaction. (right) Mass shift curve for $K^- + {}^3$He $\rightarrow \Sigma^0 pn$ reaction.

Table 4.5 Parameters for mass shift curve

Channel		Parameters $F(x) = p_0 + p_1 \cdot x + p_1 \cdot x^2 + p_2 \cdot x^3$			
		p_0	p_1	p_2	p_3
$K^- + {}^3$He $\rightarrow \Lambda pn$	w/o Kin. fit	11.3552	-2.95268	-1.72226	0.301761
	w/ Kin. fit	-22.3799	11.4513	4.30227	-2.21766
$K^- + {}^3$He $\rightarrow \Sigma^0 pn$	w/o Kin. fit	-294.339	60.5277	53.3794	-16.2189
	w/ Kin. fit	-1221.24	1224.31	-443.004	56.126

4.7 The obtained Λp invariant-mass spectrum

After the kinematical fit, the final Λp invariant-mass spectrum in the $^3\mathrm{He}\,(K^-,\Lambda p)\,n$ reaction is obtained, as shown in Fig.4.20. The peak structure around K^-pp mass-threshold still remains. But, the peak width became a bit narrower than that in the previous spectrum shown in Fig.4.13. At the last, a survival ratio of each selection in the analysis is listed in Tab.4.6, and there are 6415 events in the final Λp invariant-mass spectrum in the $^3\mathrm{He}\,(K^-,\Lambda p)\,n$ reaction. The invariant-mass resolution less than 10 MeV/c^2 was achieved in the mass region below the $K-pp$ threshold.
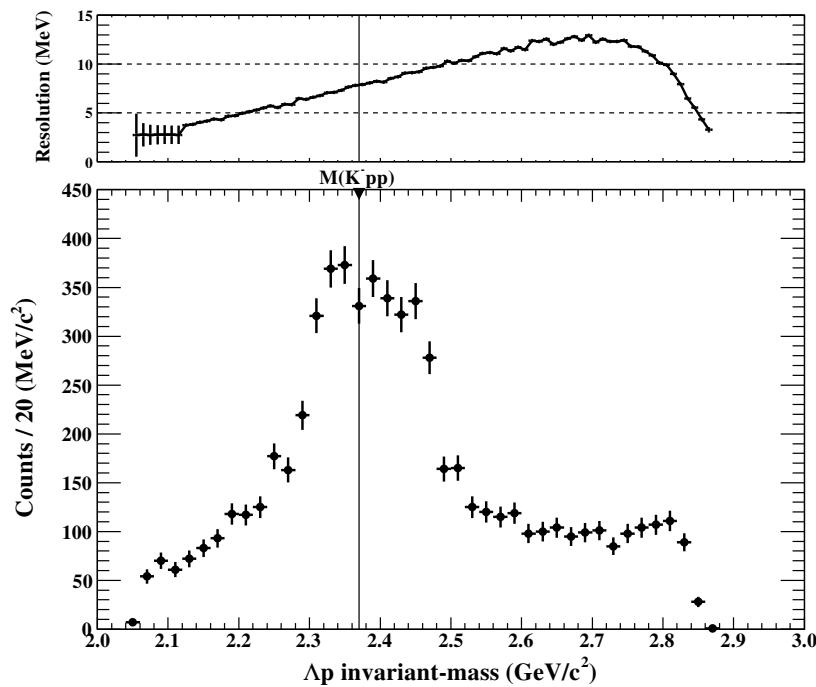
Fig. 4.20 Λp invariant-mass distribution(bottom) and its resolution(top) after performing the kinematical fit in the $^3\mathrm{He}\,(K^-,\Lambda p)\,"n"$ reaction.

Table 4.6 Survival ratio in each selection

Selection	Number of events		Reduction ratio	
	Examined	Passed	Relative	Total
Beam analysis	-	1.14291×10^8	-	1.0
KCDH3 trigger	1.14291×10^8	8.65497×10^7	0.757	0.757
3 hits in CDH	8.65497×10^7	6.04107×10^7	0.698	0.529
3 tracks in CDC	6.04107×10^7	1.75808×10^7	0.291	0.154
No charged in FWD	1.75808×10^7	1.56612×10^7	0.891	0.137
3 combinations in CDS	1.56612×10^7	1.24677×10^7	0.796	0.109
2 protons and pion	1.24677×10^7	2.52879×10^6	0.203	2.21×10^{-2}
$\chi^2 < 30$	2.52879×10^6	2.51202×10^6	0.993	2.20×10^{-2}
2 track combination	2.51202×10^6	2.12065×10^6	0.844	1.86×10^{-2}
Λ-reconstruction	2.12065×10^6	698126	0.329	6.11×10^{-3}
Vertex decision-1	698126	76819	0.110	6.72×10^{-4}
Vertex decision-2	76819	66352	0.846	5.81×10^{-4}
"n"-selection	66352	6415	0.0976	5.61×10^{-5}

Chapter 5

Results and discussion

In this chapter, the observed Λp invariant-mass spectrum is discussed in detail. The Λp invariant-mass spectrum has major peak structure below and above the $K^- pp$ mass-threshold as described in the previous chapter. Before discussing about the peak structure, the correlation between Λp invariant-mass and other quantities, such as neutron emission angle or momentum transfer in the reaction, will be discussed.

5.1   Correlation between Λp invariant mass and other quantities

The correlations between the Λp invariant-mass and the neutron emission angle or momentum transfer are studied to discuss about origin of the observed peak around the $K^- pp$ mass-threshold.

5.1.1   Neutron emission angle

First of all, the correlation between the Λp invariant-mass and the neutron emission angle $\cos\theta_n^{CM}$ is shown. The neutron emission angle in the center of mass frame is defined as

$$\cos\theta_n^{CM} = \frac{\mathbf{p}_{K^-}^{CM} \cdot \mathbf{p}_n^{CM}}{|\mathbf{p}_{K^-}^{CM}| \cdot |\mathbf{p}_n^{CM}|}, \tag{5.1}$$

where $\mathbf{p}_{K^-}^{CM}$ and $\mathbf{p}_n^{CM}$ denote momentum vectors in the center of mass frame.

Fig.5.1 shows a 2-dimensional plot of the Λp invariant-mass versus $\cos\theta_n^{CM}$. It was observed that events in the peak structure above and below the $K^- pp$ mass-threshold were concentrated in a region of $\cos\theta_n^{CM}$ greater than 0.7.
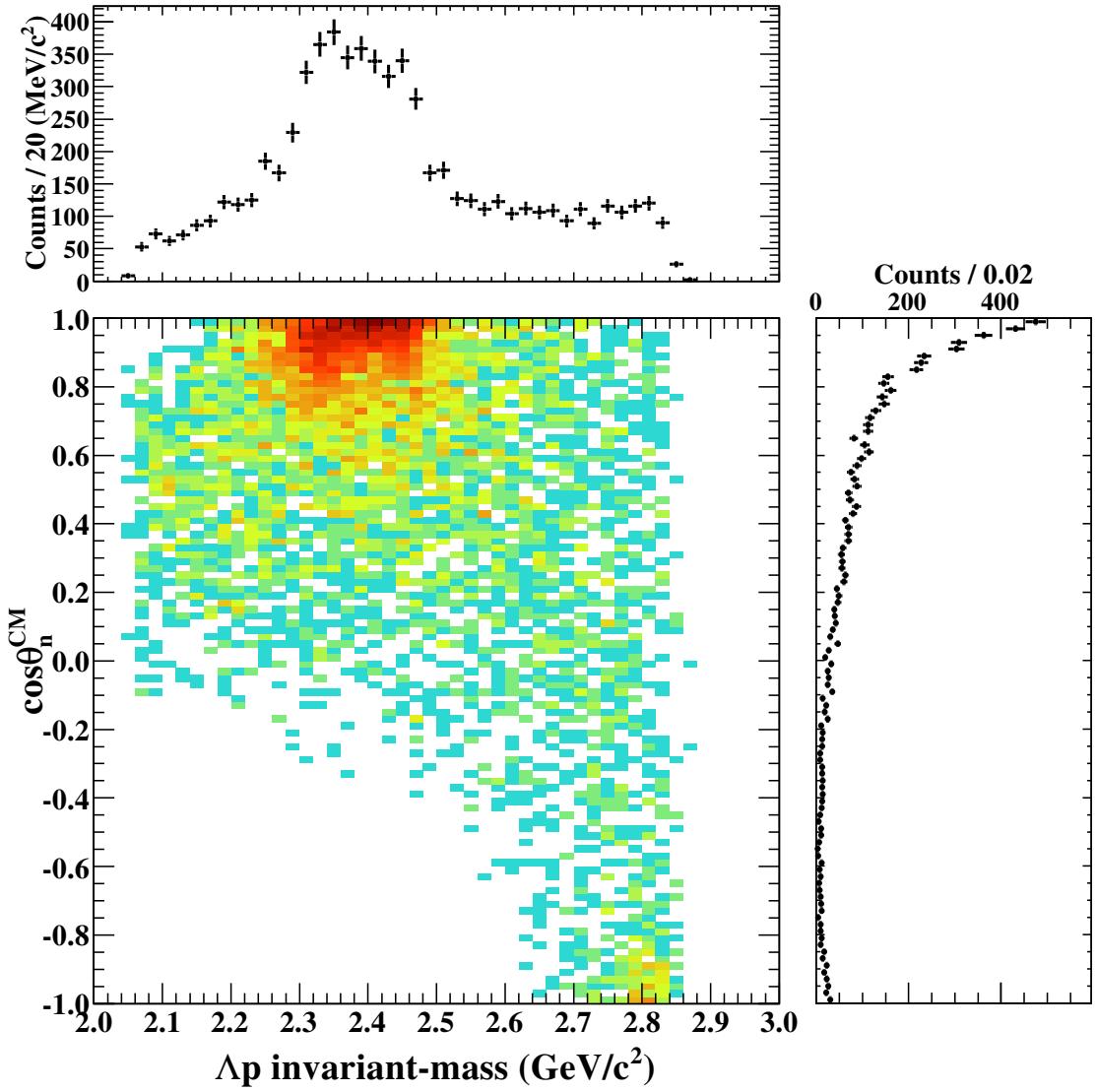
Fig. 5.1 Λp invariant-mass versus $\cos\theta_n^{CM}$ distribution. The top and right side figures show the projected spectrum to X and Y axis, respectively. The structure around $K^- pp$ mass-threshold is located in the region of forward neutron emission angle, which is $\cos\theta_n^{CM}$ more than 0.7. Note that less yield in the region of very forward angle and invariant-mass of 2.1-2.2 GeV/c^2 is due to acceptance limit of the detector system.

This behavior was clearly observed in the invariant-mass spectrum sliced by a 0.1 bin width of $\cos\theta_n^{CM}$ as shown in Fig.5.2. The yield of the peak component decreases as $\cos\theta_n^{CM}$ decreasing. In the backward region of the neutron emission angle, from $\cos\theta_n^{CM}$ of -1.0 to -0.7, we find a small event concentration around the Λp invariant-mass of 2.8 GeV/c^2. These events are considered as a two nucleon absorption process where a kaon is absorbed by two nucleons in ^{3}He. The other neutron acts as a spectator and its momentum remains as small as a Fermi momentum.

Since, the region where the invariant-mass less than 2.2 GeV/c^2 and $\cos\theta_n^{CM}$ greater than 0.8 is out of detector acceptance, the spectrum shape is distorted in that region. In $\cos\theta_n^{CM}$ greater than 0.7, the largest contribution is the peak structure around the K^-pp mass-threshold. In contrast, there is only continuum contribution in the $\cos\theta_n^{CM}$ range from 0.0 to 0.7.

5.1.2 Momentum transfer

The relation between the Λp invariant-mass and momentum transfer to the Λp system is also studied as shown in Fig.5.3. The momentum transfer to the Λp system is calculated by

$$q = |\mathbf{p}_{K^-} - \mathbf{p}_n|, \tag{5.2}$$

where $\mathbf{p}_{K^-}$ and $\mathbf{p}_n$ are the momentum vectors of beam K^- and scattered neutron in the laboratory frame. Especially, the relation between the Λp invariant-mass and the momentum transfer kinematically corresponds to that between the Λp invariant-mass and $\cos\theta_n^{CM}$. Due to the kinematical limit, there is no event in the left-bottom region in Fig.5.3. The peak component around the K^-pp mass-threshold is strongly concentrated on around the momentum transfer less than 0.5 GeV/c.

Fig.5.4 shows the Λp invariant-mass spectra sliced by the momentum transfer. In the region of the momentum transfer less than 0.3 GeV/c, yield below the K^-pp mass threshold was small due to the kinematical limit. The peak below the K^-pp mass threshold was clearly observed in the momentum transfer from 0.3 to 0.6 GeV/c region.

5.2 Fitting the Λp invariant-mass spectrum

Fitting of the Λp invariant-mass spectrum was performed to study for the peak structure observed around the K^-pp mass-threshold. First of all, to extract the peak component, the spectra selected in two different regions, $0.0<\cos\theta_n^{CM}<0.7$ and $0.7<\cos\theta_n^{CM}<1.0$, are prepared as shown in Fig.5.5. The former spectrum has only a continuum component which distributes
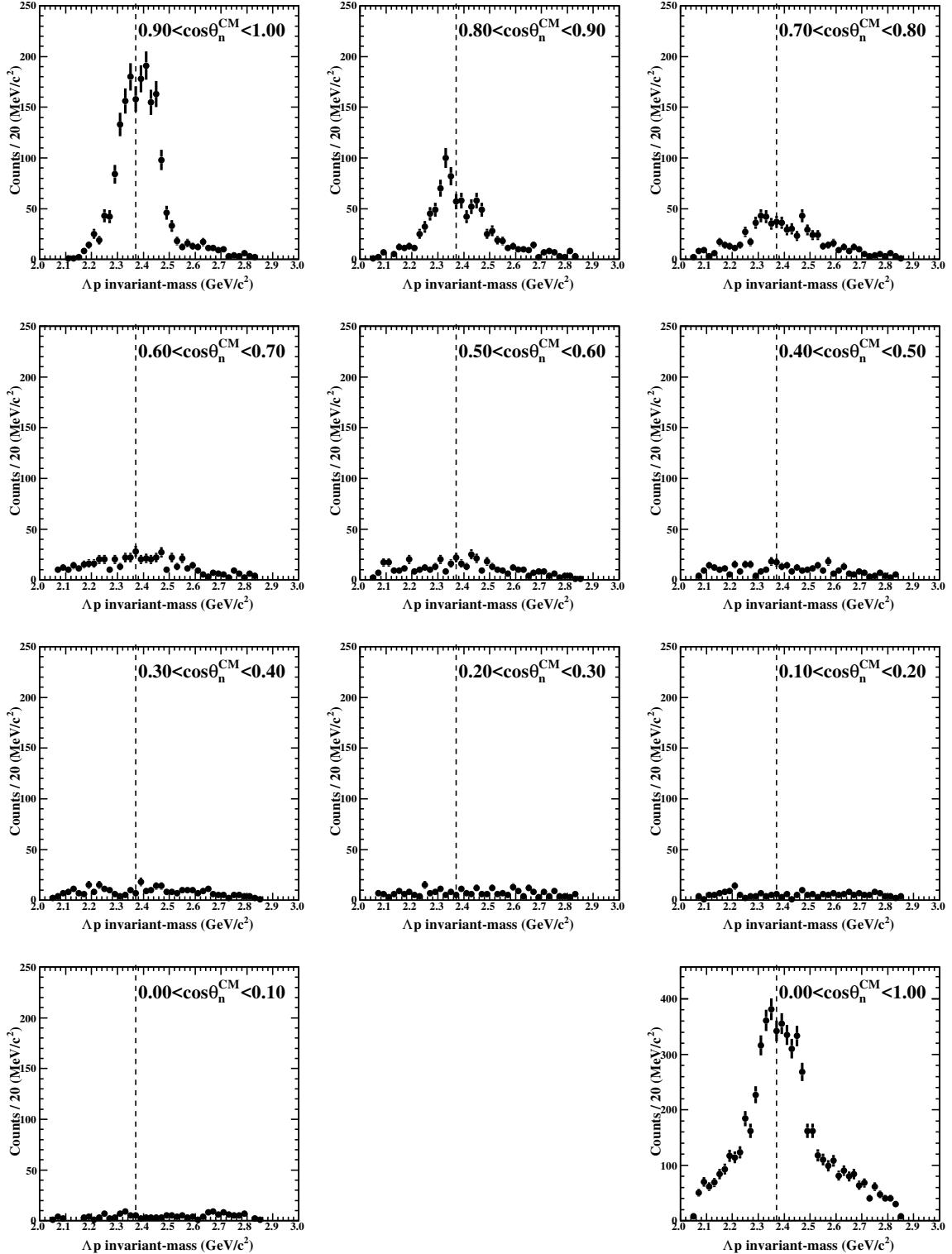
Fig. 5.2 Λp invariant-mass spectrum for slicing each $\cos\theta_n^{CM}$. The left-top figure shows $\cos\theta_n^{CM}$ from 0.9 to 1.0, and the others are in series of each $\cos\theta_n^{CM}$ slice with 0.1 width. The right-bottom one shows sum of the all spectrum whose $\cos\theta_n^{CM}$ is more than 0.0.
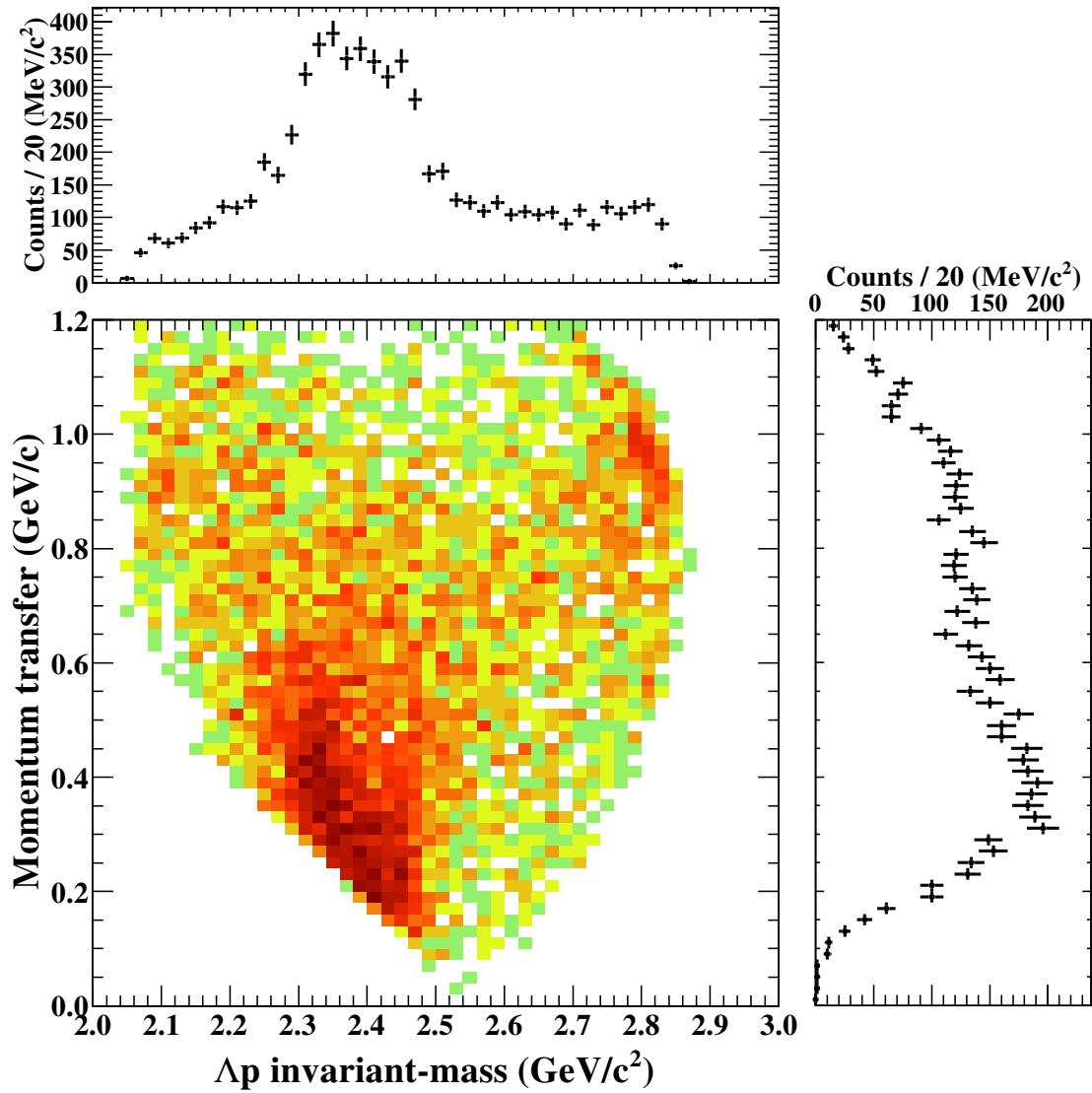
Fig. 5.3 Λp invariant-mass versus momentum transfer to p system plot. The top and right figures show the projected spectrum of X and Y axis, respectively. Because of the kinematical limit, these is no event in the region of left-bottom side in the 2D plot. The peak structure around $\bar{p}p$ mass-threshold is localized at momentum transfer from 0.2 to 0.5 GeV/c.
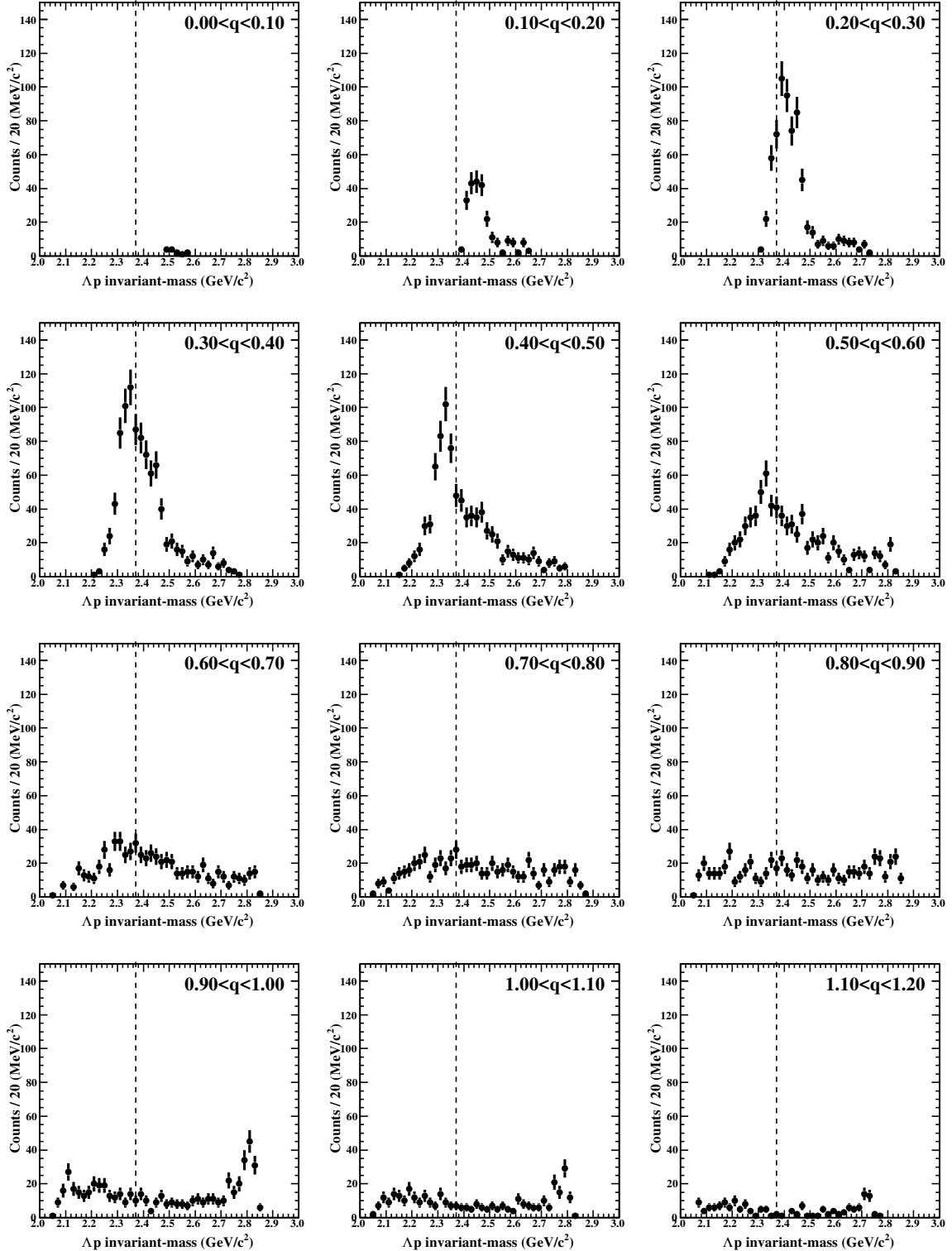
Fig. 5.4 Λp invariant-mass spectrum sliced by each momentum transfer. The right-top figure shows spectrum with selecting momentum transfer from 0.0 to 0.1 GeV/c. The sliced width of momentum transfer is 0.1 GeV/c. Due to the kinematical limit, the top three figure do not have contribution below the K^-pp mass-threshold.

widely. The latter one contains the peak component and the continuum. We call the spectrum with $\cos\theta_n^{CM}$ from 0.0 to 0.7 "*background*" and that with $\cos\theta_n^{CM}$ from 0.7 to 1.0 "*signal*". Assuming the continuum shape and its production rate does not change in each selected angular region, the continuum component in the latter spectrum can be demonstrated by that in the former spectrum.
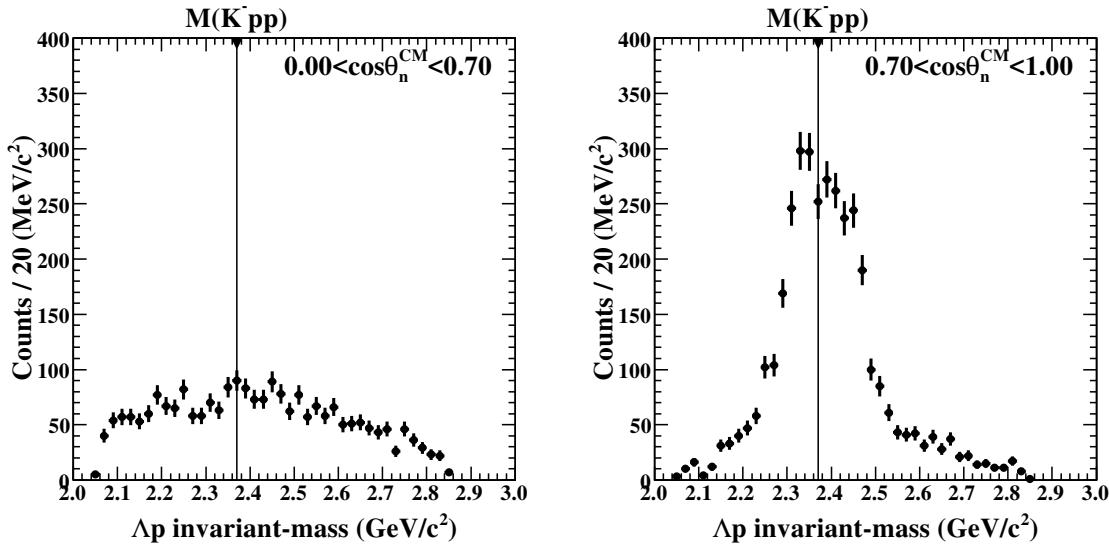
Fig. 5.5 (left)Λp invariant-mass with selecting $\cos\theta_n^{CM}$ is from 0.0 to 0.7. (right) The same spectrum with selecting $\cos\theta_n^{CM}$ is from 0.7 to 1.0. The structure around $K^- pp$ mass-threshold appears in the very forward neutron angle region. In contrast, there is only continuum contribution in the $\cos\theta_n^{CM}$ range from 0.0 to 0.7.

We made following two operations to the observed Λp invariant-mass spectrum.

1. Subtract the *background* from the *signal*.

2. The subtracted spectrum is fitted to be decomposed into a few possible subcomponents

In Step 1, the *background* spectrum is scaled to take into account the acceptance. To do that, acceptance shapes for different $\cos\theta_n^{CM}$ regions were evaluated as Fig.5.6. The background yield at mass m ($N'_{BG}(m)$) can be explained by

$$N'_{BG}(m) = \frac{A_{Sig}(m)}{A_{BG}(m)}N_{BG}(m) \qquad\qquad (5.3)$$

where N_{BG} and $A_i(m)$ denote the number of events in the *background* spectrum and acceptance in the relevant $\cos\theta_n^{CM}$ region, respectively. After scaling with acceptance, the *background*
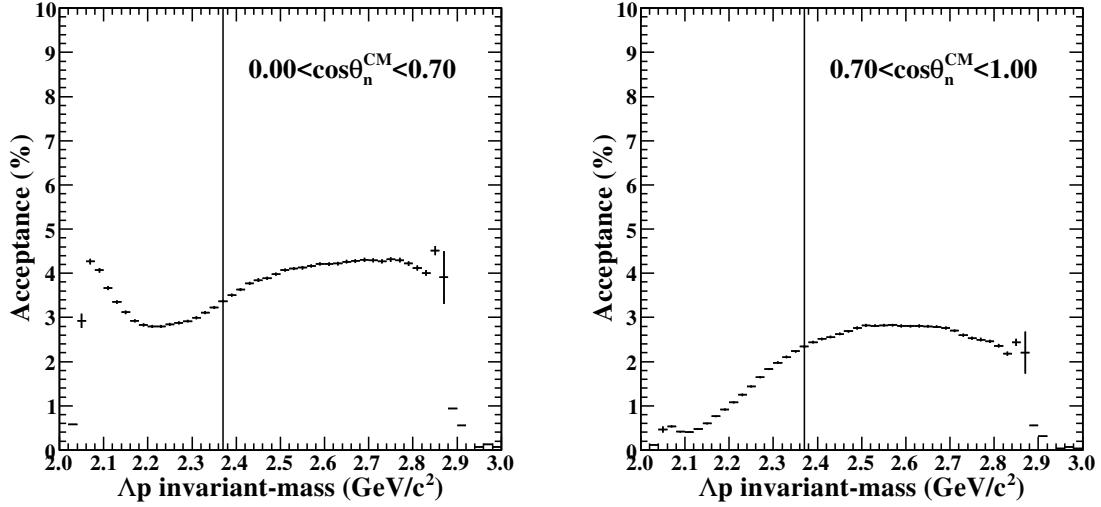
Fig. 5.6 (left)Acceptance of Λp invariant-mass with selecting $\cos\theta_n^{CM}$ is from 0.0 to 0.7. (right) The same spectrum with selecting $\cos\theta_n^{CM}$ is from 0.7 to 1.0.

shape is well reproduced the *signal* spectrum in the region above 2.6 GeV/c^2, as shown in Fig.5.7

The fitting of the second step is applied for the residual distribution as shown in Fig.5.7-(bottom). In this subtracted spectrum, there is only peak component and almost continuum contribution has been eliminated. As mentioned in Section 5.1.1, the detector has little acceptance for the Λp invariant-mass below 2.2 GeV/c^2 in the $\cos\theta_n^{CM}<0.7$. We considered the mass region above 2.2 GeV/c^2 for the fitting of the peak component, as described in the following sections.

5.2.1 Fitting with single distribution

First of all, the fitting is performed with single distribution of Gaussian or Breit-Wigner distribution

$$f_G(m) = \frac{p_0}{\sqrt{2\pi\sigma^2}}exp\left(\frac{(m-\mu)^2}{2\sigma^2}\right), \tag{5.4}$$

$$f_{BW}(m) = \frac{p_0}{2\pi}\frac{\Gamma}{\left((m-\mu)^2 + \frac{\Gamma^2}{4}\right)}, \tag{5.5}$$
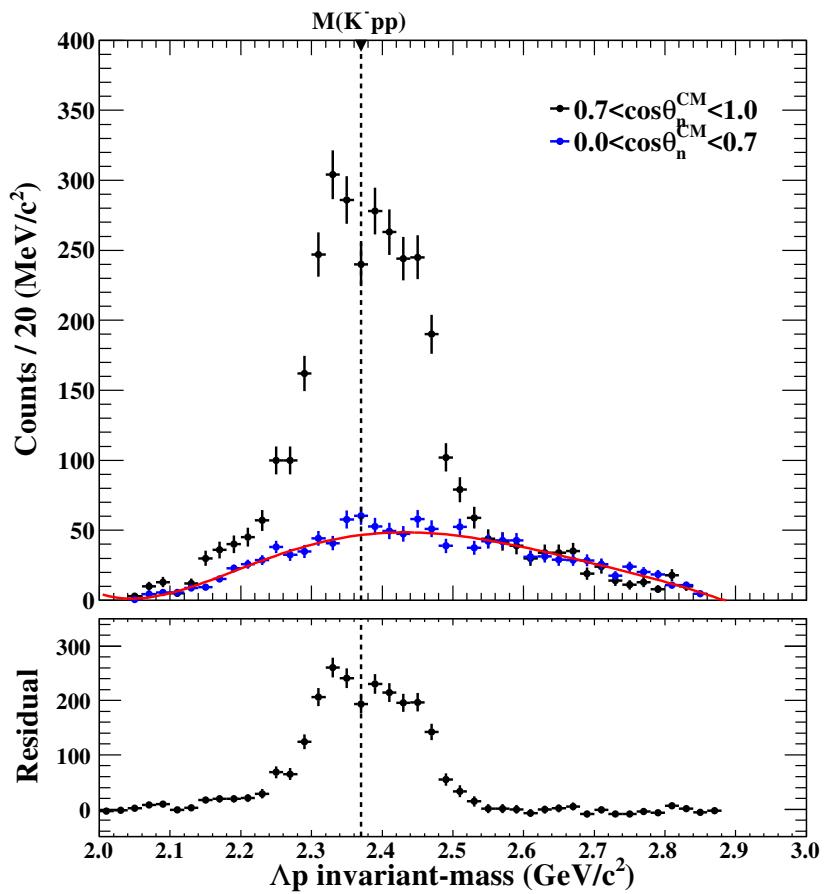
Fig. 5.7 (top)Λp invariant-mass spectrum with selecting $\cos\theta_n^{CM}$ from 0.7 to 1.0 and from 0.0 to 0.7 plotted by black and blue points, respectively. (bottom)Residual of two spectrum shown in top figure.

with free parameters of p_0, μ, σ or Γ. Also, to consider the invariant-mass resolution and acceptance, the Gaussian resolution function was convoluted to these equation as

$$f'(m) = A_{Sig}(m) \cdot (f(m) * g(m)),\qquad(5.6)$$

$$g(m) = \frac{1}{\sqrt{2\pi\sigma^2(m)}} exp\left(\frac{m^2}{2\sigma^2(m)}\right),\qquad(5.7)$$

where $g(m)$ is a resolution function, $\sigma(m)$ is an invariant-mass resolution, and $A_{Sig}(m)$ is an acceptance in the $\cos\theta_n^{CM}$ region from 0.7 to 1.0 obtained in Fig.5.6 at mass of m . The resolution $\sigma(m)$ is evaluated by the Monte Calro simulation as described in Fig.4.18.

In Fig.5.8 shows the fitting results by using Gaussian and Breit-Wigner distributions, and these with resolution convolution. In the fitting, the numbers of free parameters in the fitting function and of data points in the fitting range are 3 and 20, respectively. Thus, the number of degree of freedom (ndf) is 17. Reduced chi squares, χ^2/ndf, were 54.9/17 and 148.7/17 for the Gaussian and Breit-Wigner distributions, respectively. Deviation of the observed spectrum to the fitted function becomes large in the mass region from 2.35 to 2.45 GeV/c^2. In the next step, we employ two distribution functions to see if χ^2/ndf for the fitting is improved.

Table 5.1 Fitting results with single distribution

Formula	χ^2/ndf	p_0	μ	σ/Γ
$f_G(m)$	54.9/17	106 ± 3.0	2.359 ± 0.003	0.075 ± 0.002
$f_{BW}(m)$	148.7/17	131 ± 4.1	2.351 ± 0.003	0.135 ± 0.005

5.2.2   Fitting with two distributions

We carried out spectrum fittings with the following two distribution functions;

1. Two Gaussians

2. Two Breit-Wigners

3. Gaussian and Breit-Wigner

The numbers of free parameters and degree of freedom are 6 and 19, respectively. Fig.5.9 shows the fitting results for the above-mentioned 3 cases. We found the best χ^2/ndf in the case of 3, Gaussian and Breit-Wigner among 3 cases. The peak positions of the Gaussian and the Breit-Wigner distributions are 2.435 ± 0.005 and 2.328 ± 0.004 GeV/c^2, which are
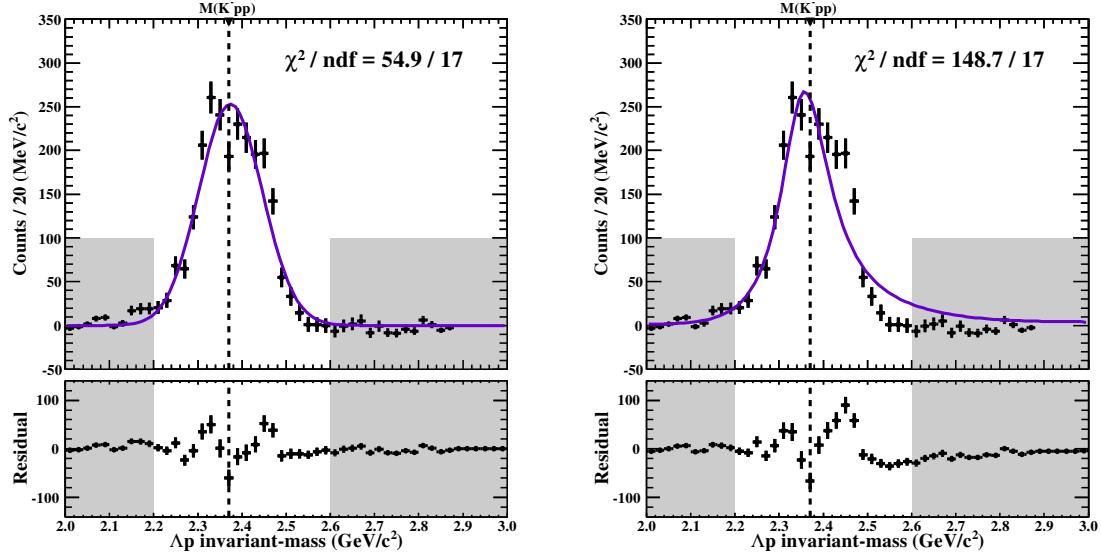
Fig. 5.8 Fitting results of Λp invariant-mass spectrum with single peak structure. (left-bottom)Fitting using Gaussian distribution with mass-resolution convolution. (left-bottom)Fitting using Breit-Wigner distribution with mass-resolution convolution.

located above and below the $K^- pp$ threshold. The widths are σ=0.038 ± 0.004 GeV/c^2 and Γ = 0.089 ± 0.007 GeV/c^2, respectively.

Table 5.2 Fitting results with two distributions

Formula	χ^2/ndf	p_i	μ_i	σ_i/Γ_i
$f_G(m) + f_G(m)$	25.3/14	81.0 ± 8.3	2.337 ± 0.006	0.057 ± 0.006
		22.8 ± 7.3	2.444 ± 0.006	0.032 ± 0.005
$f_{BW}(m) + f_{BW}(m)$	52.9/14	85.8 ± 7.9	2.330 ± 0.003	0.086 ± 0.008
		35.0 ± 6.0	2.426 ± 0.006	0.061 ± 0.009
$f_{BW}(m) + f_G(m)$	21.4/14	84.0 ± 7.2	2.326 ± 0.004	0.082 ± 0.008
		32.9 ± 4.7	2.424 ± 0.005	0.038 ± 0.004

5.2.3 Including the $\Sigma^0 pn$ contamination

As discussed in Section 4.5, $\Sigma^0 pn$ events are contaminated in the Λp invariant-mass spectrum. In this section, we estimate how the $\Sigma^0 pn$ contamination affects the fitting result. Decomposing the $^3\text{He}(K^-, \Lambda p)"X"$ missing-mass spectra for the angular regions of $0.0<\cos\theta_n^{CM}<0.7$ and $0.7<\cos\theta_n^{CM}<1.0$, as shown in Fig.5.10 and 5.11, the $\Sigma^0 pn$ contaminations in the "n"-window were obtained, as summarized in Table 5.3. The $\Sigma^0 pn$ contamination in the case of $0.0<\cos\theta_n^{CM}<0.7$ (*Background* region) is larger than that of $0.7<\cos\theta_n^{CM}<1.0$ (*Signal* region).
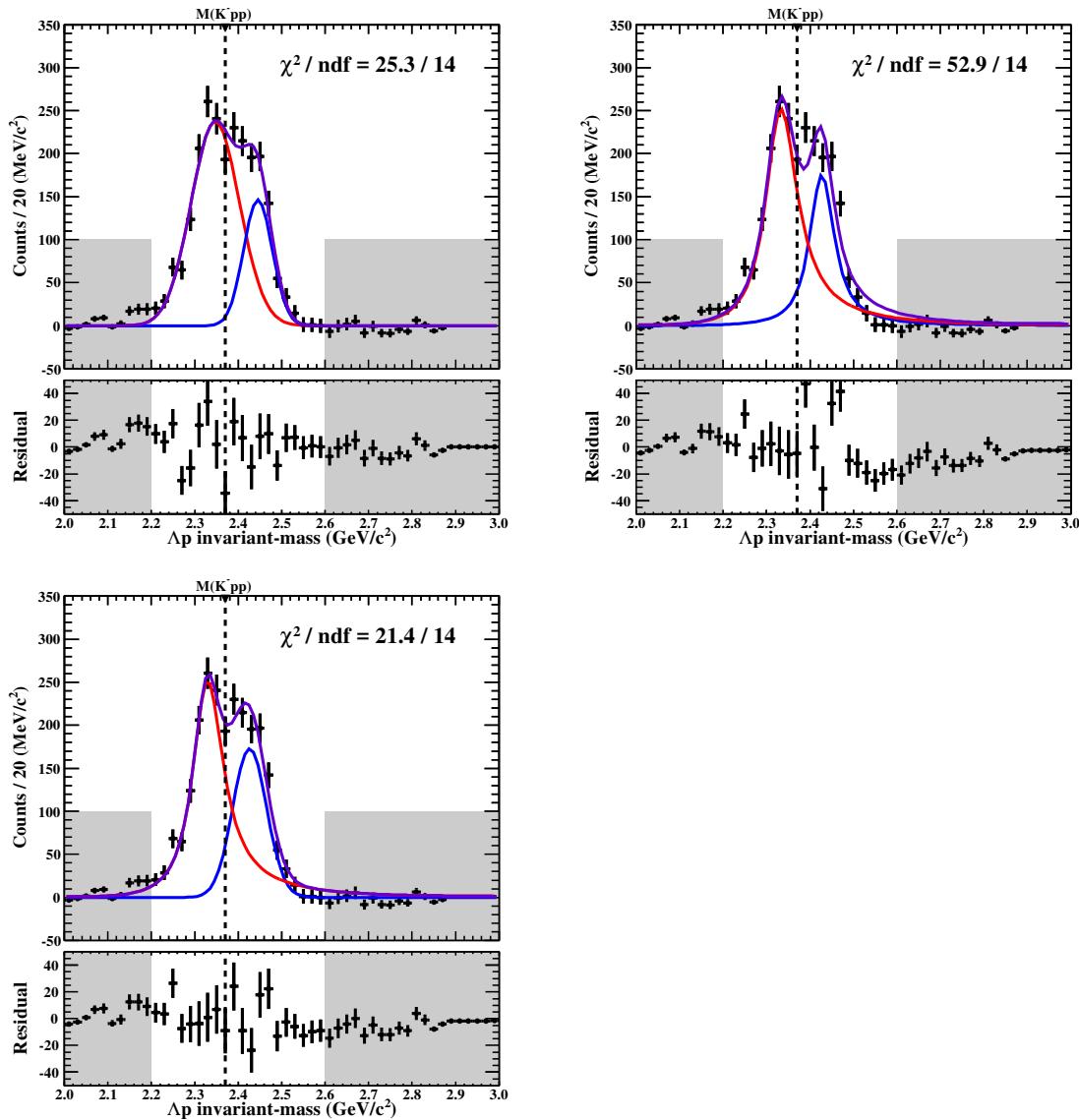
Fig. 5.9 Fitting results of Λp invariant-mass spectrum with double peak structures. (left-top)Fitting using two Gaussian distributions with mass-resolution convolution. (right-top)Fitting using two Breit-Wigner distributions with mass-resolution convolution. (left-bottom)Fitting using Gaussian and Breit-Wigner distributions with mass-resolution convolution. In the fitting using Gaussian and Breit-Wigner distribution is the best for fitting. In this fitting, the peak below and above the K^-pp mass-threshold could be considered to be Breit-Wigner form and Gaussian form, respectively.

We deduce a ratio of the $\Sigma^0 pn$ events to the Λpn events in the subtracted spectrum from the following relations;

$$N^{\Lambda pn} = N_{Sig} \cdot R_{Sig}^{\Lambda pn} - N_{BG} \cdot R_{BG}^{\Lambda pn}$$
$$N^{\Sigma^0 pn} = N_{Sig} \cdot R_{Sig}^{\Sigma^0 pn} - N_{BG} \cdot R_{BG}^{\Sigma^0 pn},$$

(5.8)

where N_{Sig}, N_{BG}, R denote the number of events in *signal* and *background* spectrum and ratio of Λpn or $\Sigma^0 pn$ event in the spectrum, respectively. In this analysis, N_{Sig} and N_{BG} was found to be 3525 and 1231, respectively. The ratios and the number of events of Λpn and Σpn final states are listed in Table 5.3. We ignored the other contaminations, which is multi-pion generation processes, as they are small. Therefore, The $N_{\Sigma^0 pn}/N_{\Lambda pn}$ ratio was found to be 0.185 ± 0.030. This value is used to fix the magnitude of the $\Sigma^0 pn$ contamination in the fitting of the spectrum.
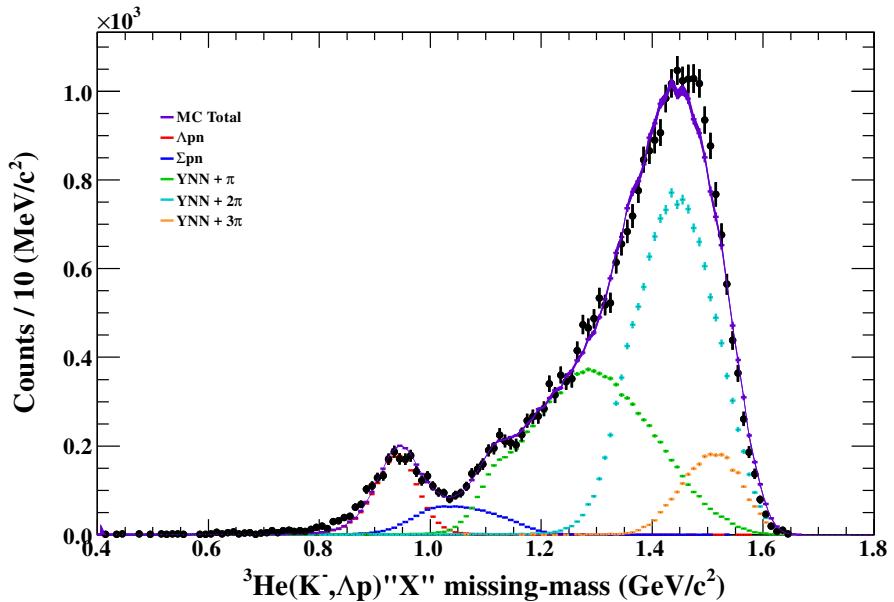
Fig. 5.10 Fitting results of $^3\mathrm{He}(K^-, \Lambda p)''X''$ missing-mass spectrum with selecting $\cos\theta_n^{CM}$ from 0.0 to 0.7.

Table 5.3 Relative yield of each contributions in different $\cos\theta_n^{CM}$ regions

Final state	$0.7 < \cos\theta_n^{CM} < 1.0$		$0.0 < \cos\theta_n^{CM} < 0.7$	
	Ratio (%)	# of events	Ratio (%)	# of events
Λpn	76.2 ± 1.6	2686 ± 57	65.1 ± 1.9	801 ± 23
$\Sigma^0 pn$	21.4 ± 1.5	754 ± 53	32.9 ± 1.4	405 ± 17
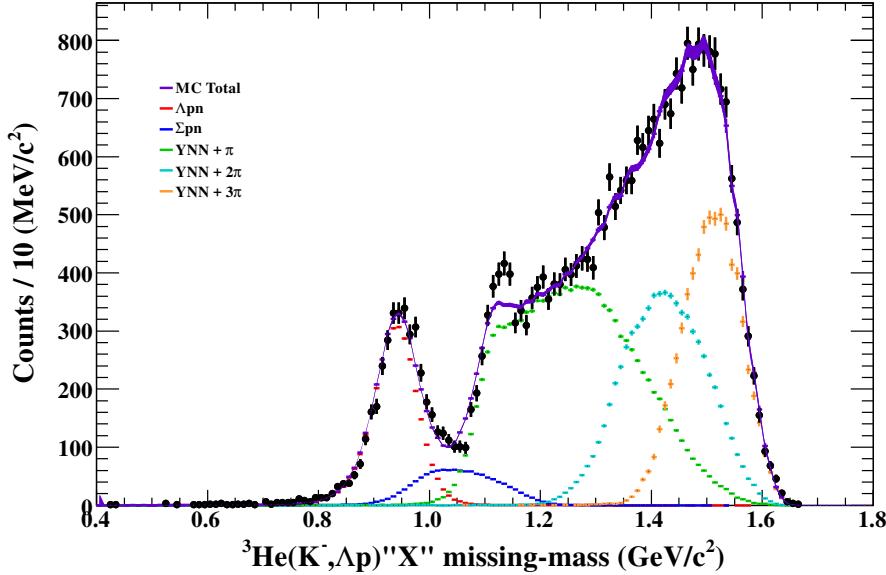
Fig. 5.11 Fitting results of $^3\text{He}(K^-, \Lambda p)''X''$ missing-mass spectrum with selecting $\cos\theta_n^{CM}$ from 0.7 to 1.0.

Next, we consider the contaminated $\Sigma^0 pn$ events contribute in the Λp invariant-mass spectrum. Given a mass of a system, which decays in to $\Sigma^0 p$, the Λp invariant-mass is shifted by the mass difference between Σ^0 and Λ, as mentioned in Sec.4.6. In the present case, Λp's with having higher momenta within a fluctuation of the resolution are selected so as to sneak in to the "n"-window. As a result, the energy shift is lower than the mass difference, depending on its kinematics. We demonstrated this shift by a Monte Calro simulation, as shown in Fig.4.19. The mass shift (difference) is obtained as a function to the third order of the polynomial function, as listed in Table 4.5. From this relation, we can estimate the location of the Λp invariant-mass distribution for the contaminated $\Sigma^0 pn$ events once a distribution of a state is determined. Therefore, the fitting function is defined as follows.

$$f'(m) = \left(\frac{p_0}{\sqrt{2\pi\sigma^2}} exp\left(\frac{(m-\mu_0)^2}{2\sigma^2} \right) + \frac{p_1}{2\pi} \frac{\Gamma}{(m-\mu_1)^2 + \frac{\Gamma^2}{4}} \right) * g_{\Lambda P}(m)$$
$$+ \left(\frac{p_0}{\sqrt{2\pi\sigma^2}} exp\left(\frac{(m-\mu_0+d(\mu_0))^2}{2\sigma^2} \right) + \frac{p_1}{2\pi} \frac{\Gamma}{(m-\mu_1+d(\mu_1))^2 + \frac{\Gamma^2}{4}} \right) * g_{\Sigma^0 p}(m),$$
$$(5.9)$$

where the first and second terms are distribution functions for Λpn and $\Sigma^0 pn$ final states, respectively. The centroid of the distribution for $\Sigma^0 pn$ is shifted by $d(\mu)$ from that for Λpn.

The energy dependence of the shift may change the distribution, but we ignore the effect. Fitting parameters are the same as those used in the previous fitting in Section 5.2.2. In this analysis, the fitting function in Eq.5.9 is also multiplied a acceptance function, $A_{Sig}(m)$,

$$f(m) = f'(m) \cdot A_{Sig}(m). \tag{5.10}$$

The fitting was done with a reasonably good value of $\chi^2/ndf = 15.2/14$, as shown in Fig.5.12. The peak position and width of the Breit-Wigner distribution for Λpn are found to be 2.326 ± 0.004 GeV/c^2 and 0.064 ± 0.008 GeV/c^2, respectively. The peak position does not change but the width becomes narrower due to additional structure caused by $\Sigma^0 pn$ contamination.

5.2.4 Systematic uncertainties of peak position and width

In this section, the systematic uncertainties of peak position and width are discussed. We consider following contents for the systematic uncertainties.

1. Magnetic field strength of the solenoid magnet
   The magnetic field strength of the solenoid magnet was evaluated to be 0.715 T as described in Chapter.3. However, there is uncertainty of the absolute value of the magnetic field strength. We consider that uncertainty as +0.005 T where the reconstructed Λ mass is consistent with that of PDG value. The systematic uncertainties from the magnetic field strength were evaluated as +3 MeV and -4 MeV for mass and width, respectively.

2. Background treatment
   The background subtraction described in Sec.5.2 was performed by using fitted function with the fifth order polynomial function. To evaluate the systematic uncertainty from this, the background subtraction was performed by using observed spectrum. The systematic uncertainties from the background treatment were evaluated as -1 MeV and -2 MeV for mass and width, respectively.

3. Kinematical fit
   To check the kinematical fit effect, we applied the fitting procedure for the spectrum without the kinematical fit. The mass position and width were slightly changed without kinematical refit, namely +1 MeV and +6 MeV for mass and width, respectively. Moreover, the Λp invariant-mass would shift about 1 MeV systematically as shown in Fig.4.19. This shift is added up as systematic uncertainty. We evaluated the systematic

uncertainties form kinematical refit was found to be +1/-1 MeV and +6/-0 MeV for mass and width, respectively.

4. Contamination ratio of the $\Sigma^0 pn$ events
   We consider the systematic error the $\Sigma^0 pn$ ratio within its error described in Sec.5.2.3. From ambiguity of the contamination ratio of the $\Sigma^0 pn$ events was found to be -2 MeV only for the width.

5. Binning of the spectrum
   The different binning spectrum which has bin shifted a half bin size, 10 MeV, was prepared to evaluate the systematic error from binning. The differences of peak position and width were obtained as +3 MeV and +8 MeV in different binning spectrum.

We performed the same fitting procedures for these spectrum, and systematic uncertainties are obtained as listed in Tab.5.4. Each uncertainties are considered as independently on each other. Therefore, the total systematic uncertainty is evaluated as sum of all uncertainties. The peak position and width of the Breit-Wigner distribution including the systematic uncertainties were found to be $2.326 \pm 0.004(stat.)^{+0.007}_{-0.002}(sys.)$ GeV/c^2 and $0.064 \pm 0.008(stat.)^{+0.014}_{-0.007}(sys.)$ GeV/c^2, respectively.

Table 5.4 Systematic uncertainties of peak position and width

	mass (MeV/c^2)	width (MeV/c^2)
Magnetic field strength	+3/-0	+0/-4
Background treatment	+0/-1	+0/-2
Kinematical fit	+1/-1	+6/-0
$\Sigma^0 pn$ ratio	+0/-0	+0/-1
Binning	+3/-0	+8/-0
Total	+7/-2	+14/-7

5.2.5 Fitting for fine $\cos\theta_n^{CM}$ sliced spectra

In order to obtain the behaviours of the structure below and above the $K^- pp$ mass-threshold, we applied the same fitting procedure as that described in the previous section 5.2.3 for the spectra sliced with $\cos\theta_n^{CM}$. For each spectrum, the $N_{\Sigma^0 pn}/N_{\Lambda pn}$ ratio is evaluated, as summarized in Table 5.5. The ratios seem slightly scattered but they are close taking the statistical errors into count. For the fitting, the $N_{\Sigma^0 pn}/N_{\Lambda pn}$ ratios were fixed at the central values listed in Table 5.5.

Also, the acceptance for each $\cos\theta_n^{CM}$ regions were evaluated as shown in Fig.5.13.
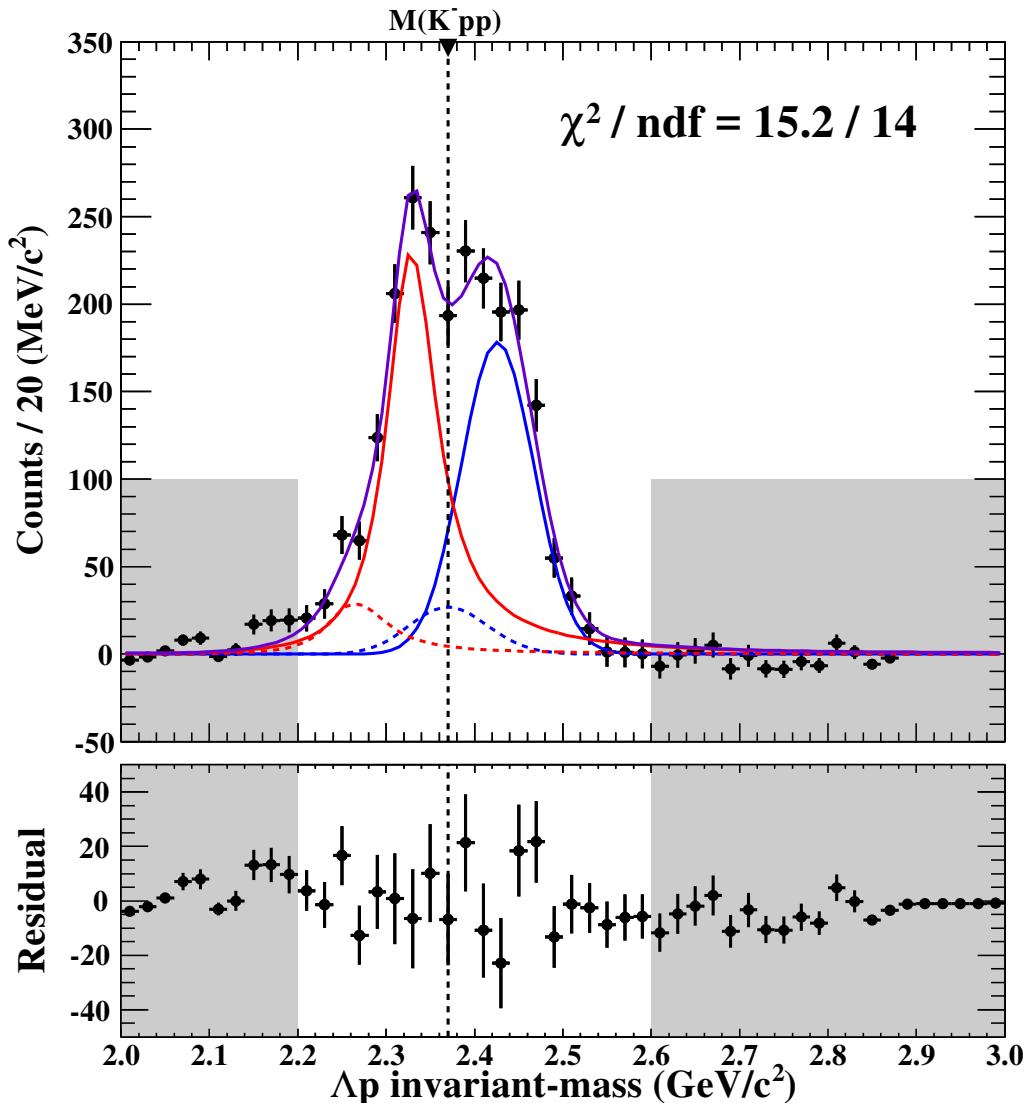
Fig. 5.12 Fitting result of Λp invariant-mass spectrum with Gaussian and Breit-Wigner distributions with mass-resolution convolution including $\Sigma^0 pn$ contamination. The χ^2/ndf of 14.1/19 is the best value in all fitting results. The contributions from Λpn and $\Sigma^0 pn$ final states are indicated by solid and dashed-lines, respectively.

Table 5.5 $\Sigma^0 pn/\Lambda pn$ ratio in each $\cos\theta_n^{CM}$ selection

$\cos\theta_n^{CM}$ region	Ratio (%)		# of events		$\Sigma^0 pn/\Lambda pn$ ratio
	Λpn	$\Sigma^0 pn$	Signal	Background	
0.95 - 1.00	75 ± 3	23 ± 3	1057	296	0.31 ± 0.06
0.90 - 0.95	82 ± 3	15 ± 3	820	220	0.18 ± 0.05
0.85 - 0.90	78 ± 4	20 ± 4	556	208	0.26 ± 0.09
0.80 - 0.85	79 ± 5	18 ± 5	410	204	0.23 ± 0.14
0.75 - 0.80	74 ± 5	24 ± 5	367	208	0.32 ± 0.19
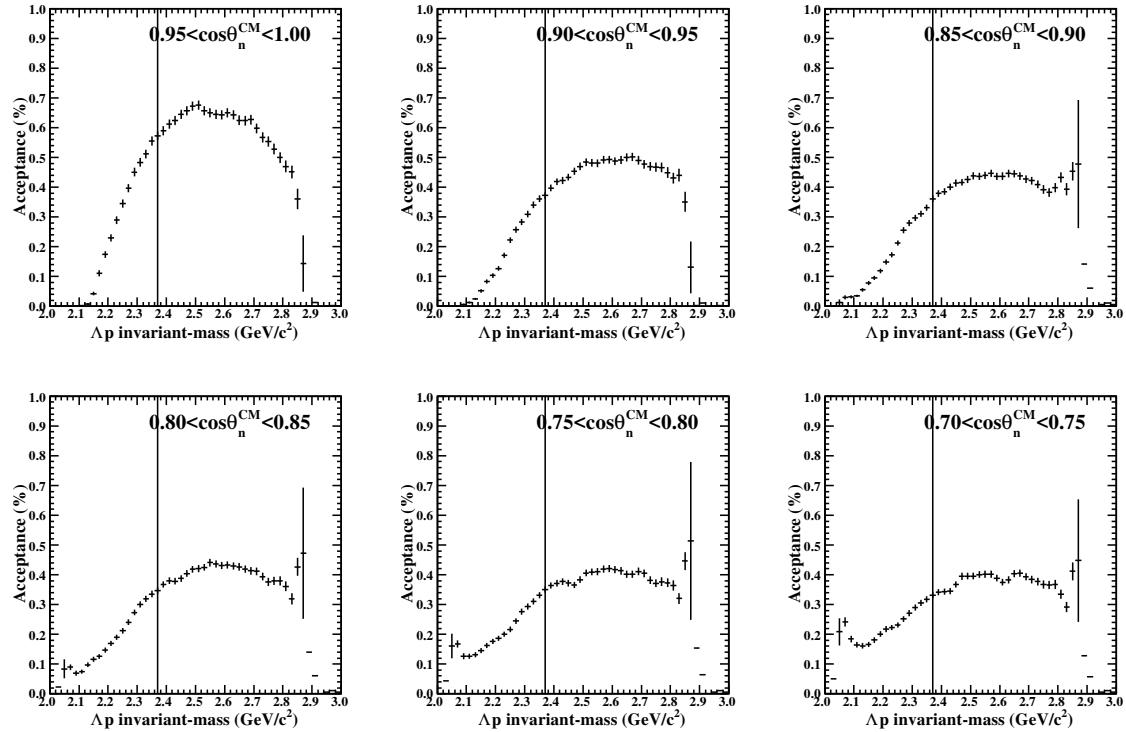
Fig. 5.13 Acceptance of Λp invariant-mass with selecting $\cos\theta_n^{CM}$ region as shown in each figures.

Figs.5.14 - 5.18 show the fitting results for each Λp invariant-mass spectra with $\cos\theta_n^{CM}$ sliced by 0.95 - 1.00, 0.90 - 0.95, 0.85 - 0.90, 0.80 - 0.85, and 0.75 - 0.80, respectively. In the fitting, all 6 parameters of Breit-Wigner and Gaussian were set as free parameters.
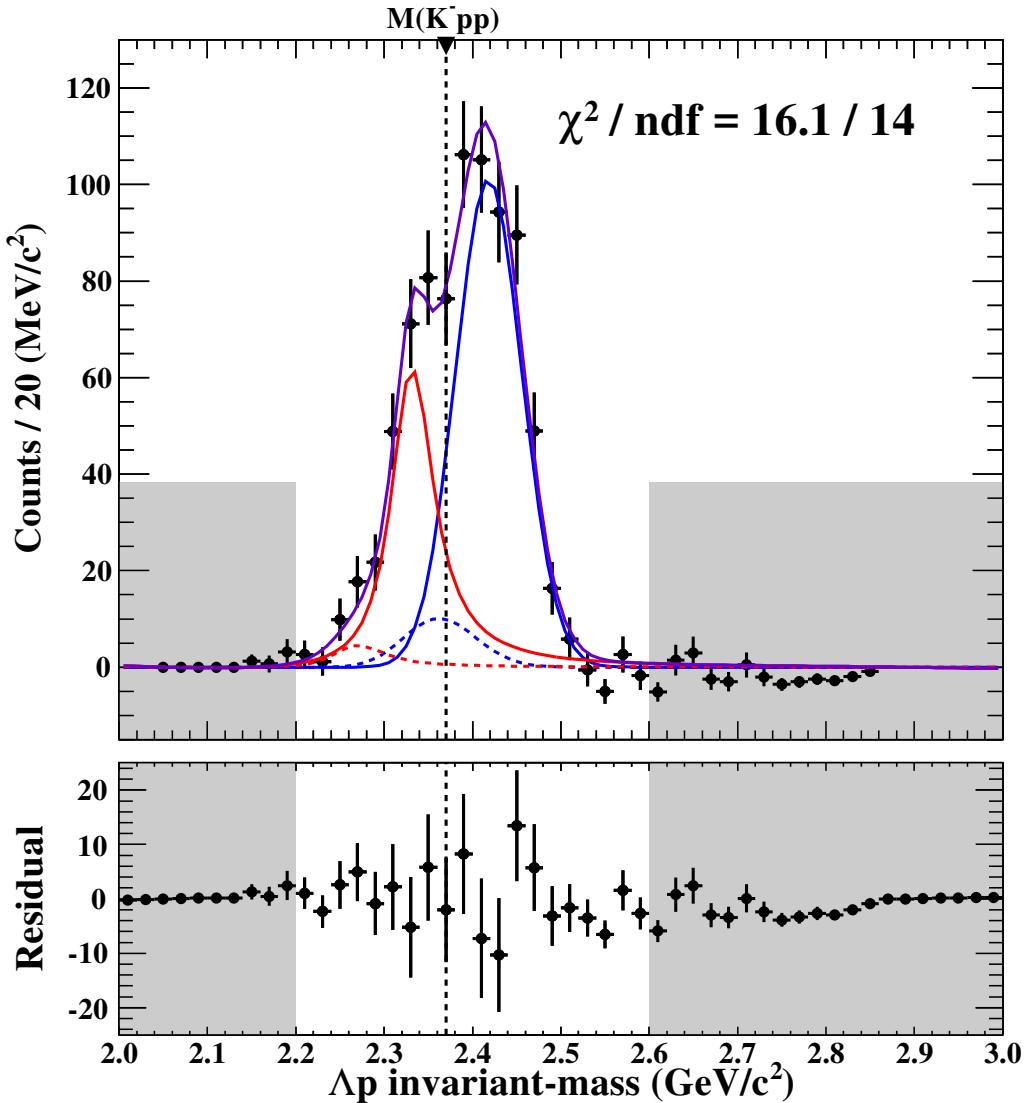
Fig. 5.14 The same figure as Fig.5.12, but $\cos\theta_n^{CM}$ selection is from 0.95 to 1.00.

The positions and widths of the lower (Breit-Wigner) and higher (Gaussian) peaks were plotted in Fig.5.19. Dashed lines indicate fitting results with the constant values for the plots. The fittings were performed with reasonable χ^2/ndf value. The lower peak position does not change as $\cos\theta_n^{CM}$ changes. On the other hand, the higher peak position seems to move to the higher mass as $\cos\theta_n^{CM}$ decreases.
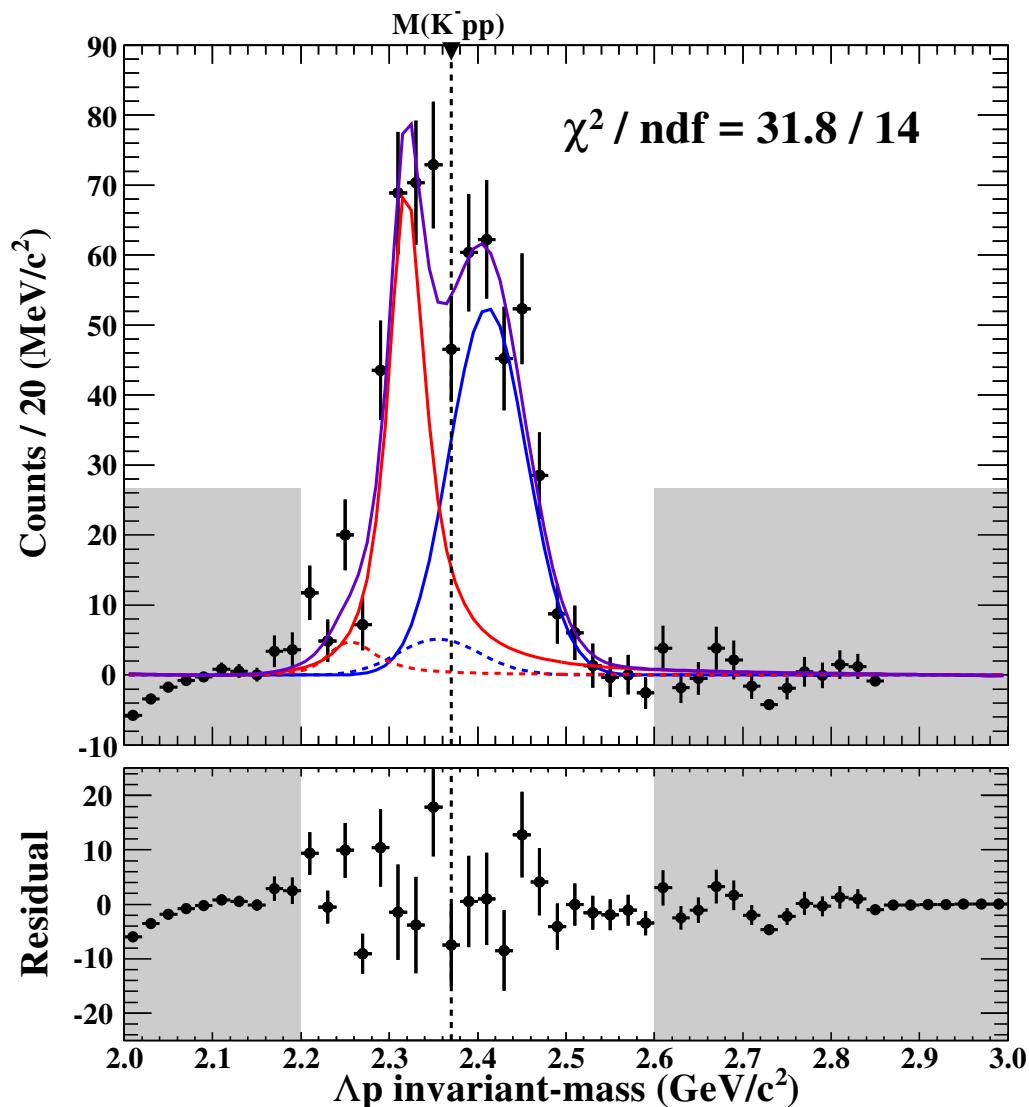
Fig. 5.15 The same figure as Fig.5.12, but $\cos\theta_n^{CM}$ selection is from 0.90 to 0.95.
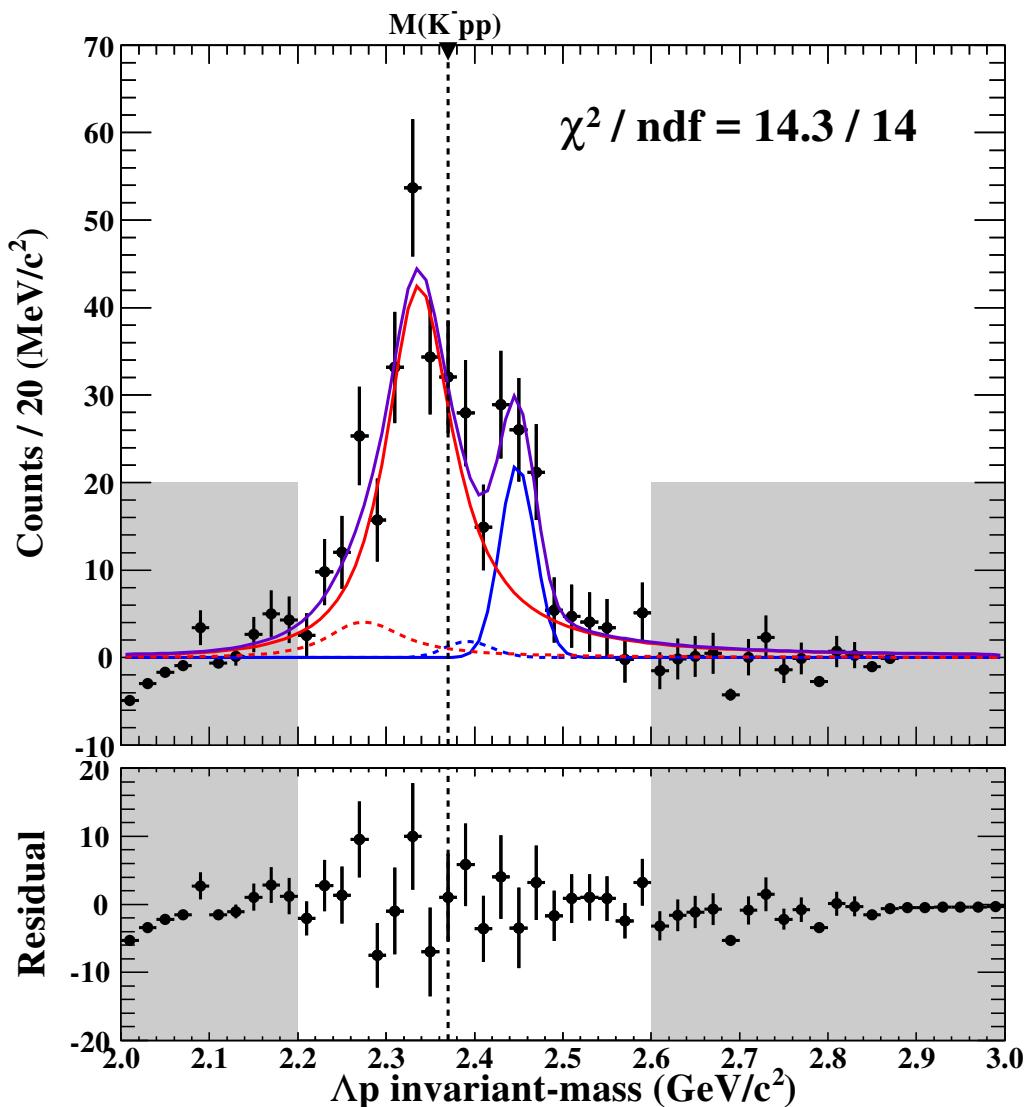
Fig. 5.16 The same figure as Fig.5.12, but $\cos\theta_n^{CM}$ selection is from 0.85 to 0.90.
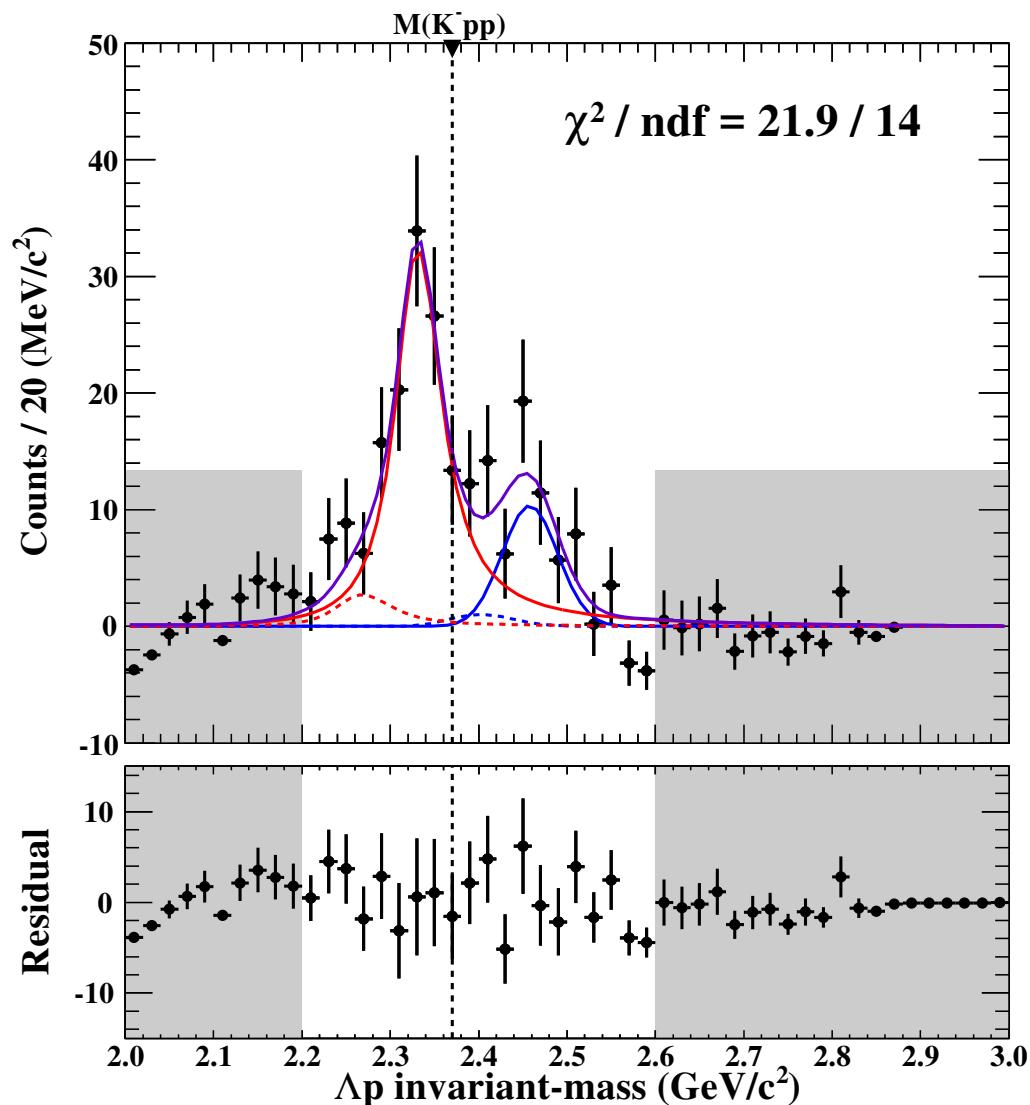
Fig. 5.17 The same figure as Fig.5.12, but $\cos\theta_n^{CM}$ selection is from 0.80 to 0.85.
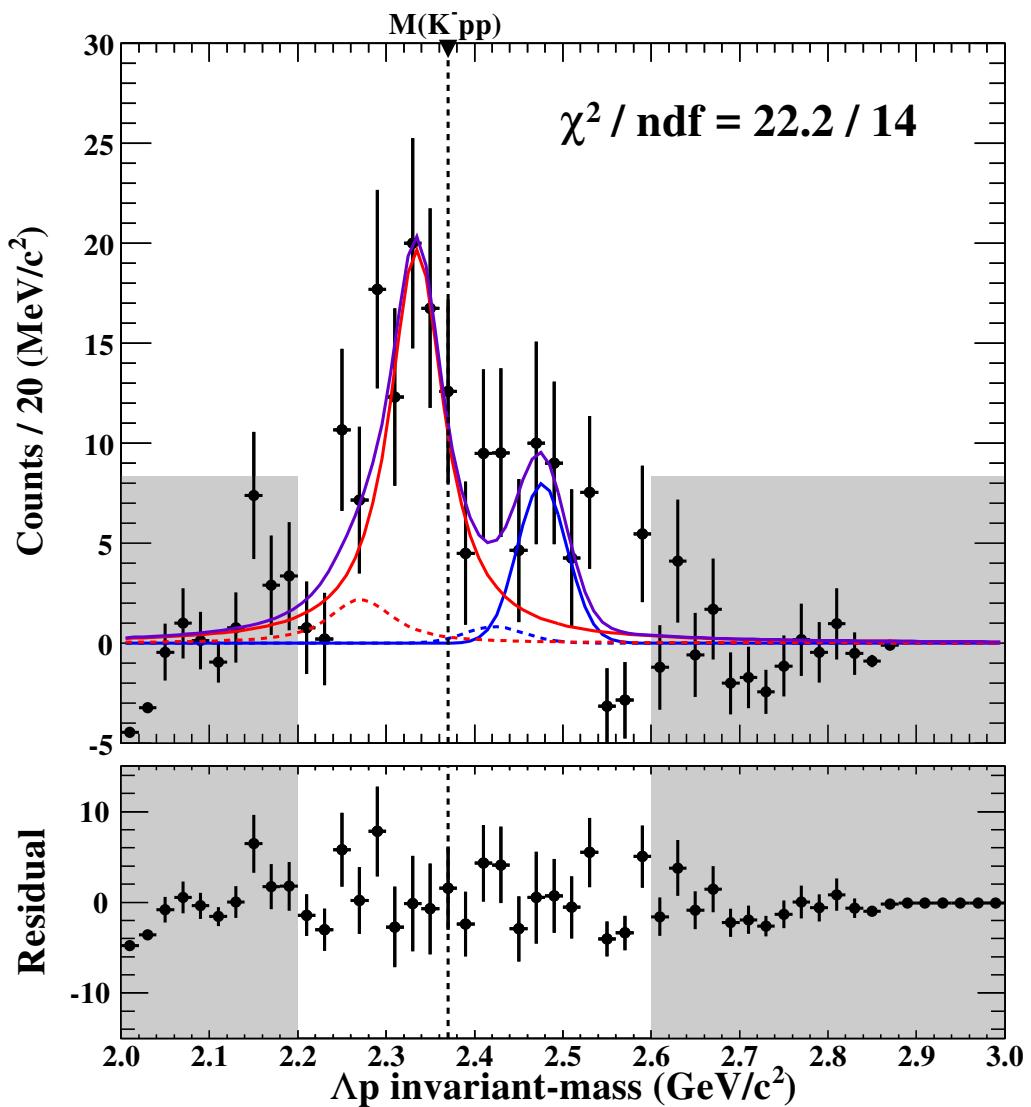
Fig. 5.18 The same figure as Fig.5.12, but $\cos\theta_n^{CM}$ selection is from 0.75 to 0.80.
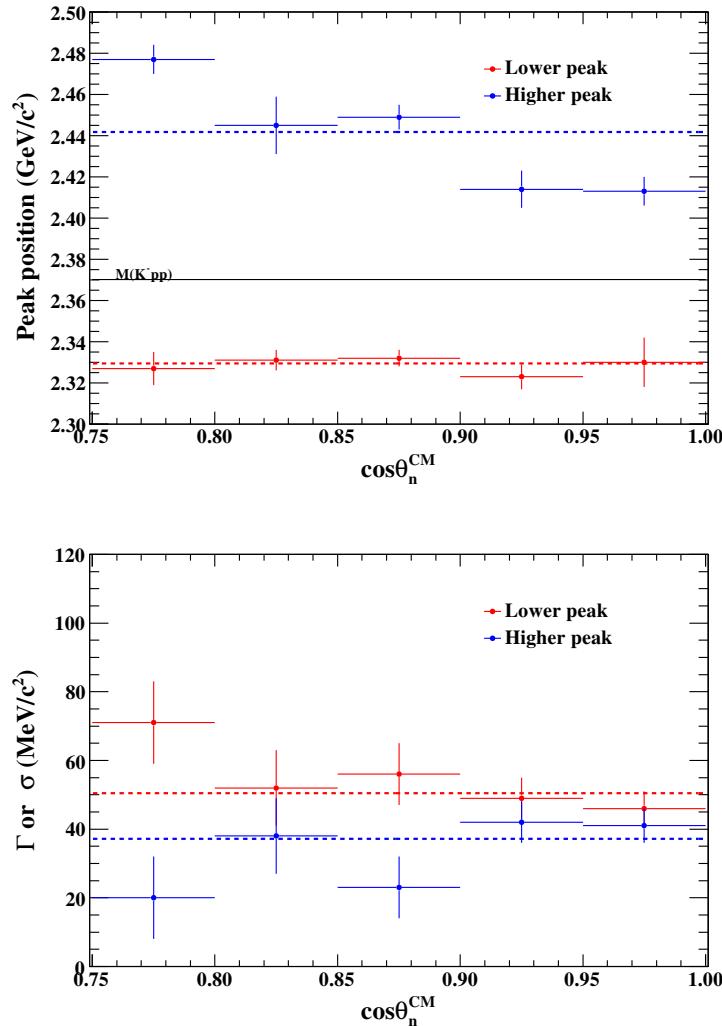
Fig. 5.19 (top)Peak position of the lower and the higher peak structure fitted by using Breit-Wigner and Gaussian distributions, respectively. The dashed lines indicated mean value. (bottom)Width (Γ for Breit-Wigner and σ for Gaussian) of the lower and the higher peak structure. The dashed lines indicated mean value.

5.3   Discussion

5.3.1   Mass position and width of peaks

To explain the fact that higher peak position moves to higher mass as the neutron scattering angle decreases, we consider a two-step reaction as follows.

$$K^- + {}^3\text{He} \rightarrow K^-_{recoil} + n + "p_{spec}p_{spec}", \tag{5.11}$$

$$K^-_{recoil} + "p_{spec}p_{spec}" \rightarrow \Lambda + p, \tag{5.12}$$
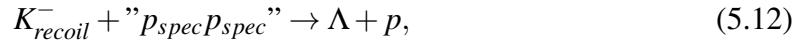
In this reaction, an incident kaon knocks out a neutron in a forward angle. The kaon is recoiled in a backward angle. The recoiled kaon and a spectator proton are denoted as K^-_{recoil} and p_{spec}. In the region above the K^-pp mass-threshold, K^-_{recoil} is expected to be almost an on-shell particle. The first step of the reaction (5.11) is the so-called quasi-free process. The quasi-free peak (M_{QF}) is located at

$$M_{QF} = M_{K^-pp} + \frac{Q^2}{2M_{K^-}}, \tag{5.13}$$

where M_{K^-pp} and M_{K^-} are a sum of K^-pp masses and the K^- mass. The quantity Q is a momentum transfer in the elastic $n(K^-,n)K^-$ scattering. Because Q is denoted as $Q^2 = p_K^2 + p_n^2 - 2p_K p_n \cos\theta_n$, M_{QF} is proportional to $\cos\theta_n$. In a nuclear target, the spectrum is distributed around the QF peak due to Fermi motion of a nucleon bound in the nucleus. M_{QF} calculated by Eq.5.13 is plotted by a dashed line in Fig.5.20. The line is well reproduced observed angular dependence of the peak position.

To confirm that the QF process contributes to the higher peak, a MC simulation was made to compare with the observed spectrum. In the MC simulation, a 2 step process was considered as such a QF process, which is,

$$K^- + n \rightarrow n + K^- \ \ followed \ by \ K^- + p + p \rightarrow \Lambda + p$$

. A spectrum distributed in all 3-body phase space (3ps) was generated to demonstrate a broad contribution. To evaluate the $\cos\theta_n^{CM}$ distribution in each process, the data spectrum was checked again. For 3ps and QF $\cos\theta_n^{CM}$ process, $\cos\theta_n^{CM}$ distribution with selecting invariant-mass of Λp from 2.6 to 3.0 GeV/c^2, and from 2.44 to 2.6 GeV/c^2 regions are used which are shown in Fig.5.21.

In Fig.5.22, Λp invariant-mass spectra in different $\cos\theta_n^{CM}$ regions are shown with MC spectra. The MC simulation well reproduce peak positions of the higher peak structure, as
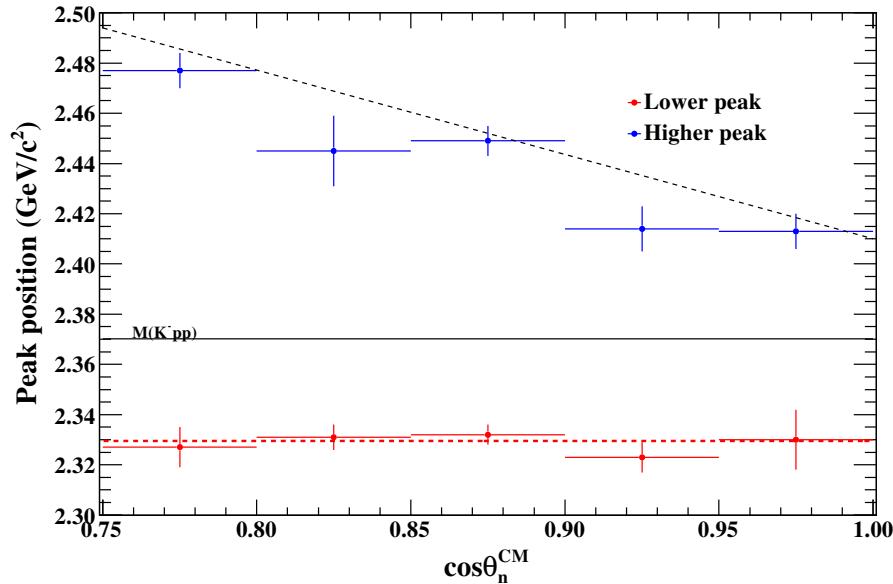
Fig. 5.20 Peak position of the lower and the higher peak structure fitted by using Breit-Wigner and Gaussian distributions, respectively. The black dashed line shows estimated value of the quasi-free peak position by using Eq.5.13.
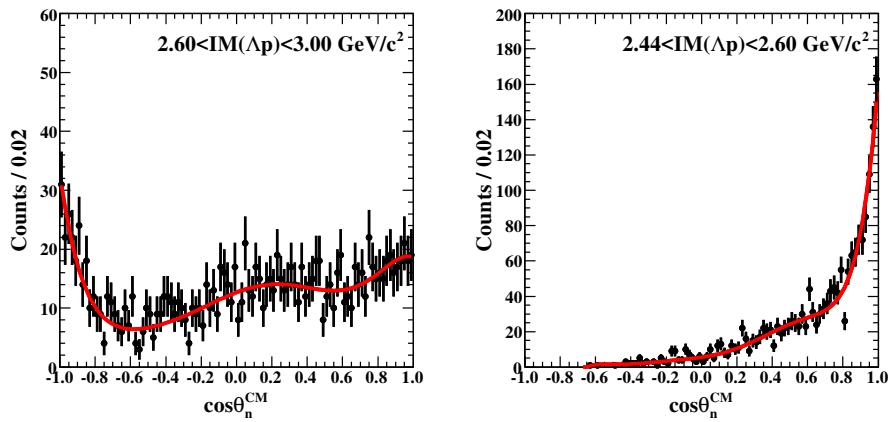

Fig. 5.21 $\cos\theta_n^{CM}$ distributions with (left) $2.6 - 3.0$ GeV/c^2, and (right) $2.44 - 2.6$ GeV/c^2, respectively The red lines show fit results with 7th polynomial function.

considered in the previous section. Also, fitting of Λp invariant-mass is applied with using the MC spectrum. In this fitting, the same routine as described in Sec.5.2.2 was applied. But, only lower peak region (2.2 - 2.37 GeV/c^2) was considered because the higher part has already been reproduced by the MC spectrum.

The fitting result is shown in Fig.5.23. It is demonstrated that the spectrum was well reproduced by a Breit-Wigner and the MC. The mass position and width are found to be 2.341 ± 2 GeV/c^2 and 0.069 ± 5 GeV/c^2, respectively. These values are consistent with previous fitting results, but only peak position slightly moves to the higher mass side. This is because the MC simulation only treats the recoiled kaon as a real (an on-mass shell) particle, which obviously underestimates the contribution of the QF process at around and below the $K^- pp$ mass threshold. As this results, the origin of higher peak can be explain as quasi-free process. The spectrum shape above the $K^- pp$ threshold except for the threshold region, are well explained by the QF process (QF K^- absorbed by pp converted into Λp).

5.3.2   Origin of the lower peak structure

As described in the previous section, the lower peak position is rather stable against the neutron scattering angle. This fact supports that the lower structure is a possible new state with the baryon number of 2 and the strangeness equal to -1. However, we considered some other possibilities below.

Quasi-free Y^* production

We consider a Y^* production followed by a reaction that Y^* collides with a spectator proton and converted into Λ and p.

$$K^- + {}^3\mathrm{He} \rightarrow Y^* + n + p_{spec},$$

$$Y^* + p_{spec} \rightarrow \Lambda + p,$$
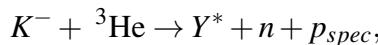
where Y^* represents $\Sigma^0(1385)$ or $\Lambda(1405)$. Among these, $\Sigma^0(1385)$ can be a candidate because the lower peak is already below the $\Lambda(1405)$ production threshold. It is expected that the quasi-free Y^* production peak depends on the neutron scattering angle. Thus, these options can be discarded.

As discussed in the previous section, the observed structure above the $K^- pp$ mass threshold could be explained as the so-called QF $K^- pp \rightarrow \Lambda p$ process. The Quasi-free Y* production process mentioned here may contribute in part to the structure above the $K^- pp$ threshold. In this case, distribution of the Y* production process is expected to be located
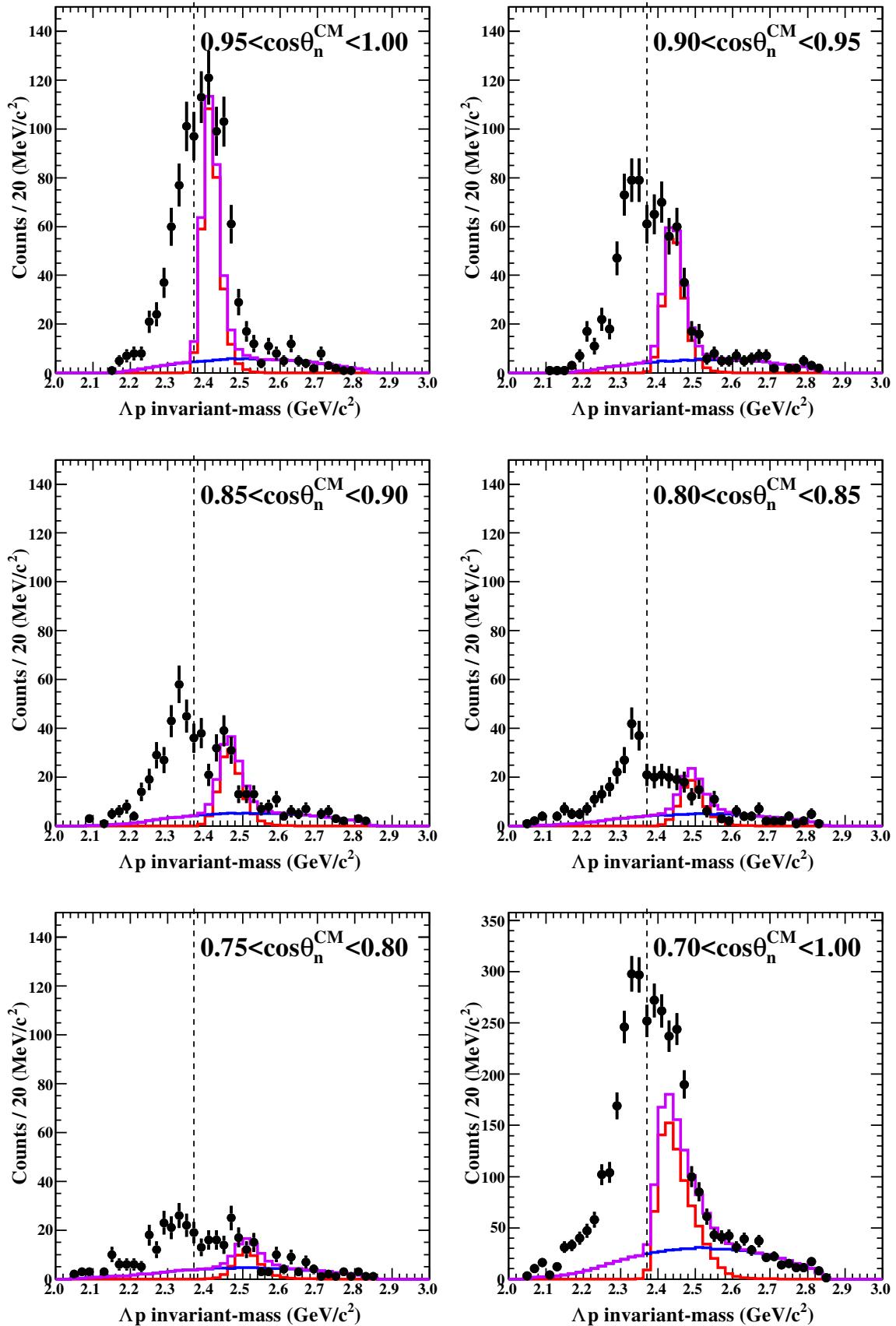
Fig. 5.22 Λp invariant-mass spectra for each $\cos\theta_n^{CM}$ regions. Red, blue and violet spectra show QF, 3ps, and sum of them generated by MC simulation, respectively.
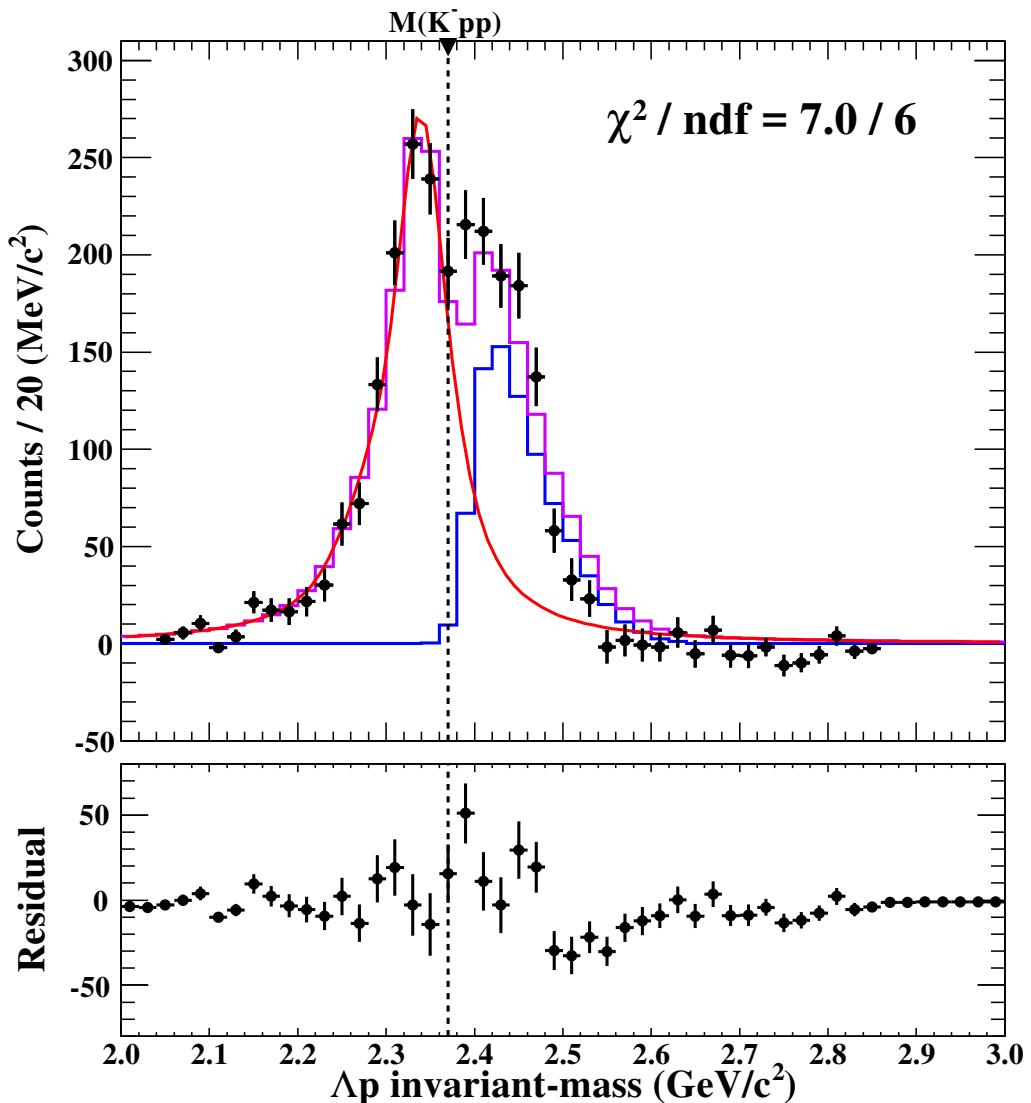
Fig. 5.23 Fitting result of the Λp invariant-mass spectrum. Red line and Blue histogram show the Breit-Wigner function and MC spectrum, respectively. The fitting range is from 2.2 to 2.37 GeV/c^2 and only Breit-Wigner function is modified.

near the K^-pp threshold and move to the higher mass direction as a neutron scattering angle increases [70]. Unfortunately, it is difficult to clearly separate the contribution of the Quasi-free Y* production from the distribution of the QF $K^-pp \to \Lambda p$ process. Furthermore, yields of such Y^* production processes are not be measured. However, we performed a Monte Calro simulation to demonstrate QF Y^* processes. As described in appendix C, the simulated spectra of $\Sigma(1385)$ and $\Lambda(1405)$ can not reproduce the observed peak structure, even though the yield is the same order of that of Λpn final state. This situation, which is the ratio of $\Lambda pn/Y^*pn$ events is approximately 1, would be maximum yield of $\Sigma(1385)$ or $\Lambda(1405)$ production.

We expect to clarify a contribution from the component of the QF Y* production process if we can measure a strength (cross section) of the final $\pi\Sigma n$ ($\pi\Lambda n$) state identifying $\Lambda(1405)$ ($\Sigma(1385)$) production in the $\pi\Sigma$ ($\pi\Lambda$) state. This would be solved in future study.

Threshold effect of the Y^*N threshold

The $\Sigma^0(1385)p$ and $\Lambda(1405)p$ thresholds are located near the lower peak position observed. One may claim that threshold cusps make peak-like structure, although it is unclear if such threshold effects reproduce the observed, large peak-like structure. If such a cusp effect is dominant, the production cross section of $\Sigma^0(1385)$ or $\Lambda(1405)$ would be enhanced toward its production threshold. Further analysis for this problem has to be done in future.

5.3.3 Comparison with the previous experimental results

Because the lower peak is located below the K^-pp mass-threshold, the peak can be considered as the K^-pp bound state. In the other experiment searching for the K^-pp bound state, FINUDA, DISTO or J-PARC E27 group, reported the K^-pp-like structure below about 100 MeV/c^2 from K^-pp mass-threshold. In our observed spectrum, the lower peak is located about 60 MeV/c^2 above from these report. Note that, in the mass region around 100 MeV/c^2, there is no significant peak structure, or the structure can not be observed due to lack of statistics. Anyway, the peak structure was observed below about 40 MeV/c^2 from K^-pp mass-threshold. The most recent result of K^-pp bound state search performed by using KLOE detector reported that there is candidate of the K^-pp bound state decaying into $\Sigma^0 p$ final state at the binding energy and width of 40 MeV and 30 MeV, respectively [71]. But, the statistical significance was only 1 σ for obtained the K^-pp bound state. The result is not sufficient to claim the observation of the K^-pp bound state, however the binding energy is near from our observation. One possibility of the observed peak is exited state of the K^-pp bound state observed in other experiment. Note that the exited state of the K^-pp bound state

is not predicted by any theoretical calculations. However, even if the exited state exists, the relative yield of the exited state should be small compared to ground state. Because, it is natural that S-wave state is much generated than P-wave state with such low momentum transfer. Also, the reaction in the experiment, the $^3\mathrm{He}\,(K^-, \Lambda p)\,n$ reaction, enhanced S-wave contribution due to the small momentum transfer in the reaction. So that, the lower peak is probably not the exited state of the $K^- pp$ bound state. To decide the conclusion, more statistics and measurement of the its spin and parity are desired.

5.3.4   Comparison with theoretical calculations

On the theoretical approach for the $K^- pp$ bound state, there are many claim on its binding energy and width. There are two different approach to calculate this state, one is that the $\bar{K}N$ interaction has energy dependence, and other is that the interaction does not have energy dependence. Assuming the observed peak structure below the $K^- pp$ mass-threshold is $K^- pp$ bound state, the binding energy of about 40 MeV is slightly larger than predicted binding energy from theoretical calculation using energy dependent $\bar{K}N$ interaction model. However, the binding energy is not so large to comparison to the calculation using energy independent $\bar{K}N$ interaction model. From considering that situation, the $\bar{K}N$ interaction should be considered carefully in each calculation.

In the Ref.[70], the spectrum shape of the Λp invariant-mass in the $^3\mathrm{He}(K^-, \Lambda p)n$ reaction by chiral unitary approach was reported. They obtained double peak structure around the $K^- pp$ mass-threshold which is quite similar situation as our Λp invariant-mass spectrum. In the paper, one of the peak located above the $K^- pp$ threshold comes from an uncorrelated $\Lambda(1405)p$ system which has the same behavior on the neutron emission angle as obtained in our result. On the other hand, the peak located below the $K^- pp$ threshold is generated by $K^- pp$ bound state. The peak position in the report looks higher than that of our result. So that, if the peak located below the $K^- pp$ threshold observed in our result is the $K^- pp$ bound state, the interaction between anti-kaon and nucleus looks stronger than that predicted by their interaction model.

Chapter 6

Conclusion

In this thesis, the Λp invariant-mass spectrum in the ${}^3\mathrm{He}(K^-, \Lambda p)n$ reaction was analyzed to study for a kaon bound nuclear state, $K^- pp$ bound state, at $p_{K^-} = 1.0\ GeV/c$. The clear peak structure was observed in the Λp invariant-mass spectrum around the $K^- pp$ mass-threshold. The peak structure was localized in $\cos\theta_n^{CM}$ above 0.7 region, namely in the forward neutron emission region. This peak structure was fitted with single and double distribution, and the structure could be considered as double peak structures. The double peaks located above and below the $K^- pp$ mass-threshold were fitted with Gaussian and Breit-Wigner distribution, respectively. By fitting for fine $\cos\theta_n^{CM}$ sliced spectra, the mass position of the lower peak did not depend on $\cos\theta_n^{CM}$, while that of the higher peak clearly depended on $\cos\theta_n^{CM}$. So that, the origin of the higher peak structure could be considered as quasi-free $K^- N$ reaction followed by Λp conversion process. To confirm this, MC simulation was applied to reproduce the higher peak structure. The simple two-step process successfully represented the higher component, and the fitting result for lower peak did not change by this study.

On the other hand, the origin of the lower peak was discussed to identify the peak structure. The lower peak which is located below the $K^- pp$ mass-threshold could be the $K^- pp$ bound state. The peak position and width of the lower peak was found to be $2.326 \pm 0.004(stat.)_{-0.002}^{+0.007}(sys.)$ GeV/c^2 and $0.064 \pm 0.008(stat.)_{-0.007}^{+0.014}(sys.)$ GeV/c^2, respectively. This structrue can not be explained by any Y^* production. Threfore, the origion of the peak structrue could be the $K^- pp$ bound state. However, to understand completely the observed peak structure, the theoretical calculation is strongly desired.

References

[1] T Yamazaki, R S Hayano, K Itahashi, K Oyama, A Gillitzer, H Gilg, M Knülle, M Münch, P Kienle, W Schott, W Weise, H Geissel, N Iwasa, G Münzenberg, S Hirenzaki, and H Toki. Effective pion mass in the nuclear medium deduced from deeply bound pionic states in 207Pb. *Physics Letters B*, 418(3-4):246–251, February 1998.

[2] H Gilg, A Gillitzer, M Knülle, M Münch, W Schott, P Kienle, K Itahashi, K Oyama, R Hayano, H Geissel, N Iwasa, G Münzenberg, and T Yamazaki. Deeply bound π- states in 207Pb formed in the 208Pb(d,3He) reaction. I.2003Experimental method and results. *Phys. Rev. C*, 62(2):025201, July 2000.

[3] K Itahashi, K Oyama, R Hayano, H Gilg, A Gillitzer, M Knülle, M Münch, W Schott, P Kienle, H Geissel, N Iwasa, G Münzenberg, S Hirenzaki, H Toki, and T Yamazaki. Deeply bound π- states in 207Pb formed in the 208Pb(d,3He) reaction. II.2003Deduced binding energies and widths and the pion-nucleus interaction. *Phys. Rev. C*, 62(2):025202, July 2000.

[4] K Suzuki, M Fujita, H Geissel, H Gilg, A Gillitzer, R Hayano, S Hirenzaki, K Itahashi, M Iwasaki, P Kienle, M Matos, G Münzenberg, T Ohtsubo, M Sato, M Shindo, T Suzuki, H Weick, M Winkler, T Yamazaki, and T Yoneyama. Precision Spectroscopy of Pionic 1s States of Sn Nuclei and Evidence for Partial Restoration of Chiral Symmetry in the Nuclear Medium. *Physical Review Letters*, 92(7):072302, February 2004.

[5] T Waas and W Weise. S-wave interactions of 46 and η mesons in nuclear matter. *Nuclear Physics A*, 625(1-2):287–306, October 1997.

[6] T Waas, N Kaiser, and W Weise. Effective kaon masses in dense nuclear and neutron matter. *Physics Letters B*, 379(1-4):34–38, June 1996.

[7] Alan D Martin. Kaon - Nucleon Parameters. *Nucl.Phys.*, B179:33, 1981.

[8] M Iwasaki, R Hayano, T Ito, S Nakamura, T Terada, D Gill, L Lee, A Olin, M Salomon, S Yen, K Bartlett, G Beer, G Mason, G Trayling, H Outa, T Taniguchi, Y Yamashita, and R Seki. Observation of Kaonic Hydrogen $K\alpha$ X Rays. *Physical Review Letters*, 78(16):3067–3069, April 1997.

[9] G Beer, A Bragadireanu, M Cargnelli, C Curceanu-Petrascu, J P Egger, H Fuhrmann, C Guaraldo, M Iliescu, T Ishiwatari, K Itahashi, M Iwasaki, P Kienle, T Koike, B Lauss, V Lucherini, L Ludhova, J Marton, F Mulhauser, T Ponta, L Schaller, R Seki, D Sirghi, F Sirghi, J Zmeskal, and DEAR Collaboration. Measurement of the Kaonic Hydrogen X-Ray Spectrum. *Physical Review Letters*, 94(21):212302, June 2005.

[10] M Bazzi, G Beer, L Bombelli, A M Bragadireanu, M Cargnelli, G Corradi, A d02BCUffizi, C Fiorini, T Frizzi, and F Ghio. A new measurement of kaonic hydrogen X-rays. *Physics Letters B*, 704(3):113–117, 2011.

[11] Yoshinori Akaishi and Toshimitsu Yamazaki. Nuclear K. *Phys.Rev.C*, $65(4)$: $044005, April 2002$.

[12] Tetsuo Hyodo and Wolfram Weise. Effective K00AFN interaction based on chiral SU(3) dynamics. *Phys. Rev. C*, 77(3):035204, March 2008.

[13] K Moriya et al. Measurement of the $\Sigma\pi$ photoproduction line shapes near the $\Lambda(1405)$. *Phys. Rev*, C87(3):035206, 2013.

[14] K Moriya, R A Schumacher, K P Adhikari, D Adikaram, M Aghasyan, M J Amaryan, M D Anderson, S Anefalos Pereira, H Avakian, J Ball, N A Baltzell, M Battaglieri, V Batourine, I Bedlinskiy, M Bellis, R P Bennett, A S Biselli, J Bono, S Boiarinov, W J Briscoe, W K Brooks, V D Burkert, D S Carman, A Celentano, S Chandavar, P Collins, M Contalbrigo, O Cortes, V Crede, A D'Angelo, N Dashyan, R De Vita, E De Sanctis, A Deur, B Dey, C Djalali, D Doughty, M Dugger, R Dupre, H Egiyan, L El Fassi, P Eugenio, G Fedotov, S Fegan, R Fersch, J A Fleming, N Gevorgyan, G P Gilfoyle, K L Giovanetti, F X Girod, J T Goetz, W Gohn, E Golovatch, R W Gothe, K A Griffioen, M Guidal, N Guler, L Guo, H Hakobyan, C Hanretty, D Heddle, K Hicks, D Ho, M Holtrop, Y Ilieva, D G Ireland, B S Ishkhanov, E L Isupov, H S Jo, K Joo, D Keller, M Khandaker, A Klein, F J Klein, S Koirala, A Kubarovsky, V Kubarovsky, S V Kuleshov, S Lewis, K Livingston, H Y Lu, I J D MacGregor, D Martinez, M Mayer, M McCracken, B McKinnon, M D Mestayer, C A Meyer, T Mineeva, M Mirazita, V Mokeev, R A Montgomery, H Moutarde, E Munevar, C Munoz-Camacho, P Nadel-Turonski, R Nasseripour, C S Nepali, S Niccolai, G Niculescu, I Niculescu, M Osipenko, A I Ostrovidov, L L Pappalardo, R Paremuzyan, K Park, S Park, E Pasyuk, E Phelps, J J Phillips, S Pisano, O Pogorelko, S Pozdniakov, J W Price, S Procureur, D Protopopescu, A J R Puckett, B A Raue, D Rimal, M Ripani, B G Ritchie, G Rosner, P Rossi, F Sabatié, M S Saini, C Salgado, D Schott, E Seder, H Seraydaryan, Y G Sharabian, G D Smith, D I Sober, D Sokhan, S Stepanyan, P Stoler, S Strauch, M Taiuti, W Tang, C E Taylor, S Taylor, Y Tian, S Tkachenko, M Ungaro, B Vernarsky, M F Vineyard, H Voskanyan, E Voutier, N K Walford, D P Watts, L B Weinstein, M Williams, M H Wood, N Zachariou, L Zana, J Zhang, Z W Zhao, I Zonta, and CLAS Collaboration. Differential photoproduction cross sections of the $\Sigma^0(1385), \Lambda(1405)$, and $\Lambda(1520)$. *Phys. Rev. C*, 88(4):045201, October 2013.

[15] M Niiyama, H Fujimura, D Ahn, J Ahn, S Ajimura, H Bhang, T Chang, W Chang, J Chen, S Daté, S Fukui, H Funahashi, K Hicks, K Horie, T Hotta, K Imai, T Ishikawa, Y Kato, K Kino, H Kohri, S Makino, T Matsumura, T Mibe, K Miwa, M Miyabe, N Muramatsu, M Nakamura, T Nakano, Y Nakatsugawa, Y Ohashi, D Oshuev, J Parker, N Saito, T Sawada, Y Sugaya, M Sumihama, J Tang, M Uchida, C Wang, T Yorita, and M Yosoi. Photoproduction of $\Lambda(1405)$ and $\Sigma0(1385)$ on the proton at Eγ=1.5-2.4 GeV. *Phys. Rev. C*, 78(3):035202, September 2008.

[16] I Zychor, M B cher, M Hartmann, A Kacharava, I Keshelashvili, A Khoukaz, V Kleber, V Koptev, Y Maeda, T Mersmann, S Mikirtychiants, R Schleichert, H StrE490er,

Yu Valdau, and C Wilkin. Lineshape of the [Lambda](1405) hyperon measured through its [Sigma]0[pi]0 decay. *Physics Letters B*, 660(3):167–171, 2008.

[17] G Agakishiev, A Balanda, D Belver, A Belyaev, J C Berger-Chen, A Blanco, M Böhmer, J L Boyard, P Cabanelas, E Castro, S Chernenko, T Christ, M Destefanis, F Dohrmann, A Dybczak, E Epple, L Fabbietti, O Fateev, P Finocchiaro, P Fonte, J Friese, I Frohlich, T Galatyuk, J A Garzon, R Gernhäuser, C Gilardi, M Golubeva, D Gonzalez-Diaz, F Guber, M Gumberidze, T Heinz, T Hennino, R Holzmann, A Ierusalimov, I Iori, A Ivashkin, M Jurkovic, B Kämpfer, K Kanaki, T Karavicheva, I Koenig, W Koenig, B W Kolb, R Kotte, A Krasa, F Krizek, R Krücken, H Kuc, W Kuhn, A Kugler, A Kurepin, R Lalik, S Lang, J S Lange, K Lapidus, T Liu, L Lopes, M Lorenz, L Maier, A Mangiarotti, J Markert, V Metag, B Michalska, J Michel, E Moriniere, J Mousa, C Müntz, R Münzer, L Naumann, J Otwinowski, Y C Pachmayer, M Palka, Y Parpottas, V Pechenov, O Pechenova, J Pietraszko, W Przygoda, B Ramstein, A Reshetin, A Rustamov, A Sadovsky, P Salabura, A Schmah, E Schwab, J Siebenson, Yu G Sobolev, S Spataro, B Spruck, H Ströbele, J Stroth, C Sturm, A Tarantola, K Teilab, P Tlusty, M Traxler, R Trebacz, H Tsertos, V Wagner, M Weber, C Wendisch, J Wüstenfeld, S Yurevich, Y Zanevsky, and HADES Collaboration. Baryonic resonances close to the K[over 00AF]N threshold: The case of Λ(1405) in pp collisions. *Phys. Rev. C*, 87(2):025201, February 2013.

[18] Hiroyuki Noumi et al. . *proposal of J-PARC E31*.

[19] C J Batty, E Friedman, and A Gal. Strong interaction physics from hadronic atoms. 287(5):385–445, 1997.

[20] S Hirenzaki, Y Okumura, H Toki, E Oset, and A Ramos. Chiral unitary model for the kaonic atom. *Phys. Rev. C*, 61(5):055205, April 2000.

[21] Y Nogami. Possible existence of NN bound states. *Physics Letters*, 7(4):288–289, December 1963.

[22] R H Dalitz and S F Tuan. A possible resonant state in pion-hyperon scattering. *Physical Review Letters*, 2:425–428, 1959.

[23] S Wycech. On possibilities of narrow nuclear states of K. *Nuclear Physics A*, 450:399c–402c, 1986.

[24] T Yamazaki and Y Akaishi. (K-,[pi]-) production of nuclear bound states in proton-rich systems via [Lambda]* doorways. *Physics Letters B*, 535(1-4):70–76, 2002.

[25] Toshimitsu Yamazaki, Akinobu Dote, and Yoshinori Akaishi. Invariant-mass spectroscopy for condensed single- and double-46 nuclear clusters to be formed as residues in relativistic heavy-ion collisions. *Physics Letters B*, 587(3-4):167–174, May 2004.

[26] T Suzuki, H Bhang, G Franklin, K Gomikawa, RS Hayano, T Hayashi, K Ishikawa, S Ishimoto, K Itahashi, and M Iwasaki. Discovery of a strange tribaryon S0 (3115) in 4He (stopped K-, p) reaction. *Physics Letters B*, 597(3-4):263–269, 2004.

[27] M Sato, H Bhang, J Chiba, Seonho Choi, Y Fukuda, T Hanaki, RS Hayano, M Iio, T Ishikawa, S Ishimoto, T Ishiwatari, K Itahashi, M Iwai, M Iwasaki, P Kienle, JH Kim, Y Matsuda, H Ohnishi, S Okada, H Outa, S Suzuki, T Suzuki, D Tomono, E Widmann, T Yamazaki, and H Yim. Search for strange tribaryon states in the inclusive 4He() reaction. *Physics Letters B*, 659(1-2):107–112, 2008.

[28] H Yim, H Bhang, J Chiba, Seonho Choi, Y Fukuda, T Hanaki, R S Hayano, M Iio, T Ishikawa, S Ishimoto, T Ishiwatari, K Itahashi, M Iwai, M Iwasaki, P Kienle, J H Kim, Y Matsuda, H Ohnishi, S Okada, H Outa, M Sato, S Suzuki, T Suzuki, D Tomono, E Widmann, and T Yamazaki. Search for strange tribaryons in the reaction. *Physics Letters B*, 688(1):43–49, April 2010.

[29] T Suzuki, M Iio, K Itahashi, M Iwasaki, Y Matsuda, H Ohnishi, S Okada, H Outa, D Tomono, T Yamazaki, H Bhang, S Choi, J H Kim, H Yim, J Chiba, T Hanaki, Y Fukuda, M Sato, R S Hayano, T Ishikawa, S Ishimoto, M Iwai, S Suzuki, T Ishiwatari, P Kienle, and E Widmann. YN CORRELATIONS FROM THE STOPPED K REACTION ON 4He. *Modern Physics Letters A*, 23(27n30):2520–2523, September 2008.

[30] Tadafumi Kishimoto. Kaonic Nuclei Excited by the (K-,N) Reaction. *Physical Review Letters*, 83(23):4701–4704, December 1999.

[31] T Kishimoto, T Hayakawa, S Ajimura, S Minami, A Sakaguchi, Y Shimizu, RE Chrien, M May, P Pile, A Rusek, R Sutter, H Noumi, H Tamura, M Ukai, Y Miura, and K Tanida. Kaonic nuclei probed by the in-flight (K,n) reaction. *Nuclear Physics A*, 754:383–390, 2005.

[32] T Kishimoto, T Hayakawa, S Ajimura, F Khanam, T Itabashi, K Matsuoka, S Minami, Y Mitoma, A Sakaguchi, Y Shimizu, K Terai, R E Chrien, P Pile, H Noumi, M Sekimoto, H Takahashi, T Fukuda, W Imoto, and Y Mizoi. Kaon-Nucleus Interaction Studied through the In-Flight (K-,N) Reaction. *Progress of Theoretical Physics*, 118(1):181–186, July 2007.

[33] A Ramos, V K Magas, J Yamagata-Sekihara, S Hirenzaki, and E Oset. The (K, p) reaction on nuclei with in-flight kaons. *Nuclear Physics A*, 835(1):382–385, 2010.

[34] M Agnello, G Beer, L Benussi, M Bertani, S Bianco, E Botta, T Bressani, L Busso, D Calvo, P Camerini, P Cerello, B Dalena, F De Mori, G D'erasmo, D Di Santo, F Fabbri, D Faso, A Feliciello, A Filippi, V Filippini, E Fiore, H Fujioka, P Gianotti, N Grion, V Lucherini, S Marcello, T Maruta, N Mirfakhrai, O Morra, T Nagae, A Olin, H Outa, E Pace, M Palomba, A Pantaleo, A Panzarasa, V Paticchio, S Piano, F Pompili, R Rui, G Simonetti, H So, S Tomassini, A Toyoda, R Wheadon, A Zenoni, and FINUDA Collaboration. Evidence for a Kaon-Bound State $K-pp$ Produced in $K-$ Absorption Reactions at Rest. *Physical Review Letters*, 94(21):212303, June 2005.

[35] V Magas, E Oset, A Ramos, and H Toki. Critical view on the deeply bound K-pp system. *Phys. Rev. C*, 74(2):025206, August 2006.

[36] Grishma Mehta Pandejee, N J Upadhyay, and B K Jain. K^- $absorption at rest in nuclei followed by p\Lambda$ emission. *Physical Review C*, 82(3):034608, 2010.

[37] M Agnello, L Benussi, M Bertani, H C Bhang, G Bonomi, E Botta, M Bregant, T Bressani, S Bufalino, L Busso, D Calvo, P Camerini, B Dalena, F De Mori, G D02BCErasmo, F L Fabbri, A Feliciello, A Filippi, E M Fiore, A Fontana, H Fujioka, P Genova, P Gianotti, N Grion, V Lucherini, S Marcello, N Mirfakhrai, F Moia, P Montagna, O Morra, T Nagae, H Outa, A Pantaleo, V Paticchio, S Piano, R Rui, G Simonetti, R Wheadon, and A Zenoni. Results on Λp emission from absorption at rest on light nuclei. *Nuclear Physics A*, 914:310–314, September 2013.

[38] Toshimitsu Yamazaki and Yoshinori Akaishi. Basic K [over00AF] nuclear cluster, $K^- pp, and its enhanced formation in the p + p ß K^+ + X reaction. Physical Review C, 76(4) : 045201, 2007.$

[39] T Yamazaki, others, R Dressler, R Dressler, M. Dzemidzic, M. Dzemidzic, J Cl Faivre, J Cl Faivre, L Ferrero, L Ferrero, J Foryciarz, J Foryciarz, I Frohlich, I Frohlich, V Frolov, V Frolov, R Garfagnini, R Garfagnini, A Grasso, A Grasso, S Heinz, S Heinz, W W Jacobs, W W Jacobs, W Kuhn, W Kuhn, A Maggiora, A Maggiora, D Panzieri, D Panzieri, H W Pfaff, H W Pfaff, G Pontecorvo, G Pontecorvo, A Popov, A Popov, J Ritman, J Ritman, P Salabura, P Salabura, S Sosio, S Sosio, V Tchalyshev, V Tchalyshev, S E Vigdor, and S E Vigdor. Indication of a deeply bound compact K-pp state formed in the pp -> p Lambda K+ reaction at 2.85 GeV. *Physical Review Letters*, 104(13):132502, 2010.

[40] P Kienle, M Maggiora, K Suzuki, T Yamazaki, M Alexeev, F Balestra, Y Bedfer, R Bertini, L C Bland, A Brenschede, F Brochard, M P Bussa, M Chiosso, Seonho Choi, M L Colantoni, R Dressler, M. Dzemidzic, J Cl Faivre, A Ferrero, L Ferrero, J Foryciarz, I Frohlich, V Frolov, R Garfagnini, A Grasso, S Heinz, W W Jacobs, W Kuhn, A Maggiora, D Panzieri, H W Pfaff, G Pontecorvo, A Popov, J Ritman, P Salabura, V Tchalyshev, F Tosello, S E Vigdor, and G Zosi. Formation of the S = -1 resonance X(2265) in the reaction pp → X+K+ at 2.50 and 2.85 GeV. *The European Physical Journal A*, 48(12):183, December 2012.

[41] A Sibirtsev. Internal nuclear momentum and subthreshold kaon production. *Physics Letters B*, 359(1-2):29–32, October 1995.

[42] S Abd El-Samad, M Abdel-Bary, K Brinkmann, H Clement, J Dietrich, E Dorochkevitch, S Dshemuchadse, K Ehrhardt, A Erhardt, W Eyrich, C Fanara, D Filges, A Filippi, H Freiesleben, M Fritsch, W Gast, J Georgi, A Gillitzer, J Gottwald, J Hauffe, D Hesselbarth, H Jäger, B Jakob, R Jäkel, L Karsch, K Kilian, H Koch, M Krapp, J Kress, E Kuhlmann, A Lehmann, S Marcello, S Marwinski, S Mauro, A Metzger, W Meyer, P Michel, K Möller, H Mörtel, H P Morsch, L Naumann, N Paul, L Pinna, C Pizzolotto, C Plettner, S Reimann, M Richter, J Ritman, E Roderburg, A Schamlott, P Schönmeier, M Schulte-Wissermann, W Schroeder, T Sefzick, M Steinke, F Stinzing, G Sun, A Teufel, W Ullrich, J Wächter, G J Wagner, M Wagner, R Wenzel, A Wilms, P Wintz, S Wirth, P Wustner, and P Zupranski. Influence of -resonances on hyperon production in the channel at 2.95, 3.20 and 3.30 GeV/c beam momentum. *Physics Letters B*, 688(2-3):142–149, May 2010.

[43] A O Tokiyasu, M Niiyama, J D Parker, D S Ahn, J K Ahn, et al. Search for $K^- pp$ bound state via $\gamma d \to K^+ \pi^- X$ reaction at $E_\gamma = 1.5 - 2.4$ GeV. *Physics Letters B*, 728:616–621, January 2014.

[44] L Fabbietti, G Agakishiev, C Behnke, D Belver, A Belyaev, J C Berger-Chen, A Blanco, C Blume, M Böhmer, and P Cabanelas. pK+ Λ final state: towards the extraction of the ppK contribution. *Nuclear Physics A*, 914:60–68, 2013.

[45] T Nagae et al. proposal of J-PARC E27. *proposal of J-PARC E27.*

[46] Y. Ichikawa et al. Observation of the K^-pp-like structure in the $d(\pi^+, K^-)$ reaction at 1.69 GeV/c. *PTEP*, page 021D01, February 2015.

[47] T. Hashimoto et al. Search for the deeply bound K^-pp state from the semi-inclusive forward-neutron spectrum in the in-flight K^- reaction on helium-3. *PTEP*, page 061D01, February 2015.

[48] Y. Sada et al. Structure near the $K^- + p + p$ threshold in the in-flight ${}^3\text{He}(K^-, \Lambda p)n$ reaction. *PTEP*, page 051D01, February 2016.

[49] Avraham Gal. Recent studies of kaonic atoms and nuclear clusters. *Nuclear Physics A*, 914:270–279, 2013.

[50] N Barnea, A Gal, and E Z Liverts. Realistic calculations of , , and quasibound states. *Physics Letters B*, 712(1-2):132–137, May 2012.

[51] Akinobu Dote, Tetsuo Hyodo, and Wolfram Weise. Variational calculation of the ppK$^-$ $system based on chiral SU(3) dynamics. Physical Review C, 79(1): 014003, 2009.$

[52] Y Ikeda, H Kamano, and T Sato. Energy Dependence of FormulaN Interactions and Resonance Pole of Strange Dibaryons. *Progress of Theoretical Physics*, 124(3):533–539, September 2010.

[53] N Shevchenko, A Gal, and J Mareš. Faddeev Calculation of a K-pp Quasibound State. *Physical Review Letters*, 98(8):082301, February 2007.

[54] N V Shevchenko, A Gal, J Mareš, and J Révai. K [over00AF] NN quasibound state and the K [over00AF] N interaction: Coupled-channels Faddeev calculations of the K [over00AF] NN-πΣN system. *Physical Review C*, 76(4):044004, 2007.

[55] Y Ikeda and T Sato. Resonance energy of the K00AFNN-πYN system. *Phys. Rev. C*, 79(3):035201, March 2009.

[56] Y Ikeda and T Sato. Strange dibaryon resonance in the K [over00AF] NN-πYN system. *Physical Review C*, 76(3):035203, 2007.

[57] S Wycech and A M Green. Variational calculations for K [over00AF]–few-nucleon systems. *Physical Review C*, 79(1):014001, 2009.

[58] M Iwasaki et al. proposal of J-PARC E15. *proposal of J-PARC E15*, December 2006.

[59] TRANSPORT.

[60] K. Agari et al. The k1.8br spectrometer system at j-parc. *PTEP*, page 02B011, 2012.

[61] K. Agari et al. Secondary charged bam lines at the j-parc hadron experimental hall. *PTEP*, page 02B009, 2012.

[62] Hiroyuki Kawamuko, Tsuyoshi Nakaya, Kazunori Nitta, and Masashi Yokoyama. Fiber connector for MPPC. *PoS*, PD07:043, 2006.

[63] M Sato, S Ishimoto, T Hayashi, M Iio, M Iwasaki, and S Suzuki. Development of a super-fluid 4He target system for an experimental search for nuclear states. *Nuclear Instruments and Methods in Physics Research Section A: Accelerators, Spectrometers, Detectors and Associated Equipment*, 606(3):233–237, 2009.

[64] M Iio, S Ishimoto, M Sato, S Enomoto, T Hashimoto, S Suzuki, M Iwasaki, and R S Hayano. Development of a liquid 3 He target for experimental studies of antikaon–nucleon interaction at J-PARC. *Nuclear Instruments and Methods in Physics Research Section A: Accelerators, Spectrometers, Detectors and Associated Equipment*, 687:1–6, 2012.

[65] Y H Huang, G B Chen, X Y Li, and V Arp. Density Equation for Saturated 3He. *International Journal of Thermophysics*, 26(3):729–741, May 2005.

[66] T. K Ohska, T. K Ohska, T Taniguchi, T Taniguchi, Y Watase, Y Watase, Y Yasu, Y Yasu, Y Arai, Y Arai, R S Hayano, R S Hayano, S Inaba, and S Inaba. A New Data Acquisition System at KEK. *Nuclear Science, IEEE Transactions on*, 33(1):98–101, 1986.

[67] TKO SPECIFICATION. *KEK report*, 85-10, January 1985.

[68] M Shiozawa, O Sasaki, M Nomachi, and T. K Ohska. A new TKO system manager board for a dead-time-free data acquisition system. In *1994 IEEE Nuclear Science Symposium - NSS'94*, pages 632–635. IEEE, January 1994.

[69] J.D'Hondt et al. Fitting of event topologies with external kinematic constraints in cms. *CMS Note*, page 1, January 2006.

[70] E. Oset T. Sekihara and A. Ramos. On the structure observed in the in-flight ^{3}he$(k^-, \lambda p)n$ reaction at j-parc. *PTEP*, page 051D01, 2016.

[71] O. Vazquez Doce et al. k^- absorption on two nucleons and ppk^- bound sate search in the $\sigma^0 p$ final state. *Physics Letters B 758*, page 134, May 2016.

Appendix A

Other quantities in Λpn events

In this section, other quantities of each particles in analyzed Λpn events are shown.
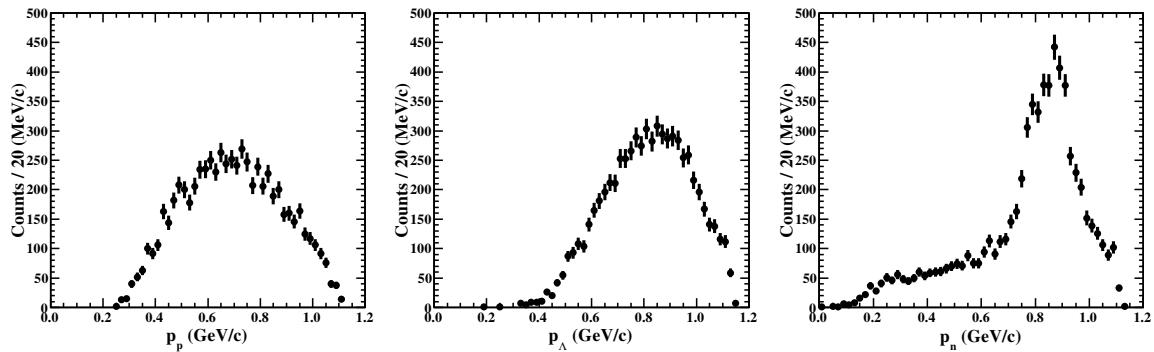
Fig. A.1 Particle momentum distributions in Λpn events.
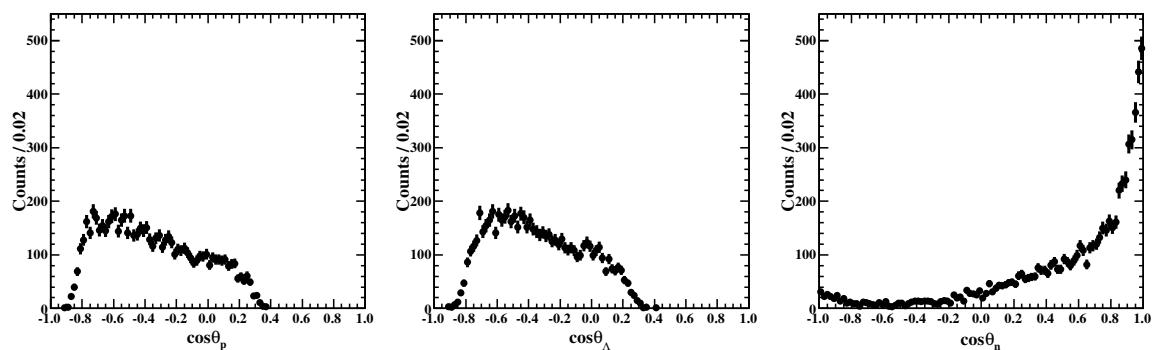

Fig. A.2 Particle angle distributions in Λpn events.
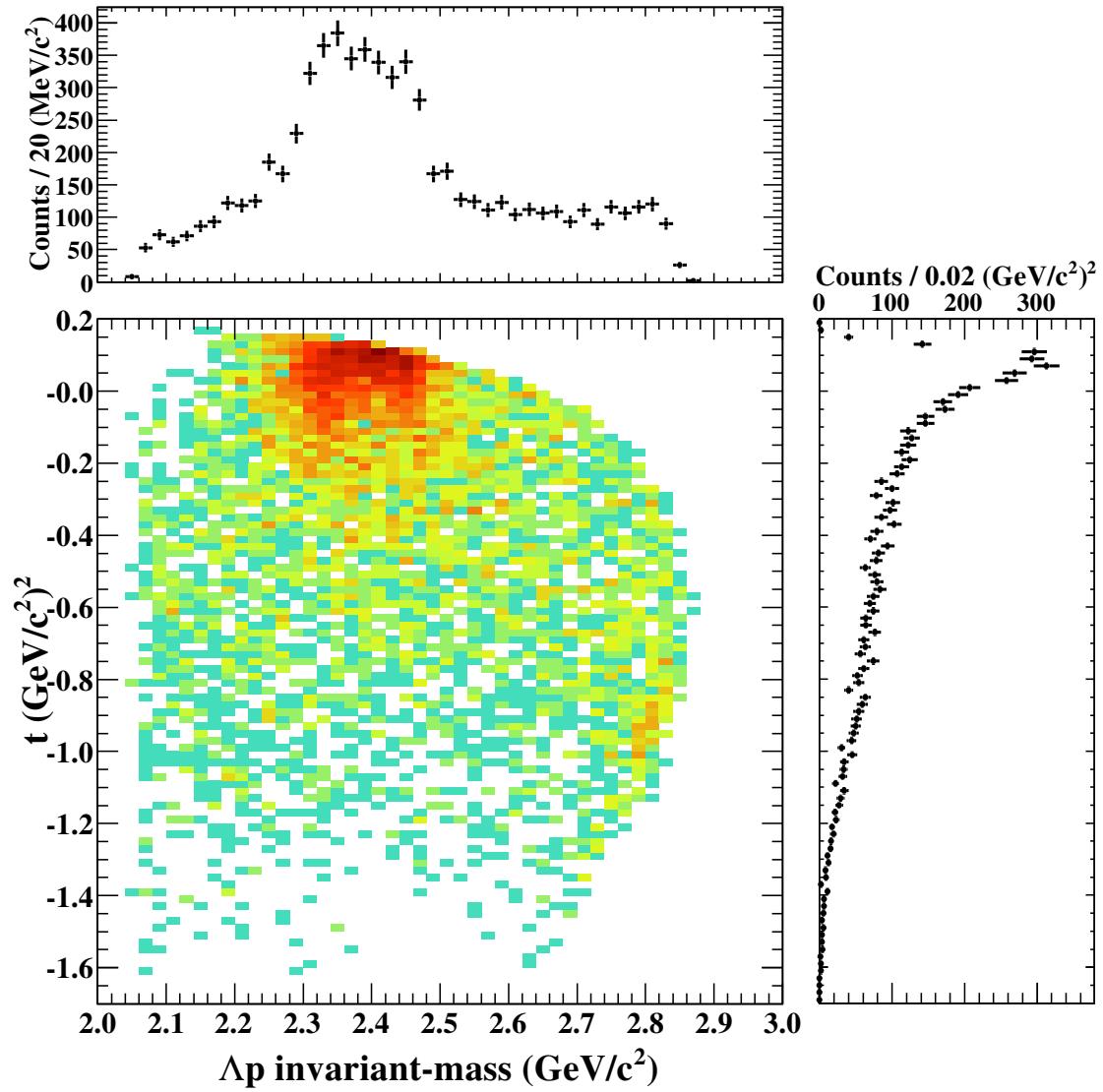
Fig. A.3 2D plot of Λp invariant-mass versus $t(=(E_n - E_{K^-})^2 - (p_n - p_{K^-}))^2)$.

Appendix B

Studying of the kinematical fit

In this section, detail conditions of the kinematical refit used for the Λpn analysis is shown.

B.1   Covariance matrix for the kinematical fit

To determine the covariance matrix, we performed the Monte Calro simulation with flat distribution in the three body phase space. Figures B.1-B.6 show the results of covariance value for each particles. The covariance values are evaluated as width of the distribution of,

$$C = y_{meas.} - y_{gene.},\tag{B.1}$$

where $y_{meas.}$ and $y_{gene.}$ are the some quantities of measured and generated one.

B.2   Difference of the Λp invariant-mass spectrum

In the analysis, we performed the kinematical fit to the measured Λpn events. To check the difference between p invariant-mass spectra with and without kinematical refit, these spectra are overlain in Fig.B.7. As mentioned in Sec.4.6, the invariant-mass resolution is more improved in higher mass region, because of the p invariant-mass strongly depends on the missing neutron's momentum. Therefore, large differences are only seen in that mass region.
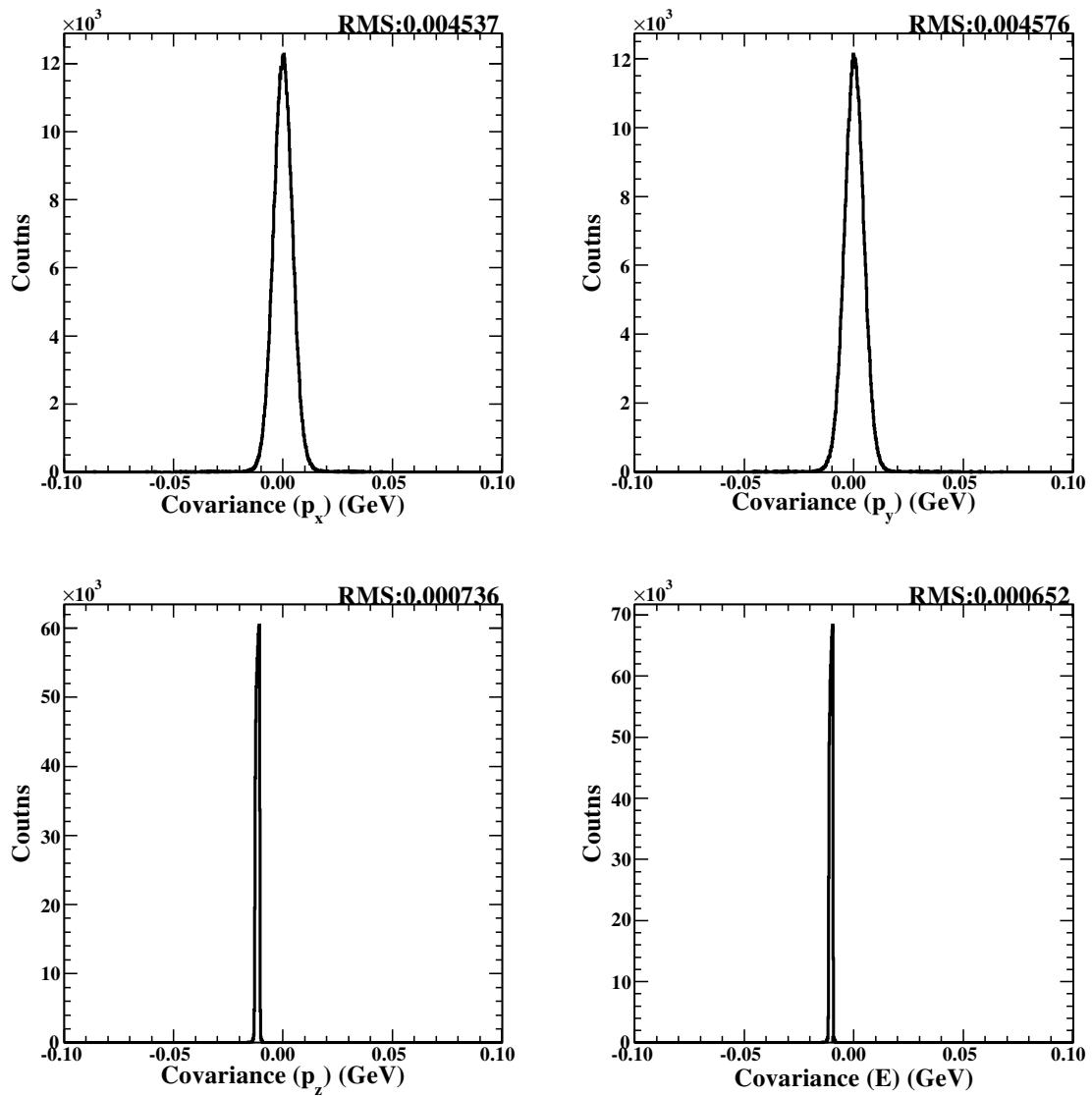
Fig. B.1 Difference of measured and truth momenta and energy of K^--beam.
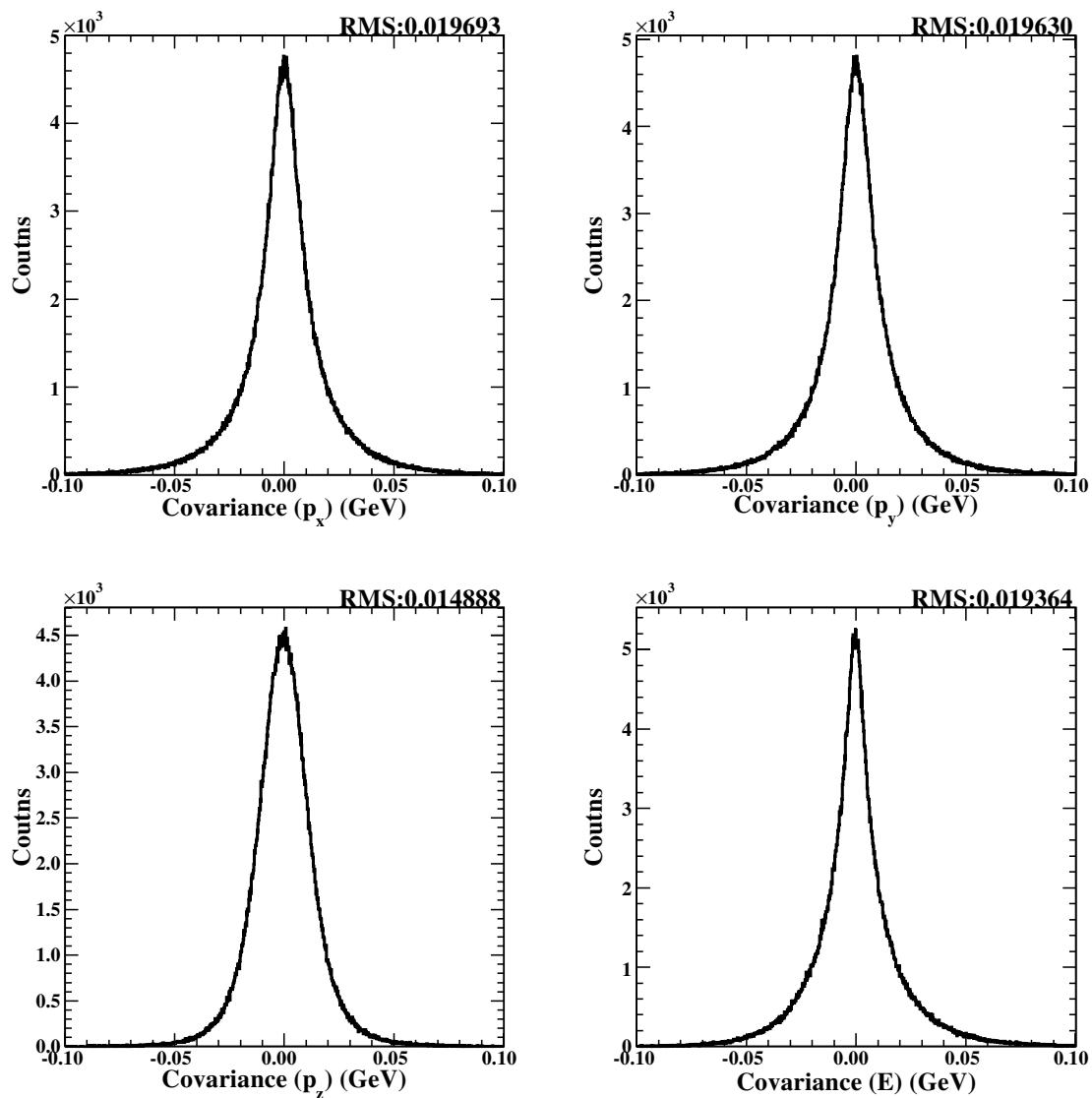
Fig. B.2 Difference of measured and truth momenta and energy of Λ.
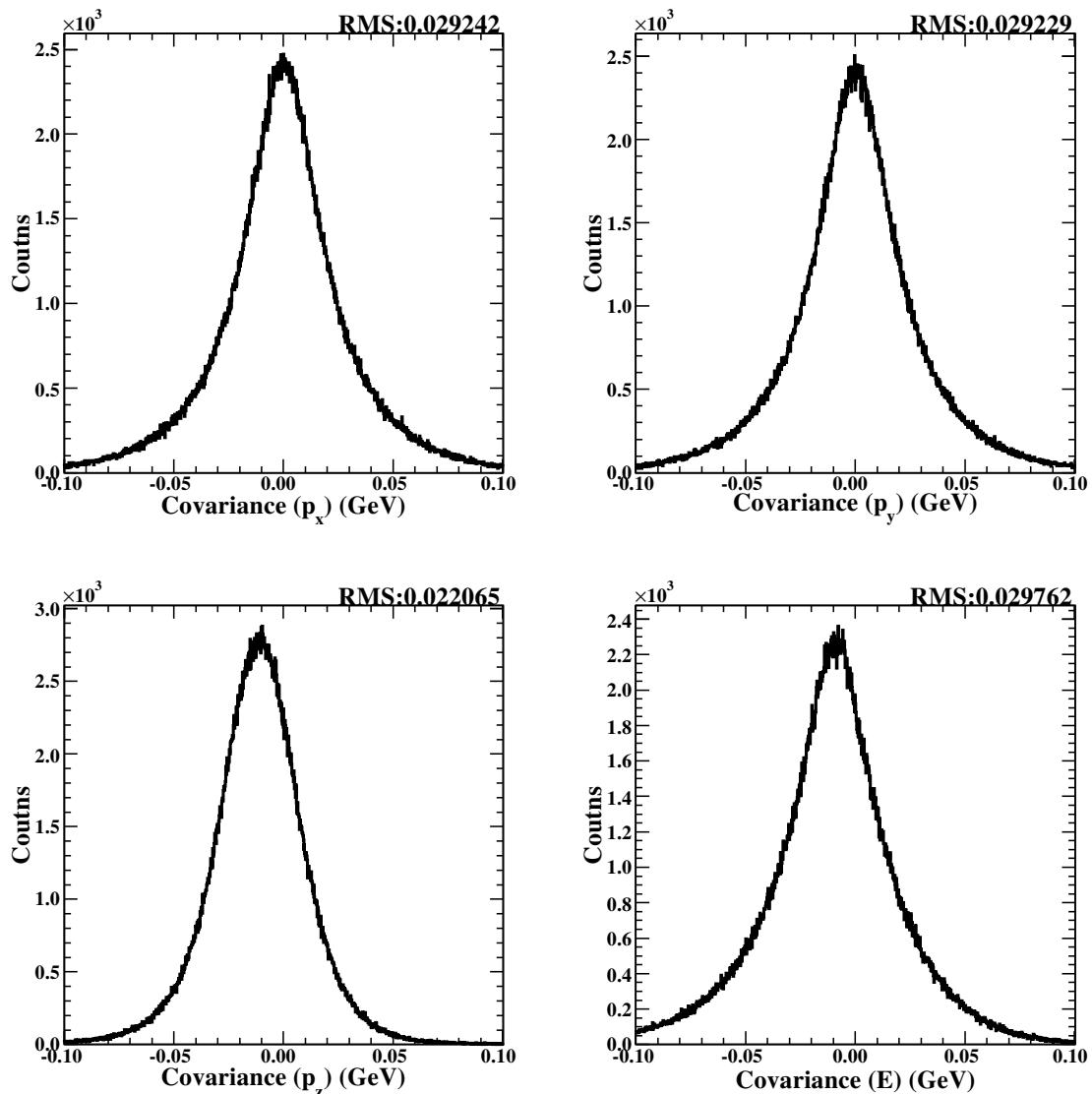
Fig. B.3 Difference of measured and truth momenta and energy of neutron.
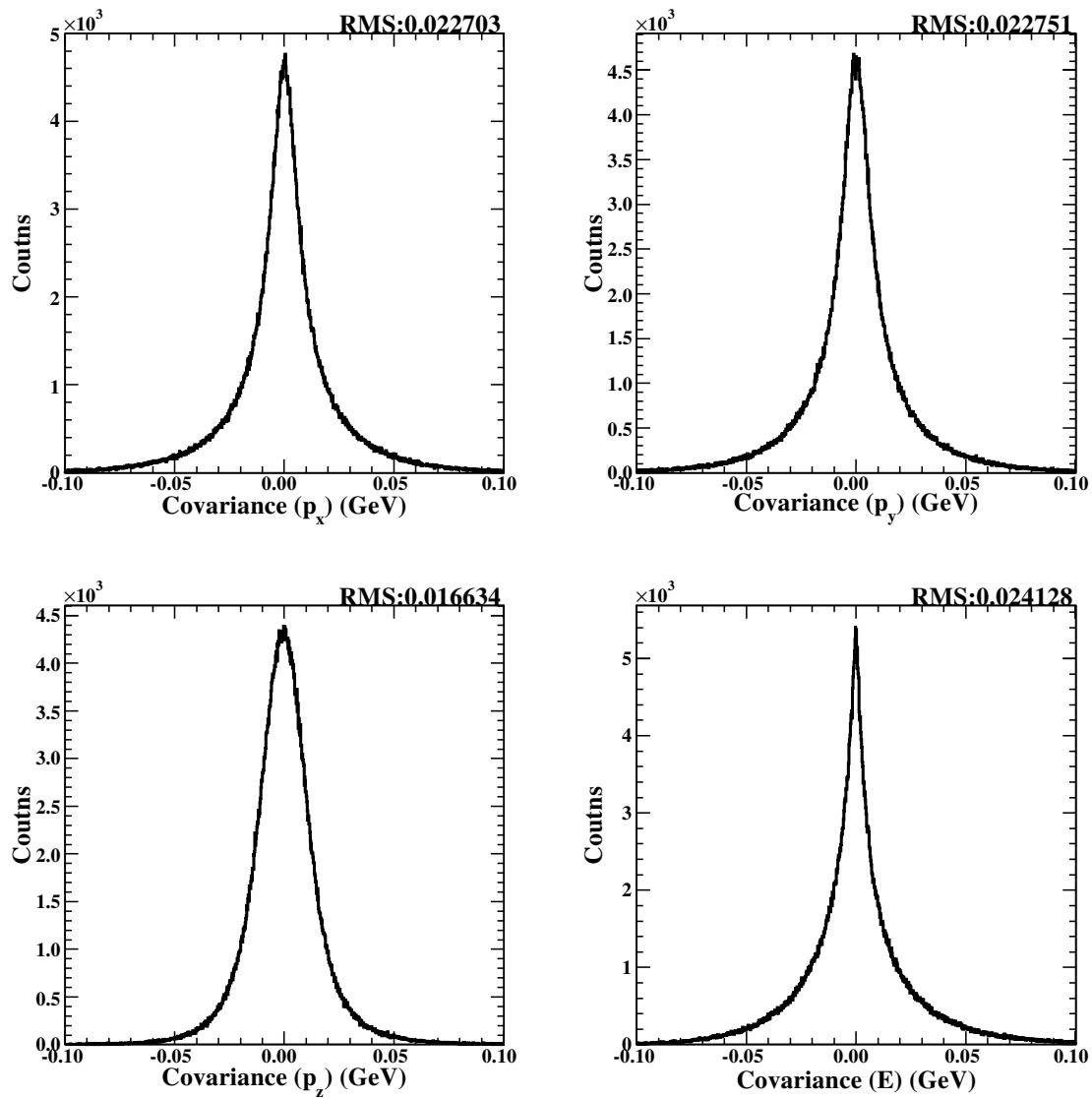
Fig. B.4 Difference of measured and truth momenta and energy of proton.
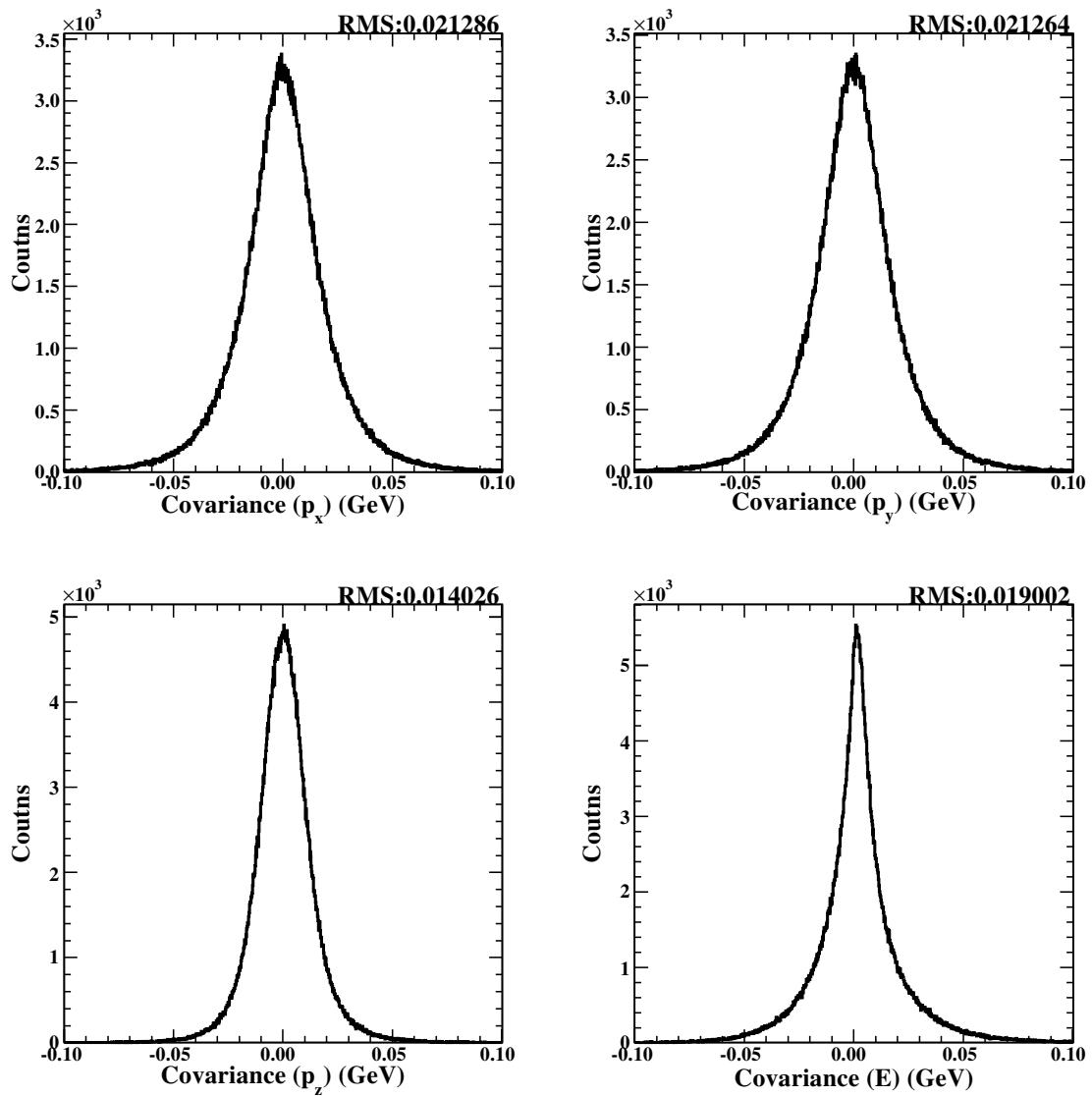
Fig. B.5 Difference of measured and truth momenta and energy of proton from Λ-decay.
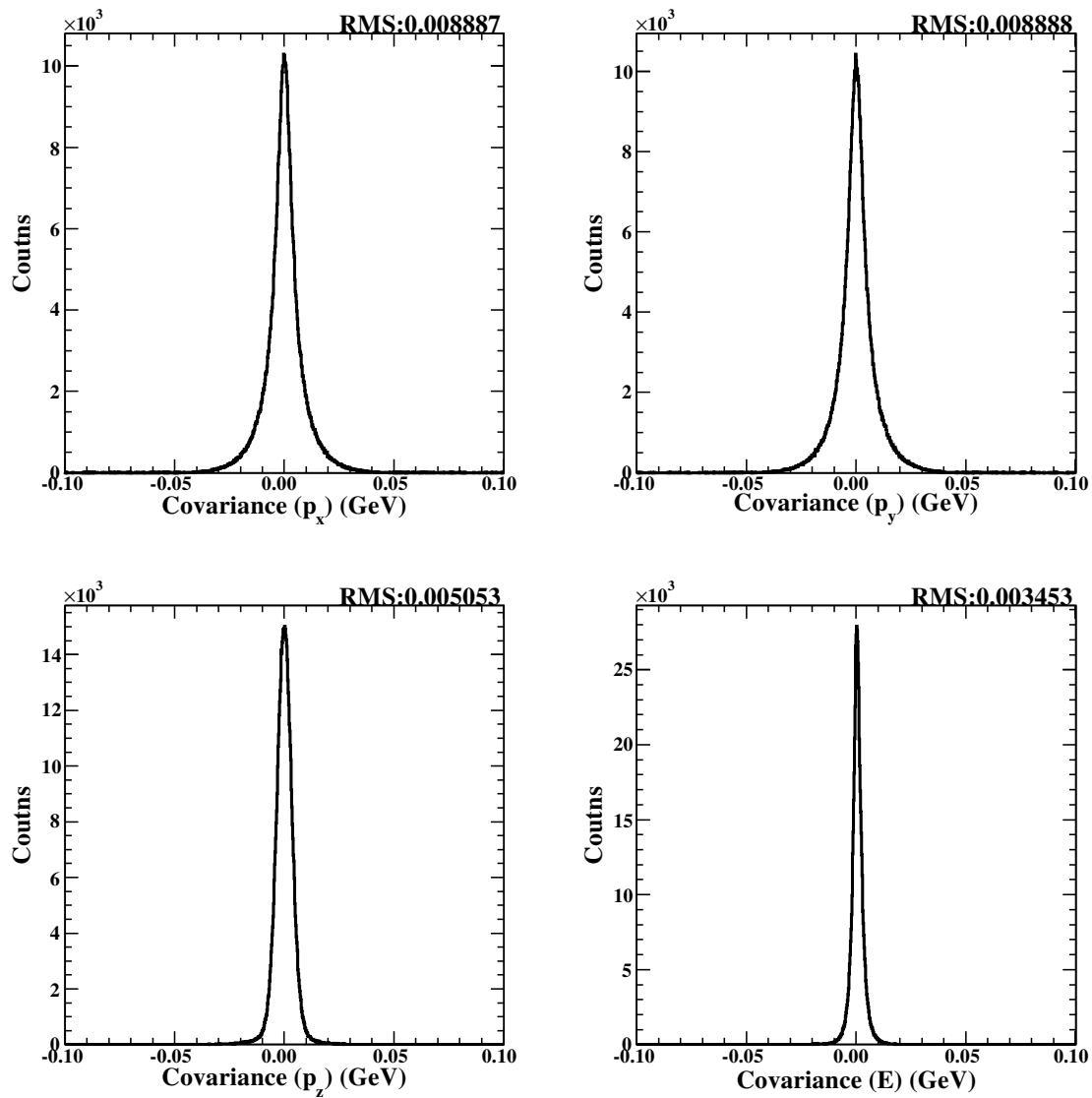
Fig. B.6 Difference of measured and truth momenta and energy of *pi*⁻ from Λ-decay.
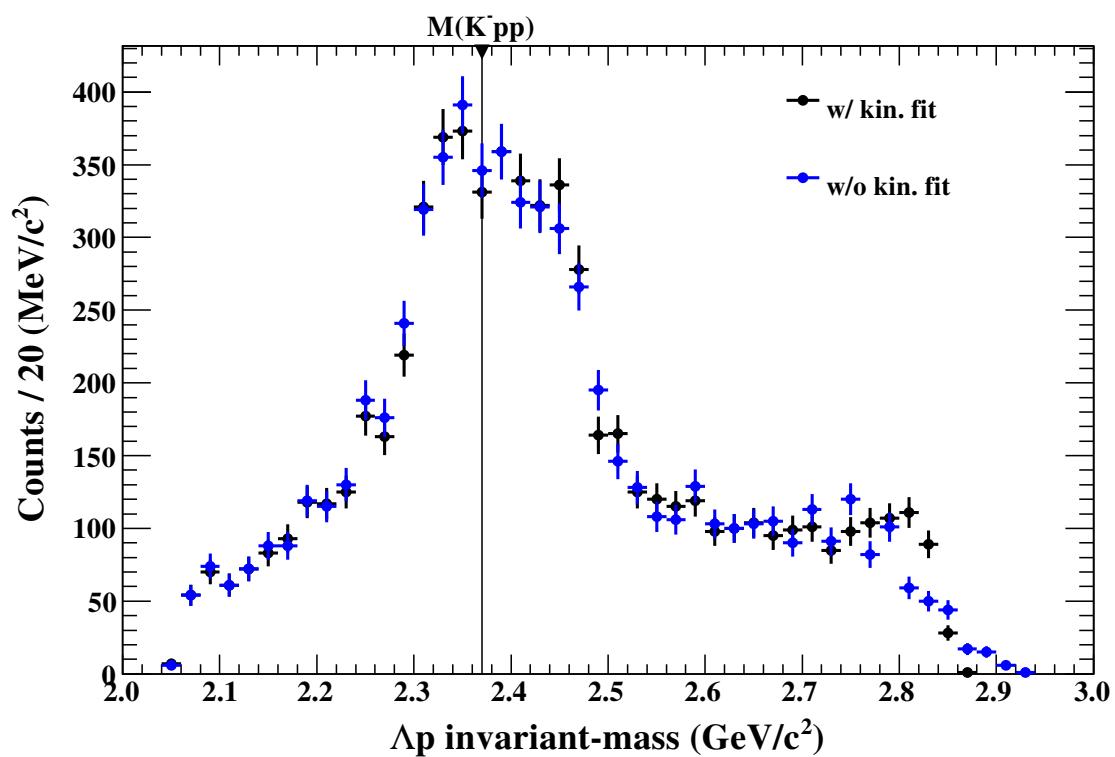
Fig. B.7 Comparison between the Λp invariant-mass spectra with(black) and without(blue) kinematical fit.

Appendix C

Y^* production study with different $MM(\Lambda p)$ region

In the analysis of the $^3\mathrm{He}(K^-, \Lambda p)"n"$ reaction, we selected the missing neutron window from 0.85 to 1.03 GeV/c^2 at the Λp missing-mass spectrum, which is shown in Fig.4.12. We observed a clear locus from the Λpn final state in Fig.4.12. Moreover, there is small locus around the Λp missing-mass around 1.1 GeV/c^2 which comes from pion production reaction, namely Y^* production. In this chapter, Λp invariant-mass spectra for each missing-mass window are studied to try to estimate a production ratio of the hyperon resonances, namely $\Sigma(1385)$ and $\Lambda(1405)$.

C.1 Λp invariant-mass spectra with different missing-mass windows

Ratios of each processes such as Λpn, Σpn, or $Y^* pn$ final states were evaluated by performing a fitting of the missing-mass spectrum, as shown in Fig.4.14. In this section, Λp invariant-mass spectra for different missing-mass windows are shown. Firstly, contributions of each processes in each missing-mass window are evaluated as listed in Tab.C.1. For each missing-mass window, the Λp invariant-mass spectrum is observed as shown in Fig.C.1. In the missing-mass region from 0.85 to 1.03 GeV/c^2, which corresponds to missing neutron, the clear peak structure was observed around $K^- pp$ mass threshold as discussed in Chap.5. There is also broad structure around $K^- pp$ mass threshold with selecting the missing-mass region above the neutron region. If there are some missing particles in the analysis, the Λp invariant-mass does not equal to produced state, and the invariant-mass resolution becomes

much worse than Λpn analysis. Therefore, it is difficult to distinguish peak structure and broad background like a present analysis described in Chap.5.

Table C.1 Relative yield of each contributions in different missing-mass window

missing-mass window (GeV/c^2)	Λpn	$\Sigma^0 pn$	$Ypn+\pi$	$Ypn+2\pi$
0.80 - 0.85	0.958	0.023	0.019	$<10^{-3}$
0.85 - 0.90	0.972	0.021	0.006	$<10^{-3}$
0.90 - 0.95	0.956	0.040	0.004	$<10^{-3}$
0.95 - 1.00	0.832	0.156	0.011	$<10^{-3}$
1.00 - 1.05	0.316	0.509	0.174	0.001
1.05 - 1.10	0.016	0.257	0.724	0.002
1.10 - 1.15	0.002	0.102	0.895	0.002
1.15 - 1.20	$<10^{-3}$	0.042	0.952	0.004
1.20 - 1.25	$<10^{-3}$	0.007	0.961	0.031

C.2   Estimation of Y^* production yield

In the previous section, the Λp invariant-mass spectra with selecting $Ypn+\gamma$ or π region were described. In order to discuss about origin of the peak structure below the $K^- pp$ mass threshold, it is important to consider about Y^* production. Because, if $\Sigma(1385)$ or $\Lambda(1405)$ is generated in the reaction, and converted with residual nucleon into ΛN, it can contribute below the $K^- pp$ mass threshold due to such Y^* has smaller mass than $K^- p$ mass. In this section, Y^* production yield is estimated even though it is difficult to distinguish each processes. We only consider $\Sigma(1385)$ and $\Lambda(1405)$ as Y^* in this analysis. Because, other higher resonances do not contribute to interesting mass region.

In chapter 4, we obtained production ratio of each processes as listed in Tab.4.3. In that list, contribution of Y^* is included in $Ypn+\pi$ final state. We evaluated the yield of Y^* production in the $Ypn+\pi$ final state events by simultaneously fitting of invariant-mass and missing-mass of Λp. Figs.C.2,C.3 show the fitting results. Because of only simple reaction, where particle momenta distributed in all phase space, is considered, fitting of Λp invariant-mass is not good. Y^* production ratio is estimated as the same value as Λpn final state events, namely $Y^* pn/\Lambda pn \sim 1$. It is difficult to fix this ratio by this analysis. To evaluate the correct $Y^* pn/\Lambda pn$ ratio, it is necessary to detect γ and/or π^0 to reconstruct Y^*. However, we consider that the order of this ratio is not so different from correct value.
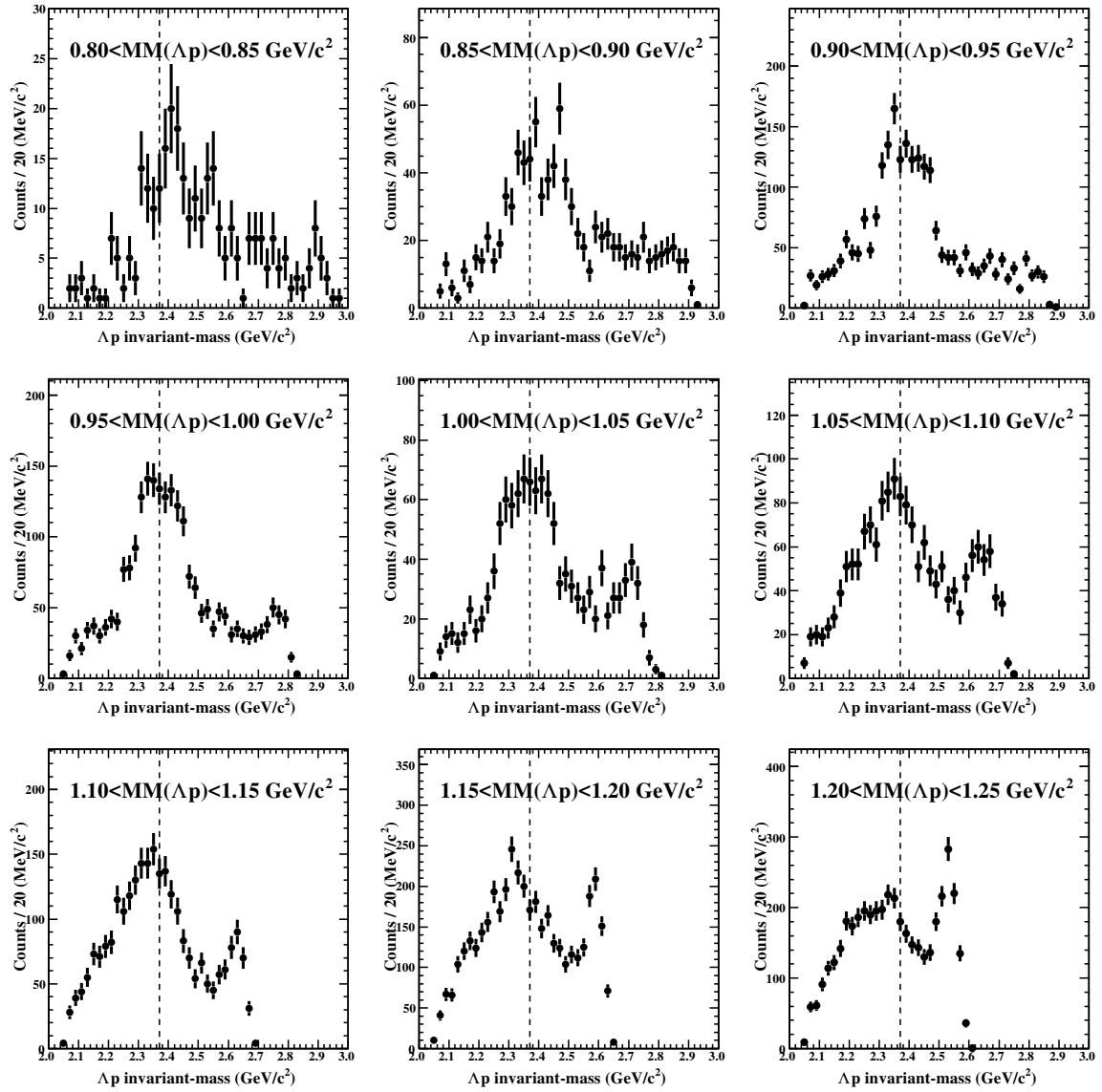
Fig. C.1 Λp invariant-mass spectra of different Λp missing-mass windows. Dashed lines in figures show $K^- pp$ mass threshold.
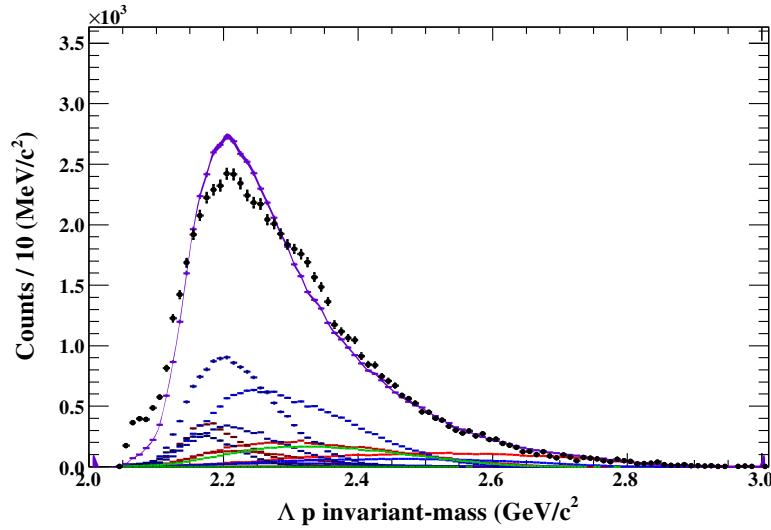
Fig. C.2 Λp invariant-mass spectrum. Color plot and line indicates fitting results.
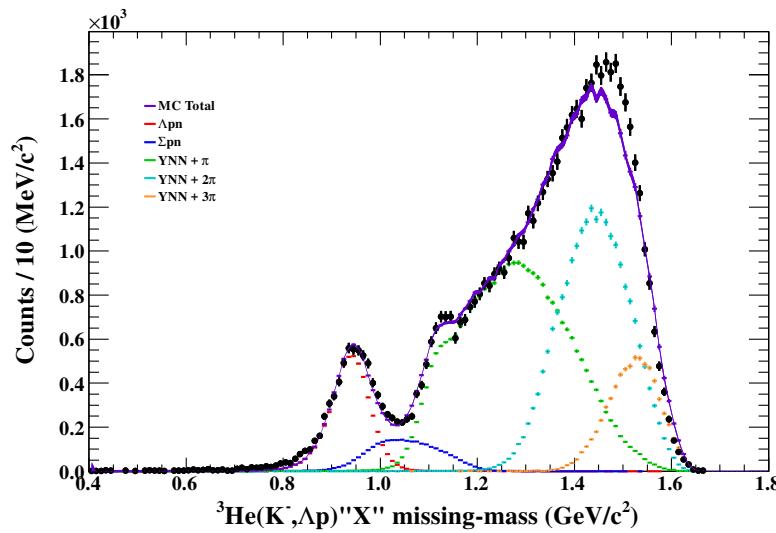

Fig. C.3 Λp missing-mass spectrum. Color plot and line indicates fitting results.

C.3   Studying for Y^* contribution in Λpn final state

The contribution of Y^* production events can be considered as following reaction,

$$K^- + {}^3\text{He} \rightarrow Y^* + n + p_{spec},$$

$$Y^* + p_{spec} \rightarrow \Lambda + p.$$
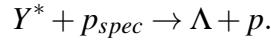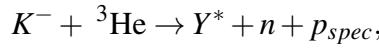
In the previous section, the ratio of $Y^*pn/\Lambda pn$, which corresponds to the first reaction, was estimated to be the same order as described in previous section. To evaluate the yield from Y^* production, we must know the strength of the second reaction which has not been measured. However, we can estimate the maximum yield from Y^* production, which is obtained by assuming the all produced Y^* go to Λpn final state. In that situation, the yield from Y^* production would be the same order of magnitude as the yield of Λpn final state. Therefore, the peak structure can be explained by only Y^* production if the spectrum shape of such process can reproduce the observed Λp invariant-mass spectrum.

To do that, we performed the Monte Calro simulation of $\Sigma(1385)$ and $\Lambda(1405)$ production processes. In Figs.C.4,C.5 show a Λp invariant-mass spectra of observed one and simulated one. In this studying, Y^* yield is modified with the order of the Y^* production is less than the yield of Λpn final state. The Monte Calro simulation, the peak position of the QF-Y^* process moves to higher mass side with decreasing $\cos\theta_n^{CM}$, as mentioned in chapter 5. Therefore, the data spectrum can not be reproduced by QF-Y^* process in the lower $\cos\theta_n^{CM}$ value, even $\cos\theta_n^{CM} \sim 1$ of $\Lambda(1405)$ production. From these studies, we conclude that the peak structure observed below the K^-pp mass threshold can not be explained by QF-Y^* processes.
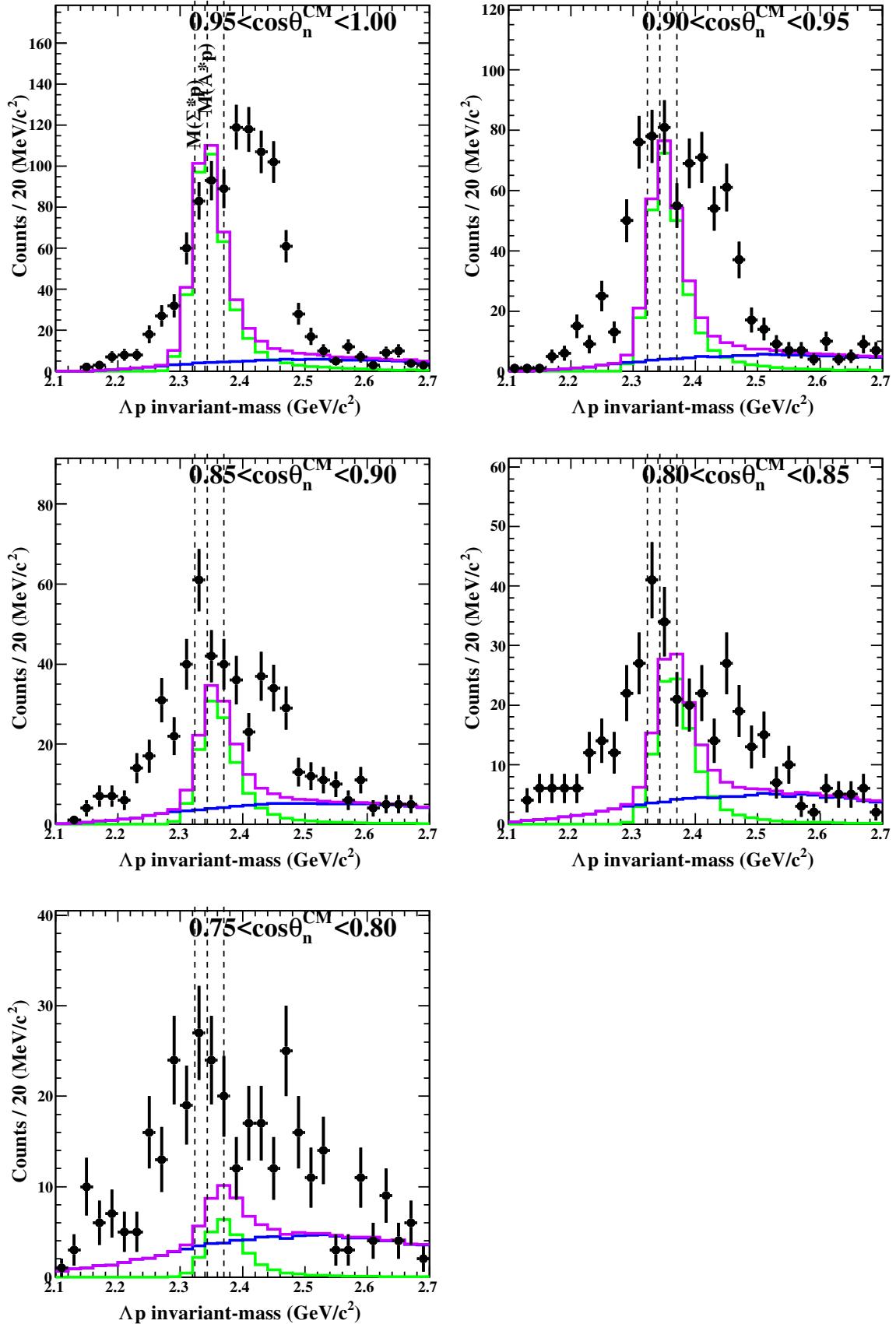
Fig. C.4 Λp invariant-mass spectra of different $\cos\theta_n^{CM}$ regions. The black plots and colored lines show data and Monte Calro simulation results, respectively. In the Monte Calro simulation, we considered three nuclear absorption process (blue) and (1385) production process (green).
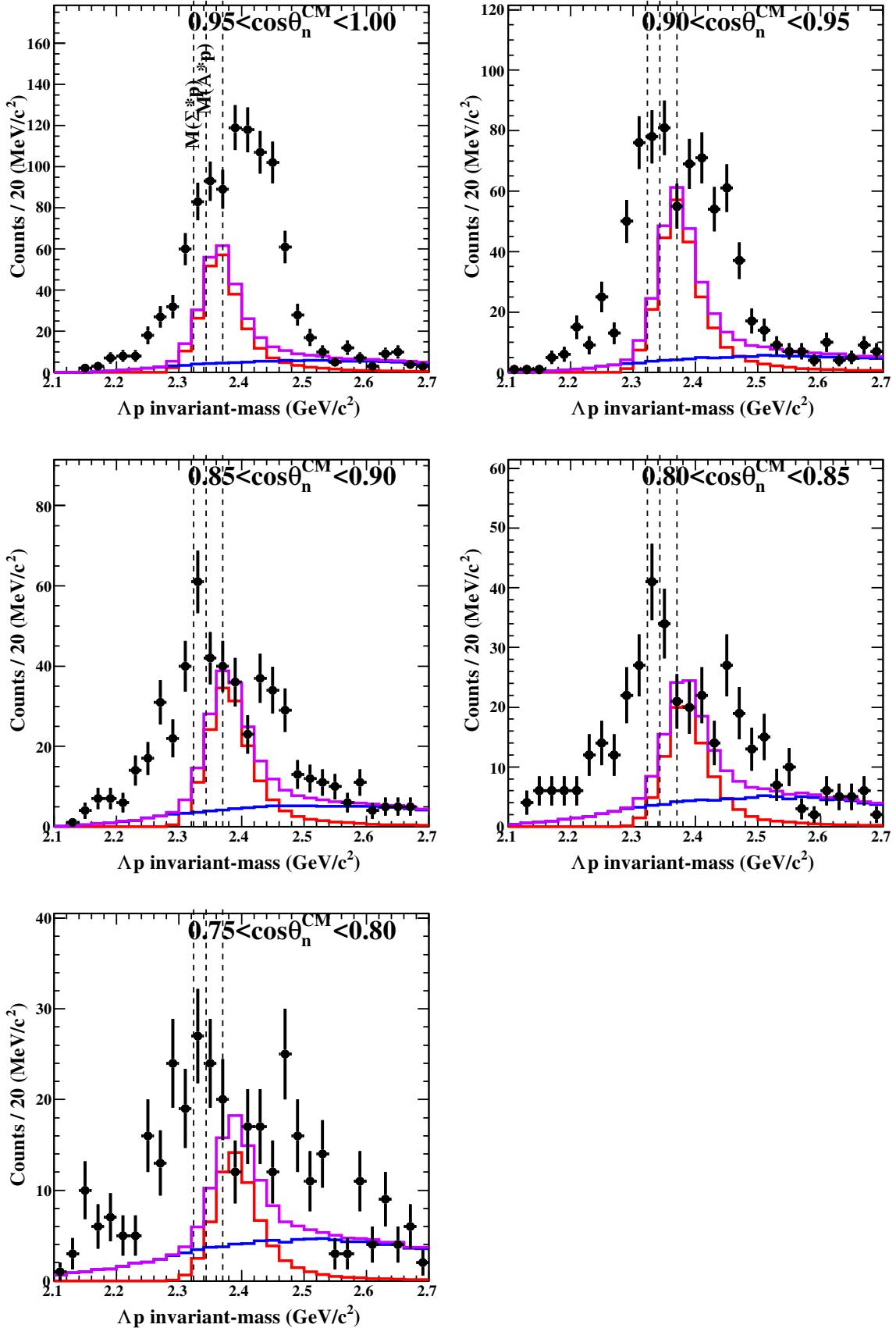
Fig. C.5 Λp invariant-mass spectra of different $\cos\theta_n^{CM}$ regions. The black plots and colored lines show data and Monte Calro simulation results, respectively. In the Monte Calro simulation, we considered three nuclear absorption process (blue) and $\Lambda(1405)$ production process (red).